6-24-2016 12:00 AM

Application Of Polarimetric SAR For Surface Parameter Inversion And Land Cover Mapping Over Agricultural Areas

Xiaodong Huang
The University of Western Ontario

Supervisor
Dr. Jinfei Wang
The University of Western Ontario

Graduate Program in Geography
A thesis submitted in partial fulfillment of the requirements for the degree in Doctor of Philosophy

Abstract

In this thesis, novel methodology is developed to extract surface parameters under vegetation cover and to map crop types, from the polarimetric Synthetic Aperture Radar (PolSAR) images over agricultural areas. The extracted surface parameters provide crucial information for monitoring crop growth, nutrient release efficiency, water capacity, and crop production. To estimate surface parameters, it is essential to remove the volume scattering caused by the crop canopy, which makes developing an efficient volume scattering model very critical.

In this thesis, a simplified adaptive volume scattering model (SAVSM) is developed to describe the vegetation scattering as crop changes over time through considering the probability density function of the crop orientation. The SAVSM achieved the best performance in fields of wheat, soybean and corn at various growth stages being in convert with the crop phenological development compared with current models that are mostly suitable for forest canopy.

To remove the volume scattering component, in this thesis, an adaptive two-component model-based decomposition (ATCD) was developed, in which the surface scattering is a X-Bragg scattering, whereas the volume scattering is the SAVSM. The volumetric soil moisture derived from the ATCD is more consistent with the verifiable ground conditions compared with other model-based decomposition methods with its RMSE improved significantly decreasing from 19 [vol.%] to 7 [vol.%].

However, the estimation by the ATCD is biased when the measured soil moisture is greater than 30 [vol.%]. To overcome this issue, in this thesis, an integrated surface parameter inversion scheme (ISPIS) is proposed, in which a calibrated Integral Equation Model together with the SAVSM is employed. The derived soil moisture and surface roughness are more consistent with verifiable observations with the overall RMSE of 6.12 [vol.%] and 0.48, respectively.

Additionally, the soil moisture and roughness extraction algorithms are also dependent on the crop types. In this thesis, a novel multi-temporal supervised binary-tree classification scheme with a criterion that maximizes the difference of polarization signature (MTSBTCS-MDPS) is developed. Compared with the Wishart distance (MTSBTCS-WD) method, the MTSBTCS-MDPS not only consumes much less processing time, but also achieves much higher overall accuracy (87.5%) and kappa coefficient (0.85).

Keywords

Polarimetric SAR, RADARSAT-2, surface scattering model, volume scattering model, model-based decomposition, soil moisture, surface roughness, polarization signature, land cover mapping.

Co-Authorship Statement

This thesis was prepared according to the integrated-article layout designated by the Faculty of Graduate Studies at The University of Western Ontario, London, Ontario Canada. All the work stated in this thesis including methods development, results validation, data analysis and manuscript drafting for publication was carried out by the author under the supervision of Dr. Jinfei Wang and Dr. Jiali Shang. Chapters 2, 3, 4 have been published and Chapter 5 is submitted under review as co-authored peer reviewed journal papers with the co-authors shown below. Dr. Wang and Dr. Shang both contributed in the valuable comments, editing and revision of the manuscripts, financial support, and software/hardware/data.

Huang, X., Wang, J., and Shang J. (2016a). Application of Polarization Signature to Crop Monitoring and Classification Using Multi-Temporal C-Band Polarimetric RADARSAT-2 Imagery, *Remote Sensing of Enviroment*, Major Revision.

Huang, X., Wang, J., and Shang J. (2016b). An Adaptive Two-Component Model-Based Decompostion on Soil Moisture Estiamtion for C-Band RADARSAT-2 Imagery over Agricultrua Fields, *IEEE Geoscience and Remote Sensing Letters*, *13*(3), 414-418.

Huang, X., Wang, J., and Shang J. (2016c). An Integrated Surface Parameter Inversion Scheme over Agricultural Fields at Early Growing Stages by Means of C-Band Polarimetric RADARSAT-2 Imagery, *IEEE Transactions on Geoscience and Remote Sensing*, *54*(5), 2510-2528.

Huang, X., Wang, J., and Shang J. (2015). A Simplified Adaptive Volume Scattering Model and Scattering Analysis of Crops over Agricultrual Fields Using the RADARSAT-2 Polarimetric SAR Imagery, *Journal of Applied Remote Sensing*, *9*(1), 096026-1-096026-18.

Dedicated to my wife, Lili Jiang

Acknowledgments

The author would like to first express his sincere gratitude to his supervisor Dr. Jinfei Wang for her valuable guidance and constant encouragement throughout the entire process of the three-year Ph.D. study. This thesis research is also partially supported by her NSERC discovery grant. Her motherhood nature is forever remembered and appreciated by the author.

Secondly, the author would also like to sincerely acknowledge Dr. Jiali Shang from Agriculture and Agri-Food Canada (AAFC) not only for her provide of the RADARSAT-2 and RapidEye data, but also for her helpful and careful review and discussion of each published peer-reviewed paper and the draft of the Ph.D. thesis. Thanks also are given to her modest, humble, and generous nature as a scientist always inspires the author in doing better research.

The author would also like to thank his committee members Dr. Micha Pazner and Dr. Phil Stooke. The smartness of Dr. Pazner is fondly remembered by the author not only in the comprehensive exams but also in the Ph.D. proposal development. Dr. Stooke's sincerity and kind efforts during the entire Ph.D. program have won the author's heartfelt appreciation.

The author would also like to thank Greg Patterson, Daryl Patterson, and Bo Shan from A&L Canada Laboratories Inc. for their selfless help of the soil sample collection, provision of the soil texture data. Thank also goes to A&L Canada Laboratories Inc. for offering me a part-time job as software developer. This valuable employment has provided me with both work experience and financial support.

The author would like to thank Dr. Minfeng Xing from the University of Electronic Science and Technology of China for his helpful advice and discussion on Chapter 4 and Chapter 5.

Boyu Feng, Zhenpei Li, Chunhua Liao, Qin Ma, Ian Pritchard, Jianbin Shi, Yang Song, and Chuiqing Zeng from the Geographic Information Technology and Application (GITA) lab are also thanked not only for their kind help during field work, but also for the wonderful time have shared together.

Last but not least, the author would like to deeply thank his wife Mrs. Lili Jiang for her love, understanding, and continuous support to the author's career choice from the other side of the Pacific Ocean. The author's parents and sister are also thanked for their love and support.

Table of Contents

Abstract i

Co-Authorship Statement iii

Acknowledgments v

Table of Contents vii

List of Tables xi

List of Figures xiii

List of Appendices xxi

List of Acronyms xxii

Chapter 1 Introduction 1

1.1 Surface Parameter Retrieval over Bare Soil 4

1.2 Volume Scattering Model over Agricultural Fields 9

1.3 Scattering Mechanisms over Agricultural Fields 11

1.4 Land Cover Mapping 18

1.5 Objectives and Organization 20

References 22

Chapter 2 Simplified Adaptive Volume Scattering Model and Scattering Analysis of Crops over Agricultural Fields 31

2.1 Introduction 31

2.2 The Framework of Model-Based Decomposition 32

2.3 Simplified Adaptive Volume Scattering Model and TCMD-SAVSM 34

2.3.1 Framework of Volume Scattering Model Construction 34

2.3.2 Simplified Adaptive Volume Scattering Model (SAVSM) 35

2.3.3 Analysis of SAVSM 38

2.3.4 The Algorithm of TCMD-SAVSM 40

2.4 Experiments and Validation 42

2.4.1 Experimental Dataset 42

2.4.2 Comparison of TCMD-SAVSM with AMD 43
2.4.3 SAVSM Validation Compared with FD-VSM, Y-VSM, An-VSM and Antropov-VSM 48
2.5 Three Components Analysis of Corn, Soybean and Wheat 52
2.5.1 Corn Analysis 53
2.5.2 Soybean Analysis 54
2.5.3 Wheat Analysis 55
2.6 Conclusion 56
References 58
Chapter 3 An Adaptive Two-Component Model-Based Decomposition on Soil Moisture Estimation 62
3.1 Introduction 62
3.2 Coherency Matrix 63
3.3 Surface Scattering Model 64
3.3.1 Bragg Scattering Model 64
3.3.2 Extended Bragg Surface Scattering 66
3.4 Volume Scattering Model 69
3.4.1 Volume Scattering Construction Framework 69
3.4.2 Probability Distribution Function 70
3.4.3 Adaptive Volume Scattering Model 71
3.5 Adaptive Two-Component Decomposition 75
3.5.1 Two-Component Decomposition 75
3.5.2 Non-negative Eigenvalue Method for f_v 76
3.5.3 Adaptive Decomposition for Optimal Solution 78
3.6 Soil Moisture Estimation 79
3.7 Experiments 82
3.7.1 Dataset, Ground Truth Measurement and Data Process 82
3.7.2 Scattering Mechanism Analysis 83
3.7.3 Qualitative Analysis 85
3.7.4 Quantitative Analysis 88

3.8 Conclusion 91
References 92
Chapter 4 An Integrated Surface Parameter Inversion Scheme over Agricultural Fields 95
4.1 Introduction 95
4.2 Study Areas and Data Collection 98
4.2.1 Data Collection 98
4.2.2 Ground Truth Measurement 100
4.3 Scattering Analysis over Agricultural Fields 103
4.3.1 Scattering Mechanisms Analysis 103
4.3.2 Threshold Selection and the ISPIS 107
4.4 Integrated Surface Parameter Inversion Scheme (ISPIS) 111
4.4.1 Bragg and X-Bragg Surface Scattering Models 111
4.4.2 Calibrated Integral Equation Model 113
4.4.3 Simplified Adaptive Volume Scattering Model (SAVSM) 115
4.4.4 Adaptive Two-Component Decomposition 120
4.5 Validation and Analysis 122
4.5.1 T_1 Maps of Different Crop Fields 122
4.5.2 Soil Moisture Validation 125
4.5.3 Surface Roughness Validation 132
4.5.4 RVI and Vegetation Water Content (VWC) of Wheat 138
4.5.5 Simple Analysis of the Two-way Attenuation by Crop Canopy 140
4.5.6 Discussion of Scattering over Bare Soils 145
4.6 Conclusion 147
References 149
Chapter 5 Application of Polarization Signature to Crop Monitoring and Classification 155
5.1 Introduction 155
5.2 Polarization Signature (PS) 158
5.2.1 Polarization Ellipse 158
5.2.2 Polarization Signature 159

5.2.3 Correlation Coefficient and Pedestal Height of PS 163
5.3 Supervised Binary-Tree Classification Scheme (SBTCS) 164
5.3.1 Maximum Difference of Polarization Signature (MDPS) 164
5.3.2 Supervised Binary-Tree Classification Scheme (SBTCS)..... 166
5.4 Scattering Analysis and Classification Validation 168
5.4.1 Dataset, Data Process and Ground Truth Photos 168
5.4.2 Polarization Signature Analysis 171
5.4.3 Classification 184
5.5 Conclusion 191
References..... 193
Chapter 6 Conclusion and Discussion 196
6.1 Summary..... 196
6.2 Conclusions and Contributions..... 199
6.3 Future Research 201
6.3.1 Volume Scattering Model Considering the Shape Parameter 201
6.3.2 Surface Parameter Inversion under Dense Vegetation Cover 203
6.3.3 Integration of Land Cover Map and Surface Parameter Inversion Scheme 204
6.3.4 Relations with the RCM 205
References..... 206
Curriculum Vitae 237

List of Tables

Table 1-1. Surface scattering models. Note: mv is the volumetric soil moisture with its unit [vol.%]; ks is the surface roughness with k wavenumber and s the root mean square of surface height. 8

Table 2-1. Comparison of SAVSM with other volume scattering models. 40

Table 2-2. RADARSAT-2 dataset acquired over southwestern Ontario, Canada. 43

Table 2-3. Comparison of TCMD-SAVSM with AMD within different ∇f_v. To test the time different algorithms consume, the configuration of the workstation is windows 7 professional with processor i7 3.20 GHZ and ram 24 GB. All programs are implemented using Matlab 2013a (64 bit). 44

Table 2-4. Results of percentages of PRM less than 0.001 for corn. 51

Table 2-5. Results of percentages of PRM less than 0.001 for soybean. 51

Table 2-6. Results of percentages of PRM less than 0.001 for winter wheat. 52

Table 3-1. Comparison with other volume scattering models. 74

Table 3-2. RADARSAT-2 datasets. IA: Incidence Angle. DoY: Day of Year. 83

Table 3-3. RMSE of different methods in wheat fields on different dates in two study areas (unit:%). 90

Table 4-1. RADARSAT-2 dataset and fieldwork schedule. The blue cell represents the data acquired on that day while grey cell means no fieldwork or dataset acquired on that day. MV: soil moisture. KS: surface roughness. The resolution (unit: m) is the one after geo-correction using the Mapready software. 99

Table 4-2. Measured ground truth on different dates in different agricultural fields. MV: soil moisture ([vol.] %). RMS: root mean square of the surface height (cm). H: height of vegetation or corn residue (cm). Note: "-" means no data was

collected on that day. The height measured in soybean field before June 4th 2014 is the height of the standing corn stubbles. 101

Table 4-3. The statistic information of the H and α on different dates in different fields. 109

Table 4-4. Comparison of the SAVSM with the Freeman and Yamaguchi volume scattering models in terms of their RVI and entropy. 120

Table 4-5. Soil texture of each site in study area 2014. 126

Table 4-6. RMSE and R^2 information on different days ([vol. %]). 130

Table 4-7. Crop parameters of different agricultural fields in study area 2014 at different growing stages for C-band RADARSAT-2 data with its frequency of 5.405 GHZ. S01: 2014 May 5th; S02: 2014 May 18th; S03: 2014 June 04th; S04: 2014 June 21st 142

Table 5-1. Polarization signatures and coherency matrices of canonical scatterings. 162

Table 5-2. Dataset. 169

Table 5-3. Pedestal height (PH). 179

Table 5-4. Look-Up Table of MTSBTCS-MDPS 185

Table 5-5. Look-Up Table of the MTSBTCS-WD. 186

Table 5-6. Overall accuracy and kappa coefficient of MDPS and WD when they are applied to the single-date image 189

Table 5-7. Confusion matrix of MTSBTCS-MDPS. Note: OA is overall accuracy, UA is user accuracy, and PA is producer accuracy. 189

Table 5-8. Execution time of algorithmS (unit: s). All algorithms are implemented by the 64 bit python program using a desktop with four cores of CPU E3-1226 3.3 GHZ. The operating system is a 64-bit windows 8.1. The RAM is 16g..... 191

Table E-1. Specific parameters for each soil type. 222

List of Figures

Figure 1-1. Brief category of surface scattering models. 4

Figure 1-2. Reflection and transmission of radar wave over a flat surface. 5

Figure 1-3. Scattering from a rough surface. 6

Figure 1-4. Volume scattering in different radar frequencies. 9

Figure 1-5. Five important scattering mechanisms over agricultural fields. 12

Figure 1-6. Water cloud model. 13

Figure 1-7. Discrete scatterers of tree canopy. Adapted from Burgin et al. (2011)..... 14

Figure 1-8. Specific intensity $I(\hat{s})$ in direction s in and out of elemental volume. 15

Figure 1-9. Scattering components in model-based decomposition. (a) surface scattering. (b) double-bounce scattering. (c) volume scattering. 17

Figure 1-10. Different scattering process simulation scenarios. 18

Figure 1-11. Relationships among the five thesis chapters. 21

Figure 2-1. PDFs of vertical adaptive volume scattering model with orientation angles. 36

Figure 2-2. Vertical volume scattering matrix: (a) components of adaptive volume scattering matrix (b) entropy, RVI and randomness of adaptive volume scattering matrix. 39

Figure 2-3. The flowchart of the TCMD-SAVSM for each pixel in covariance matrix. . 41

Figure 2-4. Pauli and RapidEye images of study area on day 152 and 160 respectively: (a) Pauli image with red $|S_{HH} - S_{VV}|^2$, green $4|S_{HV}|^2$ and blue $|S_{HH} + S_{VV}|^2$: polygons outlined fields that are sample fields that will be analyzed in next sections. (b) Optical RapidEye image. 43

Figure 2-5. Comparison of the PRM between TCMD-SAVSM and AMD on each image acquisition date over agricultural fields. 45

Figure 2-6. Decomposed components by AMD with the RADARSAT-2 image on day 152: (a) surface scattering component (b) double-bounce scattering component (c) volume scattering component (d) randomness. 46

Figure 2-7. Decomposed components by TCMD-SAVSM: (a) surface scattering (b) double-bounce scattering (c) volume scattering (d) n..... 47

Figure 2-8. Power of different crops on each date. (a) corn (b) soybean (c) wheat. 50

Figure 2-9. Ground photos of corn: (a) day 152 (b) day 176 (c) day 224 (d) day 272. 53

Figure 2-10. Ground photos of soybean field: (a) day 152 (b) day 224 (c) day 248 (d) day 272. 53

Figure 2-11. Ground photos of winter wheat: (a) day 128 (b) day 176 (c) day 200 (d) day 272. 53

Figure 2-12. Surface, double bounce, and volume components of corn..... 54

Figure 2-13. Surface, double bounce, and volume components of soybean..... 55

Figure 2-14. Surface, double bounce, and volume components of wheat. 56

Figure 3-1. Relationship between ε_r and β. 65

Figure 3-2. $y = sinc\ 4\theta$. 67

Figure 3-3. $y = e^{-8\sigma^2}$. 69

Figure 3-4. Vertical volume scattering components. 73

Figure 3-5. RVI and Entropy. 75

Figure 3-6. Relationship between soil moisture and relative dielectric constant. 80

Figure 3-7. Flowchart of soil moisture estimation using the ATCD. 81

Figure 3-8. Location of the study area and Pauli images acquired on May 9th 2013 and May 6th 2015, with red $|S_{HH} - S_{VV}|^2$, green $4|S_{HV}|^2$ and blue $|S_{HH} + S_{VV}|^2$ 83

Figure 3-9. Plots of H-α decomposition on wheat and bare soil fields on three different dates in study area 2013; from left to right, they are day 119, 129, 143, respectively. (a) Wheat field. (b) Bare soil field. 85

Figure 3-10. Histograms of orientation angles over bare soils in study area 2013. (a) day 129 (b) day 143. 85

Figure 3-11. Comparison of different soil moisture estimation methods on three different dates in study area 2013; from left to right, they are the soil moisture derived from the A-FVSM, A-YVSM, FD, YD and ATCD. (a) day 119. (b) day 129. (c) day 143. 87

Figure 3-12. Decomposed components and inversed soil moisture from ATCD on different dates in study area 2015; from left to right they are surface scattering, volume scattering, randomness, and estimated soil moisture with black areas not inverted. (a) day 126. (b) day 140. 88

Figure 3-13. Comparison of the estimated soil moisture by different methods in two study areas, different geometric shapes represent different methods. (a) Wheat fields in study area 2013 with the red is on day 119, the green is on day 129, and the blue is on day 143. (b) Wheat fields in study area 2015 with the red is on day 126, and the blue is on day 140. (c) Bare soil fields. 90

Figure 4-1. Study area locations, field polygons and Pauli images (right) from the fully polarimetric RADARSAT-2 data in 2013 and 2014. The Pauli image in 2013 is acquired on April 29th 2013 while the one at the bottom is acquired on May 5th 2014. It should be noted that only wheat fields are measured in 2013 while the soybean, corn and wheat fields are measured in 2014. 102

Figure 4-2. Ground truth photos in the corn, soybean and wheat fields on different dates in 2014: (a) corn fields (b) soybean fields (c) wheat fields. From left to right, the photos of the soybeans and corn were taken on May 5th, May 18th and June 21st, respectively, whereas the photos of the wheat were taken on May 5th, May 18th and June 11th. 103

Figure 4-3. H and α plots in three fields (from left to right: corn, soybean and wheat) from May 4th to June 21st: (a) May 4th (b) May 5th (c) May 15th (d) May 18th (e) June 11th (f) June 21st. 105

Figure 4-4. The normal distributions of H (left) and the histograms of α (right) on different dates. (a) corn field. (b) soybean field. (c) wheat field. 108

Figure 4-5. Integrated surface parameter inversion scheme (ISPIS). 111

Figure 4-6. Relationship between ε_r and β. 112

Figure 4-7. Calibrated IEM model with exponential ACF in a 40 degree incidence angle. (a) HH backscattering coefficient (b) VV backscattering coefficient. 115

Figure 4-8. V-SAVSM: (a) Elements of the V-SAVSM covariance matrix (b) Entropy and RVI. 119

Figure 4-9. Flowchart of the ATCD algorithm. 122

Figure 4-10. T_1 maps of corn, soybean and wheat fields on May 5th, May 15th, June 11th and June 21st. in study area 2014. (a) corn field on May 5th (b) corn field on May 15th (c) corn field on June 11th (d) corn field on June 21st (e) soybean field on May 5th (f) soybean field on May 15th (g) soybean field on June 11th (h) soybean field on June 21st (i) wheat field on May 5th (j) wheat field on May 15th (k) wheat field on June 11th (l) wheat field on June 21st..... 124

Figure 4-11. Soil moisture in the C2 field on different dates: (a) May 4th (b) May 5th (c) May 18th (d) June 21st..... 127

Figure 4-12. Measured and estimated soil moisture on different days: (a) Corn field on May 4th (b) Soybean field on May 4th (c) Wheat field on May 4th (d) Corn field on May 5th (e) Soybean field on May 5th (f) Wheat field on May 5th (g) Corn field on May 18th (h) Soybean field on May 18th (i) Wheat field on May 18th (j) Corn field on June 21st (k) Soybean field on June 21st (l) Wheat field on April 29th 2013 (m) Wheat field on May 9th 2013. (n) Overall RMSE of different methods. 130

Figure 4-13. Changes in soil moisture over time as estimated by RADARSAT-2 and as measured in the agricultural fields in 2014 and 2013. 132

Figure 4-14. Surface roughness histograms for the corn and soybean fields, from left to right, on different days: (a) May 5th (b) May 18th (c) June 11th (d) June 21st (e) variation of roughness over time in corn and soybean fields. 134

Figure 4-15. Measured and estimated surface roughness on different dates: (a) Corn field on May 4th (b) Soybean field on May 4th (c) Corn field on May 5th (d) Soybean field on May 5th (e) Corn field on May 18th (f) Soybean field on May 18th (g) Corn field on June 11th (h) Soybean field on June 11th (i) entire field on all days. 136

Figure 4-16. VWC of wheat on different days and its comparison with the ground truth measured by Kim et al.: (a) May 5th (b) May 18th (c) June 11th (d) June 21st (e) comparison between the ISPIS and the Kim et al. (2014) DoY: Day of Year. Note: the "DoY by Kim et al." means the day of year Kim et al. (2014), which has the same phenology corresponding to the "DoY" in this chapter. 139

Figure 4-17. Two-way attenuation coefficients of different crops at different growing stages under different incident angles. (a) wheat field on May 5th 2014 (b) wheat field on May 18th 2014 (c) wheat field on June 04 2014 (d) soybean field on May 5th (e) corn field on June 4th 2014 (f) corn field on June 21st 2014. (g) soybean field on June 21st..... 144

Figure 4-18. Histograms and cumulative distribution of functions (CDF) of H and α in C2 field on May 5th and May 15th. 146

Figure 4-19. The coefficients of the surface and volume components for the bare soils on May 5th and May 15th (from left to right is the surface and volume coefficient respectively). 147

Figure 5-1. Polarization ellipse. 158

Figure 5-2. Flowchart of MTSBTCS-MDPS. (a) the core algorithm of the binary-tree classification scheme, taking 4 classes as an example, and the Date means the data acquired on that date. (b) flowchart of the MTSBTCS-MDPS. Note: PB is the polarization basis. 168

Figure 5-3. Study area and reference data. 170

Figure 5-4. Ground truth photos of corn. (a) May 7th, (b) May 31st, (c) August 11th, (d) September 28th..... 170

Figure 5-5. Ground truth photos of soybean. (a) May 7th, (b) May 31st, (c) September 4th, (d) September 28th. 171

Figure 5-6. Ground truth photos of wheat. (a) May 7th, (b) May 31st, (c) June 24th, (d) July 18th. 171

Figure 5-7. Correlation coefficients of different classes on different days. (a) corn, (b) soybean, (c) wheat, (d) grass, (e) forest, (f) urban. 172

Figure 5-8. Polarization signatures of corn on different dates. (a) col-PS on May 7th, (b) cross- PS on May 7th, (c) col-PS on May 31st, (d) cross-PS on May 31st, (e) col-PS on June 24th, (f) cross-PS on June 24th, (g) col-PS on July 18th, (h) cross-PS on July 18th, (i) col-PS on August 11th, (j) cross-PS on August 11th, (k) col-PS on September 4th, (l) cross-PS on September 4th, (m) col-PS on September 28th, (n) cross-PS on September 28th..... 173

Figure 5-9. Polarization signatures of soybean on different dates. (a) col-PS on May 7th, (b) cross-PS on May 7th, (c) col-PS on May 31st, (d) cross-PS on May 31st, (e) col-PS on June 24th, (f) cross-PS on June 24th, (g) col-PS on July 18th, (h) cross-PS on July 18th, (i) col-PS on August 11th, (j) cross-PS on August 11th, (k) col-PS on September 4th, (l) cross-PS on September 4th, (m) col-PS on September 28th, (n) cross-PS on September 28th..... 174

Figure 5-10. Polarization signatures of wheat on different dates. (a) col-PS on May 7th, (b) cross-PS on May 7th, (c) col-PS on May 31st, (d) cross-PS on May 31st, (e) col-PS on June 24th, (f) cross-PS on June 24th, (g) col-PS on July 18th, (h)

cross-PS on July 18th, (i) col-PS on August 11th, (j) cross-PS on August 11th, (k) col-PS on September 4th, (l) cross-PS on September 4th, (m) col-PS on September 28th, (n) cross-PS on September 28th..... 175

Figure 5-11. Polarization signatures of grass on different dates. (a) col-PS on May 7th, (b) cross-PS on May 7th, (c) col-PS on May 31st, (d) cross-PS on May 31st, (e) col-PS on June 24th, (f) cross-PS on June 24th, (g) col-PS on July 18th, (h) cross-PS on July 18th, (i) col-PS on August 11th, (j) cross-PS on August 11th, (k) col-PS on September 4th, (l) cross-PS on September 4th, (m) col-PS on September 28th, (n) cross-PS on September 28th..... 177

Figure 5-12. Polarization signatures of forest on different dates. (a) col-PS on May 7th, (b) cross-PS on May 7th, (c) col-PS on May 31st, (d) cross-PS on May 31st, (e) col-PS on June 24th, (f) cross-PS on June 24th, (g) col-PS on July 18th, (h) cross-PS on July 18th, (i) col-PS on August 11th, (j) cross-PS on August 11th, (k) col-PS on September 4th, (l) cross-PS on September 4th, (m) col-PS on September 28th, (n) cross-PS on September 28th..... 178

Figure 5-13. Polarization signatures of urban on different dates. (a) col-PS on May 7th, (b) cross-PS on May 7th, (c) col-PS on May 31st, (d) cross-PS on May 31st, (e) col-PS on June 24th, (f) cross-PS on June 24th, (g) col-PS on July 18th, (h) cross-PS on July 18th, (i) col-PS on August 11th, (j) cross-PS on August 11th, (k) col-PS on September 4th, (l) cross-PS on September 4th, (m) col-PS on September 28th, (n) cross-PS on September 28th..... 179

Figure 5-14. Classification maps. (a) May 7th. The left is MDPS and the right is WD. (b) May 31st. The left is MDPS and the right is WD. (c) June 24th. The left is MDPS and the right is WD. (d) July 18th. The left is MDPS and the right is WD. (e) August 11th. The left is MDPS and the right is WD. (f) September 4th. The left is MDPS and the right is WD. (g) September 28th. The left is MDPS and the right is WD. (h) the MTSBTCS-MDPS (i) the MTSBTCS-WD. 188

Figure 6-1. Schematic representation of the scatterer shape changing with δ. 202

Figure 6-2. Scattering with a homogeneous medium. 204

Figure 6-3. Integration of land cover map and surface inversion scheme. 205

Figure A-1. Temporal trajectory of a monochromatic plane wave at a fixed abscissa $z = z_0$. Adapted from Lee & Pottier (2009). 210

Figure A-2. Polarization ellipse. 211

Figure B-1. Scattering of a plane electromagnetic wave by an object..... 212

Figure B-2. Geometry for defining the orthonormal unit system based on scattering plane. (a) forward scatter alignment (FSA). (b) back scatter alignment (BSA). . 215

Figure D-1. H-α zones. 220

Figure E-1. Time-Domain Reflectometry. 221

Figure E-2. Needle profiler. 222

Figure E-3. Surface height profile. 224

Figure F-1. Uncorrected image: P1030848.pix..... 226

Figure F-2. The reference image: ref838.pix. 226

Figure F-3. Setting up projection. 227

Figure F-4. Setting the output image extent: upper left and lower right coordinates. 229

Figure F-5. Corrected image: oP1030848.pix..... 229

Figure F-6. C1_01_P1030848.txt 233

List of Appendices

Appendix A: Polarization and Polarization Ellipse 208

Appendix B: Polarimetric Scattering Cross Section and Scattering Amplitude Matrix . 212

Appendix C: Polarimetric Scattering Matrices 217

Appendix D: Eigen-Value Decomposition 219

Appendix E: Surface Parameters over Bare Soil 221

Appendix F: Surface Roughness Measurement 225

Appendix G: Copyright Releases from Publications 235

List of Acronyms

ACF	Auto-Correlation Function
A-FVSM	ATCD method using the FVSM
ALOS	Advanced Land Observation Satellite
AMD	Adaptive Model-based Decomposition
An-VSM	An Volume Scattering Model
Antropov-VSM	Antropov Volume Scattering Model
ASF	Alaska Satellite Facility
ATCD	Adaptive Two-Component model-based Decomposition
BSA	Back Scatter Alignment
CIEM	Calibrated IEM
COSMO	COnstellation of small Satellites for Mediterranean basin Observation
DoY	Day of Year
FD	Freeman Decomposition
FD-VSM	Freeman Durden Volume Scattering Model
FSA	Forward Scatter Alignment
FVSM	Freeman Durden Volume Scattering Model
HH	Horizontal transmitting and Horizontal receiving polarization
H-SAVSM	Horizontal Simplified Adaptive Volume Scattering Model
HV	Vertical transmitting and Horizontal receiving polarization
H-VSM	Hajnsek Volume Scattering Model
IA	Incidence Angle

IEM	Integral Equation Model
ISPIS	Integrated Surface Parameter Inversion Scheme
KS	Surface Roughness
LAI	Leaf Area Index
LOS	Line of Sight
LUT	Look-Up Table
MDPS	Maximize the Difference of the Polarization Signatures
MIMICS	Michigan Microwave Canopy Scattering
MLC	Maximum Likelihood Classification
MTSBTCS-MDPS	Multi-Temporal Supervised Binary-Tree Classification Scheme to Maximize the Difference of the Polarization Signatures
MTSBTCS-WD	Multi-Temporal Supervised Binary-Tree Classification Scheme with Wishart Distance
MV	Volumetric Soil Moisture
NNED	Non-Negative Eigenvalue Decomposition Method
OA	Overall Accuracy
PA	Producer Accuracy
PB	Polarization Basis
PDF	Probability Density Function
PH	Pedestal Height
PolInSAR	Polarimetric Interferometry Synthetic Aperture Radar
PolSAR	Polarimetric Synthetic Aperture Radar
PRM	Power of the Remainder Matrix
PS	Polarization Signature

RCM	RADARSAT Constellation Mission
RMS	Root Mean Square
RMSE	Root Mean Square Error
RT	Radiative Transfer Model
RVI	Radar Vegetation Index
SAR	Synthetic Aperture Radar
SAVSM	Simplified Adaptive Volume Scattering Model
S.P.	Saturated Percentage
SPM	Small Perturbation Method
TCMD-SAVSM	Three-Component Model-based Decomposition with SAVSM
TDR	Time-Domain Reflectometry
UA	User Accuracy
VH	Horizontal transmitting and Vertical receiving polarization
V-SAVSM	Vertical Simplified Adaptive Volume Scattering Model
VV	Vertical transmitting and Vertical receiving polarization
VWC	Vegetation Water Content
WCM	Water Cloud Model
WD	Wishart Distance
Y-CIEM	CIEM with Yamaguchi volume scattering model
YD	Yamaguchi Decomposition
Y-FVSM	ATCD method using the YVSM
Y-VSM	Yamaguchi Volume Scattering Model
YVSM	Yamaguchi Volume Scattering Model

Chapter 1 Introduction

Agriculture is the cultivation of animals, plants and other life forms for food, fiber, biofuel, medicinal and other products used to sustain and enhance human life. The crops planted over agricultural land create food supplies that nurtured human beings and livestock, even the development of civilization. Crops also have significant effects on climate change, primarily through the absorb of greenhouse gases such as carbon dioxide (Jones & Vaughan, 2010). Crops are dependent on their physical environment for growth, survival, and reproduction. Hence, it is essential to monitor and understand crop response to changing environmental conditions. To do this, we need tools to quantify the environment and to measure different crop variables.

Crop variables, such as height, biomass and associated surface parameters, are important to crop growth monitoring and yield forecast; hence, they are of paramount importance to assure food security to an ever-growing human population affected by increasingly uncertain climatic conditions (Liu et al., 2013). In this thesis, only soil moisture and surface roughness are investigated. Soil moisture plays an important role in several physical processes such as field operability, agricultural drought, irrigation schedule, soil erosion, and surface runoff (Wang et al., 2016). It also plays a significant role in organic matter mineralization and the cycling of biophilic elements such as nitrogen (Guntiñas et al., 2012). Surface roughness determines how the crop interacts with the environment. It is also a critical parameter reflecting soil erosion and runoff processes and a major factor influencing wind and water erosion (Zheng et al., 2012).

Mapping and monitoring changes in the distribution of cropland provide information that can aid inventory monitoring to agriculture development and support early warning of threats to global and regional food security (McNairn et al., 2009). Crop maps are required for a variety of applications ranging from the satisfaction of general inventory requirements to the enforcement of quota limits. Furthermore, these maps often have to be updated at frequent intervals (Foody et al., 1994). However, it is impractical to map large regions by traditional survey techniques. In contrast, Earth observation technology

offers an invaluable means to estimate both the environmental conditions and crop variables in an efficient manner over large areas (Duveiller & Defourny, 2010).

Remote sensing is a spatial science used to obtain information about an object, area, or phenomenon through the analysis of data acquired by a device that is not in contact with the object, area, or phenomena under investigation (Lillesand et al., 2004). Remote sensing technology has the potential to instantaneously provide quantitative information on agricultural crops over large areas repetitively (Clevers et al., 1994). However, the usability of different optical sensors for determining environmental conditions and crop variables depends not only on daylight, but also on the actual weather conditions. Clouds and heavy rain are impenetrable for the visible spectrum with the wavelength between 400 nm and 700 nm. Infrared sensors that are applicable during the day and night are even more sensitive to weather conditions. Synthetic Aperture Radar (SAR) as an active observation technique, can transmit longer electromagnetic wavelengths from 1 mm to 1 m and receive the scattered waves after interacting with the ground targets, having proved to be valuable because of its day-and-night capability and the possibility to penetrate clouds and light rain (Berens, 2006). Of increasing importance are SAR systems that can provide multidimensional information via multiple frequencies or polarizations. One such technique is the polarimetric SAR (PolSAR) with its definition given in Appendix A, which provides an enhanced capacity for investigating Earth terrain because different frequencies and polarizations allow for the probing of different scattering mechanisms and different components of the scattering layers (Oliver et al., 2004). Compared with the single polarization SAR, PolSAR with quad polarizations is more sensitive to crop geometric structures from which the radar signal returns and has been extensively used for the land use and land cover mapping (Liu et al., 2013; Jiao et al., 2013).

In addition, PolSAR is also very sensitive to the spatial and temporal changes of surface parameters over bare soil, which has led to the development of a number of surface scattering models on surface parameter estimation. However, over vegetated areas, especially agricultural fields, they are mostly covered by the vegetation canopy, which hinders the direct application of SAR on the soil moisture and surface roughness

estimation. Fortunately, the capability of PolSAR to penetrate the vegetation canopy makes it possible to retrieve these surface parameters under vegetation cover by either separating the scattering off bare soil from the backscattering or by accurately removing the volume scattering caused by the vegetation canopy. With this notion, retrieval methods of surface parameters under vegetation cover are investigated. In addition, the soil moisture and surface roughness extraction algorithms are also dependent on the crop types and crop conditions, whereas crop conditions can be determined by the crop phenology for different crop, so the crop mapping can be very useful for surface parameters retrieval. Therefore, a land cover mapping method is also developed in this thesis. Currently, the X-, C- and L-band PolSAR systems are widely developed and in operation with their wavelength approximately 3 cm, 5.5 cm and 24 cm, respectively. The representative satellites are the German TerraSAR/TanDEM-X (X band), Canadian RADARSAT-2 (C band) and the Japanese ALOS-2 (L band). With the notion that the shorter the wavelength is, the less the penetration depth is. The application of short wavelength to the dense vegetation areas will be limited due to the significant attenuation effects. The coherent speckle noise of short wavelength is also much more severe than that of the long wavelength, but the short wavelength is more sensitive to the mirco surface structures, i.e., bare soils shown in PolSAR images of short wavelength look rougher than that of the long wavelength (Huang et al., 2016). Compromisingly, the C-band Canadian RADARSAT-2 data will be adopted for the research in the entire thesis.

1.1 Surface Parameter Retrieval over Bare Soil

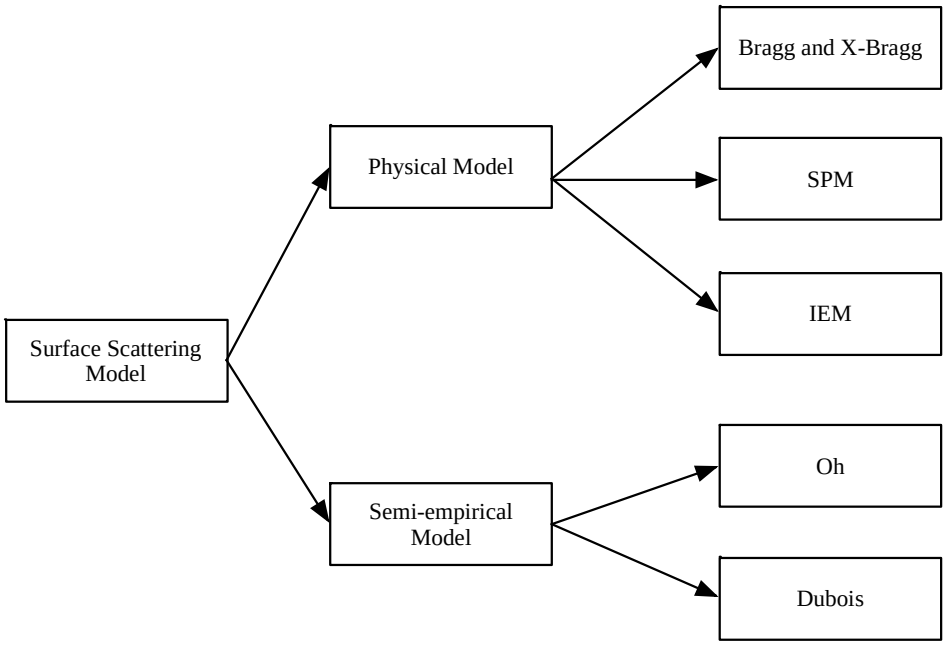

Figure 1-1. Brief category of surface scattering models.

Surface parameters over bare soil are primarily described by two indicators, soil moisture and surface roughness. Soil moisture is a key parameter in the application of hydrology and agronomy (Gorrab et al., 2015) and plays an important role in making water resource and irrigation management decisions, understanding land surface process, and estimating surface runoff and soil erosion potentials. Its measurement in field is given in Appendix E. Surface roughness defined in Appendix E plays an important role in determining how a real object will interact with its environment (Thomas Jagdhuber et al., 2012; Huang et al., 2016) and its digitization process is in given in Appendix F. Both soil moisture and surface roughness are also essential climate variables recognized by the Global Climate Observing System (Thomas Jagdhuber et al., 2012; Huang et al., 2016). To invert soil moisture and surface roughness, either physical or semi-empirical surface scattering models are required to model the microwave scattering process interacting with the surface. Surface scattering from the soil, related to soil moisture and surface roughness, is rather common over agricultural fields. Although the primary topic in this thesis is to invert the surface parameters under vegetation cover, it is still necessary to present an

overview of the development of the scattering models for bare soil because these models employ these parameters to characterize the scattering processes and are used to estimate surface parameters in turn. Hence, in this section, we mainly review the surface scattering models over bare soil, while the methods to estimate the surface parameters will be given in the sections following.

At present, in order to accurately characterize bare soil scattering, many models, based on different assumptions, have been proposed. The first set of surface models are physical models, which are derived according to electromagnetic scattering theory via solving the Maxwell Equations. The simplest surface scattering model to use to determine soil scattering would be an infinite perfectly flat surface, which is also called specular surface shown in Figure 1-2.

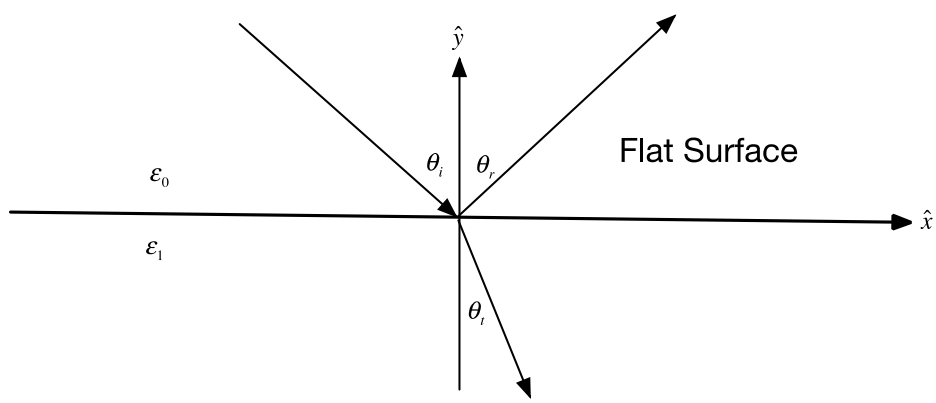

Figure 1-2. Reflection and transmission of radar wave over a flat surface.

Under the assumption of specular surface, scattering will concentrate on the specular direction, that is, reflection, which can be directly solved as the Fresnel reflection coefficient (Jin & Xu, 2013). However, in natural environments, especially in agricultural fields after plowing, most surfaces are random rough surfaces, as depicted in Figure 1-3. To model these surfaces, surface roughness must be considered as a parameter in the models.

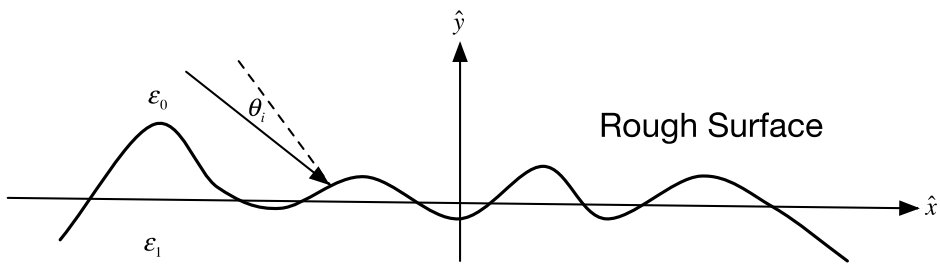

Figure 1-3. Scattering from a rough surface.

Taking into account of surface roughness, the small-perturbation method (SPM) was proposed by Rice (1963), but it was valid only when the roughness was very small compared with the radar wavelength. That is, SPM is only suitable for low frequencies, i.e., long wavelength, PolSAR systems such as the spaceborne ALOS (Advanced Land Observation Satellite) and airborne E-SAR sensors in L band with its wavelength at approximately 24 cm. In order to meet the requirement of high frequency PolSAR systems such as the X-band TerraSAR-X and C-band RADARSAT-2, the integral equation method (IEM) proposed by Fung (1994), taking into account of the scattering caused by rapid fluctuations, is more suitable and has been extensively employed (Lievens & Verhoest, 2011; Song et al., 2009; Barrett, et al., 2009). For both SPM and IEM, however, it is still difficult to retrieve surface parameters, because they require an accurate description of surface roughness, but the parameterization of roughness from field measurements is known to be problematic (Verhoest et al., 2008). To overcome this difficulty, many empirical relationships between the root mean square (RMS) of surface height and its correlation length have been developed for various wavelengths ranging from the C-band to the L-band to calibrate the IEM model (Baghdadi et al., 2002; Baghdadi et al., 2004; Baghdadi et al., 2006; Baghdadi et al., 2015).

In addition to the physical models, another group of surface scattering models are semi-empirical models. For example, the co-polarization ratio (HH to VV polarization) reaches saturation for high soil surface roughness values, thus simplifying soil moisture estimation (Oh, 2004; Oh et al., 1992). Similarly, the depolarization ratio (VH to VV polarization) has been found to be sensitive to soil surface roughness as well (Ulaby et al., 1986). Sensitivity analyses of these ratios with respect to surface roughness and soil

moisture and sensor configurations (frequency, incidence angle and polarization) led to the development of the well-known semi-empirical backscattering models for bare soil (Oh et al., 1992; Dubois et al., 1995). Although these semi-empirical scattering models relate the backscattering coefficients to soil moisture contents, it is still difficult to use these relationships for radar signal inversion without time-consuming calibration measurements (Park et al., 2009). In addition, these semi-empirical models are depending on parameters that are often site-specific and valid only under specific soil conditions.

Finally, in consideration of PolSAR, a X-Bragg model has recently been proposed in which the Bragg surface model is rotated with respect to the orientation angle induced by the azimuthal slope satisfying a certain probability density function (PDF) (Hajnsek et al., 2003; Schuler et al., 2002). According to the PDF employed, two kinds of X-Bragg models are extensively used. The first one used by Hajnsek et al. (2003) for soil moisture estimation models the surface scattering using a rotated Bragg surface model with a uniform PDF. It has been extensively applied in the polarimetric model-based target decomposition by many researchers on soil moisture estimation (Jagdhuber et al., 2013; Jagdhuber et al., 2014; Ballester-Berman et al., 2013), in which a high accuracy soil moisture map was obtained over agricultural or vineyard fields. Huang et al. (2016) employed another kind of X-Bragg model with a Gaussian PDF to estimate soil moisture over wheat fields at early growing stage. However, regardless of the PDFs employed, the X-Bragg model derived from the SPM model is only suitable to describe the agricultural field with relatively smooth surface. Furthermore, the issue of the low inversion rate of the X-Bragg model is unavoidable, and the relationship between the dielectric constant and scattering parameters reaches saturation easily when the incidence angle is steep being less than 30 degrees which makes the estimated soil moisture become biased (Huang et al., 2016). To summarize, the category of the surface scattering models is shown in Figure 1-1 with their suitability listed in Table 1-1.

Table 1-1. Surface scattering models. Note: $\boldsymbol{mv}$ is the volumetric soil moisture with its unit [vol.%]; $\boldsymbol{ks}$ is the surface roughness with $\boldsymbol{k}$ wavenumber and $\boldsymbol{s}$ the root mean square of surface height.

	Suitability		
Models	Soil moisture	Surface roughness	Incident angle
SPM	N/A	$ks < 0.3$	N/A
IEM	N/A	$ks < 3$	N/A
Bragg and X-Bragg	$mv < 30$	$ks < 0.3$	N/A
Oh (2002)	$9 < mv < 31$	$0.1 < ks < 6$	N/A
Dubois (1995)	$mv < 35$	$ks < 2.5$	$\theta < 30^{\circ}$

1.2 Volume Scattering Model over Agricultural Fields

To invert the surface parameters under vegetation cover, the key issue is to remove the effects of the scattering caused by vegetation canopy, which is called the volume scattering with its scattering process shown in Figure 1-4. However, until now this has been a challenging task to construct the volume scattering for accurate crop variable extraction due to the complex nature of the crop structure (Hajnsek et al., 2009). Many volume scattering models have been developed recently, but they can only characterize certain crop types (Huang et al., 2014). The extensively used method is to model the vegetation canopy scattering through integrating the scattering matrix of small-size scatterer with its orientation angle with respect to the line of sight (LOS) of radar satisfying a certain PDF. The small-size scatterers can be treated as needle-like dipole, spheroids, or disk-like plate depending on the size of the object compared with the radar wavelength. For long wavelength radar systems, they are often treated as needle-like dipoles; whereas for short wavelength radar systems, they are treated as spheroids or disk-like plate as shown in Figure 1-4.

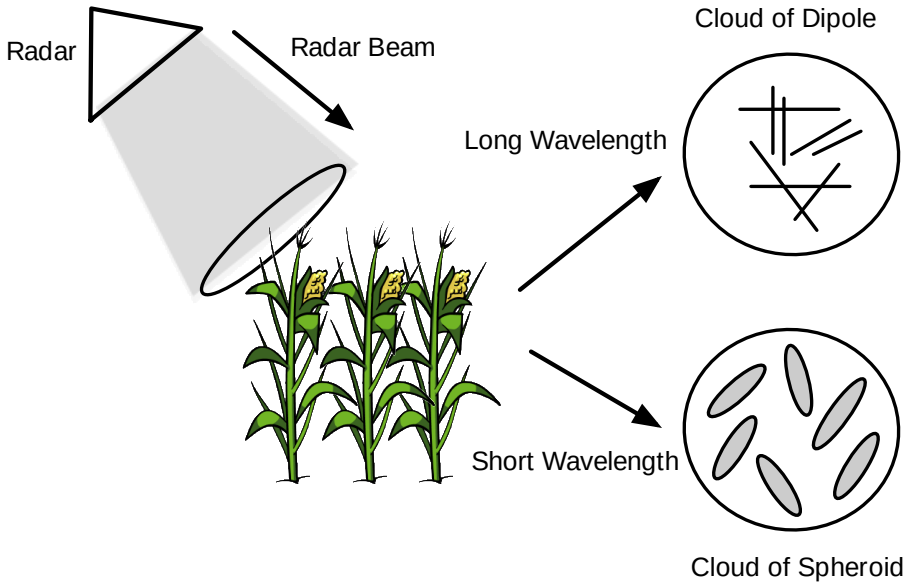

Figure 1-4. Volume scattering in different radar frequencies.

Freeman and Durden (1998) developed the first volume scattering model based on the dipole assumption using the uniform probability density function. Yamaguchi et al. (2005) found that most of the vegetation areas were either horizontal or vertical dipoles, so they added the vertical and horizontal volume scattering models to extend the Freeman-Durden volume scattering model by making use of the first order sine probability density function. The von Mises distribution is in the class of circular probability distributions with the desirable characteristic of its PDF smoothly going down to zero, which has been proposed by Neumann et al. (2009) to characterize vegetation for polarimetric interferometry SAR (PolInSAR) applications. Arii et al. (2010) developed a general scattering model based on a nth power cosine square function, but the randomness and orientation angle that are both unknown variables must be calculated simultaneously, which makes it very time-consuming. These volume scattering models are primarily developed to characterize forest canopy, but to directly apply them to agricultural areas is still limited as forest canopy always shows much higher randomness caused by the randomly distributed branches than crops that show certain orientations. To circumvent this issue, recently, a simplified adaptive volume scattering model based on the nth-power sine and cosine functions were proposed by Huang et al. (2015) attempting to describe the change of crops over time at different growing stages to sensor the C-Band RADARSAT-2 polarimetric data. Different from these above volume scattering models that use amplitude information to characterize the vegetation scattering, a novel volume scattering model based on the single-look phase distributions was developed by Lee et al. (2014) to characterize the statistics of phase difference of two polarization returns with circular Gaussian distribution, and it can better describe the distributions of the orientation angle due to the fact that orientation angles can be estimated by the phase difference between the left-left and right-right polarizations.

In summary, most of the abovementioned volume scattering models are still limited to only a few types of vegetation and cannot characterize crop development change over season. Additionally, most of these volume scattering models are based on needle-like dipoles as the elementary unit, which are valid only when the size of the objects is much smaller compared with the wavelength. Hence, for high frequency PolSAR systems such

as RADARSAT-2 in C band (5.4 cm) and TerraSAR-X in X band (3 cm), the needle-like dipole assumption is not likely satisfied. Being different from the above methods, An et al. (2010) assumed that it was only the vegetation canopy that causes scattering randomness. Based on this, they proposed a maximum entropy volume scattering model. However, Antropov et al. (2011) noted that the maximum entropy volume scattering model may require more experiments to be validated, and they proposed a generalized volume scattering model that can adapt to the sensitivity between the HH and VV co-polarizations for different types of vegetation. Additionally, the volume scattering is always related to the physical parameters of vegetation, hence, a finite-length slim cylinder is often adopted and the Rayleigh-Gans approximation method is used to model the stalk, branches or twiags of the crop (Jin & Xu, 2013). Finally, several empirical relationships were developed between polarization and/or dual frequency ratios and the physical parameters of crop fields. For instance, the radar vegetation index (RVI) computed at the L-band has been used to evaluate the biomass level of a corn crop (Kim et al., 2014). Other significant correlations have also been reported between: 1) HV/VV and soybean water content obtained in L-band (Roo et al., 2001), and 2) VV/HV and maize crop height and biomass at the S- and C-bands (Vecchia et al., 2008). As well, the HV/HH ratio at the C-band has been used to estimate the leaf area index (LAI) of sugarcane (Lin et al., 2009). Although these cross polarization ratios are almost insensitive to soil moisture, the application of these relationships is limited because they are only useful for specific crop types.

1.3 Scattering Mechanisms over Agricultural Fields

Due to the penetration capacity of the radar signals, five important scattering mechanisms can be observed over agricultural fields shown in Figure 1-5.

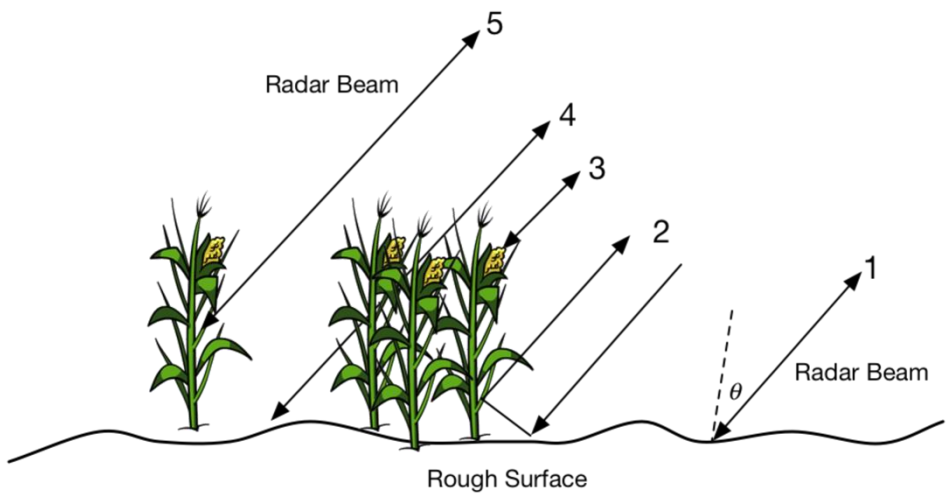

Figure 1-5. Five important scattering mechanisms over agricultural fields.

1. backscattering from a rough surface.
2. low-order multiple scattering, as occurs from dihedral effects caused by the crop stalk and the ground.
3. random volume backscatter from a non-penetrable layer of discrete scatterers.
4. surface scattering after propagation through a random medium, as occurs in the use of low frequency P- or L-band radar for penetration of vegetation layer.
5. single scattering from anisotropic structures such as corn stalks, where the backscatter can be modeled as that from a rough dielectric cylinder or other canonical object with polarization anisotropy due to shape and dielectric material structure.

To achieve accurate crop variable estimation and model the five important scattering mechanisms observed over agricultural fields, the scattering process including soil and crop canopy must be modeled so as to separate the surface and volume scattering accurately. The current widely-used methods are either backscattering model-based retrieval algorithms (Attema & Ulaby, 1978; Bindlish & Barros, 2001; Joseph, et al., 2008; Ulaby et al., 1990) or target decomposition techniques in PolSAR (Cloude & Pottier, 1996; I. Hajnsek et al., 2009; Jagdhuber et al., 2012). The representative backscattering model-based retrieval algorithm is the water cloud model (WCM), which is a semi-empirical model assuming that the vegetation consists of a collection of

spherical water droplets that are held in place structurally by dry matters (Attema & Ulaby, 1978). The primary assumption of the WCM is based the fact that the dielectric constant of dry vegetation matter is much smaller than that of the water content of vegetation, and more than 99% by volume is composed of air in vegetation canopy. Therefore, such a model was developed assuming that the canopy "cloud" called the water cloud contains identical water droplets randomly distributed within the canopy with its figure shown as Figure 1-6 and its formula written as (1-1)

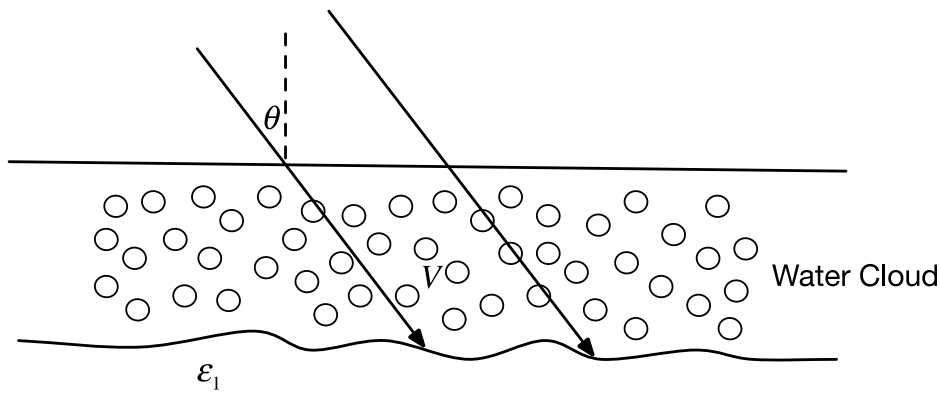

Figure 1-6. Water cloud model.

$$\sigma^{\circ} = \frac{A \cdot cos\theta}{2B \cdot WC} h\left(1 - e^{-2B \cdot WC \cdot sec\theta}\right) + \sigma_s^{\circ} e^{-2B \cdot WC \cdot sec\theta} \tag{1-1}$$

where σ° is the observed backscattering coefficient; A is a constant representing the vegetation scattering; parameter B is an empirical parameter depending on both vegetation properties and sensor configuration; h is the crop height; WC is the vegetation water content ($kg \cdot m^{-2}$). σ_s° is the backscattering form of the bare soils which are often characterized by the surface scattering models in section 1.1. Due to its simplicity, WCM has been widely used for surface and biophysical parameters estimation till now (Gherboudj et al., 2011; Lievens & Verhoest, 2011). However, the WCM is only suitable for describing dense vegetation canopies. Hence, some researchers have attempted to improve it through considering the volumetric fraction of vegetation cover (He et al., 2014).

In fact, the WCM is only a simple solution of the first-order radiative transfer (RT) model neglecting the multiple scattering and treating the vegetation canopy as a homogeneous medium. To overcome this limitation, the Michigan Microwave Canopy Scattering (MIMICS) model developed by Ulaby et al. (1990), based on a first-order solution of the RT equation, treats the tree canopy that is comprised of a crown layer, a trunk layer, and a rough-surface ground boundary as an inhomogeneous layer (Figure 1-7). Compared with the WCM, the MIMICS model provides a rigorous solution considering not only the multiple scattering but also all scatterings shown in Figure 1-5. Hence, it is suitable for vegetation-covered areas where the agents responsible for scattering have discrete configurations (Toure et al., 1994), and many studies have adopted it to characterize the scattering of crops such as wheat and soybean (Toure et al., 1994; De Roo et al, 2001).

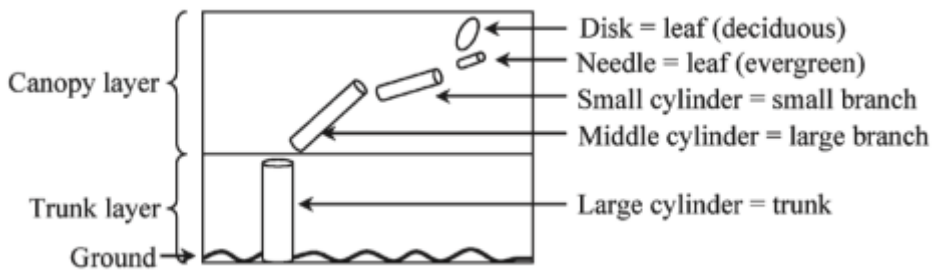

Figure 1-7. Discrete scatterers of tree canopy. Adapted from Burgin et al. (2011).

In MIMICS, the RT theory is an important method to treat multiple scattering in a medium consisting of random discrete scatterings, and the scalar RT equation is an integro-differential equation that governs the propagation of specific intensities. Considering a medium consisting of a large number of particles (Figure 1-8), according to Tsang et al. (2000), we have specific intensity $I(\bar{r}, \hat{s})$ at all location $\bar{r}$ and for all direction $\hat{s}$ due to scattering. We consider a "small" volume element $dV = dAdl$, and dl is along the direction $\hat{s}$. The small volume element is centered at $\bar{r}$. We consider the differential change in specific intensity $I(\hat{s})$ as it passes through dV. Then the differential change of power in direction $\hat{s}$ is

$$dP = -I_{in}(\hat{s})dAd\Omega + I_{out}(\hat{s})dAd\Omega$$
$$= -I(\bar{r},\hat{s})dAd\Omega + I(\bar{r} + dl\hat{s},\hat{s})dAd\Omega \quad (1\text{-}2)$$

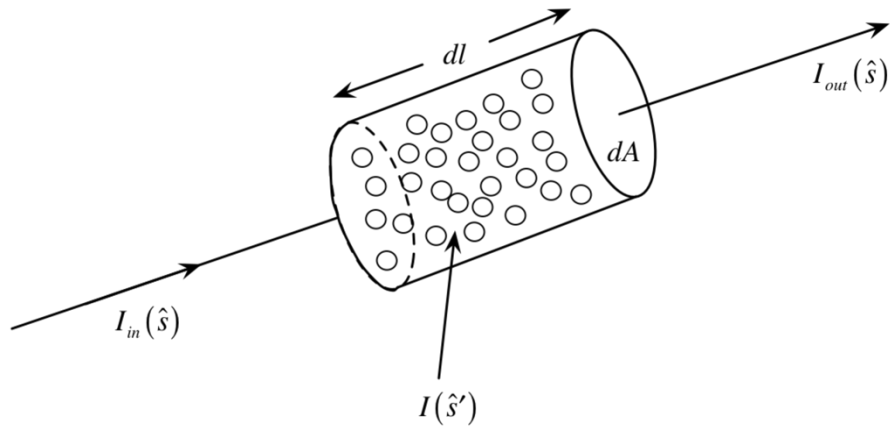

Figure 1-8. Specific intensity $\boldsymbol{I}(\hat{\boldsymbol{s}})$ in direction $\hat{\boldsymbol{s}}$ in and out of elemental volume.

In fact, the scalar RT equation can be generalized to the vector electromagnetic propagation. Using the property of incoherent addition of Stokes parameters, the vector RT equation for specific intensity is given by

$$\frac{dI(\bar{r},\hat{s})}{ds} = -\bar{\bar{k}}_e(\bar{r},\hat{s})I(\bar{r},\hat{s}) - k_{ag}(\bar{r},\hat{s})I(\bar{r},\hat{s}) + \bar{J}_e + \int_{4\pi} d\Omega'\, \bar{\bar{P}}(\bar{r},\hat{s},\hat{s}') \cdot I(\bar{r},\hat{s}') \quad (1\text{-}3)$$

where $\bar{\bar{P}}(\bar{r},\hat{s},\hat{s}')$ is the phase matrix giving the contributions from direction $\hat{s}'$ into the direction $\hat{s}$. $\bar{\bar{k}}_e$ is the extinction matrix for Stokes parameters due to the scatterers, $\bar{J}_e$ is the emission vector, and k_{ag} is the absorption coefficient for the background medium which is assumed to be isotropic. In general, extinction is a summation of absorption and scattering. However, in practice, it is still difficult to make use of it for the surface and biophysical parameters estimation because of too many unknown input parameters.

Compared with the WCM and MIMICS models that are based on the RT theory, polarimetric SAR decomposition as an important principle in PolSAR is a much more

useful and simpler tool to represent the scattering over agricultural fields. In general, there are two types of decomposition methods. One is the coherent target decomposition models, including the Krogagar Decomposition (Krogager et al. 1997) and Cameron Decomposition (Cameron et al., 1996), which are based on the single-look Sinclair matrix with its definition given in Appendix B. The second one is the incoherent decomposition models based on the multi-look covariance or coherency matrix with their definitions given in Appendix C, such as the Cloude-Pottier decomposition (Cloude & Pottier, 1997) that is based on the eigenvalue analysis (Appendix D) and the Freeman-Durden model-based decomposition (Freeman & Durden, 1998). Crops over agricultural fields are distributed targets (incoherent targets) due to their change with time. Hence, the incoherent decomposition is primarily investigated in this thesis, in which the Freeman-Durden model-based decomposition describes the scattering process as the incoherent linearly summation of the surface, double and volume scattering model. Due to its simplicity and intuitiveness, many decomposition methods were developed (An et al., 2010; An et al., 2011; Shan et al., 2012; Yamaguchi et al., 2005; Yamaguchi et al., 2006) based on its model-based framework and have been widely applied to vegetation information extraction (Ballester-berman et al., 2010; Trudel et al., 2009). The equation of the model-based decomposition is written as

$$C_3 = f_s C_s + f_d C_d + f_v C_v \tag{1-4}$$

where C_3 is the measured covariance matrix; C_s, C_d and C_v are the covariance matrices of surface, double-bounce, and volume scattering models, respectively. f_s, f_d and f_v are the contribution coefficients of the surface, double-bounce and volume scatterings. These three components are shown in Figure 1-9. The summarized scenarios of the scattering process are shown in Figure 1-10.

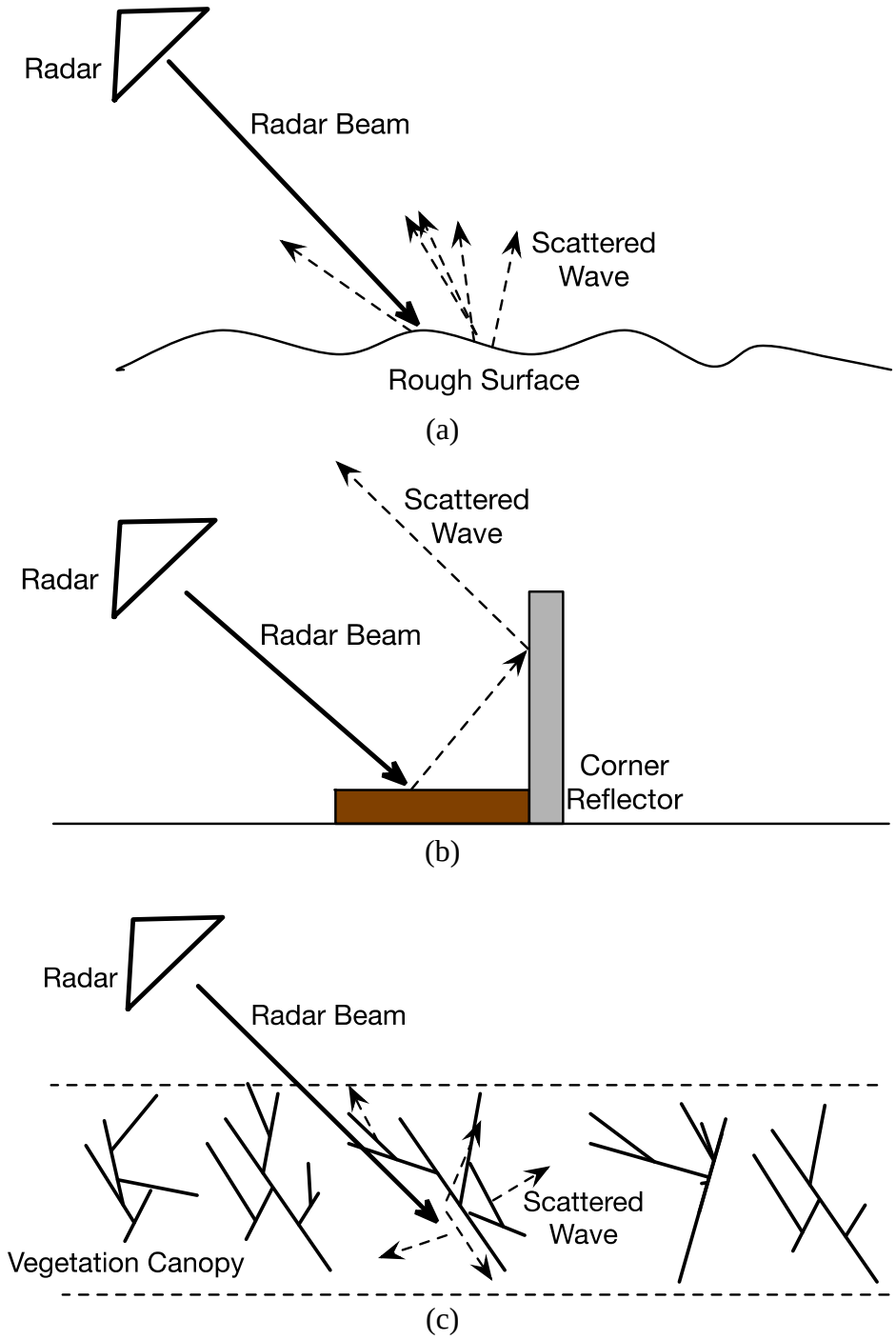

Figure 1-9. Scattering components in model-based decomposition. (a) surface scattering. (b) double-bounce scattering. (c) volume scattering.

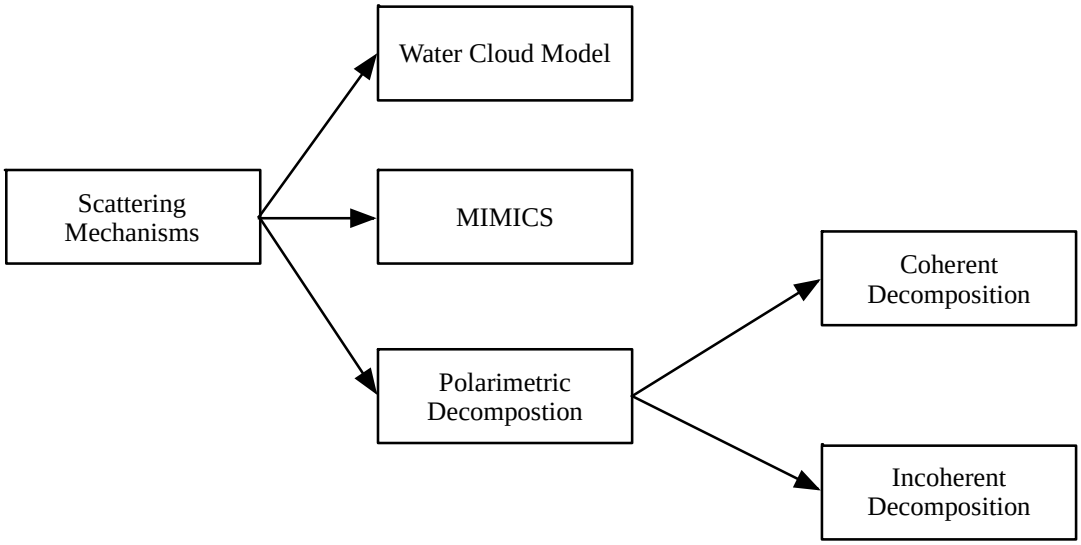

Figure 1-10. Different scattering process simulation scenarios.

1.4 Land Cover Mapping

The soil moisture and surface roughness extraction algorithms are also dependent on the crop types and crop conditions, whereas crop conditions can be determined by the crop phenology for different crop, so the crop mapping can be very useful for surface parameters retrieval. Furthermore, PolSAR with four compositions of polarization channels has more potential to reveal the target scattering mechanisms than the single polarization SAR, which can facilitate us to analyze the scattering of various targets in different shapes and structures so as to distinguish them (Lee & Pottier, 2009). Therefore, many classification methods were developed making use of the PolSAR information for land cover mapping instead of the single polarization SAR.

Over years, many researchers have investigated various algorithms to perform classification using PolSAR data. These algorithms can primarily be divided into three categories. The first one is to classify different targets according to their scattering mechanisms. The representative one is the eigen-value decomposition method proposed by Cloude and Pottier (1997), which classifies targets as eight classes according to eight zones divided in its H-α plot, and has been widely used for polarimetric image segmentation (Cao et al., 2007; Park & Moon, 2007). However, the classes falling on the

preset zone boundaries will easily cause misclassification and the predefined number of classes might not correspond to the appropriate number of classes in the PolSAR data. The second one is based on the statistical distribution, in which the extensively used one is based on the maximum likelihood classification (MLC) with Wishart distribution (Lee et al., 1994; Lee et al., 1999). Since it makes fully use of the scattering matrix, it is more suitable for PolSAR classification than for single polarization. However, in the Wishart classification, the physical scattering characteristics are always ignored. To overcome this issue, Lee et al. (2004) developed the third kind of classification methods by integrating the Freeman-Durden decomposition and the Wishart classification to preserve the scattering mechanisms, but misclassification still happens between rough bare soil and vegetation, especially for the short wavelength such as the C- and X-band.

These classification methods are mostly applied to the single-date image, and targets that change over time such as crops will reduce its classification accuracy due to the similar scattering mechanisms caused by their similar geometric structure that the PolSAR primarily senses. These aforementioned classification methods are mostly pixel-based, in which each pixel is individually assigned to a designated class and the resulting maps are often very noisy due to high spatial variance in the landscape conditions. Moreover, the coherent nature of SAR results in noise, which contributes to high class variance, reducing the accuracies derived from these pixel-based classification algorithms. Therefore, to eliminate the inherent “salt and pepper” noise of the pixel-based classification, an object-orientated classification proposed by Benz et al., (2004) is also used for classification. The object-oriented classification is first applied to the PolSAR images by Benz and Pottier (2001) based on the H-α-A decomposition. After that, many object-oriented classification methods were developed for polarimetric SAR land use and land cover mapping (Jiao et al. 2013; Qi et al. 2012; Qi et al. 2015). A novel four-component algorithm that makes fully use of the polarimetric information including polarimetric decomposition and polarimetric interferometric SAR to map land use and land cover was developed by Qi et al. (2012), which achieved much higher overall accuracy and kappa coefficient than the traditional Wishart classification. After that, a method to detect the short-term land development based on the object-oriented

classification method was also proposed (Qi et al., 2015). Recently, Jiao et al. (2014) made use of the multi-temporal polarimetric RADARSAT-2 data for crop mapping and monitoring, and obtained a higher classification accuracy than that of the single-date image when the object-oriented classification method was adopted. Based on the pixel-based classification method, Liu et al. (2013) also obtained high classification accuracy through making use of the multi-year RADARSAR-2 data. Hence, both the pixel- and object-based methods demonstrate the potential of the multi-temporal data on the improvement of the classification accuracy.

1.5 Objectives and Organization

This thesis attempts to validate both the qualitative and quantitative applications of the polarimetric SAR technique in retrieving soil moisture and surface roughness in a quantitative manner and mapping land cover types in a qualitative manner. Quantitative models and land cover mapping algorithms have been developed with four objectives shown as

(1) Develop an adaptive volume scattering model to characterize the scattering from crops at various growing stages as a basis for the surface parameter estimation;
(2) Develop an adaptive model-based decomposition to retrieve surface parameters over vegetated areas by removing the volume scattering;
(3) Develop an integrated surface parameter inversion scheme over agricultural fields including vegetated and unvegetated areas;
(4) Develop a multi-temporal land cover classification scheme.

The developed methods will contribute to the farmers to monitor their fields near real-time and to the Canadian government for the crop inventory and monitoring. To retrieve the surface parameters under vegetation cover over agricultural fields, the core task is to remove the effects of the scattering from the crop canopy, whereas an efficient volume scattering model is required to describe the crop canopy scattering. Therefore, the objective of Chapter 2 is to develop a simplified adaptive volume scattering model (SAVSM) to describe the volume scattering caused by different crops such as corn,

soybean and wheat. The experimental results demonstrate that it is more efficient than other existing volume scattering models. The SAVSM provides theoretical basis for the surface parameter retrieval models in Chapter 3 and Chapter 4. Hence, by integrating the SAVSM and the X-Bragg surface scattering model, Chapter 3 is to investigate the potential of the current model-based decompositions and an adaptive two-component model-based decomposition (ATCD) is proposed to inverse the soil moisture over wheat fields at its early growing stage. However, the estimated soil moisture becomes biased and unreliable when the measured soil moisture is greater than 30 [vol%]. To overcome this issue, an integrated surface parameter inversion scheme (ISPIS) is developed in Chapter 4 making use of a calibrated IEM instead of the X-Bragg surface scattering model. Chapter 5 develops a multi-temporal supervised binary-tree classification scheme to maximize the difference of the polarization signatures (MTSBTCS-MDPS). Overall, the relationships among these five chapters are illustrated in Figure 1-11.

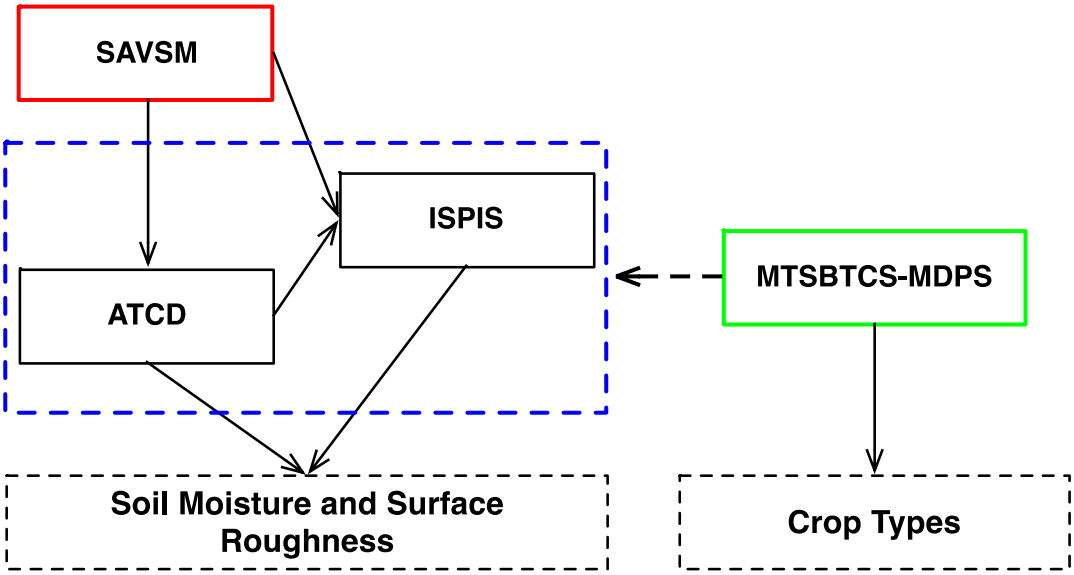

Figure 1-11. Relationships among the five thesis chapters.

References

An, W., Cui, Y., Yang, J., & Member, S. (2010). Three-Component Model-Based Decomposition for Polarimetric SAR Data, *IEEE Transactions on Geoscience and Remote Sensing*, *48*(6), 2732–2739.

An, W., Xie, C., Yuan, X., Cui, Y., & Yang, J. (2011). Four-Component Decomposition of Polarimetric SAR Images with Deorientation. *IEEE Geoscience and Remote Sensing Letters*, *8*(6), 1090–1094.

Antropov, O., Rauste, Y., & Häme, T. (2011). A Generalzied Radar Backsattering Model Based on Wave Theory for Multilayer Multispecies Vegetation. *IEEE Transactions on Geoscience and Remote Sensing*, *49*(12), 4832-4845.

Arii, M., van Zyl J. J., & Kim, Y. (2010). A General Characterization for Polarimetric Scattering from Vegetation Canopies. *IEEE Transactions on Geoscience and Remote Sensing*, *48*(9), 3349-3357.

Attema, E. P. W., & Ulaby, F. T. (1978). Vegetation Modeled as a Water Cloud. *Radio Science*, *13*(2), 357-364.

Ballester-berman, J. D., & Lopez-sanchez, J. M. (2010). Applying the Freeman–Durden Decomposition Concept to Polarimetric SAR Interferometry. *IEEE Transactions on Geoscience and Remote Sensing*, *48*(1), 466-479.

Ballester-Berman, J. D., Vicente-Guijalba, F., & Lopez-Sanchez, J. M. (2013). Polarimetric SAR Model for Soil Moisture Estimation over Vineyards at C-Band. *Progress in Electromagnetics Research-Pier*, *142*, 639-665.

Benz, U. C., Hofmann, P., Willhauck, G., Lingenfelder, I., & Heynen, M. J (2004). Multi-Resolution Object-Oriented Fuzzy Analysis of Remote Sensing Data for GIS-ready Information. *ISPRS Journal of Phototgrammetry and Remote Sesning*, *58*(3), 239-258.

Burgin, M., Clewley, D., Lucas, R. M., & Moghaddam, M. (2011). A Generalzied Radar Backsattering Model Based on Wave Theory for Multilayer Multispecies Vegetation. *IEEE Transactions on Geoscience and Remote Sensing*, *49*(12), 4832-4845.

Cao, F., Hong, W., Wu, Y. R., & Pottier, E. (2007). An Unsupervised Segmentation with an Adatpive Number of Clusters Using the SPAN/H/Alpha/A Space and the Complex Wishart Clustering for Fully Polarimetric SAR Data Analysis. *IEEE Transactions on Geoscience and Remote Sensing*, *45*(11), 3454-3467.

Baghdadi, N., King, C., Chanzy, A., & Wigneron, J. P. (2002). An Empirical Calibration of the Integral Equation Model Based on SAR Data, Soil Moisture and Surface Roughness Measurement over Bare Soils. *International Journal of Remote Sensing*, *23*(20), 4325-4340.

Baghdadi, N., Gherboudj, I., Zribi M., Sahebi, M., King, C., & Bonn, F. (2004). Semi-Empirical Calibration of the IEM Backscattering Model Using Radar Images and Moisture and Roughness Field Measurements. *International Journal of Remote Sensing*, *25*(18), 3593-3623.

Baghdadi, N., Holah, N., & Zribi, M. (2006). Calibration of the Integral Equation Model for SAR Data in C-Band and HH and VV Polarizations," *International Journal of Remote Sensing*, *27*(4), 805-816.

Baghdadi, N., Zribi, M., Paloscia, S., Verhoest, N., Lievens, H., Baup, F., & Mattia, F. (2015). Semi-Empirical Calibration of the Integral Equation Model for Co-Polarized L-Band Backscattering. *Remote Sensing*, *7*(10), 13626-13640.

Barrett, B. W., Dwyer, E., & Whelan, P. (2009). Soil Moisture Retrevial from Active Spaceborne Microwave Obervations: An Evaluation of Current Techniques. *Remote Sensing*, *1*, 210-242.

Berens, P. (2006). *Introduction to Synthetic Aperture Radar (SAR)*. FGAN-FHR Research Inst for High Frequency Physicas and Radar Techniques Wachtberg (Gernmany).

Bindlish, R., & Barros, A. P. (2001). Parameterization of Vegetation Backscatter in Radar-Based, Soil Moisture Estimation. *Remote Sensing of Environment*. *76*(1), 130-137.

Cameron, W. L., Youssef, N. N., & Leung, L. K. (1996). Simulated Polarimetric Signatures of Primitive Geometrical Shapes. *IEEE Transactions on Geoscience and Remote Sensing*, *34*(3), 793-803.

Clevers, J. G. P. W., Buker, C., Vanleeuwen, H. J. C., & Bouman, B. A. M. (1994). A Framework for Monitoring Crop Growth by Combining Directional and Spectral Remote-Sensing Information. *Remote Sensing of Environment, 50*(2), 161-170.

Cloude, S. R., & Pottier, E. (1996). A Review of Target Decomposition Theorems in Radar Polarimetry. *IEEE Transactions on Geoscience and Remote Sensing, 34*(2), 498-518.

Cloude, S. R., & Pottier, E. (1997). An Entropy Based Classification Scheme for Land Applications of Polarimetric SAR. *IEEE Transactions on Geoscience and Remote Sensing, 35*(1), 68-78.

Dubois, P. C., van zyl, J. J., & Engman, T. (1995). Measuring Soil Moisture with Imaging Radars. *IEEE Transactions on Geoscience and Remote Sensing, 33*(4), 915-926.

Duveiller, G., & Defourny, P. (2010). A Conceptual Framework to Define the Spatial Resolution Requirements for Agricultural Monitoring Using Remote Sensing. *Remote Sensing of Environment, 114*(11), 2637-2650.

Foody, G. M., Mcculloch, M. B., & Yates, W. B. (1994). Crop Classification from C-Band Polarimetric Radar Data. *International Journal of Remote Sensing,15*(14), 2871-2885.

Freeman, A., & Durden, S. L. (1998). A Three-Component Scattering Model for Polarimetric SAR Data. *IEEE Transactions on Geoscience and Remote Sensing, , 36*(3), 963-973.

Fung, A.K. (1994). *Microwave Scattering and Emission Models and Their Applications*, Artech House, Norwood, MA

Gherboudj, I., Magagi, R., Berg, A. a., & Toth, B. (2011). Soil Moisture Retrieval over Agricultural Fields from Multi-Polarized and Multi-Angular RADARSAT-2 SAR Data. *Remote Sensing of Environment, 115*(1), 33-43.

Gorrab, A., Zribi, M., Baghdadi, N., Mougenot, B., Fanise, P., & Chabaane, Z. L. (2015). Retrevial of Both Soil Moistureand Texture Using TerraSAR-X Iamges, *Remote Sensing, 7*(8), 10098-10116.

Guntiñas, M.E., Leirós, M.C., Trasar-Cepeda, C., & Gil-Sotres, F. (2012). Effects of Moisture and Temperature on Net Soil Nitrogen Mineralziation: A Laboratory Study，*European Journal of Soil Biology*, *48*, 73-80.

Hajnsek, I., Jagdhuber, T., Schon, H., & Papathanassiou, K. P. (2009). Potential of Estimating Soil Moisture under Vegetation Cover by Means of PolSAR. *IEEE Transactions on Geoscience and Remote Sensing*, *47*(2), 442-454.

Hajnsek, I., Pottier, E., & Cloude, S. R. (2003). Inversion of surface parameters from polarimetric SAR. *IEEE Transactions on Geoscience and Remote Sensing*, *41*(4), 727-744.

He, B., Xing, M., & Bai, X. (2014). A Synergistic Methodology for Soil Moisture Estimation in an Alpine Prairie Using Radar and Optical Satellite Data. *Remote Sensing*, *6*(11), 10966-10985.

Huang, X., Wang, J., and Shang J. (2015). A Simplified Adaptive Volume Scattering Model and Scattering Analysis of Crops over Agricultrual Fields Using the RADARSAT-2 Polarimetric SAR Imagery, *Journal of Applied Remote Sensing*, *9*(1), 096026-1-096026-18.

Huang, X., Wang, J., and Shang J. (2016). An Adaptive Two-Component Model-Based Decompostion on Soil Moisture Estiamtion for C-Band RADARSAT-2 Imagery over Agricultrua Fields, *IEEE Geoscience and Remote Sensing Letters*, *13*(3), 414–418.

Huang, X., Wang, J., and Shang J. (2016). An Integrated Surface Parameter Inversion Scheme over Agricultural Fields at Early Growing Stages by Means of C-Band Polarimetric RADARSAT-2 Imagery, *IEEE Transactions on Geoscience and Remote Sensing*, *54*(5), 2510–2528.

Ishimaru, A. (1978). *Wave Propagation and Scattering in Random Media*, Academic Press, New York.

Jagdhuber, T., Hajnsek, I., Bronstert, A., & Papathanassiou, K. P. (2013). Soil Moisture Estimation under Low Vegetation Cover Using a Multi-Angular Polarimetric Decomposition. *IEEE Transactions on Geoscience and Remote Sensing*. *51*(4), 2201-2215.

Jagdhuber, T., Hajnsek, I., Bronstert, A., & Papathanassiou, K. P. (2014)., An Iterative, Generalized, Hybrid Decomposition on Fully Polarimetric SAR Data for Soil Moisture Retrieval under Vegetation, *10th European Conference on Synthetic Aperture Radar*, Berlin, Germany, 818-821.

Jiao X., Kovacs, J., Shang, J., McNairn, H., Walters, D., Ma, B., & Geng, X. (2014). Object-Oriented Crop Mapping and Monitoring Using Multi-Temporal Polarimetric RADARSAT-2 Data. *ISPIS Journal of Photogrammetry and Remote Sensing*, *96*, 38-46.

Jin, Y. Q., & Xu, F. (2013). *Polarimetric Scattering and SAR Information Retrieval*. John Wiley & Sons.

Jones, H. G., & Vaughan, R. A. (2010). *Remote sensing of vegetation : principles, techniques, and applications*. Oxford, UK ; New York: Oxford University Press.

Joseph, A. T., Velde, R. van der, O'Neill, P. E., Lang, R. H., & Gish, T. (2008). Soil Moisture Retrieval during a Corn Growth Cycle Using L-Band (1.6 GHz) Radar Observations. *IEEE Transactions on Geoscience and Remote Sensing*, *46*(8), 2365-2374.

Kim, Y., Jackson, T., Bindlish, R., Hong, S., Jung G., & K. Lee. (2014). Retrieval of Wheat Growth Parameters with Radar Vegetation Indices. *IEEE Geoscience and Remote Sensing Letters*, *11*(4), 808-812.

Krogager, E., Boerner, W. M. & Madsen, S. N. (1997). Feature-Motivated Sinclair matrix (sphere/diplane/helix) Decomposition and Its Application to Target Sorting for Land Feature Classification. *Proc. SPIE Conference on Wideband Interferometric Sensing and Imaging Polarimetry*, *3120*(1), 144-154.

Lee, J. S., Grunes, M. R., & Kwok, R. (1994). Classification of Multi-Look Polarimetric SAR Imagery Based on Complex Wishart Distribution. *International Journal of Remote Sesning*, *15*(1), 2299-2311.

Lee, J. S., Grunes, M. R., Ainsworth T. L., Du, L. J., Schuler D. L., & Cloude S. R. (1999). Unsupervised Classification using Polarimetric Decomposition and The Complex Wishart Classifier. *IEEE Transactions on Geoscience and Remote Sensing*, *37*(5), 2249-2258.

Lee, J. S., & Pottier, E. (2009). *Polarimetric radar imaging : from basics to applications*. Boca Raton: CRC Press.

Lee, J. S., Ainsworth T. L., Thomas L., & Wang Y. (2014). Generalized Polarimetric Model-Based Decompositions Using Incoherent Scattering Models. *IEEE Transactions on Geoscience and Remote Sensing*, *52*(5), 2474-2491.

Lee, J. S., Grunes, M. R., Pottier, E., & Ferro-Famil, L. (2004). Unsupervised Terrain Classification Preserving Polarimetric Scattering Characteristics. *IEEE Transactions on Geoscience and Remote Sensing*, *42*(4), 722-731.

Lievens, H., & Verhoest, N. E. C. (2011). On the Retrieval of Soil Moisture in Wheat Fields from L-Band SAR Based on Water Cloud Modeling, the IEM, and Effective Roughness Parameters. *IEEE Geoscience and Remote Sensing Letters*, *8*(4), 740-744.

Lillesand, T. M., Kiefer, R. W., & Chipman, J. W. (2004). *Remote sensing and image interpretation* (5th editon). New York: Wiley.

Lin, H., Chen, J., Pei, Z., Zhang, S., & Hu, X. (2009). Monitoring Sugarcane Growth Using ENVISAT ASAR Data. *IEEE Transactions on Geoscience and Remote Sensing*, *47*(8), 2572-2580.

Liu, C., Shang, J. L., Vachon, P. W., & McNairn, H. (2013). Multiyear Crop Monitoring Using Polarimetric RADARSAT-2 Data. *IEEE Transactions on Geoscience and Remote Sensing*, *51*(4), 2227-2240.

McNairn, H., Shang, J., Jiao, X. & Champagne, C. (2009). The Contribution of ALOS PALSAR Multipolariztion and Polarimetric Data to Crop Classification. *IEEE Transactions on Geoscience and Remote Sensing*, *47*(12), 3981-3992.

Neumann, M., Ferro-Famil, L., & Reigber, A. (2009). Improvement of Vegetation Parameter Retrieval from Polarimetric SAR Interferomety Using a Simple Polarimetric Scatteing Model. *European Space Agency*, *668*.

Oh, Y. (2004). Quantitative Retrieval of Soil Moisture Content and Surface Roughness from Multipolarized Radar Observations of Bare Soil Surfaces. *IEEE Transactions on Geoscience and Remote Sensing*, *42*(3), 596-601.

Oh, Y. (2002). Semi-Empirical Model of The Ensemble-Averaged Differential Mueller Matrix for Microwave Backscattering from Bare Soil Surfaces. *IEEE Transactions on Geoscience and Remote Sensing*, *40*(6), 1348-1355.

Oh, Y., Sarabandi, K., & Ulaby, F. T. (1992). An Empirical Model and an Inversion Technique for Radar Scattering from Bare Soil Surfaces. *IEEE Transactions on Geoscience and Remote Sensing*, *30*(2), 370-381.

Oliver, C., Quegan, S., & Knovel. (2004). *Understanding synthetic aperture radar images*. SciTech radar and defense series.

Park, S. E., & Moon, W . M. (2007). Unsupervised Classifcation of Scattering Mechanisms in Polarimetric SAR Data Using Fuzzy Logic in Entropy and Alpha Plane. *IEEE Transactions on Geoscience and Remote Sensing*, *45*(8), 2652-2664.

Park, S. E., Moon, W. M., & Kim, D. (2009). Estimation of Surface Roughness Parameter in Intertidal Mudflat Using Airborne Polarimetric SAR Data. *IEEE Transactions on Geoscience and Remote Sensing*, *47*(4), 1022–1031.

Qi, Z., Yeh, A. G., Li, X., & Lin Z. (2012). A Novel Algorithm for Land Use and Land Cover Classification Using RADARSAT-2 Polarimetric SAR Data. *Remote Sensing of Environment*, *118*, 21-39.

Qi, Z., Yeh, A. G., Li, X., Xian, S., & Zhang, X. (2015). Monthly Short-Term Detection of Land Development Using RADARSAT-2 Polarimetric SAR Imagery. *Remote Sensing of Environment*, *164*, 179-196.

Rice, S.O. (1963). *Reflection of Electromagnetic Waves by Slightly Rough Sufaces, Interscience*, New York.

Roo, R. D. de, Du, Y. D. Y., Ulaby, F. T., & Dobson, M. C. (2001). A Semi-Empirical Backscattering Model at L-band and C-band for a Soybean Canopy with Soil Moisture Inversion. *IEEE Transactions on Geoscience and Remote Sensing*, *39*(4), 864-872.

Santi, E., Paloscia, S., Pettinato, S., & Fontanelli, G. (2016). Application of Artificial Neural Networks for the Soil Moisture Retrieval from Active and Passive Microwave Spaceborne Sensors. *International Journal of Applied Earth Obervation and Geoinformation*, *48*, 61-73.

Schuler, D. L., Kasilingam, D., & Nesti, G. (2002). Surface Roughness and Slope Measurements Using Polarimetric SAR Data. *IEEE Transactions on Geoscience and Remote Sensing*, *40*(3), 687-698.

Shan, Z., Wang, C., Zhang, H., & An, W. (2012). Improved Four-Component Model-Based Target Decomposition for Polarimetric SAR Data. *IEEE Geoscience and Remote Sensing Letters*. *9*(1), 75-79.

Song, K., Zhou, X., & Fan, Y. (2009). Empirically Adopted IEM for Retrieval of Soil Moisture from Radar Backscattering Coefficients. *IEEE Geoscience and Remote Sensing Letters*. *47*(6), 1662-1672.

Trudel, M., Magagi, R., & Granberg, H. B. (2009). Application of Target Decomposition Theorems over Snow-Covered Forested Areas. *IEEE Transactions on Geoscience and Remote Sensing*, *47*(2), 508-512.

Tsang, L., Kong, J. A., & Ding, K.-H. (2000). *Scattering of Electromagnetic Waves. Theories and applications*. New York: Wiley.

Ulaby, F. T., Moore, R. K., & Fung, A. K. (1986). *Microwave Remote Sensing: Active and Passive. Volume 3 - from Theory to Applications*. New York: Addison-Wesley Pub. Co., Advanced Book Program/World Science Division.

Ulaby, F. T., Sarabandi, K., McDonald, K., Whitt, M., & Dobson, M. C. (1990). Michigan Microwave Canopy Scattering Model. *International Journal of Remote Sensing*, *11*(7), 1223-1253.

Vecchia, A. Della, Ferrazzoli, P., Guerriero, L., Ninivaggi, L., Strozzi, T., & Wegmuller, U. (2008). Observing and Modeling Multifrequency Scattering of Maize During the Whole Growth Cycle. *IEEE Transactions on Geoscience and Remote Sensing*, *46*(11), 3709-3718.

Verhoest, N. E., Lievens, H., Wagner, W., Álvarez-Mozos, J., Moran, M. S., & Mattia, F. (2008). On the Soil Roughness Parameterization Problem in Soil Moisture Retrieval of Bare Surfaces from Synthetic Aperture Radar. *Sensors*, *8*(7), 4213-4228.

Wang, Y., Liu, H., & Bo, J. (2014). Coherency Matrix Decomposition Based on Constrained Sparse Representation. *IEEE Transactions on Geoscience and Remote Sensing*, *52*(9), 5906-5922.

Wang, H., Magagi, R., Goita, K., Jagdhuber, T., & Hajnsek, I. (2016). Evaluation of Simplified Polarimetric Decomposition for Soil Moisture Retrieval over Vegetated Agricultural Fields. *Remote Sensing*, *8*(2), 1-24.

Yamaguchi, Y., Moriyama, T., Ishido, M., & Yamada, H. (2005). Four-Component Scattering Model for Polarimetric SAR Image Decomposition. *IEEE Transactions on Geoscience and Remote Sensing*, *43*(8), 1699-1706.

Yamaguchi, Y., Yajima, Y., & Yamada, H. (2006). A Four-Component Decomposition of POLSAR Images Based on The Coherency Matrix. *IEEE Geoscience and Remote Sensing Letters*, *3*(3), 292-296.

Zheng, Z. C., He, S. Q., & Wu, F. Q. (2012). Relationship between Soil Surface Roughness and Hydraulic Roughness Coefficient on Sloping Farmland. *Water Science and Engineering*, *5*(2), 191-201.

Chapter 2 Simplified Adaptive Volume Scattering Model and Scattering Analysis of Crops over Agricultural Fields*

2.1 Introduction

Mapping and monitoring changes in cropland can provide valuable information to aid the decision-making for sustainable agriculture production and market access (Liu et al., 2013; McNairn et al., 2012). Compared with optical sensors, microwave signal has the day and night capability and can penetrate clouds and light rain with negligible attenuation, thus allowing for reliable repeat measurements over the short dynamic crop growing season (Moran et al., 2011). Fully polarimetric SAR (PolSAR) with four channels and the phase component contains much more information than the single-polarization and dual-polarization SAR, and hence has greater potential for retrieving crop biophysical parameters.

Polarimetric SAR decomposition in PolSAR is a very useful tool for characterizing crop scattering mechanisms that can be used for crop classification and crop growth condition monitoring. In general, there are two types of decomposition methods. One is the coherent target decomposition represented by the Krogagar and Cameron Decompositions (Krogager et al., 1997; Cameron et al., 1996) which are based on the single-look Sinclair matrix; the other is the non-coherent decomposition based on the multi-look covariance or coherency matrix, such as the Cloude-Pottier decomposition (Cloude & Pottier, 1997) which is based on the eigenvalue analysis and the Freeman-Durden model-based decomposition (Freeman & Durden, 1998) that describes the scattering process as the linear sum of the surface, double-bounce and volume scattering. Due to its simplicity and intuition, many decomposition methods (An et al., 2010; An et al., 2011; Yamaguchi et al., 2005; Yamaguchi et al., 2006; Yajima et al., 2008;

---

* A version of this chapter has been published as "Huang, Xiaodong, Wang, Jinfei, and Shang, Jiali (2015). A Simplified Adaptive Volume Scattering Model and Scattering Analysis of Crops over Agricultrual Fields Using the RADARSAT-2 Polarimetric SAR Imagery, *Journal of Applied Remote Sensing*, *9*(1), 096026-1-096026-18."

Yamaguchi et al., 2011; Sato et al., 2012; Shan et al., 2012) were developed based on the Freeman-Durden model-based framework and have been widely applied to vegetation information extractions (Trudel et al., 2009; Ballester-Berman & Lopez-Sanchez, 2010). More recently, Chen et al. (2013; 2014; 2014) also proposed several model-based decompositions, but their work is primarily focusing on separating the built-up area from volume scattering.

Volume scattering as a characterization of vegetation scattering is a key component in model-based decompositions. However, it remains a challenging task to construct the volume scattering for accurate information extractions. Although many volume scattering models have been developed in recent years, they are limited to characterize only certain types of vegetation. Freeman and Durden (1998) first developed a volume scattering model using the uniform probability density function. Yamaguchi et al. (2005) added the vertical and horizontal volume scattering models to extend the Freeman-Durden volume scattering model by making use of the first order sine probability density function. An et al. (2010) proposed a maximum entropy volume scattering model, but it requires more experiments to validate. Antropov et al. (2011) proposed a generalized volume scattering model which can adapt to the sensitivity between the HH and VV co-polarizations for different types of forests. Arii et al. (2010), van Zyl et al. (2011) and Arii et al. (2011) developed a general scattering model based on an n-power cosine square function. However, with the randomness and orientation angle both being the unknown variables, they must be calculated simultaneously, which makes the computation very time-consuming. Overall, most of these existing models are vegetation type dependent and very difficult to fully characterize crop changes with time. Therefore, in this chapter, a simplified adaptive volume scattering model (SAVSM) is proposed with a three-component model-based decomposition combing with SAVSM is developed (TCMD-SAVSM).

2.2 The Framework of Model-Based Decomposition

The model-based decomposition framework proposed by Freeman and Durden (1998) can be described as

$$\mathrm{C} = f_s C_s + f_d C_d + f_v C_v \tag{2-5}$$

where C is the covariance matrix measured by polarimetric SAR sensors, C_s, C_d and C_v represent the covariance matrix of surface, double-bounce and volume scattering model respectively, and f_s, f_d and f_v correspond to the coefficients of each scattering. The C_s, C_d and C_v can be described as

$$C_s = \begin{bmatrix} |\beta|^2 & 0 & \beta \\ 0 & 0 & 0 \\ \beta^* & 0 & 1 \end{bmatrix} C_d = \begin{bmatrix} |\alpha|^2 & 0 & \alpha \\ 0 & 0 & 0 \\ \alpha^* & 0 & 1 \end{bmatrix} C_v = \begin{bmatrix} 3/8 & 0 & 1/8 \\ 0 & 1/4 & 0 \\ 1/8 & 0 & 3/8 \end{bmatrix} \tag{2-6}$$

where β and α are the surface and double-bounce parameters respectively; they are related to the dielectric constant of the medium and can also be used to retrieve soil moisture (Hajnsek et al., 2009). Although the model-based decomposition is intuitive in reflecting the scattering process, a critical problem arises when it is applied to an area under vegetation cover, i.e., the negative power problem in which the power of surface or double-bounce scattering is negative after decomposition, which is conflicting with reality. To circumvent this problem, several researchers developed different models by adding in de-orientation or improving volume scattering models (An et al., 2010; An et al., 2011; Yamaguchi et al., 2005; Yamaguchi et al., 2006; Yajima et al., 2008; Yamaguchi et al., 2011; Sato et al., 2012; Shan et al., 2012). However, in order to avoid the negative power and consider the physical realization, the non-negative eigenvalue decomposition method (NNED) proposed by van Zyl et al. (2011) was adopted, while the de-orientation process will not be considered in this chapter because the orientation angles derived from the C-band RADARSAT-2 data contain too much noise (Lee & Thomas, 2011).

2.3 Simplified Adaptive Volume Scattering Model and TCMD-SAVSM

2.3.1 Framework of Volume Scattering Model Construction

The general volume scattering model construction has been widely used in literatures (Freeman & Durden, 1998; Yamaguchi et al., 2005; Arii et al., 2010), which can be described as follows,

$$\mathrm{C}_v = \int_a^b \mathrm{p}(\theta)\mathrm{C}(\theta)d\theta \tag{2-7}$$

Where $\mathrm{p}(\theta)$ is the probability distribution function (PDF) of the orientation angles of dipoles, and $\mathrm{C}(\theta)$ is the covariance matrix rotated θ with respect to the line of sight (LOS), C_v is the volume scattering model, a and b are the integration limits. In general, the Sinclair matrix used for constructing volume scattering matrix can be described as,

$$S = \begin{bmatrix} \mathrm{S}_{hh} & 0 \\ 0 & \mathrm{S}_{vv} \end{bmatrix} \tag{2-8}$$

When $\mathrm{S}_{hh} = 1, \mathrm{S}_{vv} = 0$, it represents horizontal dipoles; while $\mathrm{S}_{hh} = 0, \mathrm{S}_{vv} = 1$, it represents vertical dipoles; when $\mathrm{S}_{hh} = 1, \mathrm{S}_{vv} = 1$, it represents the sphere or thin flat plate. After rotation with respect to the LOS with angleθ, the scattering matrix can be described as

$$S(\theta) = \begin{bmatrix} \cos\theta & \sin\theta \\ -\sin\theta & \cos\theta \end{bmatrix} \begin{bmatrix} \mathrm{S}_{hh} & 0 \\ 0 & \mathrm{S}_{vv} \end{bmatrix} \begin{bmatrix} \cos\theta & -\sin\theta \\ \sin\theta & \cos\theta \end{bmatrix} \tag{2-9}$$

Then, the Lexicographic feature vector can be described as,

$$\mathrm{L} = \left[(\cos\theta)^2\mathrm{S}_{hh} + (\sin\theta)^2\mathrm{S}_{vv} \quad \sqrt{2}\cos\theta\sin\theta(\mathrm{S}_{vv} - \mathrm{S}_{hh}) \quad (\cos\theta)^2\mathrm{S}_{vv} + (\sin\theta)^2\mathrm{S}_{hh}\right]^T \tag{2-10}$$

Where L is the Lexicographic vector, according to $\mathrm{C} = \mathrm{L} \cdot \mathrm{L}^{H}$, where H denotes the complex conjugation and transposition, then, the covariance matrix after rotation can be shown as,

$$\mathrm{C}(\theta) = \begin{bmatrix} \mathrm{C}_{11} & \mathrm{C}_{12} & \mathrm{C}_{13} \\ \mathrm{C}_{21} & \mathrm{C}_{22} & \mathrm{C}_{23} \\ \mathrm{C}_{31} & \mathrm{C}_{32} & \mathrm{C}_{33} \end{bmatrix} \tag{2-11}$$

Where

$\mathrm{C}_{11} = ((\cos\theta)^2 \mathrm{S}_{hh} + (\sin\theta)^2 \mathrm{S}_{vv})^2$

$\mathrm{C}_{12} = \mathrm{C}_{21} = \sqrt{2}/2\,((\cos\theta)^2 \mathrm{S}_{hh} + (\sin\theta)^2 \mathrm{S}_{vv})(\cos\theta\sin\theta \mathrm{S}_{hh} - \cos\theta\sin\theta \mathrm{S}_{vv})$

$\mathrm{C}_{13} = \mathrm{C}_{31} = ((\cos\theta)^2 \mathrm{S}_{hh} + (\sin\theta)^2 \mathrm{S}_{vv})((\cos\theta)^2 \mathrm{S}_{vv} + (\sin\theta)^2 \mathrm{S}_{hh})$

$\mathrm{C}_{22} = 2(\cos\theta\sin\theta \mathrm{S}_{hh} - \cos\theta\sin\theta \mathrm{S}_{vv})^2$

$\mathrm{C}_{23} = C_{32} = \sqrt{2}/2\,((\sin\theta)^2 \mathrm{S}_{hh} + (\cos\theta)^2 \mathrm{S}_{vv})(\cos\theta\sin\theta \mathrm{S}_{hh} - \cos\theta\sin\theta \mathrm{S}_{vv})$

$\mathrm{C}_{33} = ((\cos\theta)^2 \mathrm{S}_{vv} + (\sin\theta)^2 \mathrm{S}_{hh})^2$

2.3.2 Simplified Adaptive Volume Scattering Model (SAVSM)

It is logical to select either horizontal or vertical Sinclair scattering matrix as the basic dipole to construct the covariance matrix since their orientation angles only have a $\frac{\pi}{2}$ phase difference. In this chapter, the horizontal dipole i.e. $\mathrm{S}_{hh} = 1, \mathrm{S}_{vv} = 0$ was adopted. Then, covariance matrix (2-7) can be simplified as,

$$\mathrm{C}(\theta) = \begin{bmatrix} (\cos\theta)^4 & -\sqrt{2}(\cos\theta)^3\sin\theta & (\cos\theta)^2(\sin\theta)^2 \\ -\sqrt{2}(\cos\theta)^3\sin\theta & 2(\cos\theta)^2(\sin\theta)^2 & -\sqrt{2}(\sin\theta)^3\cos\theta \\ (\cos\theta)^2(\sin\theta)^2 & -\sqrt{2}(\sin\theta)^3\cos\theta & (\sin\theta)^4 \end{bmatrix} \tag{2-12}$$

Accounting for the PDF of the vegetation orientation angles, Freeman and Durden (1998) argued that the orientation angles satisfied the uniform distribution, while Yamaguchi et al. (2005) added the vertical dipoles volume scattering based on the first order sine

function. However, crops at different phenological stages could have different architectures which can result in different scattering mechanisms. Corn is a good example of this; the scattering mechanisms when leaves are dense and green are different from that when leaves become sparse and yellow and start to bend down. From this perspective, neither the Freeman-Durden volume scattering model nor the Yamaguchi volume scattering model can adequately describe the variation of crops over the entire growing season. Different from the above-mentioned volume scattering models, Huang and Wang (2014) added the nth power to the first order sine function to adapt to the variation of crops for RADARSAT-2 imagery, but it is restricted to only characterize the vertical volume scattering. To enhance its suitability, in this chapter, the nth power cosine function is added to describe the horizontal volume scattering. Then, the PDFs of SAVSM in this chapter are described as,

$$p_h(\theta) = \frac{(Sin\theta)^n}{\int_0^{\pi}(Sin\theta)^n d\theta} \text{ and } p_v(\theta) = \frac{(Cos\theta)^n}{\int_{-\frac{\pi}{2}}^{\frac{\pi}{2}}(Cos\theta)^n d\theta} \tag{2-13}$$

Different PDFs with different n for vertical volume scattering models are shown in Figure 2-1.

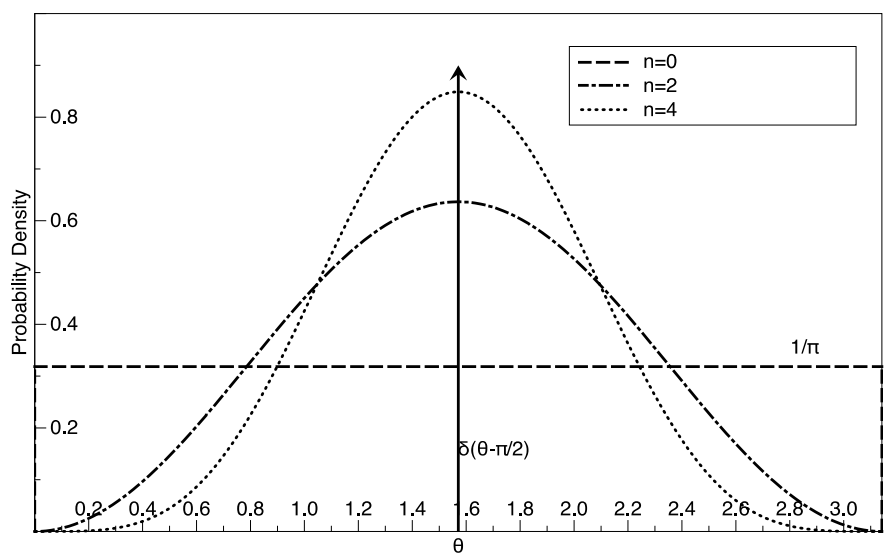

Figure 2-1. PDFs of vertical adaptive volume scattering model with orientation angles.

When $n = 0$, $\mathrm{p}(\theta) = \frac{1}{\pi}$ is the uniform distribution function which is the same as Freeman and Durden (1998). When $n = 1 \cdots k$, $\mathrm{p}(\theta)$ becomes narrower as n increases. When$n \to \infty$, $\mathrm{p}(\theta) = \delta(\theta - \frac{\pi}{2})$ is the Dirac function representing the pure vertical dipole. Substituting (2-8) and (2-9) with (2-3), after integration, the vertical and horizontal adaptive volume scattering model (V-SAVSM and H-SAVSM) can be re-written as:

V-SAVSM:

$$\mathrm{C}_v 11 = \frac{1}{A} \cdot \frac{3\sqrt{\pi}\Gamma\left(\frac{n+1}{2}\right)}{4\Gamma\left(\frac{n}{2}+3\right)}$$

$$\mathrm{C}_v 12 = \mathrm{C}_v 21 = \mathrm{C}_v 23 = \mathrm{C}_v 32 = 0, \mathrm{C}_v 22 = \frac{1}{A} \cdot \frac{\sqrt{\pi}\Gamma\left(\frac{n+3}{2}\right)}{\Gamma\left(\frac{n}{2}+3\right)} \tag{2-14}$$

$$\mathrm{C}_v 13 = \mathrm{C}_v 31 = \frac{1}{A} \cdot \frac{\sqrt{\pi}\Gamma\left(\frac{n+3}{2}\right)}{2\Gamma\left(\frac{n}{2}+3\right)}, \mathrm{C}_v 33 = \frac{1}{A} \cdot \frac{\sqrt{\pi}\Gamma\left(\frac{n+5}{2}\right)}{\Gamma\left(\frac{n}{2}+3\right)}$$

H-SAVSM：

$$\mathrm{C}_v 11 = \frac{1}{A} \cdot \frac{3\sqrt{\pi}\Gamma\left(\frac{n+1}{2}\right)}{4\Gamma\left(\frac{n}{2}+3\right)}$$

$$\mathrm{C}_v 12 = \mathrm{C}_v 21 = \mathrm{C}_v 23 = \mathrm{C}_v 32 = 0, \mathrm{C}_v 22 = \frac{1}{A} \cdot \frac{\sqrt{\pi}\Gamma\left(\frac{n+3}{2}\right)}{\Gamma\left(\frac{n}{2}+3\right)} \tag{2-15}$$

$$\mathrm{C}_v 13 = \mathrm{C}_v 31 = \frac{1}{A} \cdot \frac{\sqrt{\pi}\Gamma\left(\frac{n+3}{2}\right)}{2\Gamma\left(\frac{n}{2}+3\right)}, \mathrm{C}_v 33 = \frac{1}{A} \cdot \frac{\sqrt{\pi}\Gamma\left(\frac{n+5}{2}\right)}{\Gamma\left(\frac{n}{2}+3\right)}$$

Where $A = \int_0^{\pi} (Sin\theta)^n d\theta = \int_{-\frac{\pi}{2}}^{\frac{\pi}{2}} (Cos\theta)^n d\theta = \frac{\sqrt{\pi}\Gamma\left(\frac{n+1}{2}\right)}{\Gamma\left(\frac{n}{2}+1\right)}$ and $\Gamma(a) = \int_0^{\infty} e^{-t} t^{a-1} dt$. It should be noted that n is greater than 0, but not limited to the integer. It can be seen that

the difference between V-SAVSM and H-SAVSM is only in the HH and VV components. The HH component of the V-SAVSM is equal to the VV component of the H-SAVMS, and *vice versa*. It should also be noted that the combined V-SAVSM and H-SAVSM is referred as SAVSM in the sections follow.

2.3.3 Analysis of SAVSM

Without loss of generality, the V-SAVSM is analyzed only in this section. The components of the V-SAVSM are plotted in Figure 2-2. Figure 2-2(a) shows that, as the n increases, the HH component decreases, while the VV component increases. At the same time, the HH-VV components increase first then decrease at the point where $n = 1$. The radar vegetation index (RVI) proposed by Kim and van Zyl (2001) as an indicator of randomness in scattering by vegetation can be described as,

$$\mathrm{RVI} = \frac{4min(\lambda_1, \lambda_2, \lambda_3)}{\lambda_1 + \lambda_2 + \lambda_3} \tag{2-16}$$

Where λ_1, λ_2 and λ_3 are the eigenvalues of adaptive volume scattering models. The RVI and the scattering entropy proposed by Cloude and Pottier (1997) are both depicted in Figure 2-2(b). Both entropy and RVI decrease as n increases. However, RVI has a steeper decreasing curve than entropy does. Considering this, the curve of RVI can be used to limit the range of n, thereby accelerate finding the optimum n in practice. It can be seen that the RVI is very low and almost stays unchanged from $n = 20$ onwards, so the maximum n in this chapter should be 20. However, since the RADARSAT-2 imagery is in short wavelength (5.4cm), and is adopted for validation and analysis, the vegetation shows much more randomness compared with other long wavelength microwave such as the L (25cm) and P-band (60cm) (Arii et al., 2011). Therefore, the maximum value set in this chapter is 5 practically.

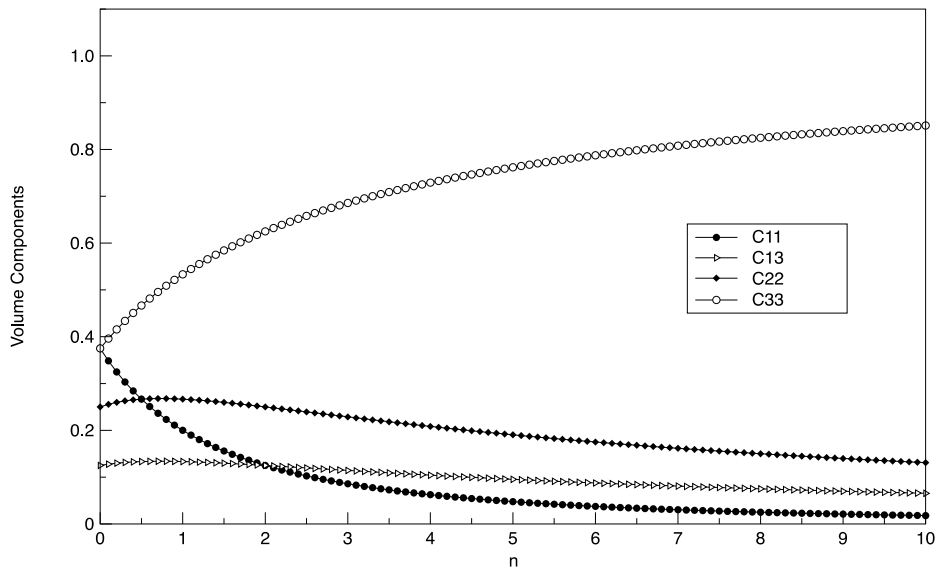

(a)

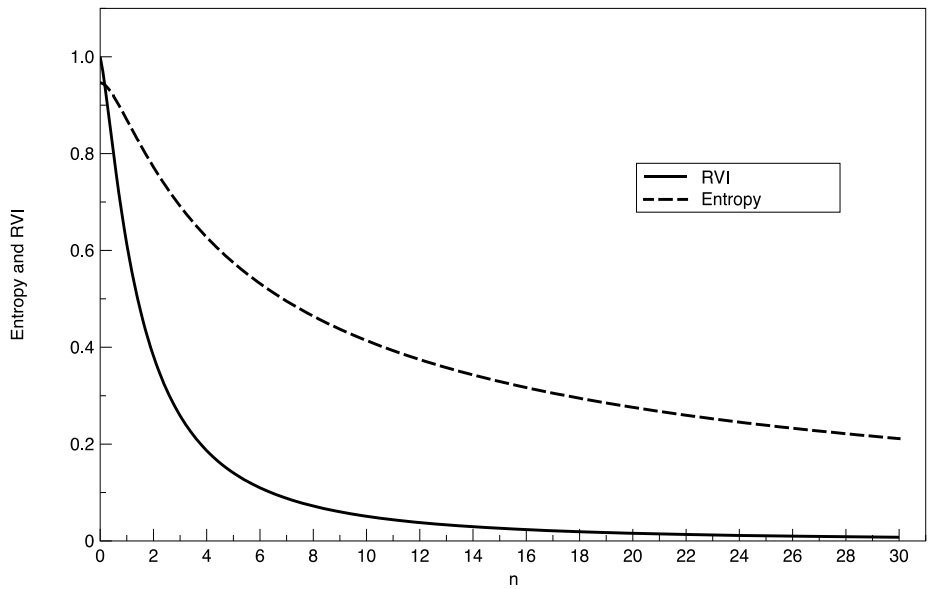

(b)

Figure 2-2. Vertical volume scattering matrix: (a) components of adaptive volume scattering matrix (b) entropy, RVI and randomness of adaptive volume scattering matrix.

Next, some n are selected to compare with other volume scattering models proposed by Freeman and Durden (1998) (FD-VSM), Yamaguchi et al. (2005) (Y-VSM) and Hajnsek et al. (2009) (H-VSM), which are listed in Table 2-1. It can be seen that the SAVSM not only includes the FD-VSM, Y-VSM and H-VSM, but also continues to respond to n.

From this view, it has a better potential to describe changes in crops with time than FD-VSM, Y-VSM and H-VSM. Finding the optimum n to fit with crop variations over time is very important, so in the next section, the procedures on how to calculate the optimum n to construct the TCMD-SAVSM based on SAVSM are introduced.

Table 2-1. Comparison of SAVSM with other volume scattering models.

n	V-SAVSM	H-SAVSM	Reference
0	$\begin{bmatrix} 0.375 & 0 & 0.125 \\ 0 & 0.250 & 0 \\ 0.125 & 0 & 0.375 \end{bmatrix}$	$\begin{bmatrix} 0.375 & 0 & 0.125 \\ 0 & 0.250 & 0 \\ 0.125 & 0 & 0.375 \end{bmatrix}$	FD-VSM
1	$\begin{bmatrix} 0.200 & 0 & 0.133 \\ 0 & 0.267 & 0 \\ 0.133 & 0 & 0.533 \end{bmatrix}$	$\begin{bmatrix} 0.533 & 0 & 0.133 \\ 0 & 0.267 & 0 \\ 0.133 & 0 & 0.200 \end{bmatrix}$	Y-VSM
3.68	$\begin{bmatrix} 0.688 & 0 & 0.107 \\ 0 & 0.215 & 0 \\ 0.107 & 0 & 0.567 \end{bmatrix}$	$\begin{bmatrix} 0.567 & 0 & 0.107 \\ 0 & 0.215 & 0 \\ 0.107 & 0 & 0.688 \end{bmatrix}$	H-VSM

2.3.4 The Algorithm of TCMD-SAVSM

As mentioned by van Zyl et al. (2011), there is a remainder matrix existing in the model-based decomposition after applying the NNED method, which can be described as,

$$C_{remainder} = \mathrm{C} - f_s C_s - f_d C_d - f_v C_v \tag{2-17}$$

where $C_{remainder}$ is the remainder matrix. Ideally, the sum of the power of the optimum volume scattering model and surface and double-bounce scattering is equal to the total power, which means the power of the remainder matrix (PRM) should be zero. However, it is very difficult to do so for each pixel due to the complexity of the scattering. In order to achieve the optimum volume scattering model, an optimum n is needed, which can make the PRM minimal. However, there are two volume scattering models proposed in this chapter: V-SAVSM and H-SAVSM. Being different from Yamaguchi et al. who used the $10\log_{10}(VV/HH)$ as the criterion to select the suitable volume scattering from three types, i.e., horizontal, vertical and random volume scattering models, whether the V-SAVSM or the H-SAVSM is adopted in this chapter depends on which one can better minimize the PRM. Based on this criterion, the procedure and flowchart of the three-

component model-based decomposition with SAVSM (TCMD-SAVSM) algorithm proposed in this chapter can be described as

Step 1*: the V-SAVSM is applied to the TCMD-SAVSM.*

Step 2*: looping from $n = 0$ to 5 with steps of 0.01 to find the optimum n based on the NNED method, and f_v is obtained first.*

Step 3*: f_s and f_d are calculated by the Freeman-Durden decomposition based on the sign of $Re(HH * VV^*)$ which is to determine whether the surface or double bounce is dominant.*

Step 4*: the H-SAVSM is also applied and step 3 and 4 are repeated.*

Step 5*: f_s, f_d and f_v will be selected according to V-SAVSM and H-SAVSM depending on which one could make the PRM minimum.*

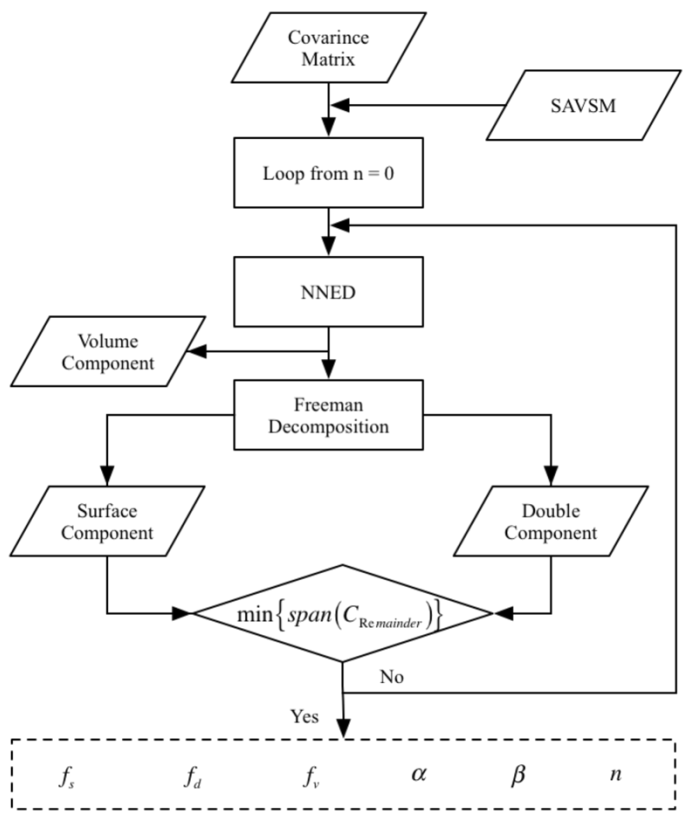

Figure 2-3. The flowchart of the TCMD-SAVSM for each pixel in covariance matrix.

2.4 Experiments and Validation

2.4.1 Experimental Dataset

The study area selected is near the city of London in southwestern Ontario, Canada. Multi-temporal RADARSAT-2 C-band polarimetric data used in this chapter are shown in Table 2-2, which were from May 7th to September 28th 2012, and the day of year (DoY) s was from day 128 to 272. These images are in the same Fine Quad (FQ) mode with the incidence angle 40.2 degrees. There is no special reason why only this mode is employed in this chapter, while other modes can also be adopted as long as they are available and can cover the entire crop growing season, whereas these images must keep the same incidence angle as well. In addition, although the SAVSM does not consider the incidence angle, the powers of decomposed components closely depend on the incidence angle. Figure 2-4 depicts the Pauli image on day 152 and the optical RapidEye image on day 160. There are three major crops in this area: corn, winter wheat, and soybean. Every data layer was geocoded using the MapReady3.2.1 software (https://www.asf.alaska.edu/data-tools/mapready/) with a digital elevation model at a pixel spacing of 10m. A 25-multi-look processing with 5-pixel window size in each direction was performed using the PolSARPro 4.2 software (http://earth.eo.esa.int/polsarpro/Download/) before the TCMD-SAVSM was applied. After these processes, the size of the image becomes 642×713 pixels.

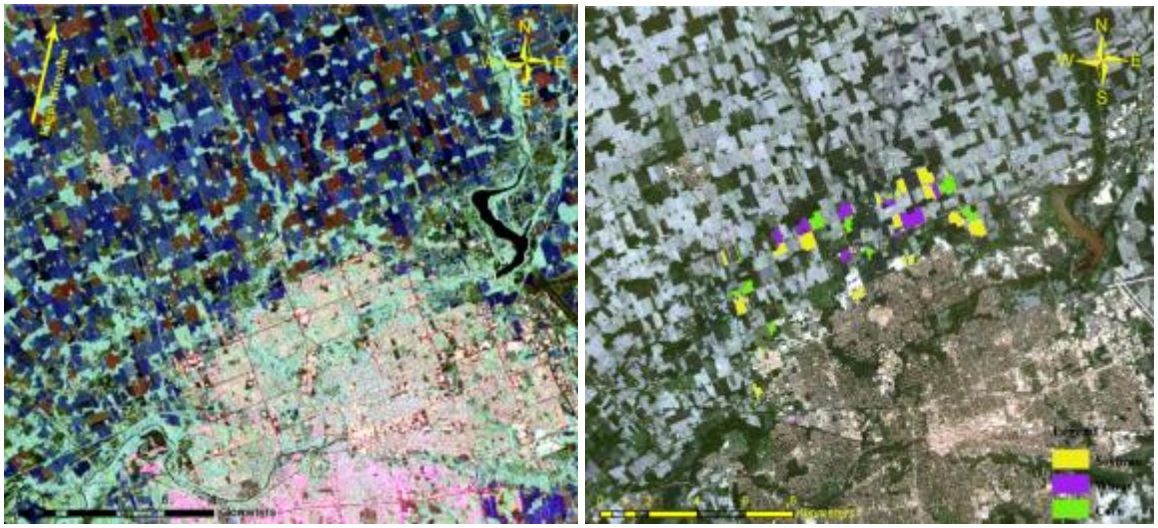

(a) (b)

Figure 2-4. Pauli and RapidEye images of study area on day 152 and 160 respectively: (a) Pauli image with red $|\boldsymbol{S_{HH}} - \boldsymbol{S_{VV}}|^{\mathbf{2}}$, green $\mathbf{4}|\boldsymbol{S_{HV}}|^{\mathbf{2}}$ and blue $|\boldsymbol{S_{HH}} + \boldsymbol{S_{VV}}|^{\mathbf{2}}$: polygons outlined fields that are sample fields that will be analyzed in next sections. (b) Optical RapidEye image.

Table 2-2. RADARSAT-2 dataset acquired over southwestern Ontario, Canada.

Date	DoY	Sensor mode-Incidence angle	Orbit	Look direction
2012-05-07	128	FQ21-40.2°	Ascending	Right
2012-05-31	152	FQ21-40.2°	Ascending	Right
2012-06-24	176	FQ21-40.2°	Ascending	Right
2012-07-18	200	FQ21-40.2°	Ascending	Right
2012-08-11	224	FQ21-40.2°	Ascending	Right
2012-09-04	248	FQ21-40.2°	Ascending	Right
2012-09-28	272	FQ21-40.2°	Ascending	Right

2.4.2 Comparison of TCMD-SAVSM with AMD

The adaptive model-based decomposition (AMD) proposed by Arii et al. (2011) described the volume scattering model with two parameters: orientation angle and the randomness of the vegetation. In theory, it has the potential to achieve better performance due to more parameters used to characterize the vegetation variation. Hence, to demonstrate the TCMD-SAVSM adequately, in this section, the TCMD-SAVSM is compared with AMD on two aspects: the time they consume and their decomposed components. The AMD depends on three factors: the increment of the randomness ($\nabla\delta$), the increment of the orientation angle ($\nabla\theta$), and the increment of the coefficient of volume scattering model (∇f_v). How to select the suitable values for these increments is the key, and also a problem. The range of the randomness δ is from 0 to 1. When a smaller $\nabla\delta$ is selected, better decomposed components can be obtained, but it can be very time consuming. It is the same with $\nabla\theta$ and ∇f_v. Therefore, in practice, we first fix $\nabla\theta = 1^o$ when θ is from 0 to 180 degrees, and $\nabla\delta = 0.1$ with its range from 0 to 1. All of the RADARSAT-2 data have been pre-processed to sigma naught, therefore, the total power (not in decibel unit) of the majority of pixels in the entire image is from 0 to 1. Hence, it is feasible to select a ∇f_v less than 1. Generally, the smaller the ∇f_v is set, the better the decomposed results the AMD will have. However, when ∇f_v is set to 0.001, each line (713 pixels) of the image will consume approximately 11 minutes, which will result in the total time of the entire image being (642×11 minutes) around 117.7 hours

(about 5 days). Practically, three ∇f_v are selected in this chapter for comparison: $\nabla f_v = 0.01$, $\nabla f_v = 0.05$ and $\nabla f_v = 0.1$. The time, the mean and standard deviation of the PRM of the entire image were computed by a workstation with the Windows 7 Professional 64-bit operating system, i7 3.20 GHZ processor ad 24 GB installed memory. In addition, all programs in this chapter are implemented using Matlab 2013a (64 bit).

Table 2-3. Comparison of TCMD-SAVSM with AMD within different $\boldsymbol{\nabla f_v}$. To test the time different algorithms, the configuration of the workstation is windows 7 professional with processor i7 3.20 GHZ and ram 24 GB. All programs are implemented using Matlab 2013a (64 bit).

Methods	DoY	Time (hours)	Mean of PRM	Std. of PRM
AMD with $\nabla f_v = 0.01$	128	23.2469	**0.0111**	0.0214
	152	19.9989	**0.0077**	0.0211
	176	24.1933	**0.0100**	0.0210
	200	23.1633	**0.0100**	0.0214
	224	27.5708	**0.0117**	0.0218
	248	26.4711	**0.0117**	0.0240
	272	23.9531	**0.0086**	0.0215
AMD with $\nabla f_v = 0.05$	128	12.2311	0.0130	0.0219
	152	11.7794	0.0114	0.0211
	176	12.5983	0.0120	0.0213
	200	12.9581	0.0125	0.0217
	224	13.5164	0.0136	0.0222
	248	13.0806	0.0135	0.0244
	272	12.1022	0.0113	0.0217
AMD with $\nabla f_v = 0.10$	128	10.6292	0.0187	0.0225
	152	10.5714	0.0157	0.0217
	176	10.8139	0.0172	0.0220
	200	10.8044	0.0169	0.0225
	224	11.0703	0.0173	0.0228
	248	10.8669	0.0176	0.0250
	272	10.5792	0.0160	0.0222
The proposed TCMD-SAVSM	128	3.4967	**0.0051**	0.0221
	152	3.4847	**0.0040**	0.0221
	176	3.4794	**0.0050**	0.0224
	200	3.5142	**0.0053**	0.0227
	224	3.6142	**0.0057**	0.0234
	248	3.5253	**0.0054**	0.0230
	272	3.3339	**0.0040**	0.0224

From Table 2-3, the mean of the PRM increases but the time decreases as ∇f_v increases. $\nabla f_v = 0.01$ has lower mean of PRM on each date compared with the other two ∇f_v; therefore, only AMD with $\nabla f_v = 0.01$ is compared with TCMD-SAVSM in this section. The AMD consumes around 6.6 times more time than that of the proposed TCMD-

SAVSM and the mean PRM is about twice more than that of the proposed TCMD-SAVSM as well. However, the standard deviation is similar between the two. In addition, the mean of the PRM listed in Table 2-3 is for the entire image, i.e., it also includes the urban and forest areas besides agricultural fields. Hence, the mean and standard deviation of the PRM in the sample agricultural fields shown as polygons in Figure 2-4, are shown in Figure 2-5.

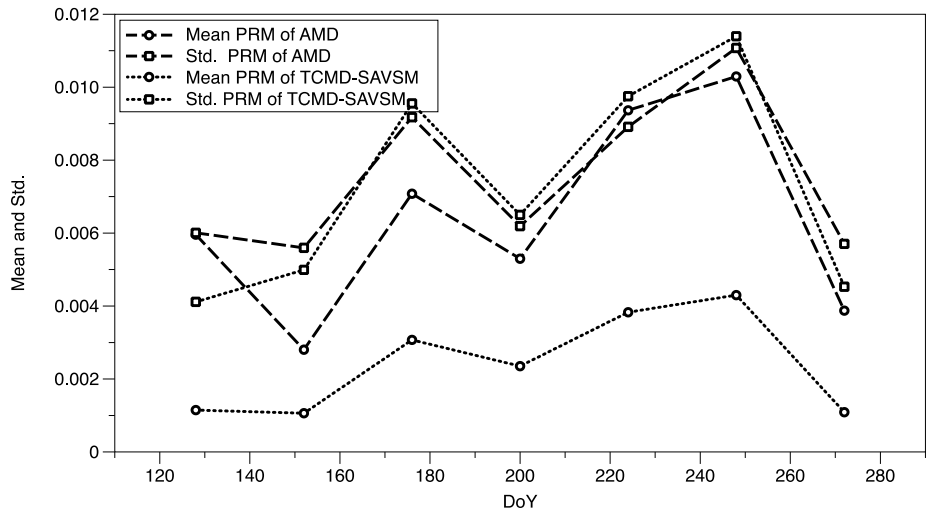

Figure 2-5. Comparison of the PRM between TCMD-SAVSM and AMD on each image acquisition date over agricultural fields.

From Figure 2-5, we may infer that the TCMD-SAVSM can characterize crops that change over time better than AMD does since TCMD-SAVSM has the minimum mean of PRM compared with AMD on each date while both standard deviations are almost the same. Among all dates with $\nabla f_v = 0.01$, the mean of the PRM on day 152 is smaller than other days. Hence, the decomposed results of the TCMD-SAVSM and AMD on day 152 are compared further, which are highlighted in Table 2-3.

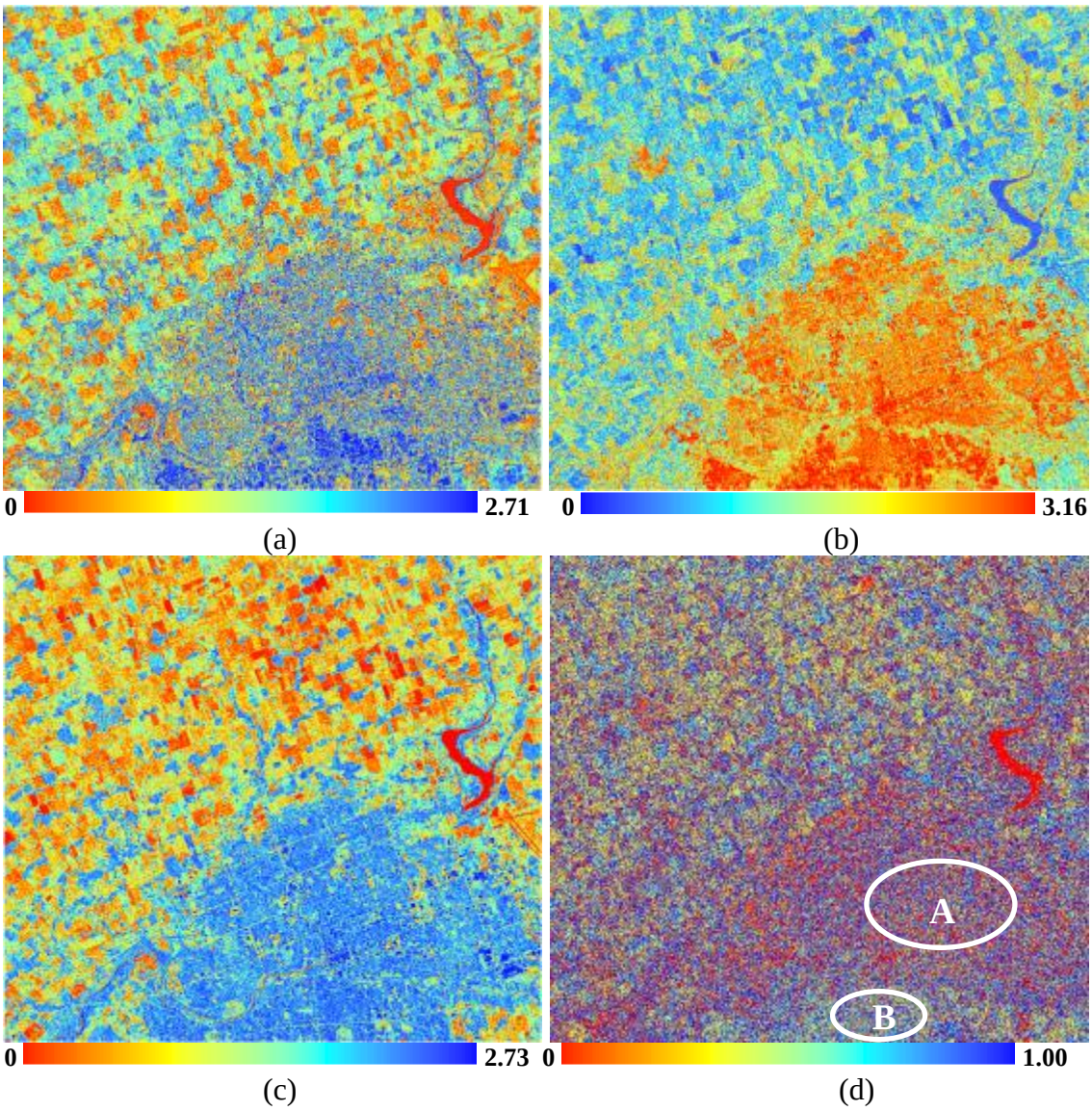

Figure 2-6. Decomposed components by AMD with the RADARSAT-2 image on day 152: (a) surface scattering component (b) double-bounce scattering component (c) volume scattering component (d) randomness.

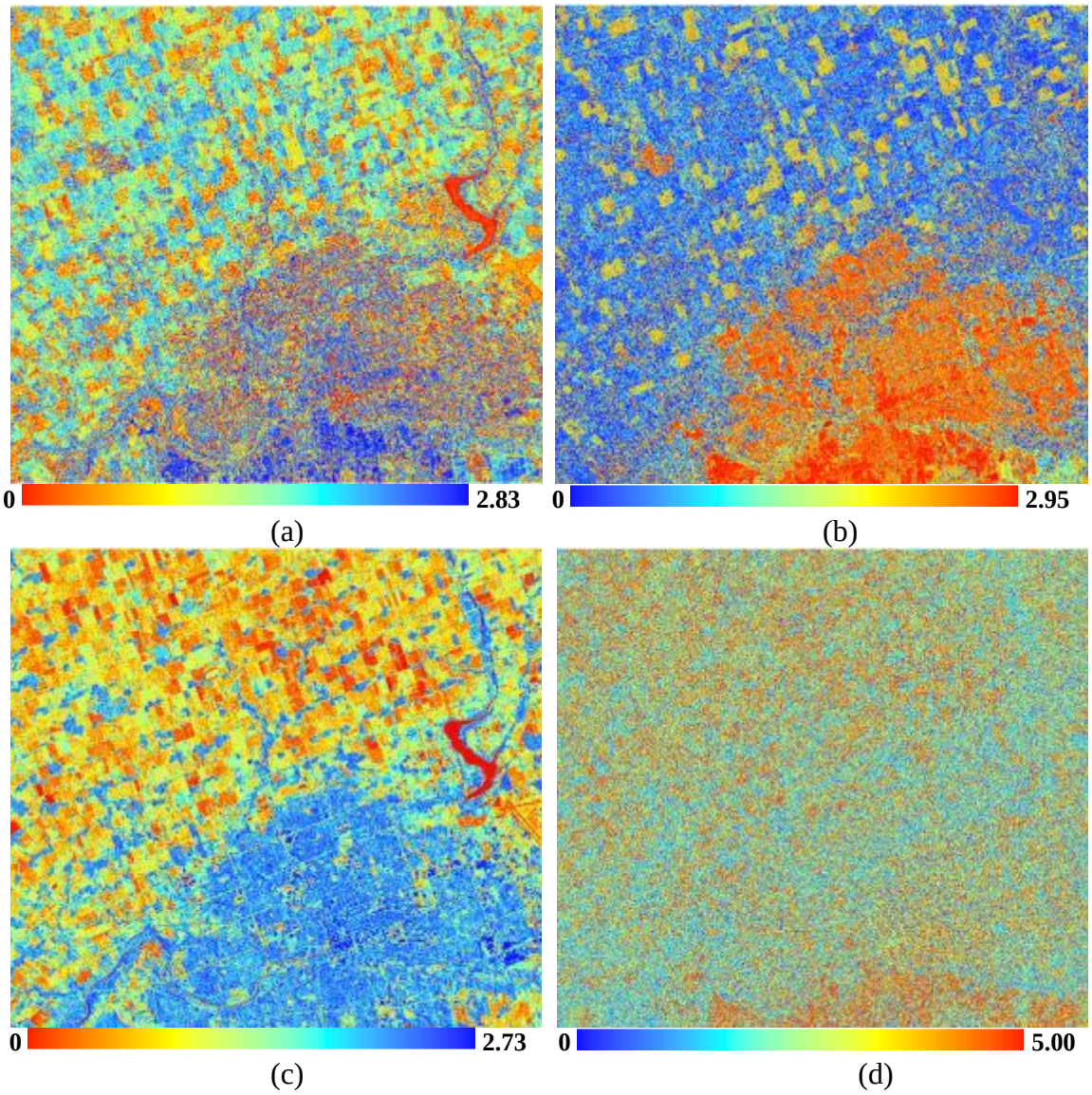

Figure 2-7. Decomposed components by TCMD-SAVSM: (a) surface scattering (b) double-bounce scattering (c) volume scattering (d) n.

Compared Figure 2-6(a) with 2-7(a), the surface scattering of TCMD-SAVSM in urban areas has less power than that of AMD; hence, the TCMD-SAVSM is more consistent with reality that the dominant scattering in urban areas should be double-bounce and volume scatterings due to the reflective building corners, and the corners of tree trunks and the ground. Water area also shows very low surface scattering because its total power is already low due to the specular reflection. On the other hand, from Figure 2-6(b) and Figure 2-7(b), both double-bounce scatterings are prominent in the urban areas. It should

be noted that crops were short and sparse on day 152, in which the double-bounce scattering should be less than other components. However, the double-bounce scattering of the AMD shows more power than TCMD-SAVSM in agricultural fields. Figure 2-6(c) and Figure 2-7(c) reveal the same pattern in volume scattering with higher values distributed in the urban and forest areas. Because on day 152 corn and soybean were not emerging yet, their fields show low volume scattering because the fields were bare. It should be noted that there is a negative relationship between n and the randomness. As n increases, the randomness decreases because the SAVSM will become either more horizontal or vertical. Even though n is shown noisy in Figure 2-7(d), most of n in forest areas are smaller compared with that in urban and agricultural areas. To compare the randomness further, two different urban areas are selected, the first is the area labeled as A in Figure 2-6(d) with weak double-bounce scattering, while the other is the area labeled as B in Figure 2-6(d) with strong double-bounce scattering. In theory, the double-bounce component in our model-based decomposition is a strong coherent scattering with small randomness values; hence, area B should be less random than that of A. However, the AMD result shows the opposite trend; while in the TCMD-SAVSM result, the values of n are higher in area B than in A with lower randomness in B than A.

2.4.3 SAVSM Validation Compared with FD-VSM, Y-VSM, An-VSM and Antropov-VSM

To validate the simplified adaptive volume scattering model (SAVSM) proposed in this chapter, different currently available volume scattering models, such as Freeman and Durden (1998) (FD-VSM), Yamguchi et al. (2005) (Y-VSM), An et al. (2010) (An-VSM) and Antropov et al. (2011) (Antropov-VSM) volume scattering models, are compared based on the PRM, a criterion used to find the optimum n as mentioned above. In order to validate the suitability for describing changes in crops with time, all volume scattering models are applied to the NNED and the average percentage of the PRM less than 0.001 is calculated for corn, soybean and wheat separately. The value of 0.001 is adopted to enlarge the difference between the SAVSM and other volume scattering models, so as to demonstrate the advantage of the SAVSM completely. For instance, we assume that the

percentage of the PRM less than 0.001 of SAVSM is 90% while FD-VSM is 80%. However, when the threshold is set to 0.1, the percentage of the PRM less than 0.1 of both models may be 95%, which makes no difference. In addition, from Fig. 8, the average power of corn, soybean and wheat are all almost greater than 0.1 on each date, which means when the threshold of 0.001 is selected, only 1% margin of error is present.

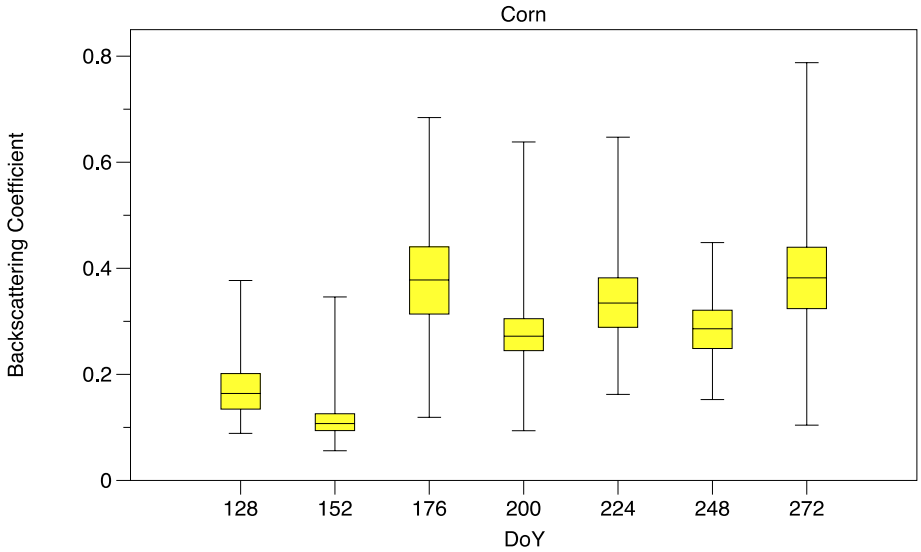

(a)

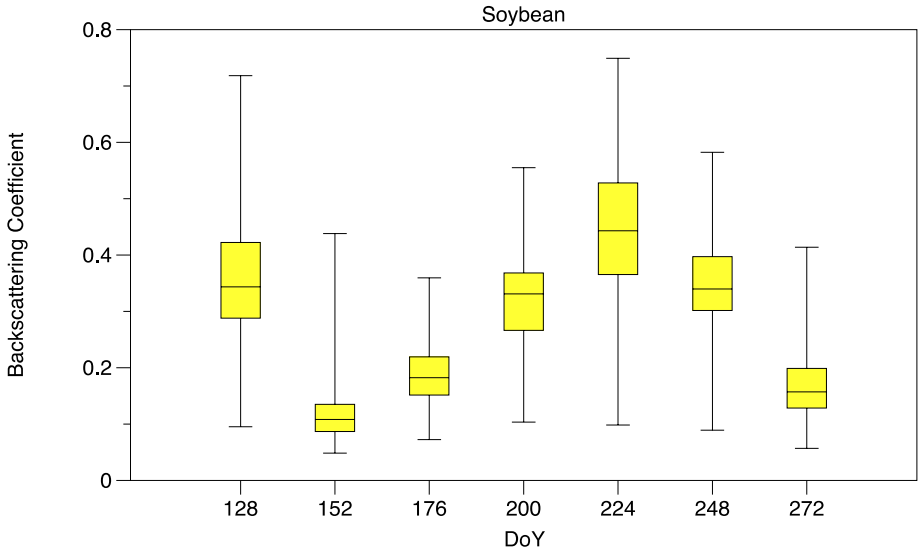

(b)

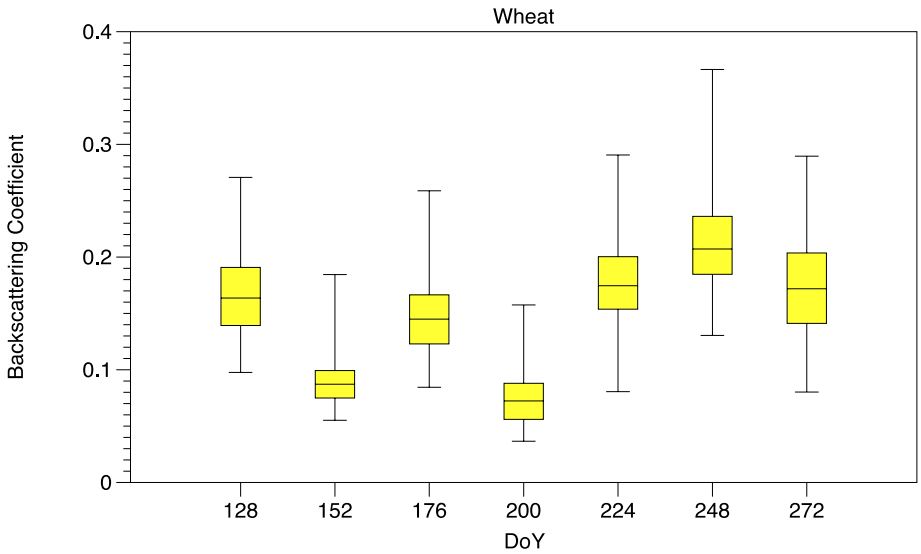

(c)

Figure 2-8. Power of different crops on each date. (a) corn (b) soybean (c) wheat.

The statistical results of corn are shown in Table 2-4. It depicts that the SAVSM has the highest percentage of PRM less than 0.001 on each date with an average of 95.29%. The standard deviation is 3.86 which is the lowest compared with the other models. Therefore, we may conclude that the SAVSM can better characterize changes in corn development over time. In contrast, the percentages of Freeman-Durden, Yamaguchi et al., An et al. and Antropov et al. are all very low with the average of 17.00%, 20.10%, 19.59% and 18.69% respectively, and their standard deviations are very high, about six times more than that of SAVSM. It also shows that as the corn grows taller and denser, the percentage of PRM less than 0.001 for Freeman, Yamaguchi et al., An et al. and Antropov et al. decrease sharply from day 128 to day 200. But as the corn leaves become dry and yellow on day 272 (Figure 2-9(d)), their percentages are increasing gradually from day 200 to day 272, suggesting that their models cannot fully characterize the changes in corn with time.

Table 2-4. Results of percentages of PRM less than 0.001 for corn.

Volume Scattering Models	DoY							Ave.	Std.
	128	152	176	200	224	248	272		
FD-VSM	69.50	75.34	43.10	29.51	36.82	46.37	58.27	51.27	17.00
Y-VSM	89.63	77.41	48.45	37.70	39.99	60.39	74.90	61.21	20.10
An-VSM	81.89	78.56	47.46	37.26	46.32	65.79	85.65	63.28	19.59
Antropov-VSM	86.09	78.78	49.32	38.63	43.59	62.68	75.67	62.11	18.69
SAVSM	97.44	99.45	98.69	95.91	94.16	93.18	88.22	95.29	3.86

The statistic results of soybean are depicted in Table 2-5. The average percentage of the PRM less than 0.001 for soybean is 95.80%, which is still the highest among all volume scattering models. Similar to corn, as the soybean going through vegetative growth, the percentages of Freeman, Yamaguchi et al., An et al. and Antropov et al. decrease gradually with standard deviations of 23.35, 21.30,15.61 and 20.18 respectively, which are two times more than that of the SAVSM. On day 248, take note that the percentage of the SAVSM is a little low with the percentage of 74.60%. The reason for this is because some leaves of the soybean become brown and dry, and this can be seen in Figure 2-10(c). The microwave can penetrate the dry leaves more easily to interact with the branches perhaps resulting in multiple scatterings. Besides the dominant volume scattering, other multiple scattering may also occur due to the interaction with the intricate branches. At any rate, the percentage of the SAVSM is still higher than that of other models on this date. From this perspective, the SAVSM is also suitable to describe changes in soybean with time.

Table 2-5. Results of percentages of PRM less than 0.001 for soybean.

Volume Scattering Models	DoY							Ave.	Std.
	128	152	176	200	224	248	272		
FD-VSM	86.52	88.46	73.72	59.08	59.68	28.89	97.01	70.48	23.35
Y-VSM	88.39	88.95	79.28	65.10	63.51	35.15	97.75	74.02	21.30
An-VSM	89.23	89.06	78.08	64.46	64.67	56.05	97.43	77.00	15.61
Antropov-VSM	89.13	89.66	79.52	66.64	65.55	38.53	97.78	75.26	20.18
SAVSM	99.89	99.72	99.40	98.24	98.73	74.60	100.00	95.80	9.37

The statistic results of the winter wheat are shown in Table 2-6. Different from corn and soybean, the percentages of PRM less than 0.001 of all the volume models increase as the wheat is growing. The reason why on day 128 their percentages are low is because the wheat was very short and the stems were either vertical or horizontal and are very difficult to describe with this variation. As the wheat grows taller, the percentage of PRM becomes higher. After day 200, the wheat was harvested and volunteer wheat was growing, this is an interesting note. The mixture of wheat stubbles and the re-growth makes the scattering more complex. Therefore, on day 248, the percentages of Freeman, Yamaguchi et al, An et al. and Antropv et al. models are all very low, and their standard deviations are 20.51, 15.83, 18.11 and 16.07 which are three times more than that of the adaptive model, suggesting that they cannot describe the changes of wheat with time completely, while the SAVSM can adapt to its variation.

Table 2-6. Results of percentages of PRM less than 0.001 for winter wheat.

Volume Scattering Models	**DoY**							**Ave.**	**Std.**
	128	**152**	**176**	**200**	**224**	**248**	**272**		
FD-VSM	32.63	75.98	80.78	85.19	73.97	41.04	57.66	63.89	20.51
Y-VSM	63.76	90.19	84.78	87.19	77.88	48.35	60.66	73.26	15.83
An-VSM	63.56	93.89	95.20	87.49	82.38	49.65	59.96	76.02	18.11
Antropov-VSM	63.76	91.59	86.69	88.09	78.98	49.35	61.96	74.35	16.07
SAVSM	83.98	94.49	92.59	99.70	97.30	93.59	99.60	94.46	5.42

2.5 Three Components Analysis of Corn, Soybean and Wheat

The TCMD-SAVSM is also validated by comparing with other volume scattering models for corn, soybean and wheat. In this section, we will analyze the variation of the surface, double and volume scatterings of each crop, which may help assist in identifying or classifying crops over different growing stages in the future. To present the decomposed results clearly, the percentage power of each component is calculated rather than the power itself. Three types of crops (corn, soybean and winter wheat) typical to this region are selected for this analysis. The ground photos shown in Figure 2-9, 2-10 and 2-11 are

used to help with the interpretation. It should be noted that on day 128, the corn and soybean have not emerged yet, and on day 176, the winter wheat was already harvested.

(a) (b) (c) (d)

Figure 2-9. Ground photos of corn: (a) day 152 (b) day 176 (c) day 224 (d) day 272.

(a) (b) (c) (d)

Figure 2-10. Ground photos of soybean field: (a) day 152 (b) day 224 (c) day 248 (d) day 272.

(a) (b) (c) (d)

Figure 2-11. Ground photos of winter wheat: (a) day 128 (b) day 176 (c) day 200 (d) day 272.

2.5.1 Corn Analysis

The variation of the three components of corn can be shown in Figure 2-12. On day 128, the corn field had very strong surface scattering since there were no corns on this date but only the bare soil. Until day 152, the corn was growing, but it was very short and sparse as can be seen on Figure 2-9(a), so the surface scattering was still dominant although it decreased over that time. After day 176, as the corn grew taller and the canopy started to

close, as can be seen in Figure 2-9(b), the surface scattering decreased until day 272. In terms of the volume scattering, as corn became taller and denser, the volume scattering increased gradually until day 248. However, on day 272, the leaves turned yellow and dry and started to bend down or fell off. As a result, the canopy became less dense as can be seen on Figure 2-9(d). Hence the volume scattering reduced since the microwave can penetrate the canopy more easily. Conversely, the percentage of the double bounce had been very low until day 248 because when the corn grew denser, it was very difficult for the microwave to penetrate the canopy to reach the corn stalks to induce double bounce through the stalk and ground interaction. However, on day 272, the double bounce increased due to the bounce of corn stalk and the ground. It should be noted that, being different from the soybean and wheat, the diameter of the corn stalk is about 2cm which cannot be considered as dipole since k$a \approx 1.14$ with a being the radius of the cylinder is greater than 1.

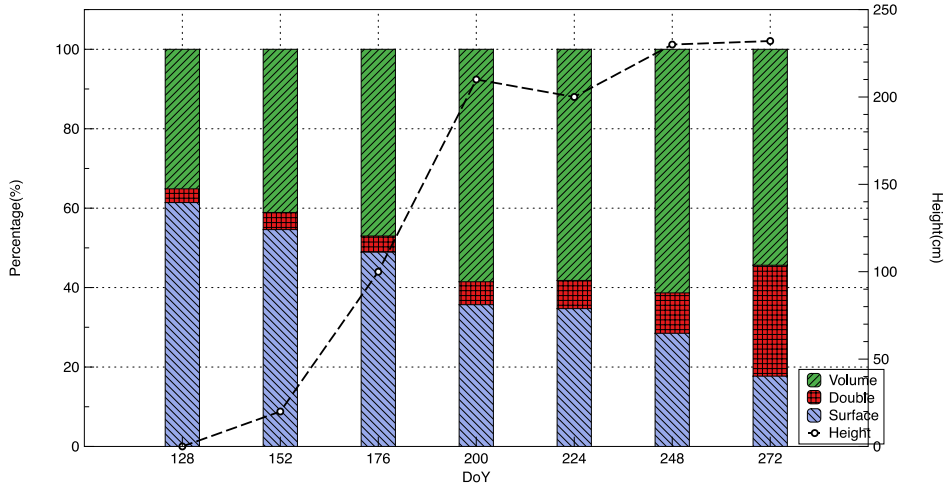

Figure 2-12. Surface, double bounce, and volume components of corn.

2.5.2 Soybean Analysis

The three components of soybean can be seen on Figure 2-13. At the beginning of its growth stage, the volume scattering of the soybean increased gradually until day 200. However, on day 224, the density was very high as can be seen on Figure 2-10(b). Because the wavelength of the C-band is very short (5.4 cm), so the surface scattering

increased. On day 248, the leaves became dry and brown as can be seen on Figure 2-10(c), the microwave could penetrate the dry leaves more easily and interacted with the branches of the soybean resulting in very high volume scattering. It is mainly because the volume scattering model we construct in this chapter is based on the dipoles and the diameter of its branch is about 3mm with $ka \approx 0.17$ less than 1 and can be considered as dipoles. At the end of September, on day 272, although soybeans were not yet harvested, they had lost all their leaves and the stems and pods were very dry and the diameter of the stem is also very small as can be seen on Figure 2-10(d), the microwave can penetrate them easily. There were also more soils exposed to the sensor, so the surface scattering was dominant. Unlike corns that have many double bounces, the stem diameter of the soybean is very small, only 3mm compared with the corn's 2cm.

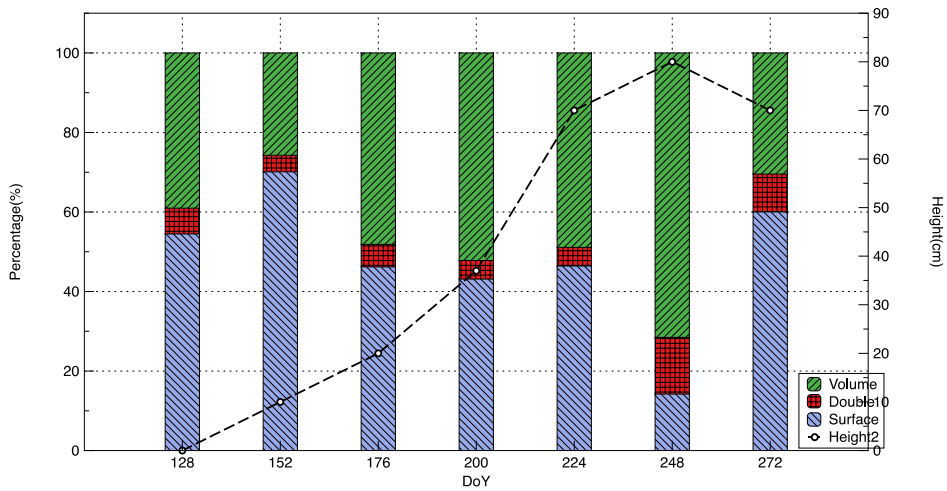

Figure 2-13. Surface, double bounce, and volume components of soybean.

2.5.3 Wheat Analysis

The three components of wheat can be seen on Figure 2-14. From day 128 to 176, the wheat was in vegetative growth as can be seen on Figure 2-11(a) and 2-11(b), so the volume scattering was dominant. However, when the wheat was harvested before day 200 (white arrow), the ground seemed to be flat since the stem diameter is only 1.5mm which is very small compared with the C band wavelength (5.4cm). Therefore, the surface scattering was dominant on day 200. After that, the volume scattering was still

increasing steadily, which was induced by the re-growth. At the end of September (on day 272), then the volunteer wheat started to die down as can be seen on Figure 2-11(d), and the surface scattering became dominant.

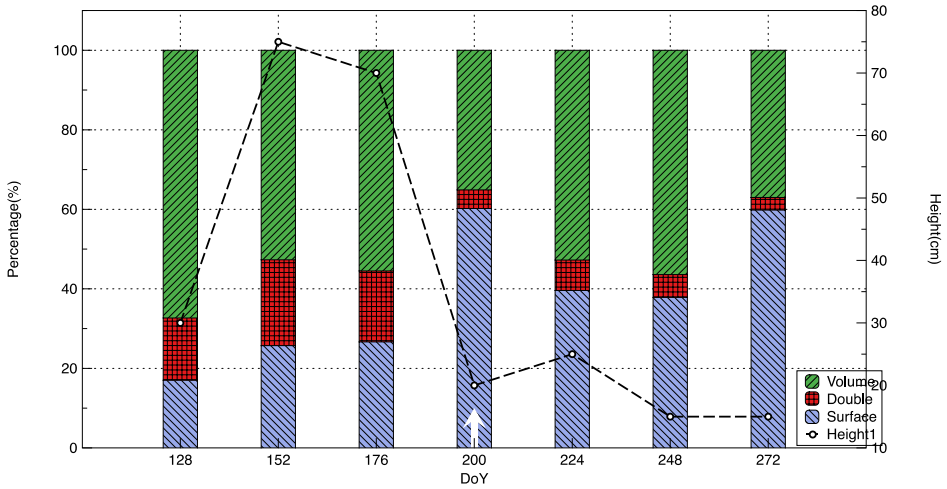

Figure 2-14. Surface, double bounce, and volume components of wheat.

2.6 Conclusion

This chapter developed a simple adaptive volume scattering model (SAVSM) for RADARSAT-2 based on the nth power sine and cosine functions to characterize crop development over time. A three-component model-based decomposition with SAVSM (TCMD-SAVSM) is also implemented based on the NNED method in which the minimum remainder power matrix is used as a criterion to find the optimum n. Multi-temporal RADARSAT-2 data were used to validate the SAVSM for crop monitoring. Compared with AMD, the TCMD-SAVSM consumes much less time and its surface and double-bounce scatterings are more consistent with reality. Even though AMD may have better results when very small increments are adopted, the time it consumes will be huge and unrealistic when the general configuration of computer is in use. Comparing the SAVSM with other volume scattering models, it is concluded that the SAVSM is highly suitable to describe the corn, wheat and soybean changes over time.

Based on the analysis of the three components, it suggests that for corn, the volume scattering is always increasing while the surface scattering is always decreasing through

most part of the growth cycle. At the end of September, the double bounce increases prominently because the corn leaves become yellow and dry and the microwave can penetrate them more easily. In terms of soybean, it should be noted that the maximum percentage of volume scattering is not on day 200 or 224 when they were very dense; instead, it was on day 248 when their leaves became a little yellow. For wheat, because it was harvested before day 176, the dominant scattering was volume scattering from day 128 to 176. After this date, the re-growth in the harvested wheat field also influenced the scattering in addition to the wheat stubbles. Overall, these analyses can help interpret the growth of crops. In further work, the method will be introduced to crop classification and surface parameters retrieval.

References

An, W., Cui, Y., Yang, J., & Member, S. (2010). Three-Component Model-Based Decomposition for Polarimetric SAR Data, *IEEE Transactions on Geoscience and Remote Sensing*, *48*(6), 2732–2739.

An, W., Xie, C., Yuan, X., Cui, Y., & Yang, J. (2011). Four-Component Decomposition of Polarimetric SAR Images with Deorientation. *IEEE Geoscience and Remote Sensing Letters*, *8*(6), 1090–1094.

Antropov, O., Rauste, Y., & Häme, T. (2011). A Generalzied Radar Backsattering Model Based on Wave Theory for Multilayer Multispecies Vegetation. *IEEE Transactions on Geoscience and Remote Sensing*, *49*(12), 4832-4845.

Arii, M., van Zyl J. J., & Kim, Y. (2010). A General Characterization for Polarimetric Scattering from Vegetation Canopies. *IEEE Transactions on Geoscience and Remote Sensing*, *48*(9), 3349-3357.

Arii, M., van Zyl J. J., & Kim, Y. (2011). Adaptive Model-Based Decomposition of Polarimetric SAR Convariance Matrices. *IEEE Transactions on Geoscience and Remote Sensing*, *49*(3), 1104-1113.

Ballester-berman, J. D., & Lopez-sanchez, J. M. (2010). Applying the Freeman–Durden Decomposition Concept to Polarimetric SAR Interferometry. *IEEE Transactions on Geoscience and Remote Sensing*, *48*(1), 466-479.

Cameron, W. L., Youssef, N. N., & Leung, L. K. (1996). Simulated Polarimetric Signatures of Primitive Geometrical Shapes. *IEEE Transactions on Geoscience and Remote Sensing*, *34*(3), 793-803.

Chen, S. W., Wang, X. S., Li, Y. Z., & Sato, M. (2014). Adaptive Model-Based Polarimetric Decomposition Using PolInSAR Coherence. *IEEE Transactions on Geoscience and Remote Sensing*, *52*(3), 1705-1718.

Chen, S. W., Ohki, M., Shimada, M., & Sato, M. (2013). Deorienation Effect Investigation for Model-Based Decompostion over Oriented Built-Up Areas. *IEEE Geoscience and Remote Sensing Letters*. *10*(2), 273-277.

Chen, S. W., Wang, X. S., Xiao S. P., & Sato, M. (2014). General Polarimetric Model-Based Decomposition for Coherency Matrix. *IEEE Transactions on Geoscience and Remote Sensing*, *52*(3), 1843-1855.

Cloude, S. R., & Pottier, E. (1997). An Entropy Based Classification Scheme for Land Applications of Polarimetric SAR. *IEEE Transactions on Geoscience and Remote Sensing*, *35*(1), 68-78.

Freeman, A., & Durden, S. L. (1998). A Three-Component Scattering Model for Polarimetric SAR Data. *IEEE Transactions on Geoscience and Remote Sensing*, , *36*(3), 963-973.

Hajnsek, I., Jagdhuber, T., Schon, H., & Papathanassiou, K. P. (2009). Potential of Estimating Soil Moisture under Vegetation Cover by Means of PolSAR. *IEEE Transactions on Geoscience and Remote Sensing*, *47*(2), 442-454.

Huang, X., & Wang, J. (2014)., An Adaptive Volume Scattering Model for Fully Polarimetric RADARSAT-2 Data. *10th European Conference on Synthetic Aperture Radar*, Berlin, Germany, 568-571.

Kim, Y., & van Zyl J. J. (2001). Comparison of Forest Estimation Techniques Using SAR Data. *IEEE International Geoscience and Remote Sensing on Geoscience and Remote Sensing Symposium*, Sydney, Australia, 1395-1397.

Krogager, E., Boerner, W. M. & Madsen, S. N. (1997). Feature-Motivated Sinclair matrix (sphere/diplane/helix) Decomposition and Its Application to Target Sorting for Land Feature Classification. *Proc. SPIE Conference on Wideband Interferometric Sensing and Imaging Polarimetry*, *3120*(1), 144-154.

Lee, J. S., & Thomas, L. (2011). The Effect of Orientation Angle Compensation on Coherency Matrix and Polarimetric Target Decompositions. *IEEE Transactions on Geoscience and Remote Sensing*, *49*(1), 53-64.

Liu, C., Shang, J. L., Vachon, P. W., & McNairn, H. (2013). Multiyear Crop Monitoring Using Polarimetric RADARSAT-2 Data. *IEEE Transactions on Geoscience and Remote Sensing*, *51*(4), 2227-2240.

McNairn, H., Shang, J. L., Jiao, X., & Champagne, C. (2012). The Contribution of ALOS PALSAR Multipolarization and Polarimetric Data to Crop Classfication. *IEEE Transactions on Geoscience and Remote Sensing*, *47*(12), 3981-3992.

Moran, M. S., Alonso, L., Moreno, J. F., Mateo, M. P. C., de la Cruz, D. F., & Montoro, A.(2012). A RADARSAT-2 Quad-Polarized Time Series for Monitoring Crop and Soil Conditions in Barrax, Spain. *IEEE Transactions on Geoscience and Remote Sensing*, *50*(4), 1057-1070.

Sato, A., Yamaguchi, Y., Singh, G., & Park, S. E. (2012). Four-Component Scattering Power Decomposition with Extened Volume Scattering Model. . *IEEE Geoscience and Remote Sensing Letters*, *9*(2), 166-170.

Shan, Z., Wang, C., Zhang, H., & An, W. (2012). Improved Four-Component Model-Based Target Decomposition for Polarimetric SAR Data. *IEEE Geoscience and Remote Sensing Letters*. *9*(1), 75-79.

Trudel, M., Magagi, R., & Granberg, H. B. (2009). Application of Target Decomposition Theorems over Snow-Covered Forested Areas. *IEEE Transactions on Geoscience and Remote Sensing*, *47*(2), 508-512.

van Zyl J. J., Arii, M., & Kim, Y. (2011). Model-Based Decomposition of Polarimetric SAR Covariance Matrices Constrained for Nonnegative Eigenvalues. *IEEE Transactions on Geoscience and Remote Sensing*, *49*(9), 3452-3459.

Yamaguchi, Y., Moriyama, T., Ishido, M., & Yamada, H. (2005). Four-Component Scattering Model for Polarimetric SAR Image Decomposition. *IEEE Transactions on Geoscience and Remote Sensing*, *43*(8), 1699-1706.

Yamaguchi, Y., Yajima, Y., & Yamada, H. (2006). A Four-Component Decomposition of POLSAR Images Based on The Coherency Matrix. *IEEE Geoscience and Remote Sensing Letters*, *3*(3), 292-296.

Yamaguchi, Y., Sato, A., Boerner, W. M., & Sato, R. (2011). Four-Component Scattering Power Decomposition with Rotation of Coherence Matrix. *IEEE Transactions on Geoscience and Remote Sensing*, *49*(6), 2251-2258.

Yajima, Y., Yamaguchi, Y., Sato, R., & Yamada, H. (2006). PolSAR Image Analysis of Wetlands Using a Modified Four-Component Scattering Power Decomposition. *IEEE Transactions on Geoscience and Remote Sensing*, *46*(6), 1667-1673.

Chapter 3 An Adaptive Two-Component Model-Based Decomposition on Soil Moisture Estimation*

3.1 Introduction

The growth, survival, and reproduction of crops are crucially dependent on their physical environment. To understand the various responses of crop development, tools are required both for the quantification of environmental conditions such as soil moisture, and for the study of crop biophysical parameters (Jones & Vaughan, 2010). Synthetic aperture radar (SAR) provides multidimensional information via multiple polarizations, which has been proved to be valuable due to its day-and-night capability as well as the capacity to penetrate the vegetative canopies (Oliver & Quegan, 2004). Polarimetric SAR (PolSAR). Such system has been frequently used for Earth terrain investigations, as the system's range of polarizations allow for the exploration of different scattering mechanisms and various components of the scattering layers (van Zyl & Kim, 2011).

To invert the soil moisture under vegetation cover over agricultural fields, the key problem is to separate the contributions of vegetation backscattering and vegetation-covered soil moisture backscattering from the sensor observed backscattering (He et al., 2014). The model-based decomposition proposed by Freeman and Durden (1998) offers an efficient way to separate the backscattering from different layers in agricultural fields and has been widely used to estimate soil moisture under vegetation cover. Hajnsek et al. (2009) first investigated the potential of surface parameter inversion under vegetation cover by comparing different model-based decompositions. Jagdhuber et al. (2013) investigated a multi-angular polarimetric decomposition to estimate soil moisture and

---

* 2016. IEEE. Reprinted, with permission, from "Huang, Xiaodong, Wang, Jinfei, and Shang, Jiali (2016). An Adaptive Two-Component Model-Based Decompostion on Soil Moisture Estiamtion for C-Band RADARSAT-2 Imagery over Wheat Fields at Early Growing Stages, *IEEE Geoscience and Remote Sensing Letters*, *13*(3), 414-418."

obtained a very high inversion rate and low root mean square error (RMSE). Subsequently, a hybrid decomposition method combining model- and eigen-based decomposition was recently presented (Jagdhuber et al., 2014), and it also obtained a very high inversion rate. However, the validations of these methods are only limited to the L-band fully polarimetric SAR data. Currently, although a two-component polarimetric decomposition model for sparse vineyards using C-band RADARSAT-2 data has been presented, no measured ground truth data have been used for validation (Ballester-Berman et al., 2013). Additionally, the Bragg surface scattering model adopted by the authors is constructed based on the assumption that the ground is flat, but this assumption is only valid when the sensor frequency is low. This chapter further investigates the model-based decomposition for soil moisture estimation using the C-band RADARSAT-2 data. An adaptive two-component decomposition method is developed that simulates the scattering process as the incoherent summation of two components, i.e., the surface scattering from the soil and the volume scattering from the crop canopy. This newly proposed method has two improvements over the existing methods. Firstly, the X-Bragg scattering model considering surface roughness is adopted based on the zero mean normal distribution. Secondly, an improved volume scattering model based on the nth power cosine and sine functions is adopted to describe the vegetation scattering.

3.2 Coherency Matrix

The Sinclair matrix of each pixel obtained from the mono-static PolSAR image is described as,

$$S = \begin{bmatrix} S_{HH} & S_{HV} \\ S_{VH} & S_{VV} \end{bmatrix} \tag{3-1}$$

Its four elements are representing four channels in different polarization composites. For example, S_{HV} represents transmitting the vertical polarization and receiving the horizontal polarization. If the reciprocity is satisfied, that is, $S_{HV} = S_{VH}$, then the Pauli vector can be written as,

$$k = \frac{1}{\sqrt{2}}[S_{HH} + S_{VV} \quad S_{HH} - S_{VV} \quad 2S_{HV}]^T \tag{3-2}$$

where T denotes transpose, and the coherency matrix is defined as,

$$T = k \cdot k^{\dagger} = \begin{bmatrix} T_{11} & T_{12} & T_{13} \\ T_{12}^* & T_{22} & T_{23} \\ T_{13}^* & T_{23}^* & T_{33} \end{bmatrix} \tag{3-3}$$

where † denotes complex conjugation and transposition and $*$ denotes complex conjugation. Then the coherency matrix after multi-look average is shown as,

$$\frac{1}{2}\begin{bmatrix} |\langle S_{HH} + S_{VV}\rangle|^2 & \langle S_{HH} + S_{VV}\rangle\langle S_{HH} - S_{VV}\rangle^* & 2\langle S_{HH} + S_{VV}\rangle\langle S_{HV}\rangle^* \\ \langle S_{HH} - S_{VV}\rangle\langle S_{HH} + S_{VV}\rangle^* & |\langle S_{HH} - S_{VV}\rangle|^2 & 2\langle S_{HH} - S_{VV}\rangle\langle S_{HV}\rangle^* \\ 2\langle S_{HV}\rangle\langle S_{HH} + S_{VV}\rangle^* & 2\langle S_{HV}\rangle\langle S_{HH} - S_{VV}\rangle^* & 4|\langle S_{HV}\rangle|^2 \end{bmatrix} \tag{3-4}$$

where $\langle\cdot\rangle$ denotes the ensemble average and $|\cdot|$ denotes the module. Physically, $|\langle S_{HH} + S_{VV}\rangle|^2$ represents the surface scattering induced by the ground, $|\langle S_{HH} - S_{VV}\rangle|^2$ represents the double-bounce scattering induced by the ground and trunk interaction, and $4|\langle S_{HV}\rangle|^2$ represents the volume scattering by vegetation canopy.

3.3 Surface Scattering Model

3.3.1 Bragg Scattering Model

Flat and bare soil scattering areas can be characterized by the Bragg surface scattering, and their scattering matrix has the form,

$$S = \begin{bmatrix} S_{HH} & 0 \\ 0 & S_{VV} \end{bmatrix} \tag{3-5}$$

where S_{HH} and S_{VV} are the Fresnel coefficients at horizontal and vertical polarization respectively, and are shown as,

$$S_{HH} = \frac{cos\theta - \sqrt{\varepsilon_r - sin^2\theta}}{cos\theta + \sqrt{\varepsilon_r - sin^2\theta}} \tag{3-6}$$

$$S_{VV} = \frac{(\varepsilon_r - 1)(sin^2\theta - \varepsilon_r(1 + sin^2\theta))}{(\varepsilon_r cos\theta + \sqrt{\varepsilon_r - sin^2\theta})^2}$$

where θ is the local incidence angle and ε_r is the relative dielectric constant that is related to the soil moisture content. According to (3-2) and (3-3), the coherency matrix of the Bragg scattering model can be written as,

$$T_{Bragg} = \begin{bmatrix} 1 & \beta^* & 0 \\ \beta & |\beta|^2 & 0 \\ 0 & 0 & 0 \end{bmatrix}, \beta = \frac{S_{HH} - S_{VV}}{S_{HH} + S_{VV}} \tag{3-7}$$

where β is the surface scattering coefficient and is real with $-1 < \beta \leq 0$. Based on this condition, the β derived by all of the methods in this chapter is forced to be negative. Within different incidence angles, the relationship between ε_r and β is depicted in Figure 3-1, revealing that when the incidence angle is very low, even a small variation in β will result in a large fluctuation of ε_r values. That is, as the incidence angle is decreasing, the relationship between ε_r and β gradually reaches saturation.

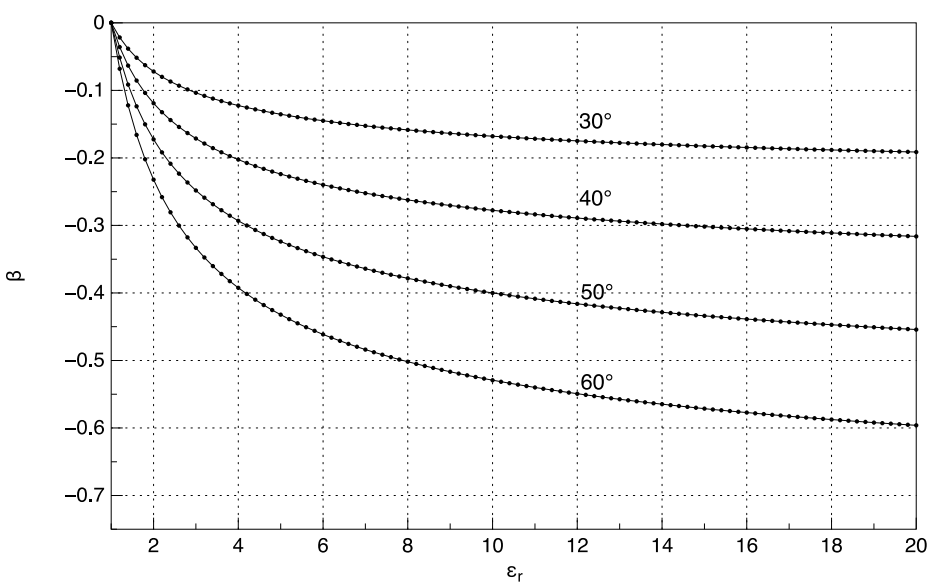

Figure 3-1. Relationship between $\boldsymbol{\varepsilon_r}$ and $\boldsymbol{\beta}$.

3.3.2 Extended Bragg Surface Scattering

The Bragg surface scattering is suitable for the characterization of flat and bare surfaces. However, in natural environments, most surfaces have some portion of rough terrain (Jin & Xu et al., 2013). Whether the surface appears rough or not also depends on the wavelength employed by the sensor (Woodhouse, 2006); as wavelength increases, the effects of surface roughness on backscatter diminish. However, for imagery retrieved using RADARSAT-2 that works in the C band (5.4 cm), the surface roughness cannot be ignored. Another way to construct the rough surface scattering model is to integrate the Bragg scattering model with respect to the azimuthal surface slope under a probability density function (PDF) (Hajnsek et al., 2003; Schuler et al., 2002), which is called the extended Bragg scattering model and can be defined as,

$$T_{Bragg}(\theta) = R \cdot T_{Bragg} \cdot R^T, R = \begin{bmatrix} 1 & 0 & 0 \\ 0 & \cos 2\theta & \sin 2\theta \\ 0 & -\sin 2\theta & \cos 2\theta \end{bmatrix} \tag{3-8}$$

Where R is the rotation matrix and θ is the azimuthal surface slope induced by surface roughness. Expanding (3-8), we obtain

$$T_{Bragg}(\theta) = \begin{bmatrix} 1 & \beta^* \cos 2\theta & -\beta^* \sin 2\theta \\ \beta \cos 2\theta & |\beta|^2 \cos^2 2\theta & -|\beta|^2 \sin 2\theta \cos 2\theta \\ -\beta \sin 2\theta & -|\beta|^2 \sin 2\theta \cos 2\theta & |\beta|^2 \sin^2 2\theta \end{bmatrix} \tag{3-9}$$

To obtain the extended Bragg scattering model, the integration by a known PDF is required, and then the extended Bragg surface scattering model is obtained by,

$$T_{E-Bragg} = \int T_{Bragg}(\theta) \cdot p(\theta)\, d\theta \tag{3-10}$$

where $p(\theta)$ is the probability density function (PDF) of azimuthal slope θ. Generally, two different PDFs are adopted. One is the uniform distribution function introduced by Hajnsek et al. (2003), and is defined as,

$$p(\theta) = \frac{1}{2\theta} \tag{3-11}$$

Where θ is from 0 to $\frac{\pi}{2}$. Substituting (3-9) and (3-11) to (3-10), we obtain,

$$T_{E-Bragg} = \int_{-\theta}^{\theta} T_{Bragg}(\theta) \cdot p(\theta) d\,\theta$$
$$= \begin{bmatrix} 1 & \beta^* sinc(2\theta) & 0 \\ \beta sinc(2\theta) & \frac{1}{2}|\beta|^2\big(1 + sinc(4\theta)\big) & 0 \\ 0 & 0 & \frac{1}{2}|\beta|^2\big(1 - sinc(4\theta)\big) \end{bmatrix} \tag{3-12}$$

Where $sinc(2\theta)$ is the $sinc$ function being defined as,

$$y = sinc(\theta) = \frac{\sin \theta\pi}{\theta\pi} \tag{3-13}$$

and is depicted in Figure 3-2,

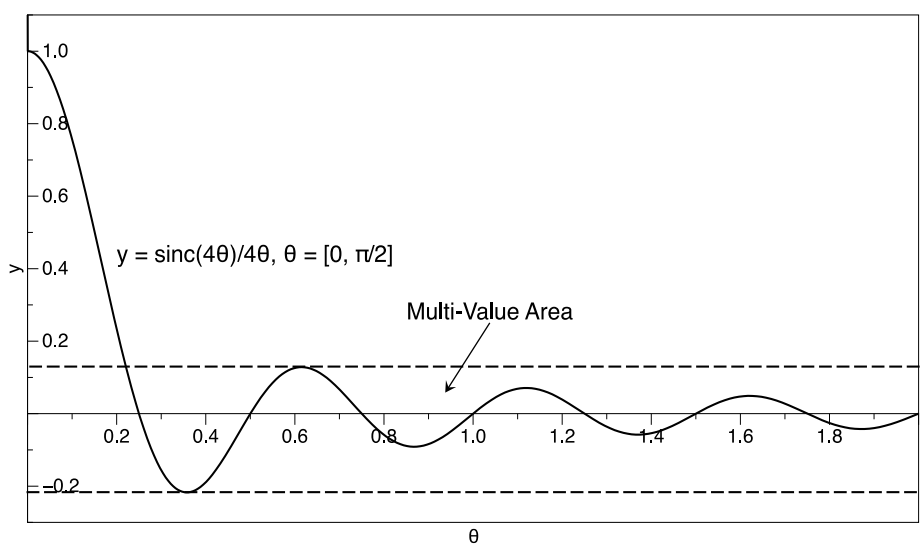

Figure 3-2. $\boldsymbol{y = sinc(4\theta)}$.

The $Sinc$ function shown in Figure 3-2 is actually a fluctuated function. It should be noted that when its value lies in the area between the two dashed lines (Figure 3-2), there are more than two θ values will be obtained when a known y value is given. The second PDF used by Schuler et al. (2002) is a zero mean normal distribution assuming that the mean height of the surface is zero, and can be defined as,

$$p(\theta) = \frac{1}{\sqrt{2\pi}\sigma} e^{-\frac{\theta^2}{2\sigma^2}} \tag{3-14}$$

where σ^2 represents the surface height variance. Substituting (3-9) and (3-14) into (3-10), then,

$$\begin{aligned} T_{E-Bragg} &= \int_{-\infty}^{+\infty} T_{Bragg}(\theta) \cdot p(\theta) d\theta \\ &= \begin{bmatrix} 1 & \beta^* e^{-2\sigma^2} & 0 \\ \beta e^{-2\sigma^2} & \frac{1}{2}|\beta|^2\left(1 + e^{-8\sigma^2}\right) & 0 \\ 0 & 0 & \frac{1}{2}|\beta|^2\left(1 - e^{-8\sigma^2}\right) \end{bmatrix} \end{aligned} \tag{3-15}$$

and the function $e^{-8\sigma^2}$ is shown in Figure 3-3.

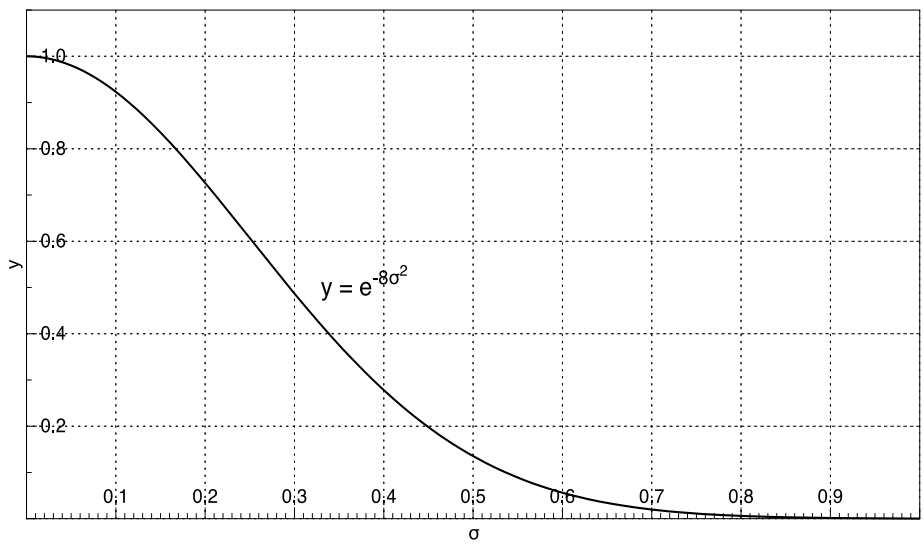

Figure 3-3. $\boldsymbol{y = e^{-8\sigma^2}}$.

Compared with the $Sinc$ function, the exponent function has no multi-value problem, and the σ^2 can describe the surface fluctuation. Therefore, this normal distribution function will be adopted in this chapter.

3.4 Volume Scattering Model

3.4.1 Volume Scattering Construction Framework

Generally, volume scattering model is constructed by integrating the vertical or horizontal dipoles with respect to the orientation angle under a given PDF, which can be described as follows,

$$T_V = \int_{\mathrm{a}}^{\mathrm{b}} \mathrm{p}(\theta) T(\theta) \mathrm{d}\theta \tag{3-16}$$

Where $\mathrm{p}(\theta)$ is the probability distribution function of the orientation angles of dipoles, and $T(\theta)$ is the coherency matrix rotated θ with respect to the line of sight (LOS), T_V is the volume scattering model, a and b are the integration limits. The elementary Sinclair matrix employed for constructing the volume scattering model can be described as,

$$S = \begin{bmatrix} S_{HH} & 0 \\ 0 & S_{VV} \end{bmatrix} \tag{3-17}$$

When $S_{HH} = 1, S_{VV} = 0$, it represents horizontal dipoles; while $S_{HH} = 0, S_{VV} = 1$, it represents vertical dipoles; when $S_{HH} = 1, S_{VV} = 1$, it represents the sphere or thin flat plate. After rotation with respect to the LOS with angle θ, the scattering matrix can be described as,

$$S(\theta) = \begin{bmatrix} \cos\theta & \sin\theta \\ -\sin\theta & \cos\theta \end{bmatrix} \begin{bmatrix} S_{HH} & 0 \\ 0 & S_{VV} \end{bmatrix} \begin{bmatrix} \cos\theta & -\sin\theta \\ \sin\theta & \cos\theta \end{bmatrix} \tag{3-18}$$

Then, the Pauli vector can be described as,

$$k = \frac{1}{\sqrt{2}} [S_{HH} + S_{VV} \quad \cos 2\theta (S_{HH} - S_{VV}) \quad -\sin 2\theta (S_{HH} - S_{VV})]^T \tag{3-19}$$

Substituting (3-19) to (3-3), the coherency matrix ($T(\theta)$) after rotation with respect to the orientation angle is shown as,

$$\frac{1}{2} \begin{bmatrix} |S_{HH} + S_{VV}|^2 & \cos 2\theta (S_{HH} + S_{VV})(S_{HH} - S_{VV})^* & -\sin 2\theta (S_{HH} + S_{VV})(S_{HH} - S_{VV})^* \\ \cos 2\theta (S_{HH} - S_{VV})(S_{HH} + S_{VV})^* & \cos^2 2\theta \, |S_{HH} - S_{VV}|^2 & -\frac{1}{2}\sin 4\theta |S_{HH} - S_{VV}|^2 \\ -\sin 2\theta (S_{HH} - S_{VV})(S_{HH} + S_{VV})^* & -\frac{1}{2}\sin 4\theta |S_{HH} - S_{VV}|^2 & \sin^2 2\theta \, |S_{HH} - S_{VV}|^2 \end{bmatrix} \tag{3-20}$$

3.4.2 Probability Distribution Function

If the horizontal dipoles are adopted, that is, $S_{HH} = 1, S_{VV} = 0$, then, (3-20) is written as,

$$T(\theta) = \frac{1}{2} \begin{bmatrix} 1 & \cos 2\theta & -\sin 2\theta \\ \cos 2\theta & \cos^2 2\theta & -\frac{1}{2}\sin 4\theta \\ -\sin 2\theta & -\frac{1}{2}\sin 4\theta & \sin^2 2\theta \end{bmatrix} \tag{3-21}$$

According to (3-16), to construct suitable volume scattering models, the probability density function must be determined. Freeman and Durden (1998) first assumed that the orientation angles of dipoles satisfy the uniform distribution, which can be seen as,

$$p(\theta) = \frac{1}{2\pi} \tag{3-22}$$

where $0 \leq \theta \leq 2\pi$, substituting (3-21) and (3-22) to (3-16), then we obtain,

$$T_{Freeman} = \int_0^{2\pi} \frac{1}{2\pi} \mathrm{T}(\theta) d\theta = \frac{1}{4} \begin{bmatrix} 2 & 0 & 0 \\ 0 & 1 & 0 \\ 0 & 0 & 1 \end{bmatrix} \tag{3-23}$$

However, Yamaguchi et al. (2005) found that most of the orientation angles of dipoles are either vertical or horizontal, thus, the vertical and horizontal volume scattering models based on the sine function are proposed, and the PDF is shown as,

$$p(\theta) = \frac{\sin\theta}{2} \tag{3-24}$$

Substituting (3-21) and (3-24) to (3-16), the vertical and horizontal volume scattering models can be described as

$$\begin{aligned} T^{H}_{Yamaguchi} &= \int_0^{\pi} \frac{\sin\theta}{2} \mathrm{T}(\theta) d\theta = \frac{1}{30} \begin{bmatrix} 15 & 5 & 0 \\ 5 & 7 & 0 \\ 0 & 0 & 8 \end{bmatrix} \\ T^{V}_{Yamaguchi} &= \int_0^{\pi} \frac{\cos\theta}{2} \mathrm{T}(\theta) d\theta = \frac{1}{30} \begin{bmatrix} 15 & -5 & 0 \\ -5 & 7 & 0 \\ 0 & 0 & 8 \end{bmatrix} \end{aligned} \tag{3-25}$$

These two models in (3-25) are currently in widespread usage (Yamaguchi et al., 2011; Sato et al., 2012; Shan et al., 2012).

3.4.3 Adaptive Volume Scattering Model

As crop phenology changes over the course of the growing season, it is very difficult to describe crops using only one volume scattering model. Additionally, Yamaguchi et al. (2005) figured out that there are many vertical and horizontal dipoles scatterings in L band besides the random volume scattering, and then they proposed the vertical and horizontal volume scattering models based on a first order sine function. However, the

first order function is only one type of vertical or horizontal dipoles, which cannot describe all the vertical or horizontal orientations completely. Furthermore, the shorter C-band senses a mean orientation closer to the vertical direction (Arii et al., 2011); as a result, most of the orientation angles of vegetation including crops are closed to 90 degrees for C-band wavelength imagery. Based on these two conditions, two new probability density functions proposed by Huang and Wang (2014) are adopted in this chapter, which can be shown as,

$$p(\theta) = \frac{sin^n\theta}{\int_0^{\pi} sin^n\theta d\theta}$$

$$p(\theta) = \frac{cos^n\theta}{\int_{-\frac{\pi}{2}}^{\frac{\pi}{2}} cos^n\theta d\theta} \tag{3-26}$$

According to (3-16), their volume Scattering models are constructed by (3-27) respectively,

$$T_V^V = \int_0^{\pi} p(\theta)\, T(\theta) d\theta$$

$$T_V^H = \int_{-\frac{\pi}{2}}^{\frac{\pi}{2}} p(\theta)\, T(\theta) d\theta \tag{3-27}$$

Substituting (3-21) and (3-26) to (3-27), these two volume scattering models are shown as,

$$T_V^V = \frac{1}{A}\begin{bmatrix} T_V^{11} & T_V^{12} & 0 \\ T_V^{12} & T_V^{22} & 0 \\ 0 & 0 & T_V^{33} \end{bmatrix}$$

$$T_V^H = \frac{1}{A}\begin{bmatrix} T_H^{11} & T_H^{12} & 0 \\ T_H^{12} & T_H^{22} & 0 \\ 0 & 0 & T_H^{33} \end{bmatrix} \tag{3-28}$$

where

$$T_H^{11} = T_V^{11} = \frac{\sqrt{\pi}\Gamma\left(\frac{n+1}{2}\right)}{2\Gamma\left(\frac{n}{2}+1\right)}, T_H^{12} = -T_V^{12} = \frac{n\sqrt{\pi}\Gamma\left(\frac{n+1}{2}\right)}{4\Gamma\left(\frac{n}{2}+2\right)}$$

$$T_H^{22} = T_V^{22} = \frac{(n^2+2n+4)\sqrt{\pi}\Gamma\left(\frac{n+1}{2}\right)}{8\Gamma\left(\frac{n}{2}+3\right)}, T_H^{33} = T_V^{33} = \frac{\sqrt{\pi}\Gamma\left(\frac{n+3}{2}\right)}{\Gamma\left(\frac{n}{2}+3\right)}$$

Where $A = \int_0^{\pi} sin^n\theta d\theta = \int_{-\frac{\pi}{2}}^{\frac{\pi}{2}} cos^n\theta d\theta = \frac{\sqrt{\pi}\Gamma\left(\frac{n+1}{2}\right)}{\Gamma\left(\frac{n}{2}+1\right)}$ and $\Gamma(a) = \int_0^{\infty} e^{-t}t^{a-1}d\mathrm{t}$

It should be noted that n is real and not limited to integer. Without the loss of generality, four components of horizontal volume scattering models are depicted in Figure 3-4,

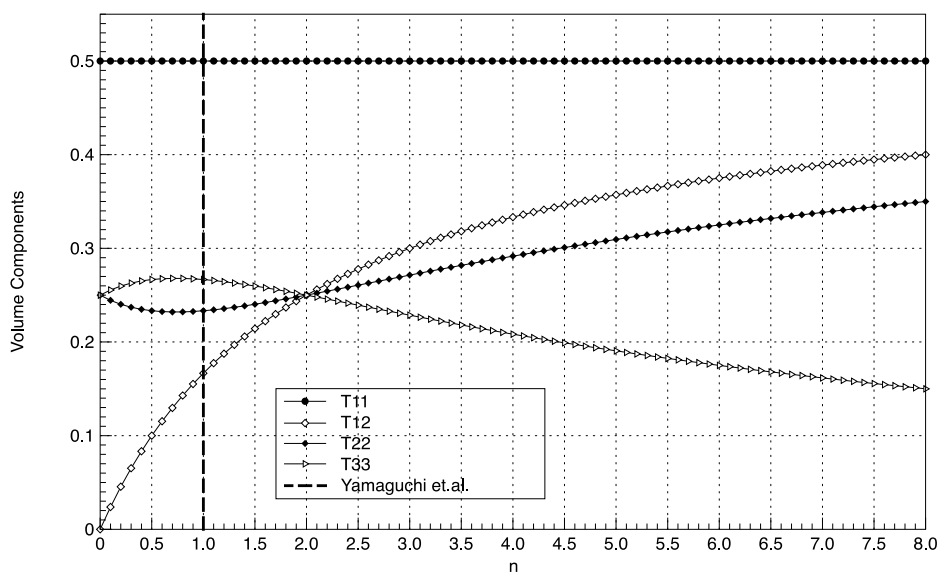

Figure 3-4. Vertical volume scattering components.

Figure 3-4 depicts that T_{11} stays stable all the time with a value of 0.5. When n is increasing, T_{22} decreases first and later increases at the point between 0.5 and 1. While T_{33} is opposite compared with T_{22}, T_{12} always increases when n increases. It should be noted that when n is equal to 0, it is Freeman volume scattering model (equation (3-23)). While n is equal to 1, it becomes Yamaguchi volume scattering model (equation (3-25)),

which is the dash line shown in Figure 3-4. The comparisons of the adaptive volume scattering and the Freeman and Yamaguchi models are shown in Table 3-1.

Table 3-1. Comparison with other volume scattering models.

n	**V-AVSM**	**H-AVSM**	**Reference**
0	$\begin{bmatrix} 0.500 & 0 & 0 \\ 0 & 0.250 & 0 \\ 0 & 0 & 0.250 \end{bmatrix}$	$\begin{bmatrix} 0.500 & 0 & 0 \\ 0 & 0.250 & 0 \\ 0 & 0 & 0.250 \end{bmatrix}$	Freeman & Durden (1998)
1	$\begin{bmatrix} 0.500 & -0.167 & 0 \\ -0.167 & 0.233 & 0 \\ 0 & 0 & 0.267 \end{bmatrix}$	$\begin{bmatrix} 0.500 & 0.167 & 0 \\ 0.167 & 0.233 & 0 \\ 0 & 0 & 0.267 \end{bmatrix}$	Yamaguchi et al. (2005)

Figure 3-4 and Table 3-1 show that the adaptive volume scattering model not only include Yamaguchi and Freeman volume scattering models, but also vary with n continuously. To demonstrate further, the RADAR vegetation index (RVI) (Kim & van Zyl, 2001) and scattering entropy (Cloude & Pottier, 1997) are calculated separately, which are shown as,

$$RVI = \frac{4min(\lambda_1, \lambda_2, \lambda_3)}{\lambda_1 + \lambda_2 + \lambda_3}$$

$$Entropy = -\sum_{i=1}^{3} p_i log_3(p_i), p_i = \frac{\lambda_i}{\lambda_1 + \lambda_2 + \lambda_3} \tag{3-29}$$

where λ_1, λ_2 and λ_3 are the eigenvalues of the adaptive volume scattering models, their curves are shown in Figure 3-5,

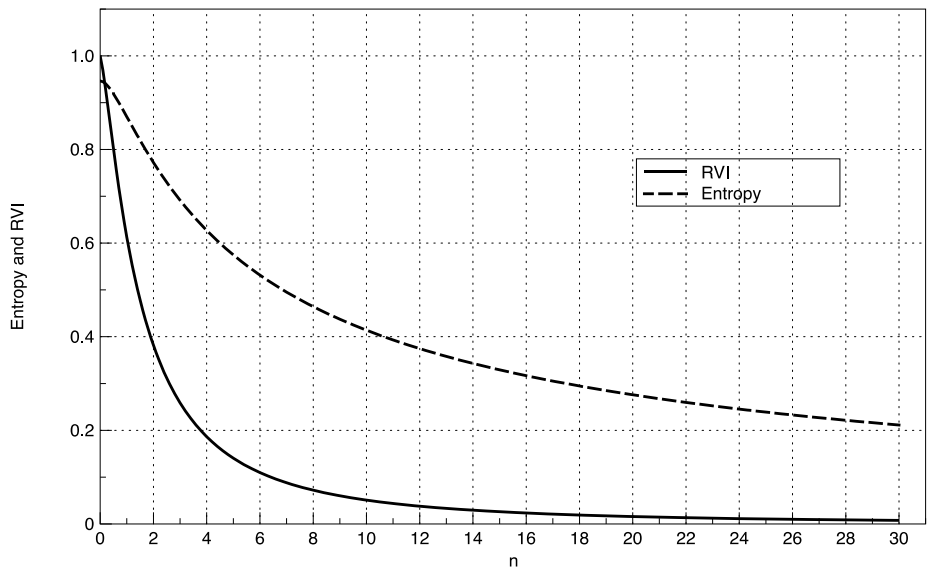

Figure 3-5. RVI and Entropy.

Figure 3-5 depicts that both entropy and RVI decrease as n increases, this is because as n increases, the adaptive volume scattering is becoming a more "pure" vertical or horizontal scattering, especially when n is close to infinite, it is becoming vertical or horizontal volume scattering. RVI has a steeper decrease than entropy does. Considering this, we can use this feature to limit the maximum range of n, thereby accelerating the process to find the optimum n in practice. It can be seen that the RVI is very low and stays almost unchangeable at the point where $n = 20$, Therefore, the maximum n we adopt in this chapter is 20.

3.5 Adaptive Two-Component Decomposition

3.5.1 Two-Component Decomposition

The reflection symmetry hypothesis, assuming that the objects are symmetric with respect to a line within the plane being vertical to the LOS, which is valid for agricultural surfaces, allows the derivation from the coherency matrix of the analytical expressions of the polarimetric parameters. In this case, the correlation between the co- and cross-polarized channels is assumed to be zero (Ainsworth et al., 2008). Therefore, the coherency matrix satisfying the reflection symmetry can be described as,

$$T = \begin{bmatrix} T_{11} & T_{12} & 0 \\ T_{12}^{*} & T_{22} & 0 \\ 0 & 0 & T_{33} \end{bmatrix} \tag{3-30}$$

The following volume scattering model is used to represent the adaptive volume scattering in this chapter, which can be shown as

$$T_V = \begin{bmatrix} T_V^{11} & T_V^{12} & 0 \\ T_V^{12*} & T_V^{22} & 0 \\ 0 & 0 & T_V^{33} \end{bmatrix} \tag{3-31}$$

Then, the two-component decomposition we proposed in this chapter is described as,

$$T = f_G T_G + f_V T_V \tag{3-32}$$

where f_G and f_V are the coefficients of ground and volume scattering, T_G is the extended surface scattering model based on the normal distribution function while T_V is the adaptive volume scattering model (3-28) proposed in this chapter. Substituting (3-15) and (3-31) to (3-32), we obtain,

$$\begin{cases} T_{11} = f_G + f_V T_V^{11} \\ T_{12} = f_G \beta^* e^{-2\sigma^2} + f_V T_V^{12} \\ T_{22} = \dfrac{1}{2} f_G |\beta|^2 \left(1 + e^{-8\sigma^2}\right) + f_V T_V^{22} \\ T_{33} = \dfrac{1}{2} f_G |\beta|^2 \left(1 - e^{-8\sigma^2}\right) + f_V T_V^{33} \end{cases} \tag{3-33}$$

The resolutions to solve this equation are discussed in the next two sections.

3.5.2 Non-negative Eigenvalue Method for f_v

To calculate f_V, the non-negative eigenvalue decomposition (NNED) method introduced by van Zyl et al. (2011) based on the energy conservation law is adopted in this chapter. We set a as the unknown variable and compute the eigenvalues of $T_{remaider}$, which can be seen in (3-34), and its three eigenvalues are shown in (3-35). Setting each eigenvalue

zero, three a are obtained, the f_V we adopt is the minimum a among them. The remainder coherency matrix after the volume scattering model is subtracted is shown as,

$$T_{remainder} = T - aT_V \tag{3-34}$$

Its three eigenvalues are shown as,

$$\lambda_1 = T_{33} - aT_V^{33}$$

$$\lambda_2 = \frac{T_{11} + T_{22} - aT_V^{11} - aT_V^{22} - \sqrt{\nabla}}{2} \tag{3-35}$$

$$\lambda_3 = \frac{T_{11} + T_{22} - aT_V^{11} - aT_V^{22} + \sqrt{\nabla}}{2}$$

where

$$\nabla = \begin{matrix} 4|T_{12}|^2 - 2T_{11}T_{22} + T_{11}^2 + T_{22}^2 + (aT_V^{11})^2 + (aT_V^{22})^2 + 4|T_V^{12}|^2a^2 - 2T_{11}T_V^{11}a + \\ 2T_{11}T_V^{22}a + 2T_{22}T_V^{11}a - 22T_{22}T_V^{22}a - 2T_V^{11}T_V^{22}a^2 - 4aT_{12}T_V^{12*} - 4T_V^{12}T_{12}^{*}a \end{matrix}$$

It can be seen from (3-35) that $\lambda_2 \leq \lambda_3$, so we can only compare λ_1 and λ_2, setting $\lambda_1 = 0$ and $\lambda_2 = 0$, we obtain,

$$\begin{cases} a_1 = \dfrac{T_{33}}{T_V^{33}} \\ a_2 = \dfrac{Z - \sqrt{Z^2 - 4(T_{11}T_{22} - |T_{12}|^2)(T_V^{11}T_V^{22} - |T_V^{12}|^2)}}{2(T_V^{11}T_V^{22} - |T_V^{12}|^2)} \end{cases} \tag{3-36}$$

Where $Z = T_{11}T_V^{22} + T_{22}T_V^{11} - T_{12}T_V^{12*} - T_{12}^{*}T_V^{12}$, and then f_V and its power P_V are shown as,

$$f_V = min(a_1, a_2)$$

$$P_V = f_V \cdot (T_V^{11} + T_V^{22} + T_V^{33}) \tag{3-37}$$

3.5.3 Adaptive Decomposition for Optimal Solution

From (3-34), with each n, f_V can be obtained based on the NNED. Subtracting the volume scattering contribution, equation (3-33) is re-written as,

$$\begin{cases} B = T_{11} - f_V T_V^{11} = f_G \\ C = T_{12} - f_V T_V^{12} = f_G \beta^* e^{-2\sigma^2} \\ D = T_{22} - f_V T_V^{22} = \frac{1}{2} f_G |\beta|^2 \left(1 + e^{-8\sigma^2}\right) \\ E = T_{33} - f_V T_V^{33} = \frac{1}{2} f_G |\beta|^2 \left(1 - e^{-8\sigma^2}\right) \end{cases} \tag{3-38}$$

where B, C, D and E are temporary variables, and then we can obtain,

$$e^{-8\sigma^2} = \frac{D + E}{D - E} \tag{3-39}$$

then,

$$\sigma^2 = -\ln\left(\frac{D + E}{D - E}\right)/8 \tag{3-40}$$

then,

$$\begin{aligned} f_G &= B \\ \beta^* &= C/\left(B \cdot e^{-2\sigma^2}\right) \\ P_G &= f_G \cdot (1 + |\beta|^2) \end{aligned} \tag{3-41}$$

However, there are four equations, only three parameters are unknown in equation (3-38). In order to achieve the optimal solution, the criterion that minimizes the power of $T_{remainder}$ is adopted with varying n. Finally, four parameters $\beta \quad P_G \quad P_V \quad and\ n$ are determined when the power of $T_{remainder}$ is minimum, and can be described as,

$$\{\beta, P_G, P_V, n\} = min\{Span(T_{remainder})\} \tag{3-42}$$

It should be noted that there are two volume scattering models: vertical and horizontal models. In contrast with Yamaguchi et al. (2005) usage of the criterion (3-43) to decide which volume scattering model is the better one to be adopted, the authors determined the volume scattering model to be used in this chapter depending on which one could minimize the power of $T_{remainder}$.

$$P_r = 10 \cdot log \frac{\langle |S_{VV}|^2 \rangle}{\langle |S_{HH}|^2 \rangle} \tag{3-43}$$

3.6 Soil Moisture Estimation

Although the soil parameter β is determined following the steps discussed above, it is still difficult to retrieve the relative dielectric constant ε_r directly, due to its complex function relationships (equation (3-6) and (3-7)). In order to accelerate the calculation of ε_r in practice, the look-up table between β and ε_r is constructed with the step of ε_r 0.01. To retrieve soil moisture from ε_r, an empirical model relating the volume soil moisture (mv) to relative dielectric constant (ε_r) is adopted, which is suitable to describe mineral soil (Topp et al., 1980) can be shown as,

$$mv_M = -0.053 + 2.92e^{-2}\varepsilon_r - 5.5e^{-4}\varepsilon_r^2 + 4.3e^{-6}\varepsilon_r^3 \tag{3-44}$$

Where the mv_M is the volumetric soil moisture of mineral soil.

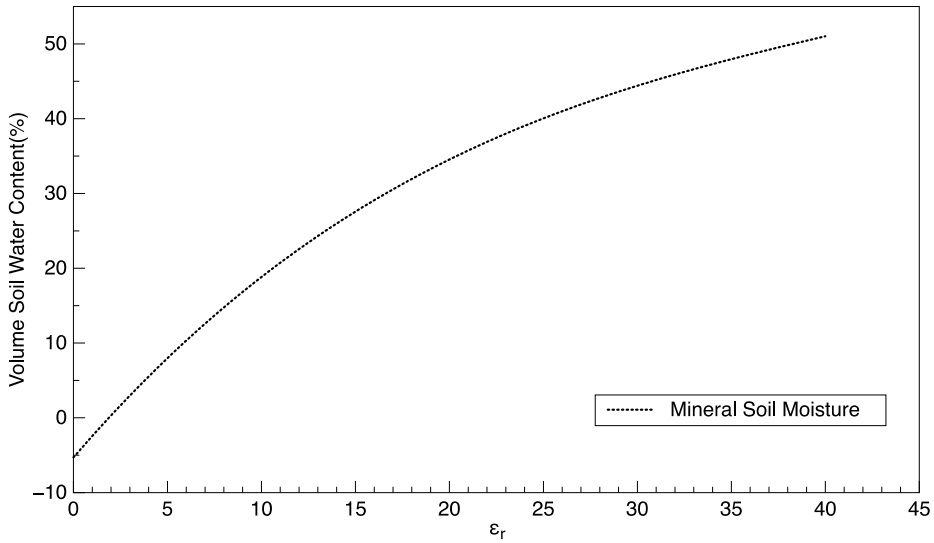

Figure 3-6. Relationship between soil moisture and relative dielectric constant.

Overall, the flowchart of soil moisture estimation based on the adaptive two-component decomposition (ATCD) can be shown in Figure 3-7,

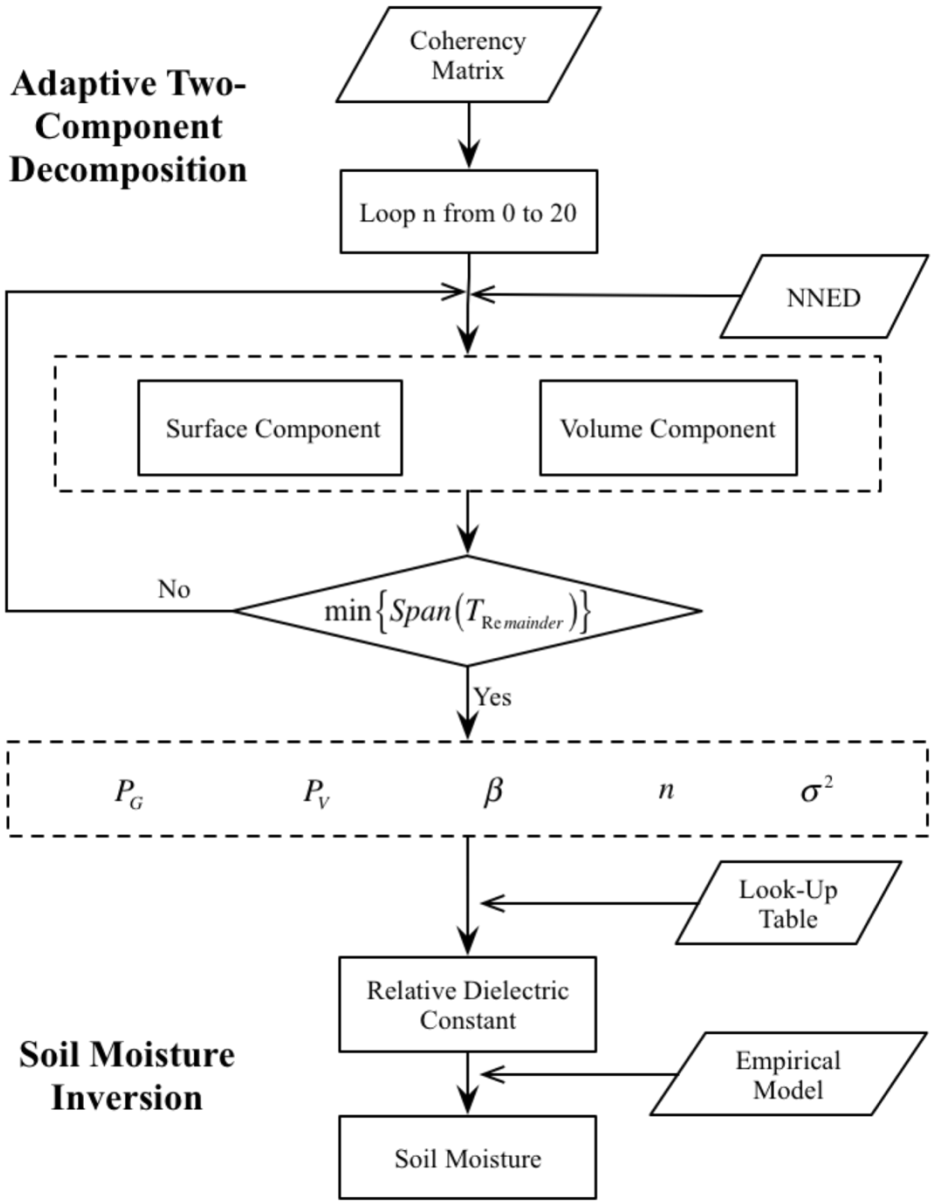

Figure 3-7. Flowchart of soil moisture estimation using the ATCD.

3.7 Experiments

3.7.1 Dataset, Ground Truth Measurement and Data Process

Figure 3-8 depicts the fully polarimetric RADARSAT-2 Pauli image acquired on May 9th, 2013 and May 6th, 2015. Both study areas (study area 2013 and study area 2015) are located in Southwestern Ontario, Canada, as observed in the blue and red points on Fig 3.8. Forests causing higher backscattering are shown in colour green, and agricultural fields with low backscattering are in colour blue. Up to the end of May, the winter wheat field was covered by sparse wheat with the height ranging from 5 to 25 cm. Concurrent with the RADARSAT-2 acquisitions, soil moisture measurements were taken in six wheat fields during the period from late April to late May. The measured soil moistures in both study areas cover a wide range, from 15 to 50 [vol. %] in study area 2013 and 5 [vol. %] to 30 [vol. %] in study area 2015. The soil moisture was measured using a TDR probe with its principle defined in Appendix E over the top 5 cm of the soil. For each sample site, the soil moisture was measured within a 10 m-by-10 m rectangle, with 6 points distributed evenly, and the soil moisture of each sample site is the averaged from the 6 points. Five RADARSAT-2 images with different beam modes were used for validation in this chapter, as shown in Table 3-2.

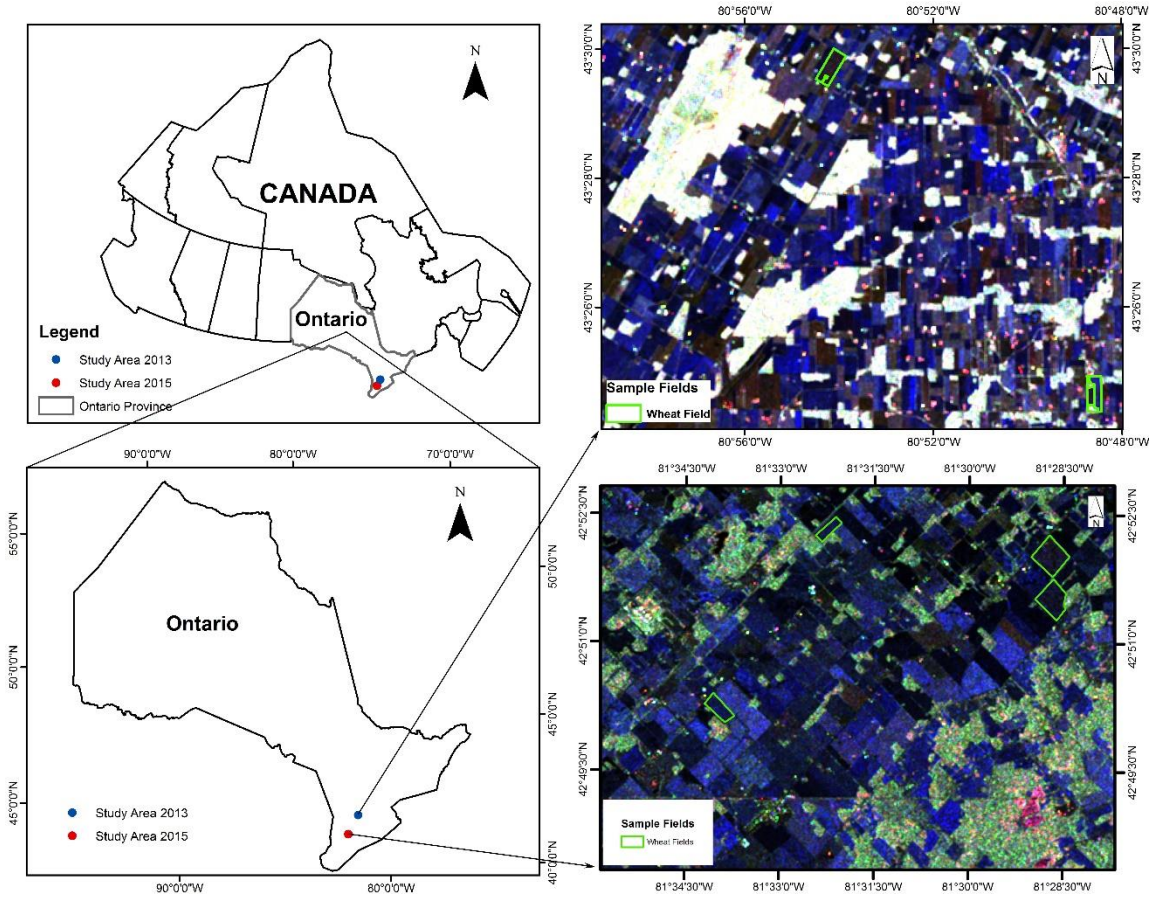

Figure 3-8. Location of the study area and Pauli images acquired on May 9th 2013 and May 6th 2015, with red $|\boldsymbol{S_{HH}} - \boldsymbol{S_{VV}}|^{\boldsymbol{2}}$, green $\boldsymbol{4}|\boldsymbol{S_{HV}}|^{\boldsymbol{2}}$ and blue $|\boldsymbol{S_{HH}} + \boldsymbol{S_{VV}}|^{\boldsymbol{2}}$.

Table 3-2. RADARSAT-2 datasets. IA: Incidence Angle. DoY: Day of Year.

Date	DoY	Orbit	Look Direction	Beam	IA
20130429	119	Ascending	Right	FQ09	29°
20130509	129	Ascending	Right	FQ19	39°
20130523	143	Ascending	Right	FQ09	29°
20150506	126	Ascending	Right	FQ10	30°
20150520	140	Ascending	Right	FQ01	20°

3.7.2 Scattering Mechanism Analysis

To analyze the scattering over wheat fields, in addition to the wheat fields in study area 2013, the field with bare soils was also selected for scattering analysis. The H-α decomposition (Cloude & Pottier, 1997) was adopted. Figure 3-9 depicts that more and more pixels in the wheat fields are dominated by volume scattering as time changes with

their entropy increasing. This is because as wheat grows taller and denser, the scattering is primarily caused by the wheat canopy; when the wheat is short and sparse, its scattering is dominated by the underlying soils. In the bare soil fields, the dominant scattering is the surface scattering over three dates. However, in the bare soil field, some of their scattering lies in the low entropy zone (Z9), which is mainly Bragg scattering from the flat bare soils. For those pixels in the medium entropy zone (Z6), their scattering is primarily caused by the surface roughness, suggesting that the roughness effects should not be ignored for C-band RADARSAT-2 data. In addition, to demonstrate the statistical distribution of the orientation angle induced by the azimuthal slope, the histograms of the orientation angle over the same bare soil fields on day 129 and 149 are calculated and shown in Figure 3-10. As these fields were plowed and flattened before the crop planting between day 129 and 143, the mean value of the orientation angle changes from 0.7 degrees to 0.2 degrees, which is very close to 0 degree. Hence, it is likely that the zero mean normal distribution assumption adopted in this chapter is suitable to describe the distribution of orientation angles. Overall, we can conclude that the dominant scattering in wheat field is comprised of surface and volume scattering at the early growing stages, and the orientation angle satisfies the zero mean normal distribution, demonstrating the feasibility of our model proposed in this chapter.

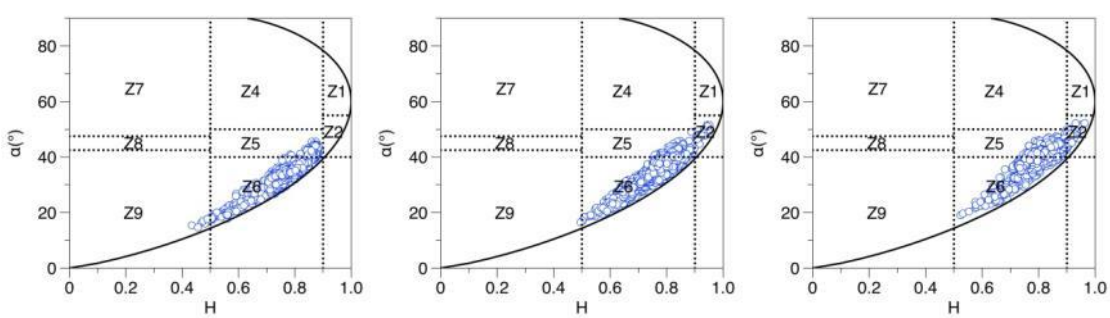

(a)

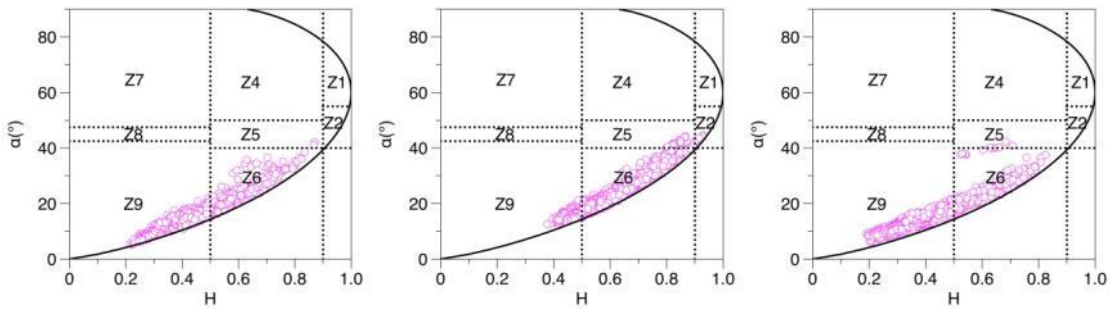

(b)

Figure 3-9. Plots of H- α decomposition on wheat and bare soil fields on three different dates in study area 2013; from left to right, they are day 119, 129, 143, respectively. (a) Wheat field. (b) Bare soil field.

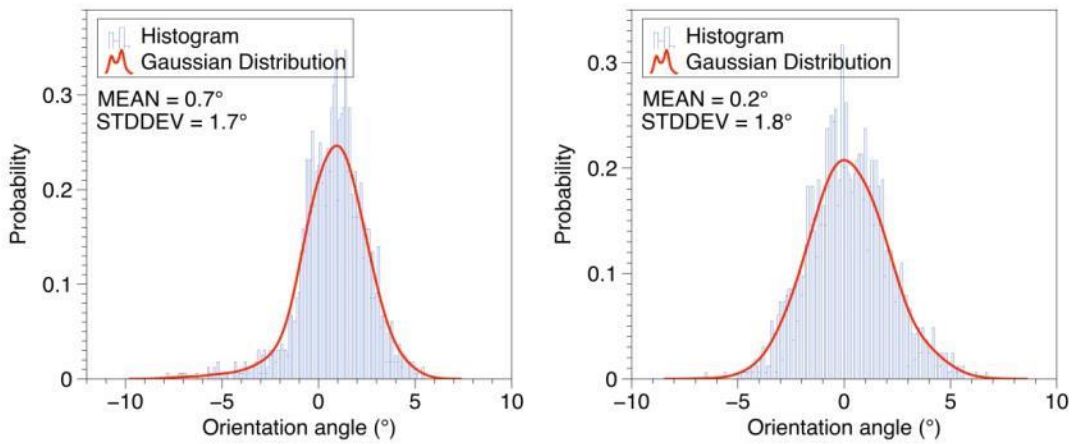

(a) (b)

Figure 3-10. Histograms of orientation angles over bare soils in study area 2013. (a) day 129 (b) day 143.

3.7.3 Qualitative Analysis

To verify the application of model-based decomposition methods on soil moisture estimation for C-band RADARSAT-2 data and to validate the ATCD, the four other methods are compared: 1. The ATCD method using the FVSM (A-FVSM); 2. The ATCD method using the YVSM (A-YVSM); 3. Freeman decomposition (FD); and 4. Yamaguchi decomposition (YD). The soil moisture values derived from these four methods and the ATCD are shown in Figure 3-11. In areas where the soil moisture derived from other four methods was less than 10 [vol. %], the image is colored purple. However, this evaluation is not consistent with the observed field conditions because

there was rain on day 119 and 143, with a recorded precipitation of approximately 10 mm within 24 hours. However, the soil moisture derived from the A-YVSM has a higher quality compared with the A-FVSM because the cyan that emerged with the soil moisture greater than 10 [vol. %]. This difference can perhaps be explained by the fact that the Yamaguchi volume scattering model contains both vertical and horizontal volume scattering models in addition to the random volume scattering model. In contrast, the A-FVSM only used the random scattering model. In terms of the soil moisture derived from the FD and the YD, most areas are still covered by purple, indicating a soil moisture content between 0 [vol. %] and 10 [vol. %]. Compared with the soil moisture derived using these four methods, the soil moisture derived from the ATCD looks much better because much cyan and green emerged. In these regions, the soil moisture value was between 10 [vol. %] and 40 [vol. %]. It can be noted that the soil moisture values obtained on day 129 were lower than those on days 119 and 143 because no rain fell on day 129; as such, the imagery results correspond better with the observed field conditions.

In addition to study area 2013, the ATCD is also performed on study area 2015 with their decomposed components shown in Figure 3-12. We can see that these agricultural fields have the dominant surface scattering while the forest area is dominated by volume scattering. The randomness was also derived by n in our volume scattering model based on the relationship proposed by Arii et al. (2011). Agricultural fields dominated by surface scattering will have low randomness, while the volume scattering caused in the forest areas tends to lead to a very high randomness. This is consistent with the decomposed components shown in Figure 3-12, in which the randomness has much lower value in agricultural fields with blue colour than that in forest areas with red colour. Furthermore, as wheat grows denser from day 126 to 140, the scattering caused by the denser wheat canopy makes the increase of scattering randomness with more red colour emerging, which can be seen from Figure 3-12. Same with study area 2013, soil moisture was not inverted over the forest area due to the short wavelength of the C-band with limited penetration. However, the soil moisture over some agricultural fields in study area 2013 on day 119 is also not inverted, which perhaps is due to the multiple scattering

caused by the crop residues (McNairn et al., 2002), which will cause a complicated scattering leading to a difficult soil moisture inversion.

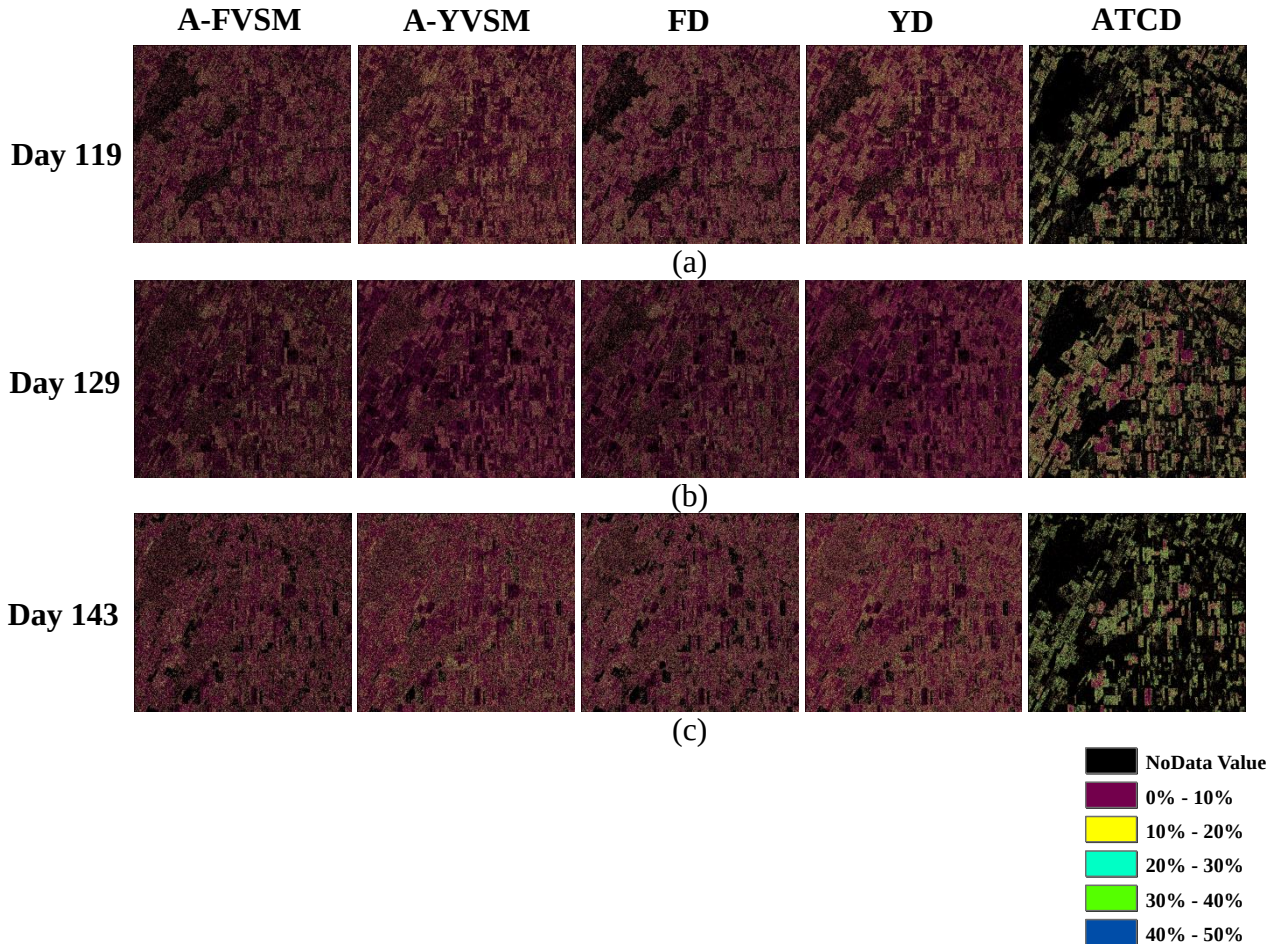

Figure 3-11. Comparison of different soil moisture estimation methods on three different dates in study area 2013; from left to right, they are the soil moisture derived from the A-FVSM, A-YVSM, FD, YD and ATCD. (a) day 119. (b) day 129. (c) day 143.

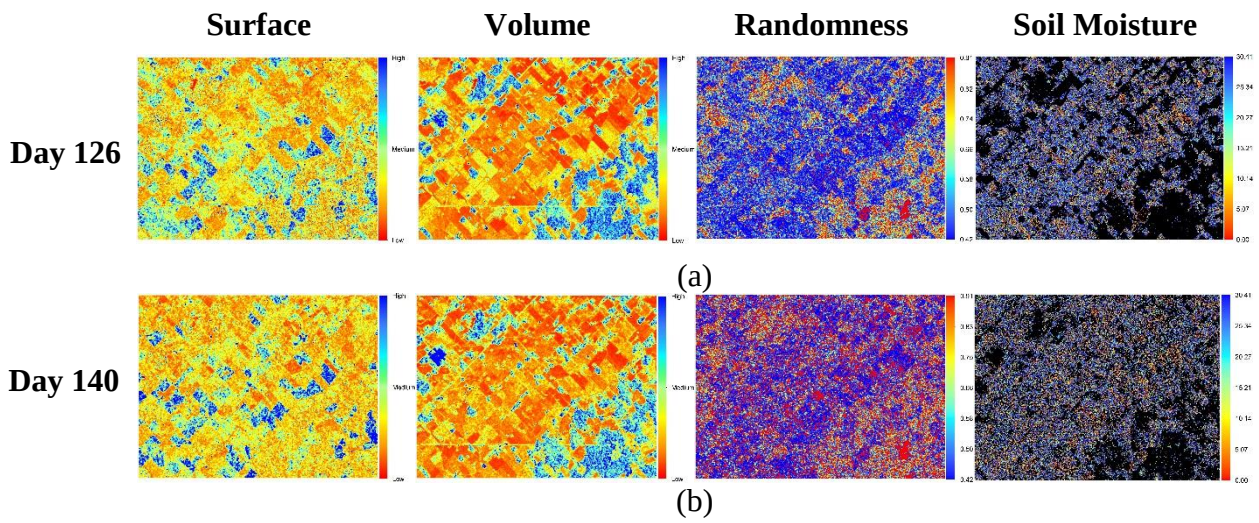

Figure 3-12. Decomposed components and inversed soil moisture from ATCD on different dates in study area 2015; from left to right they are surface scattering, volume scattering, randomness, and estimated soil moisture with black areas not inverted. (a) day 126. (b) day 140.

3.7.4 Quantitative Analysis

To validate the retrieved results quantitatively, the ground truth data collected from the wheat fields are compared for these two study areas using the RMSE. To calculate the soil moisture of the sample site, these points within a 5-by-5 window size around the sample site are averaged. Pixels that are not inverted are ignored and are not plotted. Figure 3-13 (a) and Table 3-3 show that the RMSE of the soil moisture according to the ATCD on day 119 is approximately 8.58 [vol. %] compared with the ground reference data records, whereas the soil moisture derived by other methods has a severe underestimation (most of them are under 10 [vol. %]); all of the other methods also exhibit much higher RMSEs of approximately 30 [vol. %]. On day 129, no precipitation occurred, and the soil is not wet according to observed field conditions; thus, the soil moisture values were lower than those on day 119, with the measured values less than 25%. The soil moisture derived on day 129 from the ATCD is well correlated with the measured reference data, with an RMSE of 1.51 [vol. %], whereas the RMSE of the other methods is much higher, with a value of approximately 15 [vol. %]. On day 143, the soil moisture derived from the ATCD presents a fluctuation when the soil moisture is greater

than 27 [vol. %], with an RMSE of 14.95 [vol. %]. The soil moistures derived from other methods are all less than 10 [vol. %] on either day 129 or 143, which appears to be a severe underestimation with a very high RMSE of approximately 30 [vol. %]. For study area 2015, the measured soil moisture is less than 25 [vol. %]. The soil moisture derived by ATCD has much lower RMSE approximately at 5.5 [vol. %] compared with other methods with their RMSE greater than 15 [vol. %], which can be seen from Figure 3-13(b) and Table 3-3. Being the same as day 126, the soil moisture derived on day 140 using the ATCD also has the lowest RMSE with its value of 6.20 [vol. %], while other methods have much higher RMSE. Overall, the ATCD has the lowest overall RMSE of 7.12 [vol. %] while the other methods all have the RMSE of over 20 [vol. %] when all sample sites are considered. Finally, to perform the uncertainty analysis of the ATCD, the soil moisture over bare soil is also estimated by the ATCD with a RMSE of 3.77 [vol. %], which is shown in Figure 3-13(c). Compared with the wheat fields, the overall RMSE of bare soil is less than that of wheat fields. In addition, we also observed from Table 3-3 that, in study area 2015, as wheat grows, the RMSE increases. From this perspective, we could perhaps conclude that the major uncertainty error comes from the volume scattering model, which is reasonable because the volume scattering caused by the wheat is much complex in reality. Being different from the complicated physical models, other researchers made use of a simple coherency matrix to represent the volume scattering, which is not adequate. This is also the reason why we attempt to improve the volume scattering model in this chapter. Although it is not perfect, it does improve the accuracy of the retrieved soil moisture significantly compared with the other model-based decomposition methods.

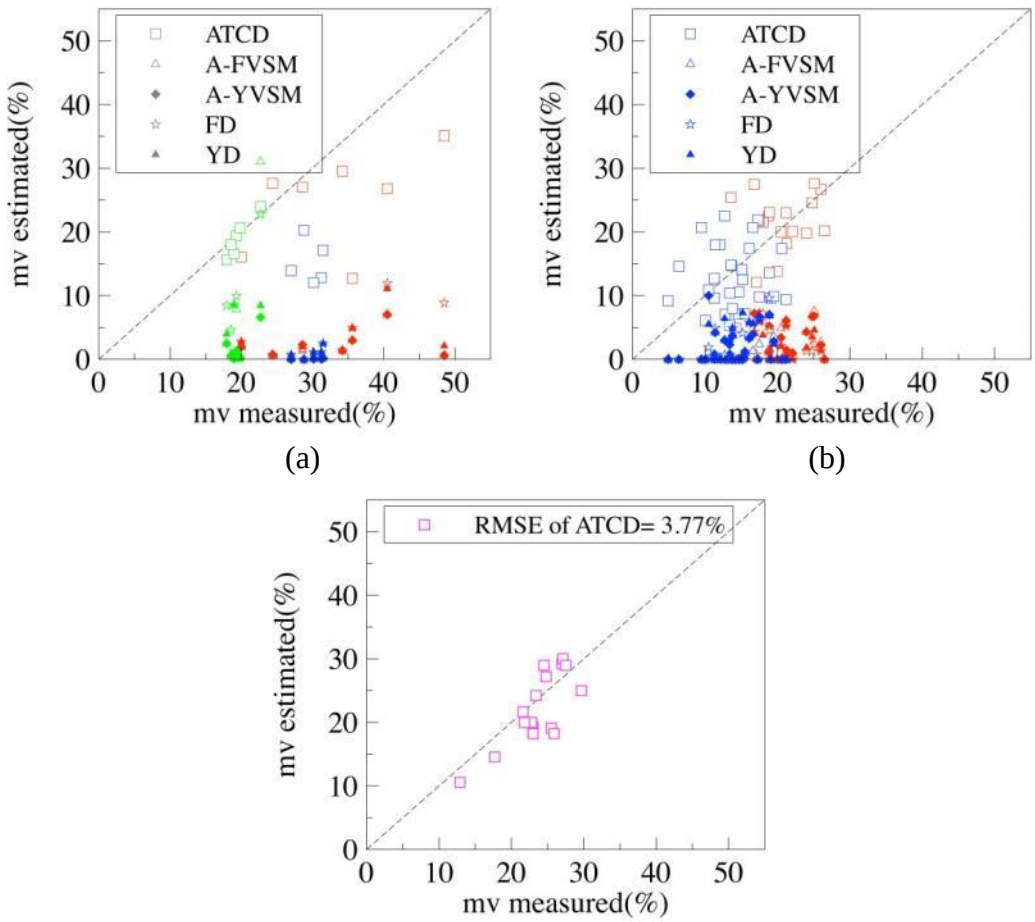

Figure 3-13. Comparison of the estimated soil moisture by different methods in two study areas, different geometric shapes represent different methods. (a) Wheat fields in study area 2013 with the red is on day 119, the green is on day 129, and the blue is on day143. (b) Wheat fields in study area 2015 with the red is on day 126, and the blue is on day 140. (c) Bare soil fields.

Table 3-3. RMSE of different methods in wheat fields on different dates in two study areas (unit: [vol. %]).

Methods	**DoY of 2013**			**DoY of 2015**		**Overall RMSE**
	119	129	143	126	140	
A-FVSM	32.01	15.84	29.72	18.1	13.58	19.27
A-YVSM	31.91	17.73	29.72	17.6	13.17	19.15
FD	29.26	12.03	28.68	18.9	13.08	18.48
YD	30.71	16.00	28.68	18.9	12.80	18.90
ATCD	**8.58**	**1.51**	**14.95**	**5.50**	**6.20**	**7.12**

It should also be noted from Table 3-3 that on day 143 in 2013, its RMSE is very high at 15 [vol. %]. This is perhaps because the measured soil moisture is greater than 30 [vol. %] on this day with its corresponding ε_r around 17, hence, the relationship between ε_r and β reaches saturation as its incidence angle is around 30 degrees, which can be seen in Figure 3-1. An interesting phenomenon is observed on day 119 that it has the same incidence angle as that on day 143, but its RMSE is only 8.59 [vol. %] around half of that on day 143. This is perhaps because the measured soil moisture both are greater than 30 [vol. %], which makes the estimated soil moisture biased and causes an unreliable RMSE.

3.8 Conclusion

Due to the limited penetration capacity of the short wavelength C-band RADARSAT-2, the soil moisture is estimated only at the early crop growing stages with short and sparse crops. Model-based decomposition methods were discussed on C-band RADARSAT-2 data for soil moisture estimation under crop cover, and an adaptive two-component decomposition (ATCD) method was developed in this chapter. The existing methods, such as the Freeman and Yamaguchi decompositions, suffer from severe underestimation and with a very large RMSE. Therefore, the direct application of the Freeman or Yamaguchi decomposition for soil moisture retrieval for C-band will lead to very poor results with the overall RMSE of around 19 [vol. %]. In contrast, the soil moisture derived by the ATCD is more consistent with the observed ground measurements with an overall RMSE of around 7 [vol. %] in wheat fields at early growing stages. However, the estimated soil moisture is perhaps biased when the soil moisture is greater than 30 [vol. %], especially when the incidence angle is low.

References

Ainsworth, T. L., Schuler, D. L., & Lee, J. S. (2008). Polarimetric SAR Characterization of Man-Made Structures in Urban Areas using Normalized Circular-pol Correlation Coefficients. *Remote Sensing of Environment*, *112*(6), 2876-2885.

Arii, M., van Zyl J. J., & Kim, Y. (2011). Adaptive Model-Based Decomposition of Polarimetric SAR Convariance Matrices. *IEEE Transactions on Geoscience and Remote Sensing*, *49*(3), 1104-1113.

Ballester-Berman, J. D., Vicente-Guijalba, F., & Lopez-Sanchez, J. M. (2013). Polarimetric SAR Model for Soil Moisture Estimation over Vineyards at C-Band. *Progress in Electromagnetics Research-Pier*, *142*, 639-665.

Cloude, S. R., & Pottier, E. (1997). An Entropy Based Classification Scheme for Land Applications of Polarimetric SAR. *IEEE Transactions on Geoscience and Remote Sensing*, *35*(1), 68-78.

Freeman, A., & Durden, S. L. (1998). A Three-Component Scattering Model for Polarimetric SAR Data. *IEEE Transactions on Geoscience and Remote Sensing*, , *36*(3), 963-973.

Hajnsek, I., Jagdhuber, T., Schon, H., & Papathanassiou, K. P. (2009). Potential of Estimating Soil Moisture under Vegetation Cover by Means of PolSAR. *IEEE Transactions on Geoscience and Remote Sensing*, *47*(2), 442-454.

Hajnsek, I., Pottier, E., & Cloude, S. R. (2003). Inversion of surface parameters from polarimetric SAR. *IEEE Transactions on Geoscience and Remote Sensing*, *41*(4), 727-744.

He, B., Xing, M., & Bai, X. (2014). A Synergistic Methodology for Soil Moisture Estimation in an Alpine Prairie Using Radar and Optical Satellite Data. *Remote Sensing*, *6*(11), 10966-10985.

Huang, X., & Wang, J. (2014)., An Adaptive Volume Scattering Model for Fully Polarimetric RADARSAT-2 Data. *10th European Conference on Synthetic Aperture Radar*, Berlin, Germany, 568-571.

Jagdhuber, T., Hajnsek, I., Bronstert, A., & Papathanassiou, K. P. (2013). Soil Moisture Estimation under Low Vegetation Cover Using a Multi-Angular Polarimetric

Decomposition. *IEEE Transactions on Geoscience and Remote Sensing*. *51*(4), 2201-2215.

Jagdhuber, T., Hajnsek, I., Bronstert, A., & Papathanassiou, K. P. (2014)., An Iterative, Generalized, Hybrid Decomposition on Fully Polarimetric SAR Data for Soil Moisture Retrieval under Vegetation, *10th European Conference on Synthetic Aperture Radar*, Berlin, Germany, 818-821.

Jin, Y. Q., & Xu, F. (2013). *Polarimetric Scattering and SAR Information Retrieval*. John Wiley & Sons. Woodhouse, I. H. (2006). *Introduction to Microwave Remote Sensing*. Boca Raton: Taylor & Francis.

Jones, H. G., & Vaughan, R. A. (2010). *Remote Sensing of Vegetation: Principles, Techniques, and Applications*. New York: Oxford University Press.

Kim, Y., & van Zyl J. J. (2001). Comparison of Forest Estimation Techniques Using SAR Data. *IEEE International Geoscience and Remote Sensing on Geoscience and Remote Sensing Symposium*, Sydney, Australia, 1395-1397.

McNairn, H., Duguay, C., Brisco, B., & Pultz, T. J. (2002). The Effect of Soil and Crop Residue Characteristics on Polarimetric Radar Response. *Remote Sensing of Environment*, *80*, 308-320.

Oliver, C., Quegan, S., & Knovel. (2004). *Understanding synthetic aperture radar images*. SciTech radar and defense series.

Sato, A., Yamaguchi, Y., Singh, G., & Park, S. E. (2012). Four-Component Scattering Power Decomposition with Extened Volume Scattering Model. . *IEEE Geoscience and Remote Sensing Letters*, *9*(2), 166-170.

Schuler, D. L., Lee, J. S., Kasilingam, D., & Nesti, G. (2002). Surface Roughness and Slope Measurements Using Polarimetric SAR Data. *IEEE Transactions on Geoscience and Remote Sensing*, *40*(3), 687-698.

Shan, Z., Wang, C., Zhang, H., & An, W. (2012). Improved Four-Component Model-Based Target Decomposition for Polarimetric SAR Data. *IEEE Geoscience and Remote Sensing Letters*. *9*(1), 75-79.

Topp, G. C., Davis, J. L., & Annan, A. P. (1980). Electromagnetic Determination of Soil-Water Content Measurements in Coaxial Transmission-Lines. *Water Resources Research*, *16*(3), 574-582.

van Zyl J. J., Arii, M., & Kim, Y. (2011). Model-Based Decomposition of Polarimetric SAR Covariance Matrices Constrained for Nonnegative Eigenvalues. *IEEE Transactions on Geoscience and Remote Sensing*, *49*(9), 3452-3459.

van Zyl, J. J., & Kim, Y. (2011). *Synthetic Aperture Radar Polarimetry*. JPL Space Science and Technology Series, New York: Wiley.

Woodhouse, I. H. (2006). *Introduction to Microwave Remote Sensing*. Boca Raton: Taylor & Francis.

Yamaguchi, Y., Moriyama, T., Ishido, M., & Yamada, H. (2005). Four-Component Scattering Model for Polarimetric SAR Image Decomposition. *IEEE Transactions on Geoscience and Remote Sensing*, *43*(8), 1699-1706.

Yamaguchi, Y., Sato, A., Boerner, W. M., & Sato, R. (2011). Four-Component Scattering Power Decomposition with Rotation of Coherence Matrix. *IEEE Transactions on Geoscience and Remote Sensing*, *49*(6), 2251-2258.

Chapter 4 An Integrated Surface Parameter Inversion Scheme over Agricultural Fields*

4.1 Introduction

Soil moisture is a key parameter in hydrological modeling, and surface roughness plays an important role in determining how a real object will interact with its environment. Synthetic Aperture RADAR (SAR), with its longer wavelength compared with the optical sensors, has the potential to retrieve surface parameters due to its increased penetration into the vegetation canopy and sensitivity to the soil dielectric constant and surface roughness (Woodhouse, 2006). Fully polarimetric SAR (PolSAR) has four polarization compositions and offers more observations than a single polarization SAR, which can assist in investigating the scattering mechanism in agricultural fields and in developing more robust methods for surface parameter retrieval (Cloude, 2010). Algorithms using PolSAR to retrieve surface parameters are primarily divided into two categories, depending on whether they are applied to bare soil or fields under vegetation cover.

To retrieve surface parameters of bare soil, the co-polarization ratio reaches saturation when soil surface roughness value is high, thus simplifying soil moisture estimation (Oh et al., 1992; Oh, 2004). Similarly, the depolarization ratio has been found very sensitive to soil surface roughness (Ulaby et al., 1981). Sensitivity analyses of these ratios with respect to the soil (roughness and moisture) and sensor (frequency, incidence angle and polarization) have led to the development of the well-known semi-empirical backscattering models for bare soil (Oh et al., 1992; Dubois et al., 1995). Although these semi-empirical scattering models relate the backscattering coefficients to the soil moisture contents, it is difficult to use these relationships for radar signal inversion without the time-consuming calibration measurements (Park et al., 2009). The physical

---

* 2016. IEEE. Reprinted, with permission, from "Huang, Xiaodong, Wang, Jinfei, and Shang, Jiali (2016). An Integrated Surface Parameter Inversion Scheme over Agricultural Fields at Early Growing Stages by Means of C-Band Polarimetric RADARSAT-2 Imagery, *IEEE Transactions on Geoscience and Remote Sensing*, *54*(5), 2510-2528."

models derived from the electromagnetic scattering theory can overcome this issue. The simplest method used to determine the soil scattering concentrates on the reflection, which is directly solved as the Fresnel reflection coefficient (Jin & Xu, 2013). However, in natural environments, most surfaces are random rough surfaces. Taking into account the surface roughness, the small-perturbation method (SPM) (Rice, 1963) is valid only when the roughness is very small compared with the sensor wavelength. To deal with soil conditions with high roughness, Hajnsek et al. (2003) developed a X-Bragg surface scattering model based on the SPM, but the low inversion rate is still a problem. The integral equation method (IEM) proposed by Fung et al. (1992), which takes into account the scattering caused by rapid fluctuations, can meet the demands of a high frequency PolSAR system. However, it is still difficult to retrieve surface parameters because an accurate description of the surface roughness is required, but the parameterization of roughness from field measurements is known to be problematic (Verhoest et al., 2008). The retention of crop residue on the ground to reduce soil erosion and maintain soil health is a common practice, and this consequently increases the fluctuated scattering in agricultural fields, which can also make the surface parameter retrieval difficult for both the physical and semi-empirical models for soils without vegetation cover (McNairn et al., 2002; McNairn et al., 2012).

In terms of the surface parameter inversion for soils under vegetation cover, the model-based polarimetric target decomposition first proposed by Freeman and Durden (1998) separates the backscattering from different layers in agricultural fields. Due to its simplicity, many decomposition methods have been developed based on its framework (Yamaguchi et al., 2005; Yamaguchi et al., 2006; Yajima et al., 2008; An et al., 2010; Yamaguchi et al., 2011; An et al., 2011; Sato et al., 2012; Chen et al., 2014; Chen et al., 2014) and have been widely employed for surface parameter inversion under vegetation cover. Hajnsek et al. (2009) investigated the potential of surface parameter inversion under vegetation cover by comparing different model-based decompositions, showing that these methods had not only low inversion rate but also the problem of severe underestimation. Jagdhuber et al. (2013) investigated the multi-angular polarimetric decomposition to estimate soil moisture with high inversion rate and low RMSE for fully

polarimetric L-band SAR data. Ballester-Berman et al. (2013) presented a two-component polarimetric decomposition model for sparse vineyards using C-Band RADARSAT-2 data, but no measured ground truth data were used for validation. More recently, a hybrid decomposition method combining both the model-based and eigen-based decompositions has been presented by Jagdhuber et al. (2014) and showed a very high inversion rate for L-band data. Ponnurangam et al. (2014) compared various polarimetric parameters for soil moisture inversion and revealing the potential of the X-Bragg model for surface parameter retrieval. However, the surface scattering adopted in the above methods is either the Bragg or X-Bragg model, which has a critical problem in that, as the soil moisture increases, the inversion becomes more difficult, especially when the incidence angle is low. In addition, the volume scattering models from the vegetation adopted by the above mentioned methods are restricted to forest areas, but agricultural fields, especially row crops, have a certain orientation (Lopez-Sanchez et al., 2012).

In response, an integrated retrieval scheme is developed in this chapter to estimate surface parameters based on the H-α zones in agricultural fields, including bare soils, fields with low vegetation cover, and fields with crop residues. The H and α parameters are first analyzed to investigate the scattering in agricultural fields in various growing stages. A calibrated IEM is employed to describe bare soils in the low entropy and low polarization angle zones. An adaptive two-component decomposition considering the surface scattering from soil and scattering from crop residue or vegetation canopy is proposed, in which the surface scattering is modeled by the calibrated IEM, whereas the simplified adaptive volume scattering model (SAVSM) with a wide range of randomness is adopted to describe the scattering from crop residue and vegetation cover in the high entropy zones. The organization of this chapter is as follows: the study area and ground truth measurement are described in section 4.2, the analysis of the H-α parameters in different agricultural fields is discussed in section 4.3, the ISPIS is presented in section 4.4, the results and validation are analyzed in section 4.5, and the conclusion is given in section 4.6.

4.2 Study Areas and Data Collection

4.2.1 Data Collection

Two study areas selected for analysis and validation in this chapter are located in the southwest of Ontario, Canada, which are shown as red and blue points in the upper left corner of Figure 4-1. We named these two different study areas as study area 2013 and study area 2014 for convenience, as the ground truth data collected in these two study areas were in 2013 and 2014 respectively. There are three major crops growing in both study areas: soybean, corn and winter wheat. For study area 2013, only two wheat fields that are shown in the Pauli image in the upper right corner of Figure 4-1 are selected, in which 13 sample sites were surveyed on April 29th and18 sample sites were surveyed on May 9th in 2013. For study area 2014, five fields were selected including two corn fields, two soybean fields, and one wheat field, with their polygons displayed in the lower left of Figure 4-1. Their distributions are shown in the Pauli image on the right side of Figure 4-1. A total of 37 sample sites were surveyed for all fields, including 17 points from the corn fields, 16 points from the soybean fields, and 4 points from the wheat field. The distribution of the sample points of each field in the polygons is shown in the lower left of Figure 4-1. Each site is labeled as the capital letter of the first letter of the crop name, plus the field number, plus a hyphen, and plus the sample site number. Take C1-08, for example, it represents the eighth sample site in the first corn field. The RADARSAT-2 data was acquired from the beginning of May to the end of June in 2014 and on April 29th and May 9th in 2013, while the fieldwork was performed simultaneously when RADARSAT-2 was over passing. The fieldwork schedule and the image acquisition dates are shown in Table 4-1.

Table 4-1. RADARSAT-2 dataset and fieldwork schedule. The blue cell represents the data acquired on that day while grey cell means no fieldwork or dataset acquired on that day. MV: soil moisture. KS: surface roughness. The resolution (unit: m) is the one after geo-correction using the Mapready software.

	FIELD WORK						**RADARSAT-2 DATASET**			
	Corn		**Soybean**		**Wheat**					
Date	***MV***	***KS***	***MV***	***KS***	***MV***	***KS***	***Mode***	***Orbit***	***Look direction***	***Resolution***
2014-05-04							FQ15-35°	Ascending	Right	5
2014-05-05							FQ19-39°	Descending	Right	5
2014-05-15							FQ09-29°	Descending	Right	5
2014-05-18							FQ05-24°	Ascending	Right	10
2014-06-04										
2014-06-11							FQ05-24°	Ascending	Right	10
2014-06-21							FQ15-35°	Ascending	Right	5
2013-04-29							FQ09-29°	Ascending	Right	10
2013-05-09							FQ19-39°	Ascending	Right	10

The soil moisture measurements were collected on April 29th and May 9th in the study area 2013 in the low and sparse wheat covered fields that are shown in Figure 4-1. For study area 2014, the soil moisture was collected on five days: May 4th, May 5th, May 18th, June 4th and June 21st, whereas the surface roughness was collected on May 5th, May 18th and June 4th in the soybean and corn fields. The soil moisture was not collected in the wheat field on June 21st because the wheat was already very high and dense with high biomass by then; the penetration of the short wavelength C-Band RADARSAT-2 sensor is limited when the agricultural field is under the dense wheat canopy cover due to the strong attenuation effects (Lopez-Sanchez & Ballester-Berman, 2009). For the same reason, the surface roughness was not measured in the wheat field on June 21st either. Although fieldwork was conducted on June 4th, no RADARSAT-2 data was available on this date. The associated ground truth photos are shown in Figure 4-2. It can be seen that at the beginning of May 2014, the soybean fields were not cultivated, with many corn residues from the previous year left on the ground; whereas the corn fields were mainly bare soils, although a few crop stalks were present. The wheat field was in the tillering stage with very low height, and there were still a lot of crop residues present, as can be seen in Figure 4-2(c). In mid-May, many crop residues in the soybean had been flattened

due to human activities. At the end of May, both the soybean and corn fields were under seedbed preparation. At the beginning of June, the corn had emerged and at early vegetative growth stage with very low vegetation cover fraction, whereas the wheat is growing taller and denser, as shown in Figure 4-2(c). Till the end of June, the corn continues to grow taller, and the soybean was budding in low height, as shown in Figure 4-2(a) and Figure 4-2(b).

4.2.2 Ground Truth Measurement

For ground truth measurements, soil moisture and surface roughness were measured in these fields during the early growing stages. Soil moisture was measured using the TDR (Time-Domain Reflectometry) Probe for all the sample sites, with an average of 6 points measured at each sample site within a 10 m by 10 m area surrounding the centroid of the sample site. The surface roughness was measured for only half of the sample sites in the corn and soybean fields using a one-meter long profiler with 200 pins and an interval of 0.5 cm. For the corn field, because it had been ploughed before May, there were many large clods in the field, and rain events made the clots smooth without obvious oriented roughness patterns. Hence, the surface roughness measurement was randomly taken 6 times from the relatively smooth and rough surfaces within a 10 m by 10 m square surrounding the centroid of the sample site, and their average is taken as the value of the roughness for that site. For the soybean field, the roughness was measured in the same way with disregard for corn residue.

For the fields covered with standing corn stubbles or vegetation, the height of the stubble or vegetation were also measured simultaneously. The ranges of the soil moisture measurements, the root mean square (RMS) of surface height and the height of vegetation or corn stubble at the early growing stage are listed in Table 4-2. The RADARSAT-2 data was pre-processed with the radiometric correction performed first to covert the data to sigma naught, i.e., the backscattering coefficient. It was then filtered using the Boxcar method with the window size of 5 by 5, and geo-corrected using the MapReady software developed by the Alaska Satellite Facility (ASF) with the resolution after geo-correction shown in Table 4-1.

Table 4-2. Measured ground truth on different dates in different agricultural fields. MV: soil moisture ([vol.] %). RMS: root mean square of the surface height (cm). H: height of vegetation or corn residue (cm). Note: "-" means no data was collected on that day. The height measured in soybean field before June 4th 2014 is the height of the standing corn stubbles.

Date	**Corn Field**			**Soybean Field**			**Wheat Field**		
	MV	***RMS***	***H***	***MV***	***RMS***	***H***	***MV***	***RMS***	***H***
2014-05-04	12-48	-	-	21-50	-	15-45	37-49	-	8-11
2014-05-05	8-45	1.5-5.3	-	15-50	1.4-4.0	15-45	15-41	-	8-11
2014-05-18	14-44	1.3-4.5	-	28-50	1.4-3.2	15-45	35-50	-	13-18
2014-06-04	11-26	1.1-2.3	5-8	15-40	1.4-2.5	-	23-33	-	20-35
2014-06-11	-	1.1-2.3	7-13	-	1.4-2.5	2-3	-	-	-
2014-06-21	5-25	-	20-26	5-35	-	5-8	-	-	-
2013-04-29	-	-	-	-	-	-	19-50	-	5-8
2013-05-09	-	-	-	-	-	-	13-34	-	10-15

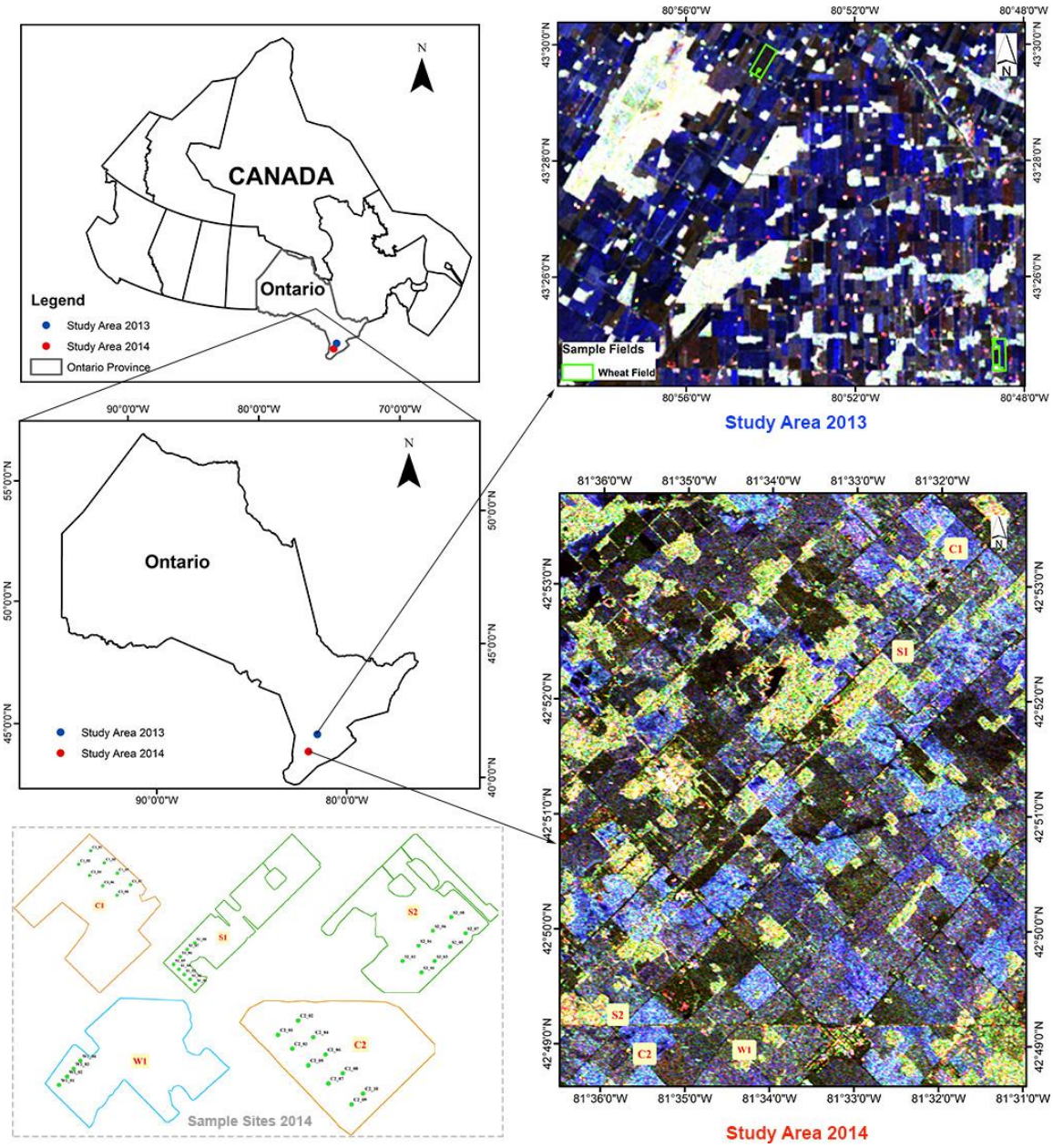

Figure 4-1. Study area locations, field polygons and Pauli images (right) from the fully polarimetric RADARSAT-2 data in 2013 and 2014. The Pauli image in 2013 is acquired on April 29th 2013 while the one at the bottom is acquired on May 5th 2014. It should be noted that only wheat fields are measured in 2013 while the soybean, corn and wheat fields are measured in 2014.

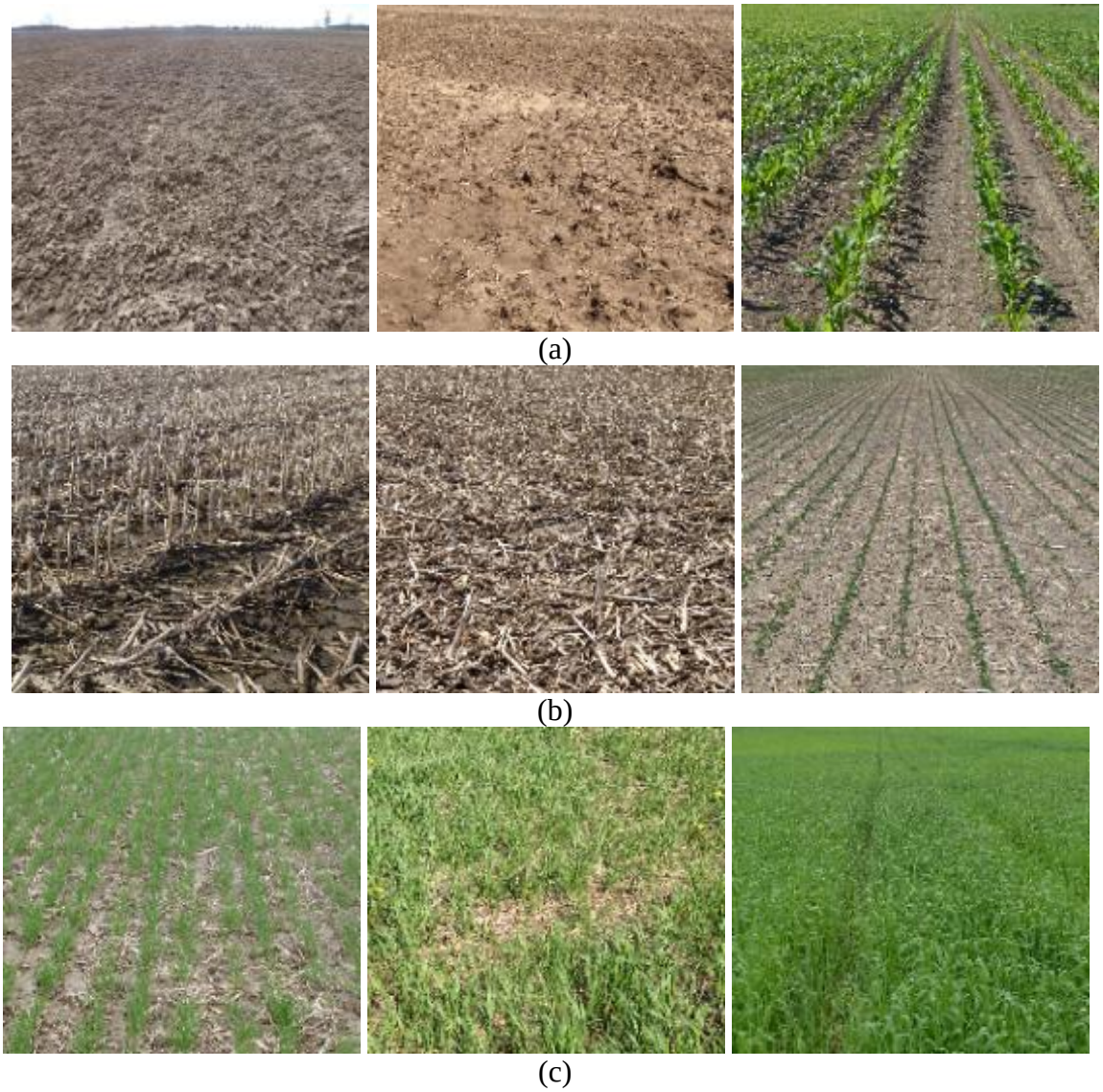

Figure 4-2. Ground truth photos in the corn, soybean and wheat fields on different dates in 2014: (a) corn fields (b) soybean fields (c) wheat fields. From left to right, the photos of the soybeans and corn were taken on May 5th, May 18th and June 21st, respectively, whereas the photos of the wheat were taken on May 5th, May 18th and June 11th.

4.3 Scattering Analysis over Agricultural Fields

4.3.1 Scattering Mechanisms Analysis

The H-α decomposition (Cloude & Pottier, 1997) is a method based on the eigen-analysis of the covariance or coherence matrix. It characterizes the backscattering in terms of two

parameters, entropy (H) and polarization angle (α), which divide the backscattering into 9 zones representing different scattering mechanisms. It is expressed as,

$$H = \sum_{i=1}^{3} -P_i log_3 P_i$$

$$P_i = \lambda_i \Big/ \sum_{j=1}^{3} \lambda_j \tag{4-1}$$

$$\bar{\alpha} = \sum_{i=1}^{3} P_i acos(e_i)$$

$$e_i = [e_{i1} \quad e_{i2} \quad e_{i3}]^T$$

where H is the entropy, $\bar{\alpha}$ is the polarization angle, λ_i is the eigenvalue, and e_i is the unit eigenvector. To analyze the scattering of these crop fields on different dates, the H-α decomposition analysis was performed on RADARSAT-2 imageries in four different sensor modes, FQ5, FQ9, FQ15 and FQ19, with the incidence angle ranging from 24 degrees to 39 degrees (Table 4-1). For presentation purposes, the S2, C2 and W1 fields in study area 2014 were selected for analysis, and their results are shown in Figure 4-3

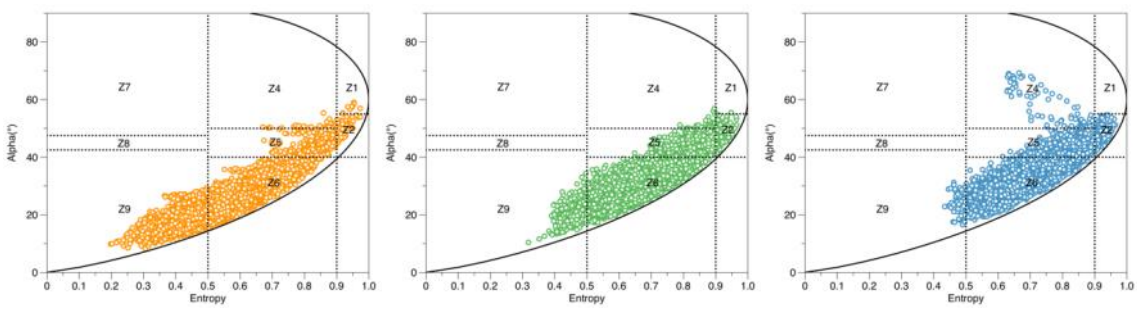

(a)

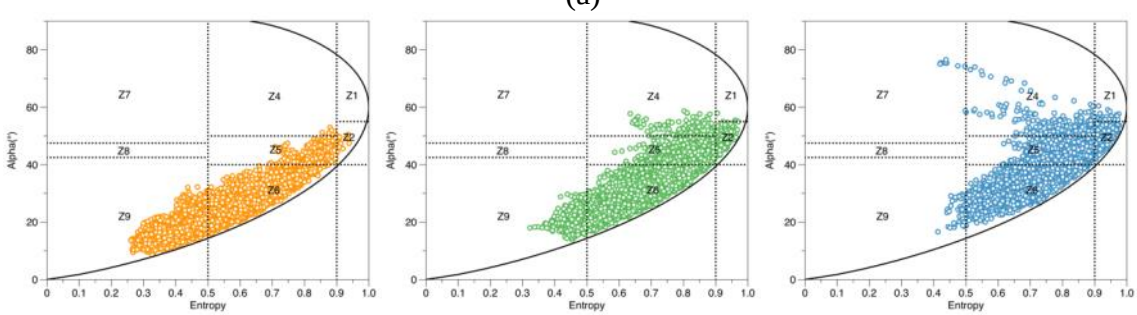

(b)

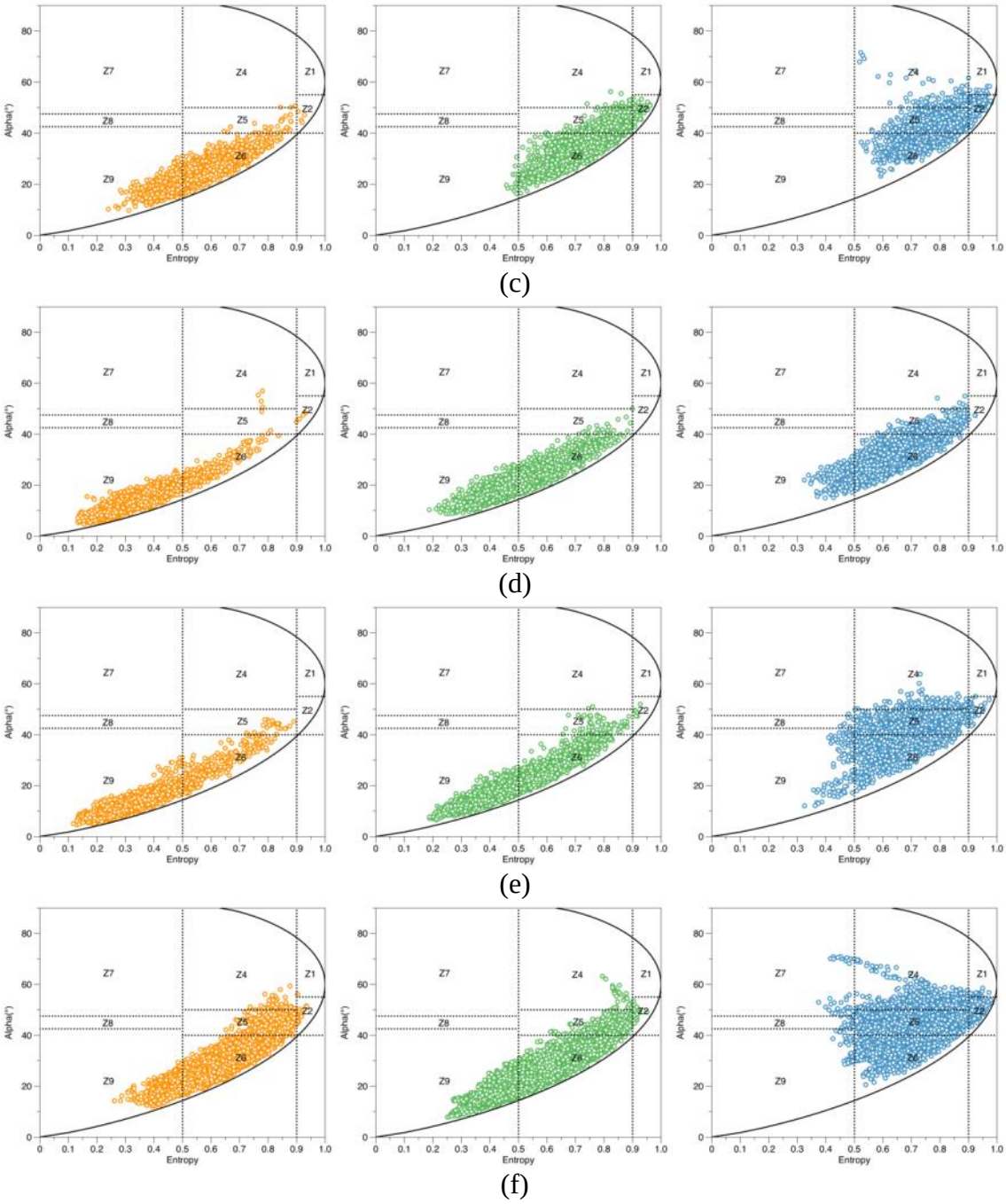

Figure 4-3. H and α plots in three fields (from left to right: corn, soybean and wheat) from May 4th to June 21st: (a) May 4th (b) May 5th (c) May 15th (d) May 18th (e) June 11th (f) June 21st.

As the corn field had been ploughed up before May, the corn fields were mainly bare soils. Hence, from May 4th to May 15th, Figure 4-3(a) through Figure 4-3(c) depict that

many pixels in the corn fields lie in Z9, which represents the dominated surface scattering with a range of entropy from 0.2 to 0.5. However, there are still many pixels in the high entropy zone from 0.6 to 0.9 that lie in Z6. This is perhaps the result of the fluctuated scattering caused by the randomly distributed stalks or the dry soil penetration effect, and more details are presented in section 4.5.6. For the soybean fields, there are many pixels in Z9 and Z5, showing the surface and volume scattering dominance. That is mainly because corn stubbles standing in these fields resulted in the fluctuation of the scattering. Hence, most of their entropy is from 0.5 to 1.0, which is higher on average than in the corn fields, where there were mainly bare soils. Figure 4-3(a) through Figure 4-3(c) depict that the wheat fields show the dominant surface and volume scatterings before June because the wheat hadn't grown very tall, with a very sparse canopy. There is a similar sensor configuration on May 4th and May 5th with a slightly different incidence angle, except that their orbits are ascending and descending, respectively. Hence, ignoring the effects of the incidence angle, the scattering difference is only observed in the soybean field, with more dipole scattering emerging on May 5th; this is mainly because the orientation angle of crop residues depends on the line of sight (LOS) of RADARSAT-2. The ascending orbit on May 4th senses little dipole scattering, but more emerges with the descending orbit on May 5th.

The entropy in the soybean and wheat fields is almost greater than 0.5 on May 15th, which is higher than that on May 5th; this is mainly due to the lower incidence angle (≈29 degrees) on May 15th, which resulted in more multiple scattering than the higher incidence angle (≈39 degrees) on May 5th. The dominant scattering of most pixels moves from high entropy fluctuated scattering to low entropy surface scattering on May 18th, as depicted in Figure 4-3(d). Theoretically, in the same agricultural area with the same radar configuration, the lower resolution RADARSAT-2 data will have higher entropy than that of the high resolution data, as the lower resolution data averages various types of scattering within a single pixel. However, the blanket fertilizer application occurred during the period from May 15th to May 18th, and the wheels of the tractor flattened many crop residues in the soybean field and made the surface roughness of the wheat and corn fields relatively smooth, resulting in a single dominant surface scattering with lower

entropy on May 18th. At the end of May, both the corn and soybean fields were under seedbed preparation; hence, on June 11th, the soybean and corn fields became smooth, and many pixels are dominated by surface scattering. Although some corn was growing, they were very small. By 21st June, the corn was growing taller, and the scattering of many pixels in the corn fields moved from surface scattering to volume scattering. Because the soybean was very short, as depicted in Figure 4-3(f), the scattering in the soybean fields is still dominated by surface scattering. It should be noted that, on 21st June, some double bounce scattering emerged from the wheat fields, which was caused by the interaction between the soil and taller wheat stalks. Overall, the scattering in agricultural fields in our study area is primarily composed of surface and volume scattering before the end of June, and the average entropy in fields with crop residues and vegetation cover is higher than that in bare soil fields.

4.3.2 Threshold Selection and the ISPIS

As both the corn and soybean fields (C2, S2) became smooth due to seedbed preparation at the end of May, four RADARSAT-2 datasets acquired on May 5th, May 15th, June 11th, and June 21st covering the periods of before and after seedbed preparation were selected to determine the threshold for distinguishing the surface and volume scatterings based on the H and α values. The W1 field was selected for analysis as well. Firstly, the normal distributions of H and the histograms of α are shown in Figure 4-4. The corresponding statistical parameters of H such as the mean and standard deviation values and the percentage of the divided surface and volume scattering components by the criteria that the H is less than 0.6 and α is less than 40 degrees are listed in Table 4-3.

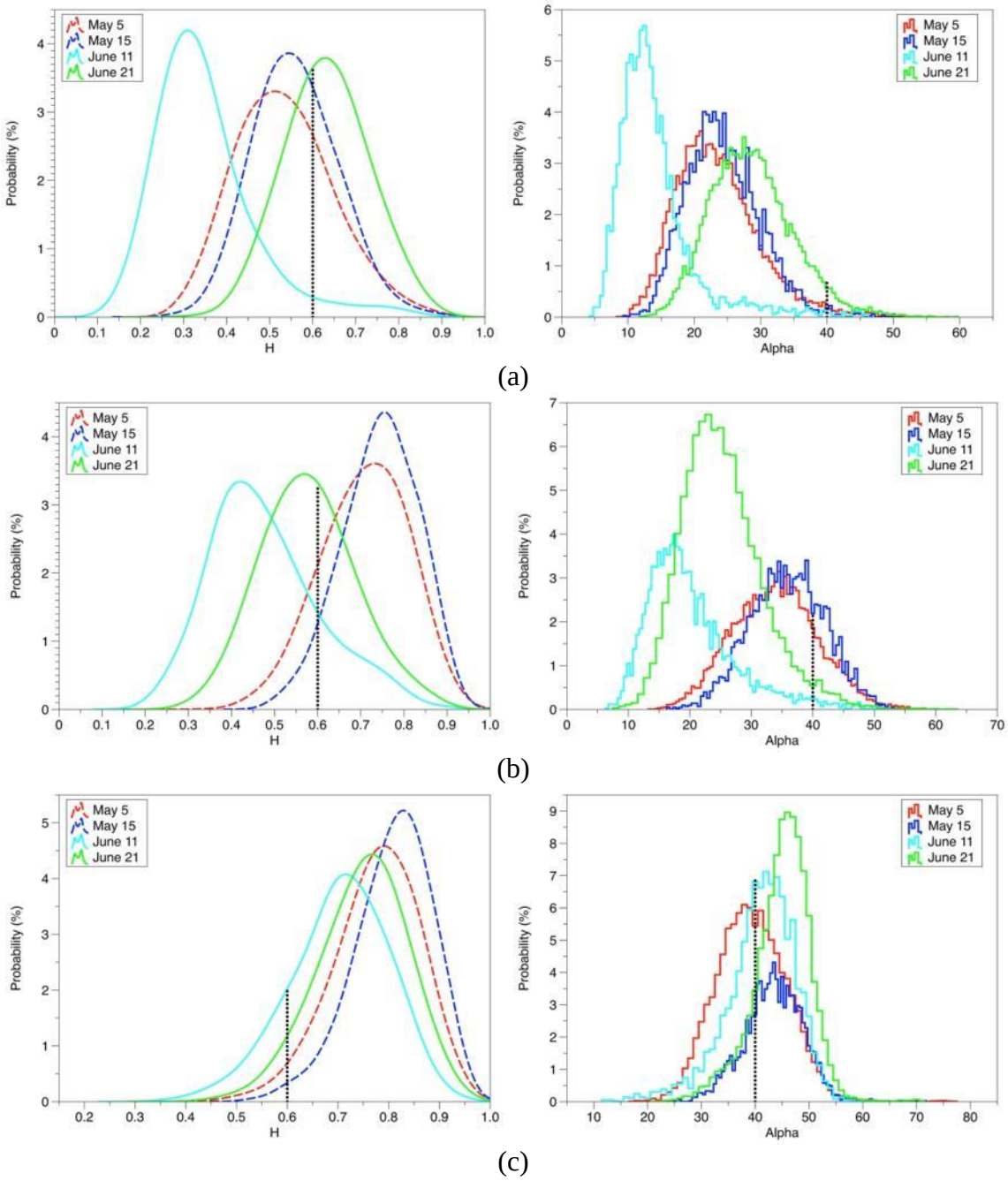

Figure 4-4. The normal distributions of H (left) and the histograms of α (right) on different dates. (a) corn field. (b) soybean field. (c) wheat field.

Table 4-3. The statistic information of the H and $\boldsymbol{\alpha}$ on different dates in different fields.

Crop Type	**Date**	**Normal Distribution Parameters of H**		**% of H**		**% of α**	
		$\boldsymbol{\mu}$	$\boldsymbol{\sigma}$	**Surface**	**Volume**	**Surface**	**Volume**
Corn Field	20140505	0.534267	0.113429	73.17	26.83	98.32	1.68
	20140515	0.559852	0.097608	67.54	32.46	98.96	1.04
	20140611	0.347310	0.116623	95.65	4.35	99.25	0.75
	20140621	0.632599	0.098117	37.68	62.32	95.46	4.54
Soybean Field	20140505	0.708732	0.100398	14.88	85.12	81.59	18.41
	20140515	0.744974	0.087116	5.78	94.22	74.18	25.82
	20140611	0.477109	0.127268	83.28	16.72	97.99	2.01
	20140621	0.577768	0.110713	59.45	40.55	97.08	2.92
Wheat Field	20140505	0.775290	0.084704	3.13	96.87	54.89	45.11
	20140515	0.808162	0.076213	1.15	98.85	24.4	75.6
	20140611	0.702328	0.097242	15.07	84.93	38.69	61.31
	20140621	0.747821	0.087515	5.80	94.20	15.17	84.83

For the bare soil fields, the majority of their pixels are dominated by surface scattering. As the crop grows over time, the volume scattering caused by the crop canopy will increase gradually. Thus, the surface scattering from the soil and the volume scattering from the vegetation canopy will be mixed together at the early growing stage when the crops are sparse, making their complete separation very difficult. In this case, we tend to classify the majority of pixels in bare soil as surface scattering because the surface and volume scattering in fields covered with crop residues or vegetation are mixed together. As the corn fields were bare on May 5th and May 15th and were covered by sparse vegetation on June 21st as shown in Figure 4-2(a), the data collected on May 5th, May 15th and June 21st are adopted for threshold determination. Figure 4-4(a) shows that the range of H from 0.55 to 0.6 can be used to distinguish the scattering in bare soil and in vegetated fields according to their normal distribution curves. However, considering surfaces with rough soils, their entropy will be greater than 0.5 as their roughness increases, and the entropy will increase to 0.6, when the scattering of bare soils is dominated by a surface cover comprised of oblate spheroidal scatterers (Cloude, 1992). Therefore, 0.6 is determined as the threshold to distinguish the bare soils from field with corn cover. In this case, Figure 4-4(a) and Table 4-3 depict that the majority of the pixels of H are occupied by surface scattering in fields of bare soils, with all of their percentages greater than 67%. For the soybean fields, the fields with corn residues on May 5th and

May 15th and the fields with bare soils on June 11th can be discriminated by the threshold of 0.57 and 0.6 respectively according to the normal distribution shown in Figure 4-4(b). Their thresholds are similar to that of the corn fields. When 0.6 is determined as the H threshold for the soybean fields with corn residues, the number of pixels on June 11th in bare soils is greater than 80%, whereas less than 15% of the pixels fall under bare soils for the fields with corn residues. In addition, the number of pixels dominated by surface scattering in the wheat fields is less than 15% because they are either influenced by the crop residues at the early growing stage or by the growing wheat canopy as time progresses. Lastly, the α threshold of less than 40 degrees is employed as the threshold to distinguish the surface scattering from the volume scattering as proposed by Cloude and Pottier (1997).

Consequently, the entropy less than 0.6 and polarization angle less than 40 degrees divide the H-α plane into two zones separating the dominating surface scattering from bare soils and volume scattering from other cases (fields with crop residues and fields under low vegetation cover) in this chapter. The ISPIS shown in Figure 4-5 is described as: bare soils (smooth and rough) are characterized by the calibrated IEM in the zone with entropy less than 0.6 and α less than 40 degrees, and the others are described by an adaptive two-component decomposition (ATCD) composed of surface and volume scatterings.

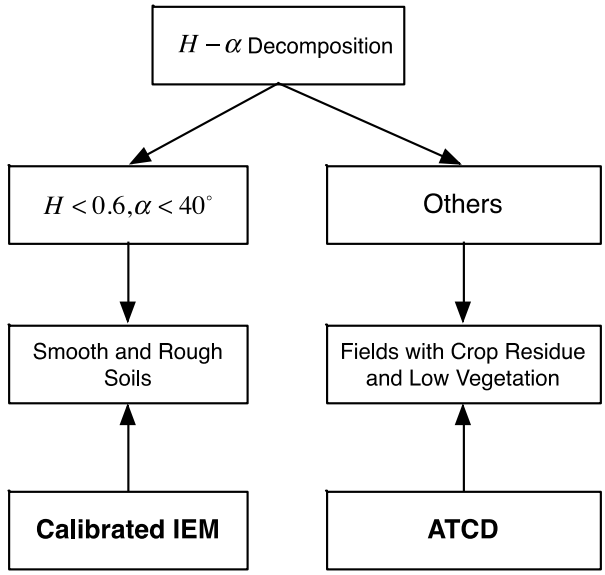

Figure 4-5. Integrated surface parameter inversion scheme (ISPIS).

4.4 Integrated Surface Parameter Inversion Scheme (ISPIS)

4.4.1 Bragg and X-Bragg Surface Scattering Models

The scattering of bare soil modeled as Bragg surface scattering (Freeman & Durden, 1998) or X-Bragg surface scattering (Hajnsek et al., 2003) derived by the SPM model with its validity condition $ks < 0.3$, where k is the wavenumber and s is the RMS of surface height, is widely used in many surface parameter retrieval schemes, and their coherency matrices have the forms,

$$T_{Bragg} = \begin{bmatrix} 1 & \beta^* & 0 \\ \beta & |\beta|^2 & 0 \\ 0 & 0 & 0 \end{bmatrix} \tag{4-2}$$

$$T_{X-Bragg} = \begin{bmatrix} 1 & \beta^* sinc(2\varphi) & 0 \\ \beta sinc(2\varphi) & \frac{1}{2}|\beta|^2\big(1+sinc(4\varphi)\big) & 0 \\ 0 & 0 & \frac{1}{2}|\beta|^2\big(1-sinc(4\varphi)\big) \end{bmatrix} \tag{4-3}$$

where φ is the surface slope, and β is equal to,

$$\beta = \frac{R_{HH} - R_{VV}}{R_{HH} + R_{VV}} \tag{4-4}$$

where R_{HH} and R_{VV} are the Bragg coefficients at horizontal and vertical polarization respectively and are shown as,

$$\begin{aligned} R_{HH} &= \frac{cos\theta - \sqrt{\varepsilon_r - sin^2\theta}}{cos\theta + \sqrt{\varepsilon_r - sin^2\theta}} \\ R_{VV} &= \frac{(\varepsilon_r - 1)(sin^2\theta - \varepsilon_r(1 + sin^2\theta))}{(\varepsilon_r cos\theta + \sqrt{\varepsilon_r - sin^2\theta})^2} \end{aligned} \tag{4-5}$$

where θ is the local incidence angle, ε_r is the relative dielectric constant, which is related to the soil moisture content. The relationship between ε_r and β for different local incidence angles is depicted in Figure 4-6.

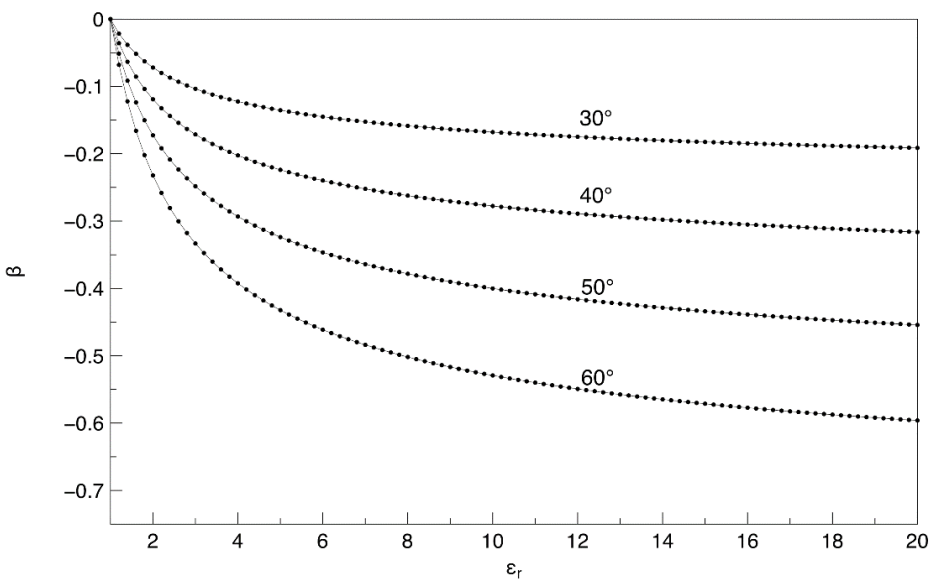

Figure 4-6. Relationship between $\boldsymbol{\varepsilon_r}$ and $\boldsymbol{\beta}$.

Figure 4-6 depicts that β is real and is greater than -1 and less than 0. It also shows that, when the incidence angle is very low, even a small variation of β will result in a large fluctuation of ε_r. This means that both the Bragg and X-Bragg surface scattering models are restricted to high incidence angles. Because the ε_r has a positive relation with volumetric soil moisture, hence, when the soil moisture becomes high, the variation of the derived β is very small as the incidence angle decreases. That means the β derived by the Bragg or X-Bragg model should be very accurate in order to obtain a high accuracy soil moisture map.

4.4.2 Calibrated Integral Equation Model

Bare soils with rough condition of $ks < 3.0$ can be described using the physical integrated equation model (IEM) (Fung et al., 1992), where k is the wavenumber equal to$\frac{2\pi}{\lambda}$. For C-band RADARSAT-2, it is approximately 1.11. s is the root mean square (RMS) of surface height. Its general form of the backscattering coefficients for vertical and horizontal polarization σ_{pp}^0 is described as,

$$\sigma_{pp}^0 = \frac{k^2}{4\pi} exp[-2k^2\sigma^2 cos^2\theta] \sum_{n=1}^{\infty} \left|I_{pp}^n\right|^2 \frac{w^{(n)}(2ksin\theta, 0)}{n!} \tag{4-6}$$

where

$$I_{pp}^n = (2k\sigma cos\theta)^n f_{pp} exp[-k^2\sigma^2 cos^2\theta] + (k\sigma cos\theta)^n F_{pp}, p = v, h$$

$$f_{vv} = \frac{2R_v}{cos\theta}, f_{hh} = \frac{-2R_h}{cos\theta}$$

$$R_h = \frac{\mu_r cos\theta - \sqrt{\mu_r\varepsilon_r - sin^2\theta}}{\mu_r cos\theta + \sqrt{\mu_r\varepsilon_r - sin^2\theta}}, R_v = \frac{\varepsilon_r cos\theta - \sqrt{\mu_r\varepsilon_r - sin^2\theta}}{\varepsilon_r cos\theta + \sqrt{\mu_r\varepsilon_r - sin^2\theta}}$$

$$F_{vv} = \left(\frac{sin^2\theta}{cos\theta} - \frac{sq}{\varepsilon_r}\right) T_v^2 - 2sin^2\theta \left(\frac{1}{cos\theta} + \frac{1}{sq}\right) T_v T_{vm} + \left(\frac{sin^2\theta}{cos\theta} + \frac{\varepsilon_r(1 + sin^2\theta)}{sq}\right) T_{vm}^2$$

$$F_{hh} = -\left[\left(\frac{sin^2\theta}{cos\theta} - \frac{sq}{\mu_r}\right)T_h^2 - 2sin^2\theta\left(\frac{1}{cos\theta} + \frac{1}{sq}\right)T_h T_{hm} + \left(\frac{sin^2\theta}{cos\theta} + \frac{\mu_r(1+sin^2\theta)}{sq}\right)T_{hm}^2\right]$$

$$T_p = 1 + R_p, T_{pm} = 1 - R_p, sq = \sqrt{\mu_r\varepsilon_r - sin^2\theta}$$

where R_p is the p-polarized Fresnel reflection coefficient; and the quantity $w^{(n)}$ is the surface spectrum corresponding to the two-dimensional Fourier transform of the surface auto-correlation coefficient (ACF) $\rho(x,y)$ raised to its nth power, $\rho^n(x,y)$, defined as,

$$w^{(n)}(u,v) = \int_{-\infty}^{\infty}\int_{-\infty}^{\infty}\rho^n(x,y)\, e^{-j2\pi(ux+vy)}dxdy \tag{4-7}$$

Although many ACFs, such as Gaussian, Exponential, Fractal, etc., have been proposed to describe the surface coefficient, the exponential function has been demonstrated to characterize the agricultural fields better than others (Shi et al., 1997; Wegmüller et al., 1994). The exponential function is described as,

$$\rho(x,y) = e^{-\frac{|x|+|y|}{L}} \tag{4-8}$$

where L is the correlation length. However, the parameterization of roughness from field measurements is known to be problematic (Verhoest et al., 2008); hence, Baghdadi et al. (2002; 2004; 2006) developed many empirical models that relate the RMS of surface height to the correlation length. The relationship for C-band RADARSAT-2 developed by Baghdadi et al. (2006) is adopted in this chapter and is described as,

$$Lopt2(rms,\theta,pp) = \delta(sin\theta)^{\mu}rms^{(\eta\theta+\xi)} \tag{4-9}$$

where θ is the incidence angle, and rms is the root mean square of the surface height. The parameters δ and ξ are dependent of the polarization, whereas parameters μ and η are found to be independent of the polarization.

$$\delta_{hh} = 4.026, \xi_{hh} = 1.551, \delta_{vv} = 4.026$$

$$\xi_{vv} = 1.222, \mu_{hh} = \mu_{vv} = -1.744, \eta_{hh} = \eta_{vv} = -0.0025.$$

The calibrated correlation length is substituted into the IEM model, and the relationship between the volumetric soil moisture and the relative dielectric constant developed by Halikainen et al. (1985) is adopted. The calibrated IEM (CIEM) describing the backscattering coefficients with rms and mv is shown in Figure 4-7. The advantage of the CIEM is that the correlation length dimension is taken off and the unknown parameters are reduced from 3 to 2, which can simplify the equation solving via the co-polarizations alone.

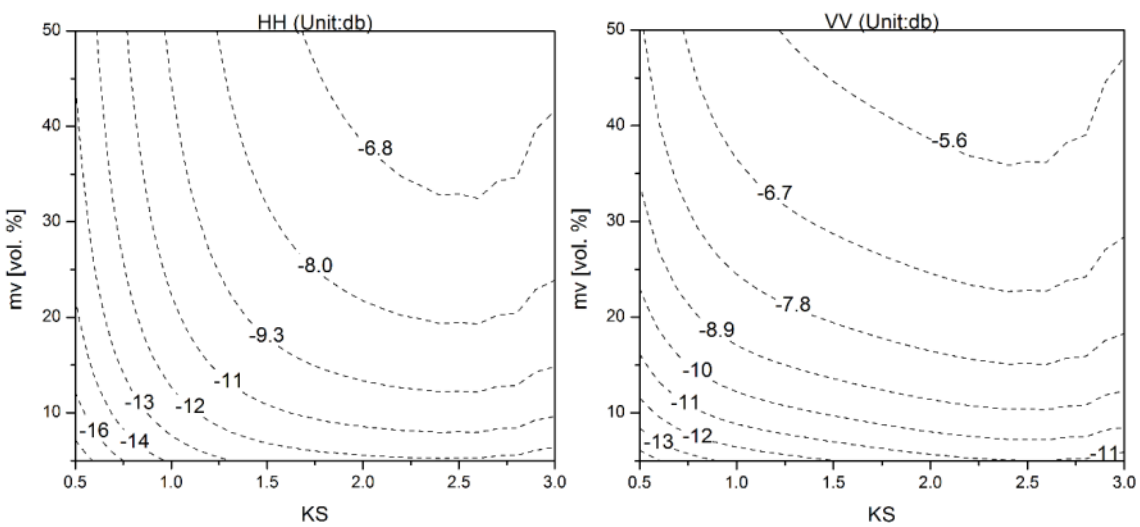

(a) (b)

Figure 4-7. Calibrated IEM model with exponential ACF in a 40-degree incidence angle. (a) HH backscattering coefficient (b) VV backscattering coefficient.

4.4.3 Simplified Adaptive Volume Scattering Model (SAVSM)

Because both crop residues and vegetation canopies can cause an increase in the cross-polarization, we treat the scattering from both of them as volume scattering in this

chapter. To model the volume scattering, Freeman and Durden (1997) argued that the distribution of the orientation angles of vegetation satisfied the uniform distribution, whereas Yamaguchi et al. (2005) added the vertical and horizontal dipoles volume scattering based on the first order sine function. Arii et al. (2010) proposed a generalized volume scattering model to describe the canopy scattering based on a cosine-squared distribution raised to the nth power for the vegetation orientation angles, demonstrating that C-band senses a mean orientation closer to the vertical direction. Huang and Wang (2014) simplified this model to be the nth power to the first order sine function to allow it to adapt to the variations of crops for RADARSAT-2 imagery because the C-band senses the vegetation in vertical orientations (Arii et al., 2010). The vertical orientation distribution function is shown in (4-10).

$$p_v(\theta) = \frac{(Sin\theta)^n}{\int_0^{\pi}(Sin\theta)^n d\theta} \tag{4-10}$$

This volume scattering model is restricted to characterize the vertical volume scattering, but the disordered orientations of crop residues may also result in horizontal volume scattering. To enhance its suitability further, we added the nth power cosine function to describe the horizontal volume scattering. The horizontal orientation distribution function is expressed as,

$$p_h(\theta) = \frac{(Cos\theta)^n}{\int_{-\frac{\pi}{2}}^{\frac{\pi}{2}}(Cos\theta)^n d\theta} \tag{4-11}$$

For both distribution functions, when $\mathrm{n} = 0$, $\mathrm{p_h}(\theta) = \mathrm{p_v}(\theta) = \frac{1}{\pi}$ is the function uniform distribution, which is the same as Freeman and Durden (1997). When $\mathrm{n} = 1$, their distributions are the same as those by Yamaguchi et al. (2005). When $\mathrm{n} = 1 \cdots \mathrm{k}$, $\mathrm{p}(\theta)$ becomes narrower as n increases. When $\mathrm{n} \to \infty$, $\mathrm{p_v}(\theta) = \delta(\theta - \frac{\pi}{2})$ and $\mathrm{p_h}(\theta) = \delta(\theta)$ are the Dirac functions representing the pure vertical and horizontal dipoles respectively. The same as the Yamaguchi et al. (2006), after integration, elements of the vertical (V-SAVSM) and horizontal (H-SAVSM) simplified adaptive volume scattering models are described as,

V-SAVSM:

$$\mathrm{C}_v11 = \frac{1}{A}\cdot\frac{3\sqrt{\pi}\Gamma\left(\frac{n+1}{2}\right)}{4\Gamma\left(\frac{n}{2}+3\right)}$$

$$\mathrm{C}_v12 = \mathrm{C}_v21 = \mathrm{C}_v23 = \mathrm{C}_v32 = 0, \mathrm{C}_v22 = \frac{1}{A}\cdot\frac{\sqrt{\pi}\Gamma\left(\frac{n+3}{2}\right)}{\Gamma\left(\frac{n}{2}+3\right)} \tag{4-12}$$

$$\mathrm{C}_v13 = \mathrm{C}_v31 = \frac{1}{A}\cdot\frac{\sqrt{\pi}\Gamma\left(\frac{n+3}{2}\right)}{2\Gamma\left(\frac{n}{2}+3\right)}, \mathrm{C}_v33 = \frac{1}{A}\cdot\frac{\sqrt{\pi}\Gamma\left(\frac{n+5}{2}\right)}{\Gamma\left(\frac{n}{2}+3\right)}$$

H-SAVSM：

$$\mathrm{C}_v11 = \frac{1}{A}\cdot\frac{\sqrt{\pi}\Gamma\left(\frac{n+5}{2}\right)}{\Gamma\left(\frac{n}{2}+3\right)}$$

$$\mathrm{C}_v12 = \mathrm{C}_v21 = \mathrm{C}_v23 = \mathrm{C}_v32 = 0, \mathrm{C}_v22 = \frac{1}{A}\cdot\frac{\sqrt{\pi}\Gamma\left(\frac{n+3}{2}\right)}{\Gamma\left(\frac{n}{2}+3\right)} \tag{4-13}$$

$$\mathrm{C}_v13 = \mathrm{C}_v31 = \frac{1}{A}\cdot\frac{\sqrt{\pi}\Gamma\left(\frac{n+3}{2}\right)}{2\Gamma\left(\frac{n}{2}+3\right)}, \mathrm{C}_v33 =\cdot\frac{3\sqrt{\pi}\Gamma\left(\frac{n+1}{2}\right)}{4\Gamma\left(\frac{n}{2}+3\right)}$$

where $A = \int_0^{\pi}(Sin\theta)^n d\theta = \int_{-\frac{\pi}{2}}^{\frac{\pi}{2}}(Cos\theta)^n d\theta = \frac{\sqrt{\pi}\Gamma\left(\frac{n+1}{2}\right)}{\Gamma\left(\frac{n}{2}+1\right)}$ and $\Gamma(a) = \int_0^{\infty} e^{-t}t^{a-1}d\mathrm{t}$. It should be noted that n is greater than 0 but not limited to integers. We can see that the HH component of the V-SAVSM is equal to the VV component of the H-AVMS, and *vice versa*. It should also be noted that we refer the V-SAVSM and H-SAVSM combined as SAVSM in the chapter. Without loss of generality, the V-SAVSM is analyzed alone in this section. The components of the V-SAVSM are plotted in Figure 4-8. Figure 4-8(a) reveals that, as n increases, the HH component decreases, whereas the VV component

increases. At the same time, the HH-VV components increase first then decrease at the point where $n = 1$. To analyze it further, the radar vegetation index (RVI) proposed by Kim and van Zyl (2001) as an indicator of scattering by vegetation can be described as,

$$RVI = \frac{4min(\lambda_1, \lambda_2, \lambda_3)}{\lambda_1 + \lambda_2 + \lambda_3} = \frac{8\sigma_{HV}}{\sigma_{HH} + 2\sigma_{HV} + \sigma_{VV}} \tag{4-14}$$

where λ_1, λ_2 and λ_3 are the eigenvalues of SAVSM, whereas σ_{HH}, σ_{VV} and σ_{HV} are the horizontal, vertical and cross polarizations, respectively. The RVI generally ranges between 0 and 1, and it is near zero for a smooth bare surface and increases as crop grows (Kim et al., 2014). It has been found that there is a high correlation between the RVI and vegetation water content (Kim et al., 2012), and it has low sensitivity to environmental condition effects (Kim & van Zyl, 2009). The RVI is in fact the ratio between the cross-polarization and total power, as shown in equation (4-14), but crop residues can also result in an increase in the cross-polarization. Therefore, theoretically, the crop residue, in addition to the vegetation canopy, can also be described by the RVI. The RVI and the scattering entropy of V-SAVSM are both depicted in Figure 4-8(b). Both entropy and RVI decrease as n increases. However, RVI has a steeper decreasing curve than entropy does. Considering this, we can use the curve of RVI to limit the range of n, thereby accelerating the discovery of the optimum n in practice. Because the entropy adopted in this chapter to separate bare soils and others is 0.6, the corresponding n is approximately 4.5. Hence, the maximum n adopted in this chapter is 5. In addition, we select some n to compare with other volume scattering models proposed by Yamaguchi et al. (2005), which are listed in Table 4-4. We can see that the SAVSM not only includes the volume scattering model developed by Freeman and Durden (1997) and Yamaguchi et al. (2005) but also continues to respond to n. From this view, it has a better potential to describe changes in crops with time than Freeman and Durden (1997) and Yamaguchi et al. (2005).

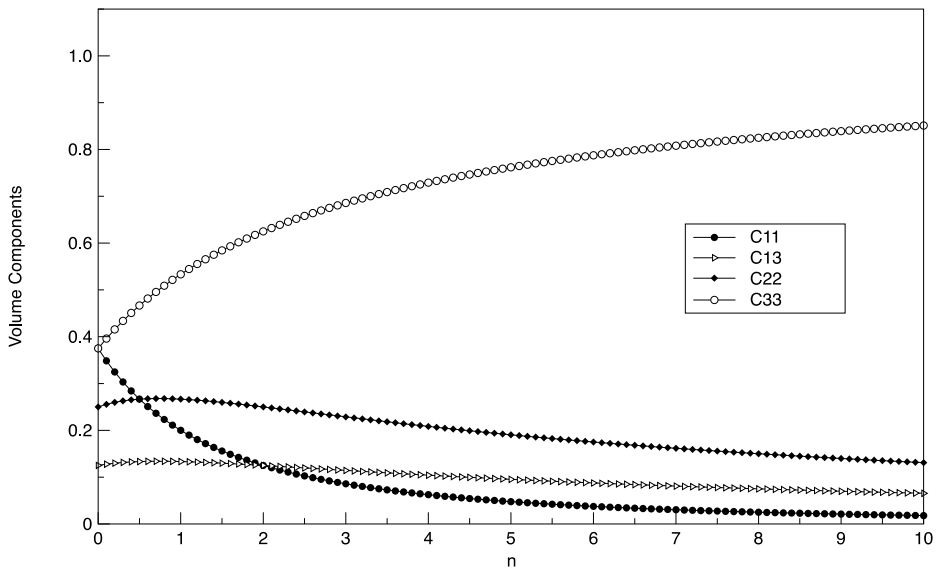

(a)

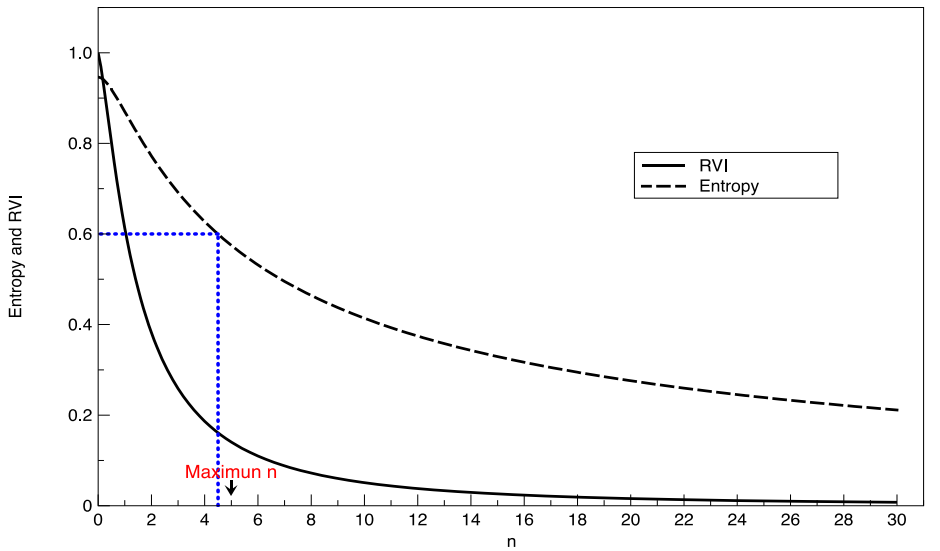

(b)

Figure 4-8. V-SAVSM: (a) Elements of the V-SAVSM covariance matrix (b) Entropy and RVI.

Table 4-4. Comparison of the SAVSM with the Freeman and Yamaguchi volume scattering models in terms of their RVI and entropy.

n	V-SAVSM	H-SAVSM	RVI	Entropy	Reference
0	$\begin{bmatrix} 0.375 & 0 & 0.12 \\ 0 & 0.250 & 0 \\ 0.125 & 0 & 0.37 \end{bmatrix}$	$\begin{bmatrix} 0.375 & 0 & 0.125 \\ 0 & 0.250 & 0 \\ 0.125 & 0 & 0.375 \end{bmatrix}$	1.00	0.95	Freeman and Durden (1997); Yamaguchi et al. (2005).
1	$\begin{bmatrix} 0.200 & 0 & 0.13 \\ 0 & 0.267 & 0 \\ 0.133 & 0 & 0.53 \end{bmatrix}$	$\begin{bmatrix} 0.533 & 0 & 0.133 \\ 0 & 0.267 & 0 \\ 0.133 & 0 & 0.200 \end{bmatrix}$	0.61	0.87	Yamaguchi et al. (2005).

4.4.4 Adaptive Two-Component Decomposition

The analysis from section 4.3 has demonstrated that the scattering from fields under vegetation cover or fields with crop residue is primarily composed of surface and volume scattering. Therefore, the scattering from the fields under vegetation cover or fields with crop residue can be modeled as the incoherent summation of the surface scattering from soil and volume scattering from vegetation cover. The adaptive two-component decomposition proposed in this chapter to describe the scattering in fields with crop residues and fields under vegetation cover is expressed as,

$$\sigma^0 = f_S \sigma_S^0 + f_V \sigma_V^0 \tag{4-15}$$

where f_S and f_V are the coefficients of surface and volume scattering, whereas σ_S^0 and σ_V^0 are the backscattering coefficients of the surface and volume scattering. The scattering from soil is described by the CIEM, whereas the scattering from vegetation cover is described by the SAVSM. Because two volume scattering models are developed in this chapter, either the H-SAVSM or the V-SAVSM is chosen depending on the criterion developed by Yamaguchi et al. (2005). In addition, because the SAVSM depends on n and RVI can be an index to describe the randomness of scattering, the optimum n is selected when it can minimize the difference between the RVI derived by the covariance matrix (RVI_C) and by the SAVSM (RVI_V). The Non-Negative Eigenvalue Decomposition (NNED) (van Zyl et al., 2011) that satisfies the energy conservation law is adopted to

calculate the scattering coefficient of volume scattering. Finally, the surface scattering is obtained by the subtraction of volume scattering. Alternatively, to accelerate inverting the soil moisture and RMS of the height using the CIEM, the look-up table (LUT) method is adopted, and the surface parameters are selected depending on which can minimize the cost function Δ representing the least square difference between the measured σ^0_{Mpp} and the simulated σ^0_{Spp} backscatter coefficients of the form,

$$\Delta = \sqrt{(\sigma^0_{Mhh} - \sigma^0_{Shh})^2 + (\sigma^0_{Mvv} - \sigma^0_{Svv})^2} \tag{4-16}$$

The flowchart of the ATCD algorithm that describes the scattering mechanism in fields with crop residue and fields under vegetation cover is described in Figure 4-9.

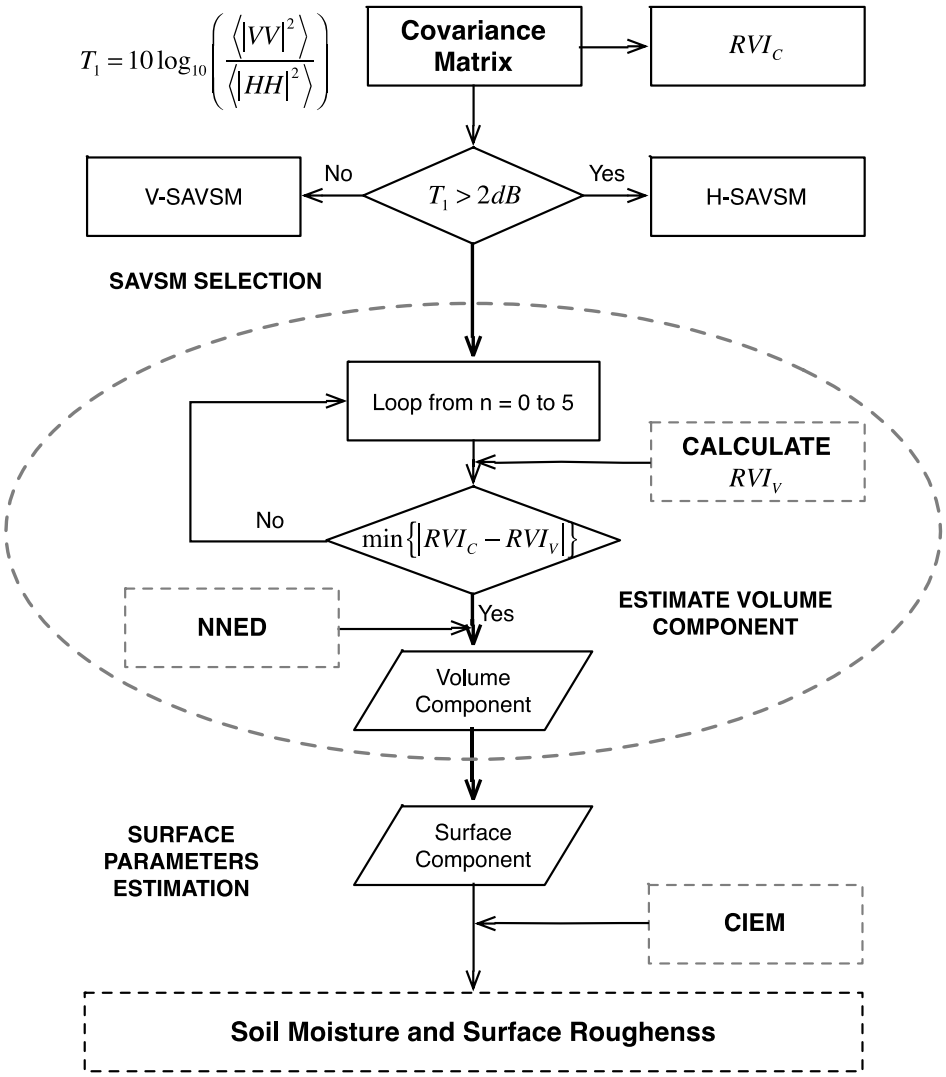

Figure 4-9. Flowchart of the ATCD algorithm.

4.5 Validation and Analysis

4.5.1 T_1 Maps of Different Crop Fields

To show the variation of T_1, i.e., $10log_{10}(|VV|^2/|HH|^2)$, in different crop fields at different growing stages, some T_1 maps of different crops at different stages shown in Figure 4-10 in study area 2014 are selected for discussion in this section.

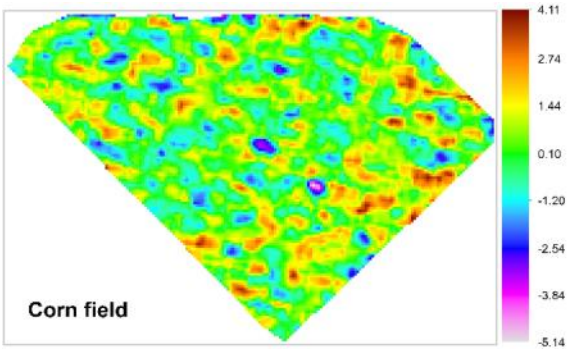
Corn field
4.11
2.74
1.44
0.10
-1.20
-2.54
-3.84
-5.14

(a)

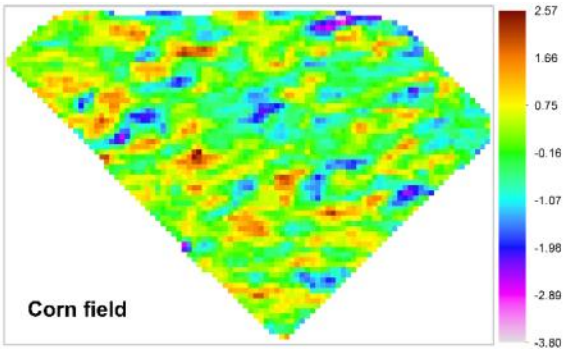
Corn field
2.57
1.66
0.75
-0.16
-1.07
-1.98
-2.89
-3.80

(b)

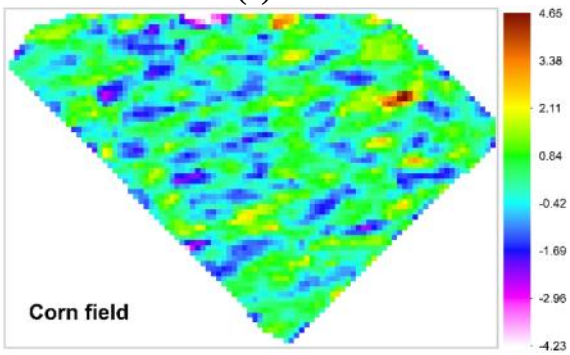
Corn field
4.65
3.38
2.11
0.84
-0.42
-1.69
-2.96
-4.23

(c)

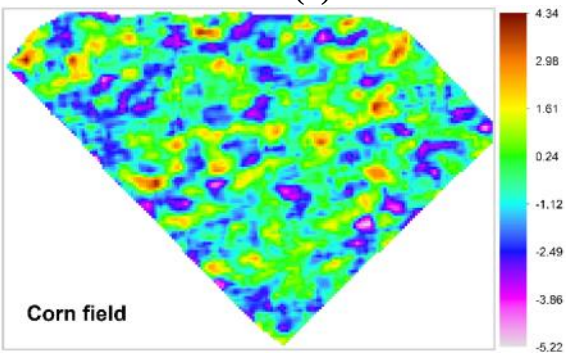
Corn field
4.34
2.98
1.61
0.24
-1.12
-2.49
-3.86
-5.22

(d)

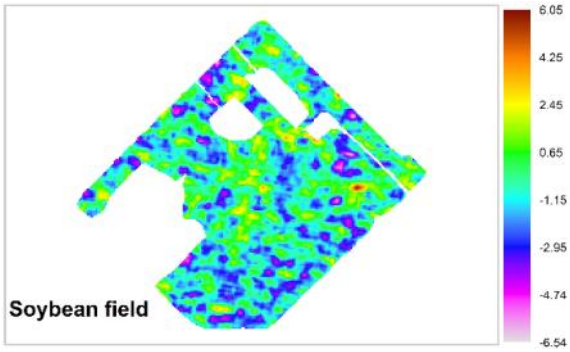
Soybean field
6.05
4.25
2.45
0.65
-1.15
-2.95
-4.74
-6.54

(e)

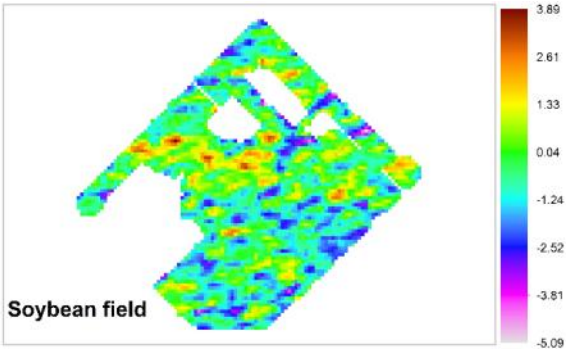
Soybean field
3.89
2.61
1.33
0.04
-1.24
-2.52
-3.81
-5.09

(f)

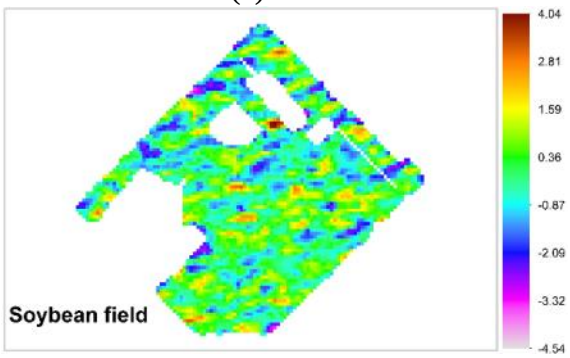
Soybean field
4.04
2.81
1.59
0.36
-0.87
-2.09
-3.32
-4.54

(g)

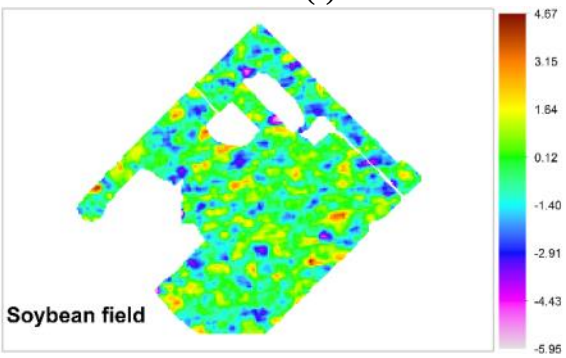
Soybean field
4.67
3.15
1.64
0.12
-1.40
-2.91
-4.43
-5.95

(h)

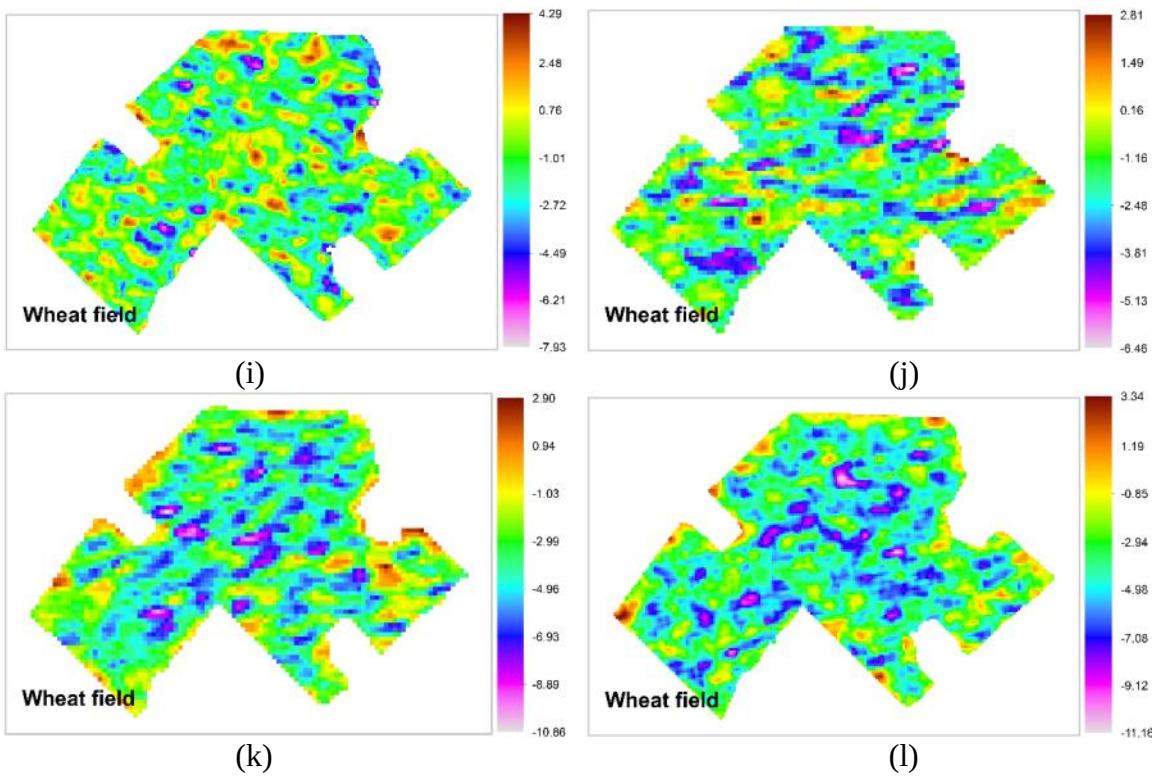

Figure 4-10. T_1 maps of corn, soybean and wheat fields on May 5th, May 15th, June 11th and June 21st. in study area 2014. (a) corn field on May 5th (b) corn field on May 15th (c) corn field on June 11th (d) corn field on June 21st (e) soybean field on May 5th (f) soybean field on May 15th (g) soybean field on June 11th (h) soybean field on June 21st (i) wheat field on May 5th (j) wheat field on May 15th (k) wheat field on June 11th (l) wheat field on June 21st.

Figure 4-10(a) to Figure 4-10(d) show the variation of T_1 in the corn field from May 5th to June 21st, revealing the backscattering coefficient of VV to be greater than that of HH from May 5th to May 18th when only bare soil exists in the corn field. This is consistent with the results simulated by the calibrated IEM model shown in Figure 4-7. The similar pattern is also observed on June 11th, as the corn was emerging from the soil and had very low height on that date. However, when the corn grew taller on June 21st, the geometry of the corn influenced the polarization of the SAR response, which resulted in a higher HH backscattering than the VV backscattering as can be seen in Figure 4-10(d). From Figure 4-10(e) to Figure 4-10(h), when many corn residues were left in the soybean field, the HH backscattering is greater than the VV backscattering, which is depicted from Figure 4-10(e) to Figure 4-10(f). However, after the field had been cultivated, the bare soils were

observed and the VV backscattering became greater than the HH gradually until June 21st. In terms of the wheat field, as the wheat grew, the HH backscattering became more prominent than the VV as shown in Figure 4-10(i) to Figure 4-10(l), which was primarily caused by the attenuation from the wheat canopy. We can conclude that when the agricultural fields are bare, they are dominated by the VV backscattering, and while fields are covered by crops or corn residues, the HH backscattering is more prominent than the VV backscattering due to the attenuation from the crop canopy. In fact, as the wheat growth progresses and the plants undergo tillering and stem elongation, the VV response decreases while the HH response stabilizes (Henderson & Lewis, 1998), and this ratio can perhaps be employed to aid in monitoring the crops at different growing stages. Here, being the same as (Yamaguchi et al., 2005; Yamaguchi et al., 2006; Yajima et al., 2008) and (Jagdhuber et al., 2013), we only employ it to determine the selection of the vertical and horizontal volume scattering models.

4.5.2 Soil Moisture Validation

Soil texture that is related to the saturated percentage (S.P.) of water (Stiven & Khan, 1996), which is the ratio of water to soil in a saturated paste multiplied by 100, was collected by A&L Canada Lab Inc. during this period. In addition, to determine the soil moisture, an empirical linear relationship with the relative dielectric constant with the coefficients representing the soil texture is employed in this chapter (Halikainen et al., 1985). Hence, it is possible that if different soil moisture and dielectric constant values over crop fields are observed, the soil texture can be determined through solving the linear equations, but this is not investigated in this chapter even in this thesis. It will be investigated in future. Both the soil texture and S.P. are listed in Table 4-5. It shows that the S1, S2, W1 and C1 fields are loamier than the C2 field, where there are three sample sites shown as sandy, C2-01, C2-09 and C2-10. Their S.P.s are lower than other samples, with the values 34.35 [vol. %], 30.81 [vol. %] and 34.03 [vol. %], respectively. Therefore, the soil moisture of these three sample sites should be less than the others for each date. The derived volumetric soil moisture of these sample sites on the four dates shown in Figure 4-11 is lower than the values of others, thereby confirming this.

Table 4-5. Soil texture of each site in study area 2014.

SAMPLE ID	Sand (%)	Silt (%)	Clay (%)	Soil Texture	S. P. [vol. %]
S1-01	43.2	36.4	20.4	Loam	49.35
S1-02	41.2	33.4	25.4	Loam	60.86
S1-03	75.2	14.4	10.4	Sandy Loam	42.52
S1-04	73.2	17.4	9.4	Sandy Loam	41.98
S1-05	69.2	21.4	9.4	Sandy Loam	42.62
S1-06	69.2	18.4	12.4	Sandy Loam	45.20
S1-07	77.2	13.4	9.4	Sandy Loam	41.34
S1-08	53.2	24.4	22.4	Sandy Loam	56.36
S2-01	10.3	38.8	50.9	Clay	87.74
S2-02	51.2	24.4	24.4	Sandy Loam	58.40
S2-03	54.3	22.8	22.9	Sandy Loam	56.62
S2-04	63.2	18.4	18.4	Sandy Loam	44.43
S2-05	23.2	41.4	35.4	Clay Loam	65.45
S2-06	41.2	29.4	29.4	Clay Loam	57.41
S2-07	35.2	37.4	27.4	Clay Loam	56.65
S2-08	29.2	42.4	28.4	Clay Loam	58.47
C1-01	63.2	15.4	21.4	Sandy Loam	47.01
C1-02	57.2	27.4	15.4	Sandy Loam	42.81
C1-03	61.2	26.4	12.4	Sandy Loam	39.59
C1-04	39.2	39.4	21.4	Loam	50.85
C1-05	34.3	34.8	30.9	Clay Loam	59.81
C1-06	41.2	38.4	20.4	Loam	49.67
C1-07	31.2	43.4	25.4	Loam	55.57
C1-08	41.2	42.4	16.4	Loam	46.23
C2-01	83.2	6.4	10.4	Loamy Sand	34.35
C2-02	79.2	8.4	12.4	Sandy Loam	36.71
C2-03	69.2	14.4	16.4	Sandy Loam	41.75
C2-04	23.2	38.4	38.4	Clay Loam	68.03
C2-05	23.2	39.4	37.4	Clay Loam	67.17
C2-06	17.2	42.4	40.4	Silty Clay	70.71
C2-07	19.2	43.4	37.4	Silty Loam	67.81
C2-08	27.2	38.4	34.4	Clay Loam	63.95
C2-09	89.2	3.4	7.4	Sand	30.81
C2-10	85.2	4.4	10.4	Loamy Sand	34.03

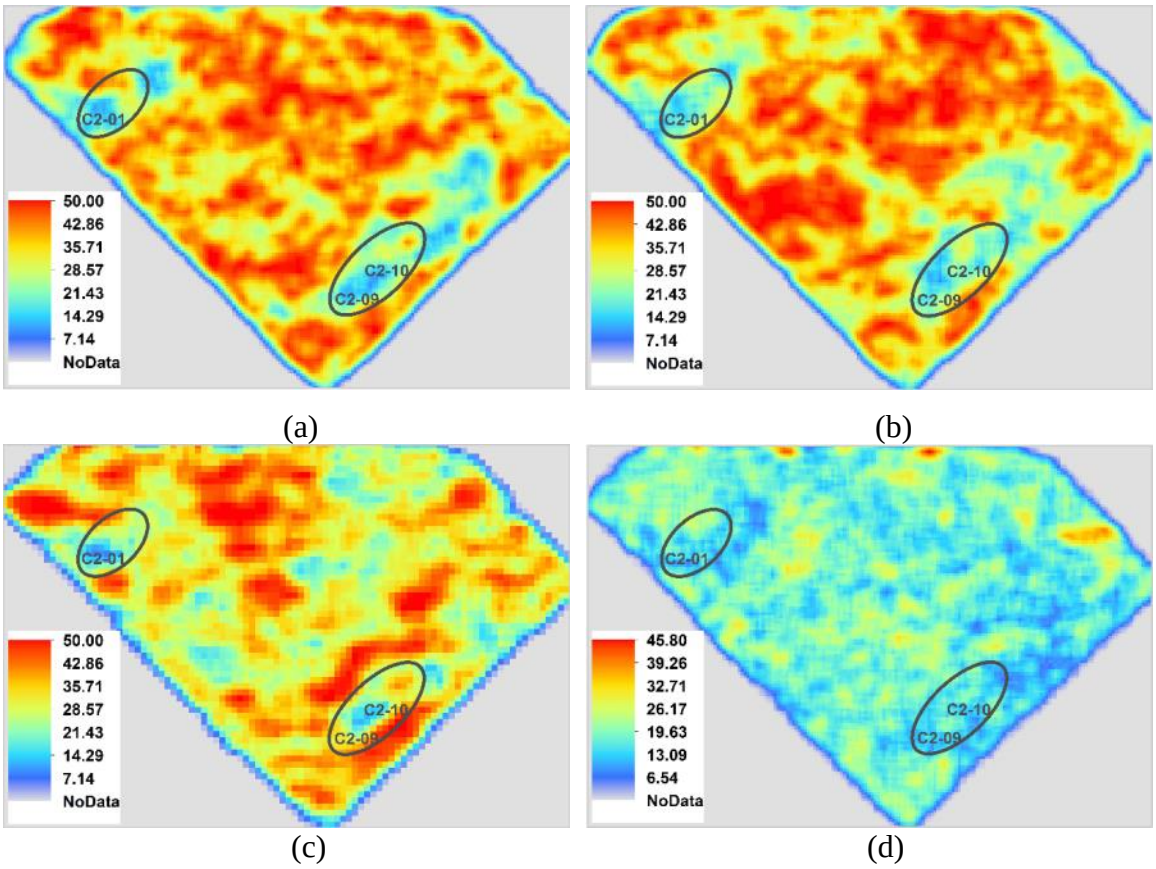

Figure 4-11. Soil moisture in the C2 field on different dates: (a) May 4th (b) May 5th (c) May 18th (d) June 21st.

For further validation, a comparison is performed based on the root mean square error (RMSE) between the estimated soil moisture via the Y-CIME and ISPIS and the measured soil moisture collected from fieldwork. The estimated soil moisture for each sample site is an average of the 5-by-5 window surrounding the sample site for the 5m resolution data while a 3-by-3 window for the 10m resolution data to achieve similar sampling resolution for the soil moisture inversion. Their results are shown in Figure 4-12, and the RMSE and R^2 information is listed on Table 4-6.

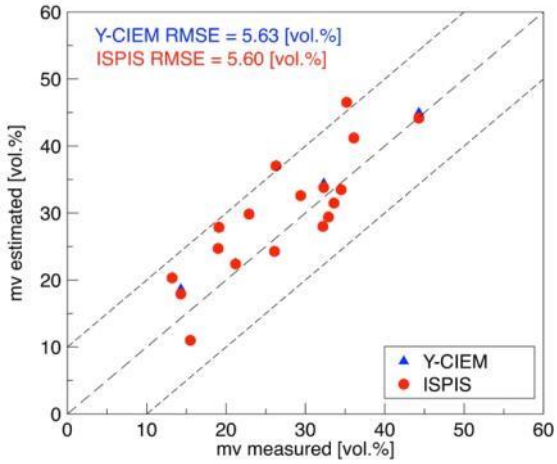
Y-CIEM RMSE = 5.63 [vol.%]
ISPIS RMSE = 5.60 [vol.%]
Y-CIEM
ISPIS
mv estimated [vol.%]
mv measured [vol.%]

(a)

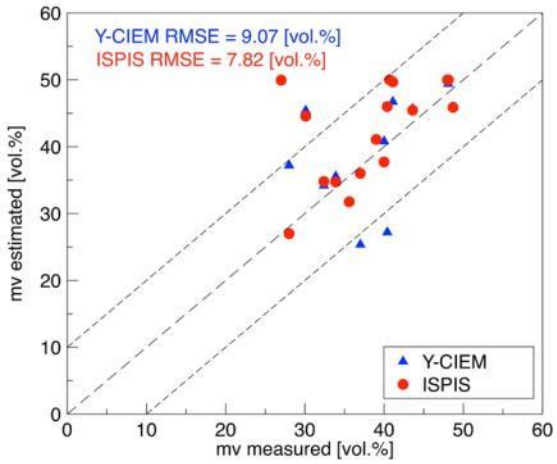
Y-CIEM RMSE = 9.07 [vol.%]
ISPIS RMSE = 7.82 [vol.%]
Y-CIEM
ISPIS
mv estimated [vol.%]
mv measured [vol.%]

(b)

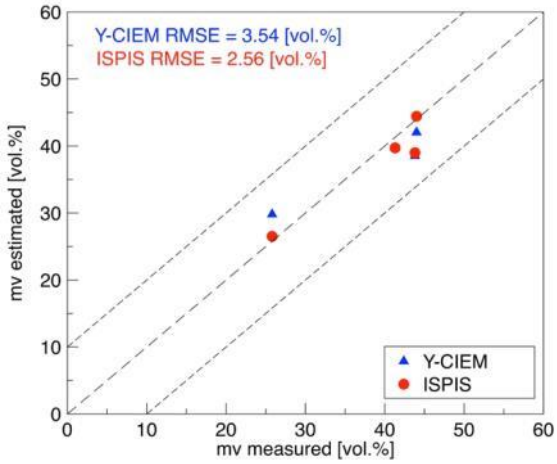
Y-CIEM RMSE = 3.54 [vol.%]
ISPIS RMSE = 2.56 [vol.%]
Y-CIEM
ISPIS
mv estimated [vol.%]
mv measured [vol.%]

(c)

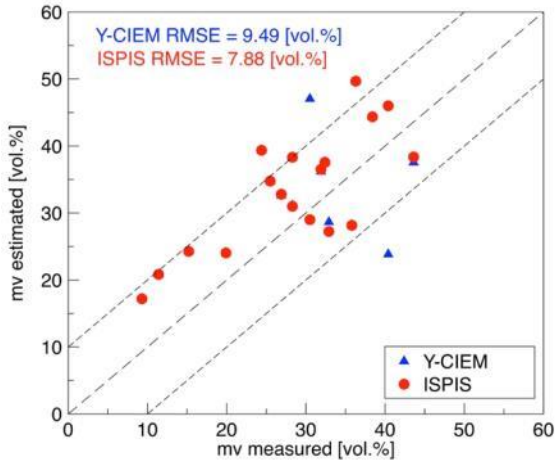
Y-CIEM RMSE = 9.49 [vol.%]
ISPIS RMSE = 7.88 [vol.%]
Y-CIEM
ISPIS
mv estimated [vol.%]
mv measured [vol.%]

(d)

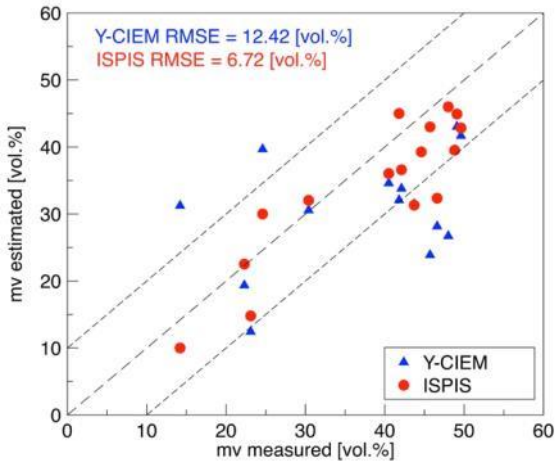
Y-CIEM RMSE = 12.42 [vol.%]
ISPIS RMSE = 6.72 [vol.%]
Y-CIEM
ISPIS
mv estimated [vol.%]
mv measured [vol.%]

(e)

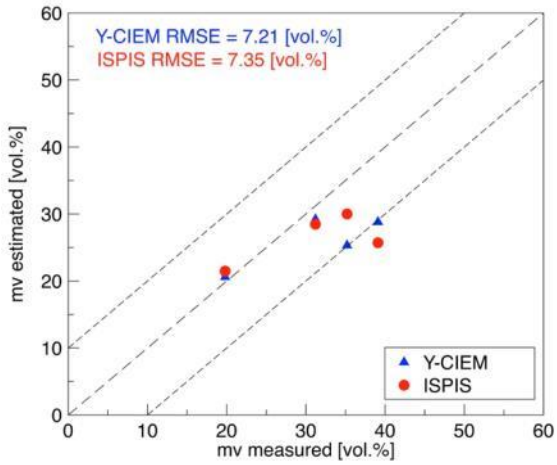
Y-CIEM RMSE = 7.21 [vol.%]
ISPIS RMSE = 7.35 [vol.%]
Y-CIEM
ISPIS
mv estimated [vol.%]
mv measured [vol.%]

(f)

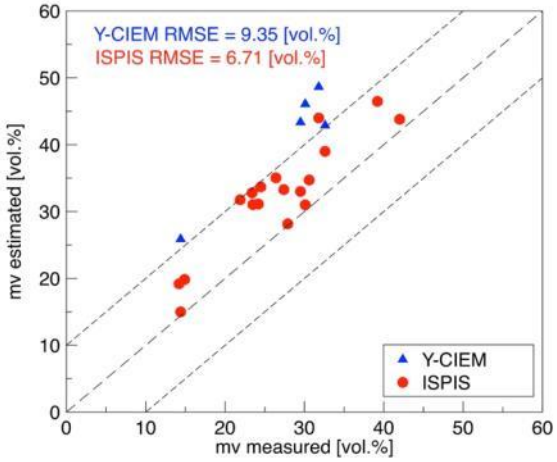
Y-CIEM RMSE = 9.35 [vol.%]
ISPIS RMSE = 6.71 [vol.%]
Y-CIEM
ISPIS
mv estimated [vol.%]
mv measured [vol.%]

(g)

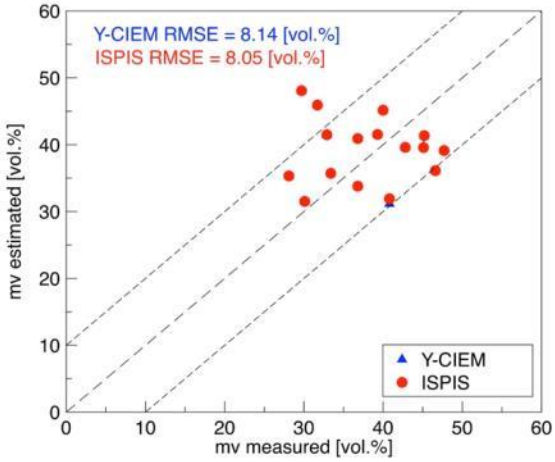
Y-CIEM RMSE = 8.14 [vol.%]
ISPIS RMSE = 8.05 [vol.%]
Y-CIEM
ISPIS
mv estimated [vol.%]
mv measured [vol.%]

(h)

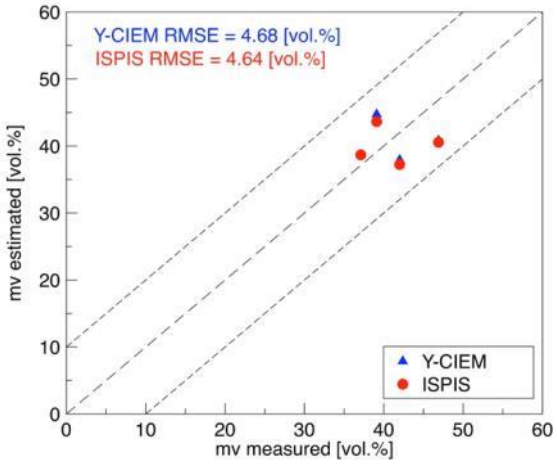
Y-CIEM RMSE = 4.68 [vol.%]
ISPIS RMSE = 4.64 [vol.%]
Y-CIEM
ISPIS
mv estimated [vol.%]
mv measured [vol.%]

(i)

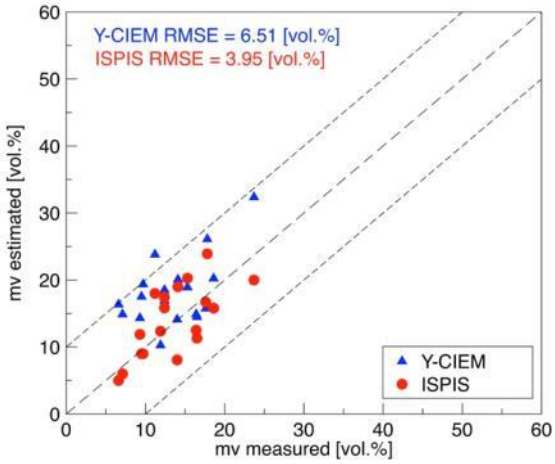
Y-CIEM RMSE = 6.51 [vol.%]
ISPIS RMSE = 3.95 [vol.%]
Y-CIEM
ISPIS
mv estimated [vol.%]
mv measured [vol.%]

(j)

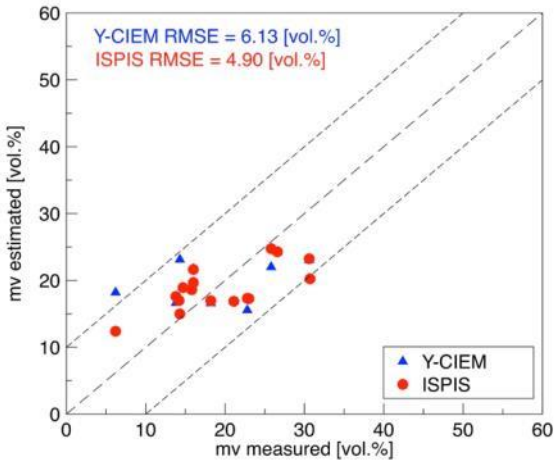
Y-CIEM RMSE = 6.13 [vol.%]
ISPIS RMSE = 4.90 [vol.%]
Y-CIEM
ISPIS
mv estimated [vol.%]
mv measured [vol.%]

(k)

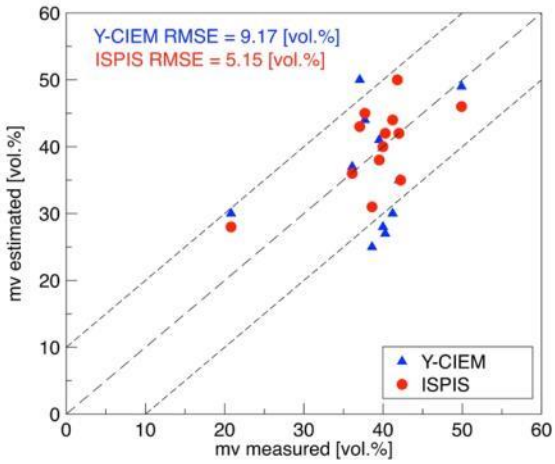
Y-CIEM RMSE = 9.17 [vol.%]
ISPIS RMSE = 5.15 [vol.%]
Y-CIEM
ISPIS
mv estimated [vol.%]
mv measured [vol.%]

(l)

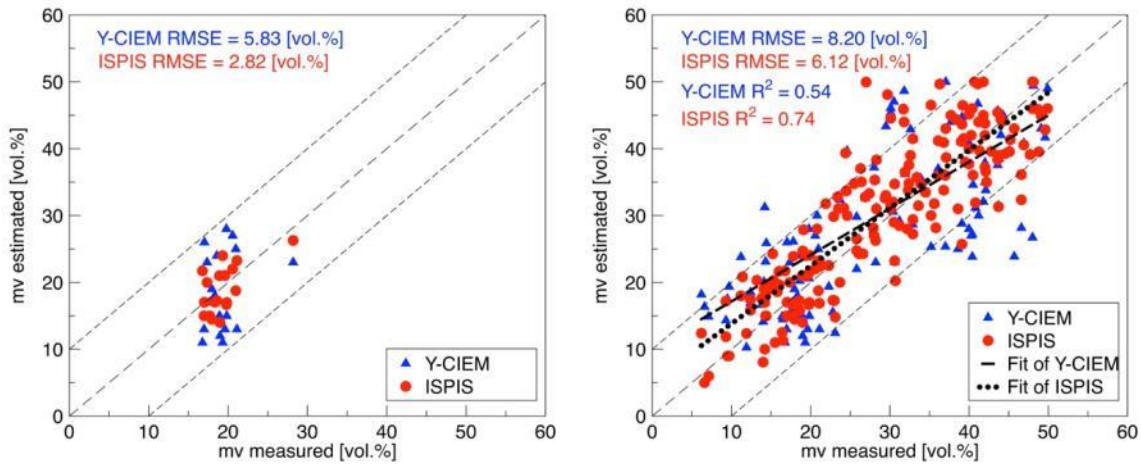

(m) (n)

Figure 4-12. Measured and estimated soil moisture on different days: (a) Corn field on May 4th (b) Soybean field on May 4th (c) Wheat field on May 4th (d) Corn field on May 5th (e) Soybean field on May 5th (f) Wheat field on May 5th (g) Corn field on May 18th (h) Soybean field on May 18th (i) Wheat field on May 18th (j) Corn field on June 21st (k) Soybean field on June 21st (l) Wheat field on April 29th 2013 (m) Wheat field on May 9th 2013. (n) Overall RMSE of different methods.

Table 4-6. RMSE and R^2 information on different days ([vol. %]).

Models	Fields	0504	0505	0518	0621	0429	0509
Y-CIEM	CORN	5.63	9.49	9.35	6.51		
	SOYBEAN	9.07	12.42	8.14	6.13		
	WHEAT	3.54	7.21	4.68		9.17	5.83
	OVERALL	**8.20**					
	R^2	**0.54**					
ISPIS	CORN	5.60	7.88	6.71	3.95		
	SOYBEAN	7.82	6.72	8.05	4.90		
	WHEAT	2.56	7.35	4.64		5.15	2.82
	OVERALL	**6.12**					
	R^2	**0.74**					

For the corn fields during the period from May 4th to May 18th, the soils were mostly bare soils, and the RMSEs of almost all methods are less than 10 [vol. %]. It should be noted that although many sample sites were bare soils in the corn field, some crop stalks were randomly present, which could affect the backscattering coefficient. From this view, both the SAVSM and Yamaguchi volume scattering model can describe the fluctuated scattering caused by crop residues, but the SAVSM is perhaps more suitable to simulate

the scattering by crop residues because the ISPIS achieved lower RMSE than that of Y-CIME. In terms of the soybean fields, their RMSEs are basically higher than those in the corn fields. The crop residues in the soybean fields are the primary reason that the scattering is more complex than in bare soils. From Figure 4-12(b), Figure 4-12(e) and Figure 4-12(i), we can see that the ISPIS and Y-CIEM have lower RMSE even if there are corn residues. However, the ISPIS has lower RMSE than that of Y-CIEM; this is mainly because the SAVSM varies with RVI, whereas the RVIs of Yamaguchi volume scattering stays constant with its values 0.61 or 1 that are depicted in Table 4-4. It should also be noted that, in the wheat fields, only four sample sites are collected in 2014. This may not be adequate to demonstrate the feasibility of the ISPIS in the wheat field. To overcome this issue, two datasets collected on April 29th and May 9th 2013 are employed for the wheat field validation with their results shown in Figure 4-12(l) and Figure 4-12(m). We can see that the ISPIS has much lower RMSE than that of the Y-CIEM on each date with their average RMSE at approximately 4.5 [vol. %] and 6.1 [vol. %], respectively. Lastly, on June 21st, the ISPIS has lower RMSE than the Y-CIEM in the corn fields when the corn has already emerged with a sparse canopy. From this view, the SAVSM is perhaps more suitable to describe the field under vegetation cover than the Yamaguchi volume scattering model. Overall, the ISPIS has lower RMSE, 6.12 [vol. %], for all fields on different dates than that of Y-CIEM, with its value of 8.20 [vol. %]. The R^2 of the ISPIS is also higher than that of the Y-CIEM with their values of 0.74 and 0.54 respectively. Therefore, we may conclude that the soil moisture derived by the ISPIS is in agreement with the ground truth in the corn, soybean and wheat fields during the period from May to June in 2013 and 2014 at the early growing stage, and the SAVSM is perhaps more suitable to describe the fluctuated scattering than the Yamaguchi volume scattering model.

In addition, because the soil moisture changes over time due to the rain events or the drying process caused by the sun, the variability of the averaged soil moisture measured at fieldwork (solid lines) and the estimated ones by the ISPIS (dash lines) is compared and presented in Figure 4-13. According to the weather records in study area 2014, it shows that the rainfall happened in late April 2014 making the corn, soybean and wheat

fields wet at the beginning of May 2014 with an average soil moisture greater than 25 [vol. %]. A small rainfall event happened before May 18th 2014 and made the measured soil moisture greater than 25 [vol. %] in these three fields as well. However, the drying period that happened at the beginning of June resulted in the measured soil moisture decreasing to values less than 20 [vol. %]. In terms of study area 2013, the wet soil on April 29th 2013 was due to the rainfall that occurred on April 29th. This later decreases to approximately 18 [vol. %] on May 9th because of the drying period happening at the beginning of May. Overall, the variation of the soil moisture estimated by the ISPIS over time shows the consistency with the measured soil moisture in those fields in 2013 and 2014, which can be seen clearly in Figure 4-13 with their correlation coefficients of 0.99, 0.95 and 0.97 in corn, soybean and wheat fields, respectively.

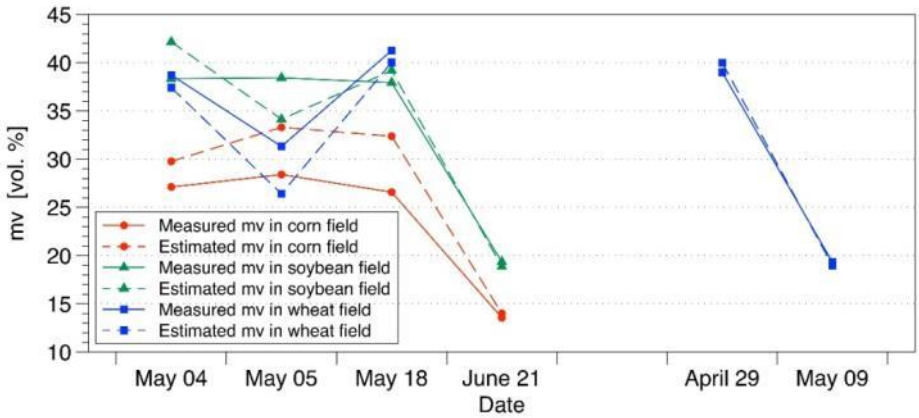

Figure 4-13. Changes in soil moisture over time as estimated by RADARSAT-2 and as measured in the agricultural fields in 2014 and 2013.

4.5.3 Surface Roughness Validation

The validation of the surface roughness is performed on two aspects: the first is its variation over time, and the other is the estimated surface roughness compared with the measured one. Specifically, the C2 and S2 fields in study area 2014 are selected for the variation analysis. The histograms of the surface roughness in their fields are shown in Figure 4-14, and the comparison between the estimated roughness and measured roughness is shown in Figure 4-15.

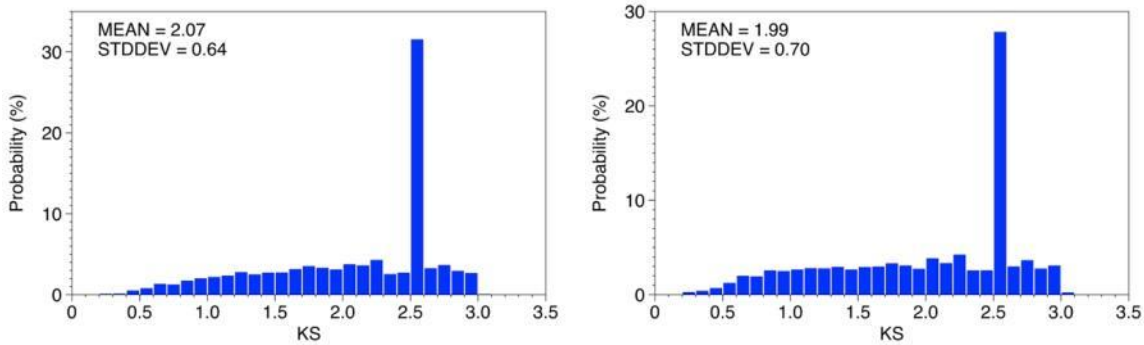
MEAN = 2.07
STDDEV = 0.64
MEAN = 1.99
STDDEV = 0.70
Probability (%)
KS

(a)

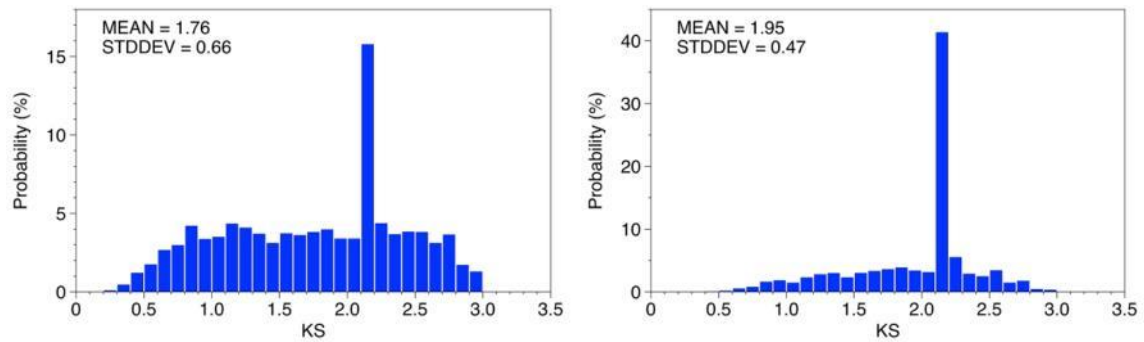
MEAN = 1.76
STDDEV = 0.66
MEAN = 1.95
STDDEV = 0.47
Probability (%)
KS

(b)

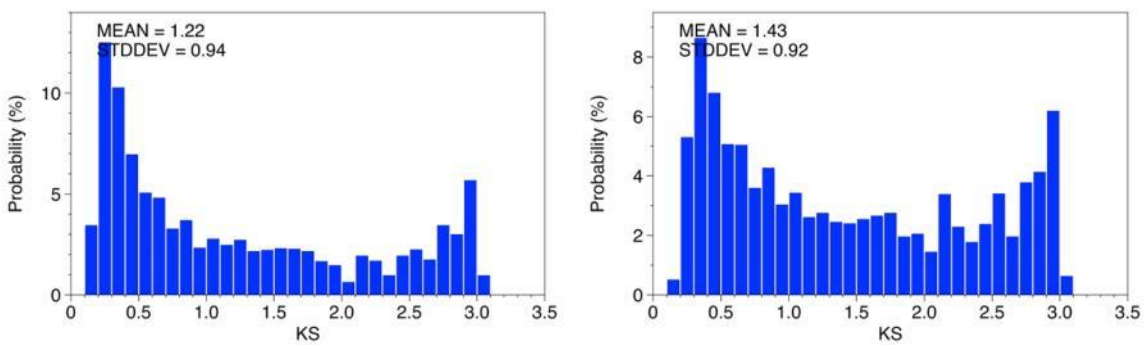
MEAN = 1.22
STDDEV = 0.94
MEAN = 1.43
STDDEV = 0.92
Probability (%)
KS

(c)

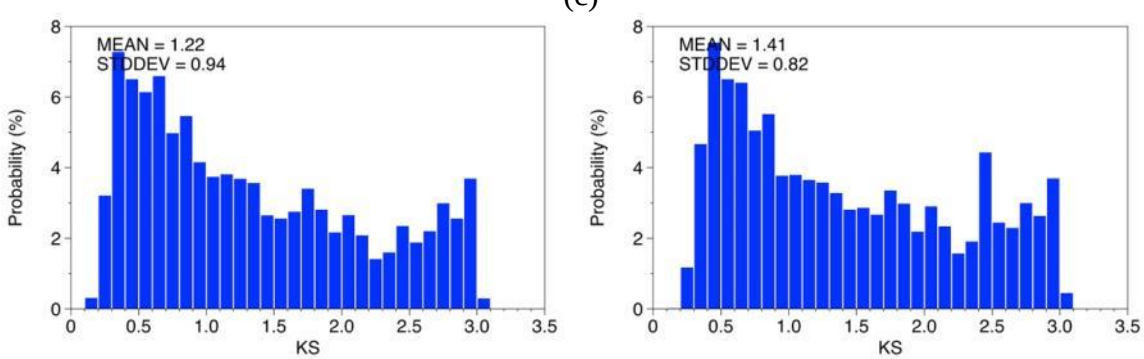
MEAN = 1.22
STDDEV = 0.94
MEAN = 1.41
STDDEV = 0.82
Probability (%)
KS

(d)

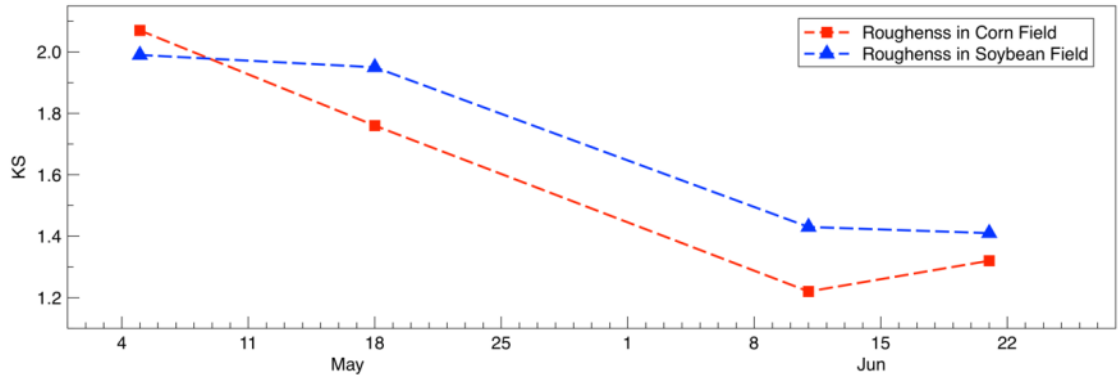

(e)

Figure 4-14. Surface roughness histograms for the corn and soybean fields, from left to right, on different days: (a) May 5th (b) May 18th (c) June 11th (d) June 21st (e) variation of roughness over time in corn and soybean fields.

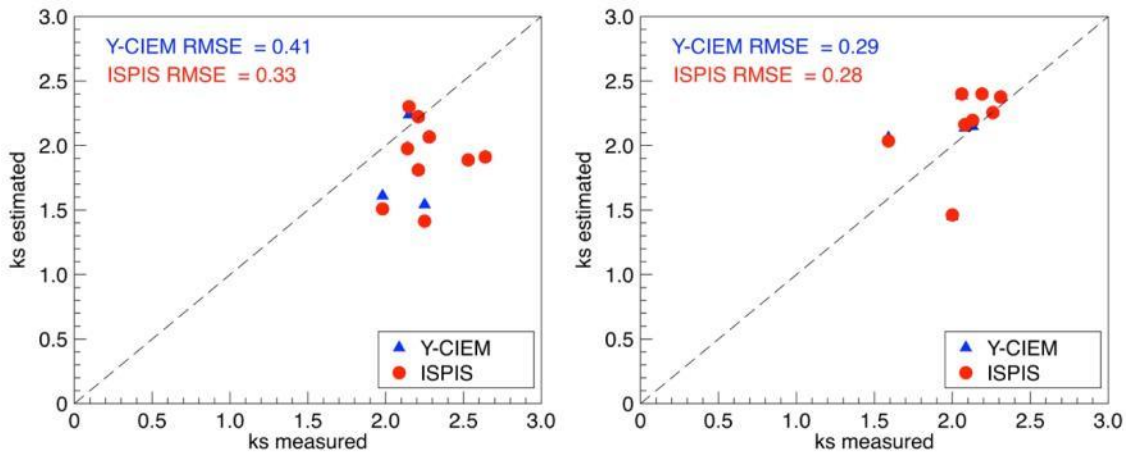

(a) (b)

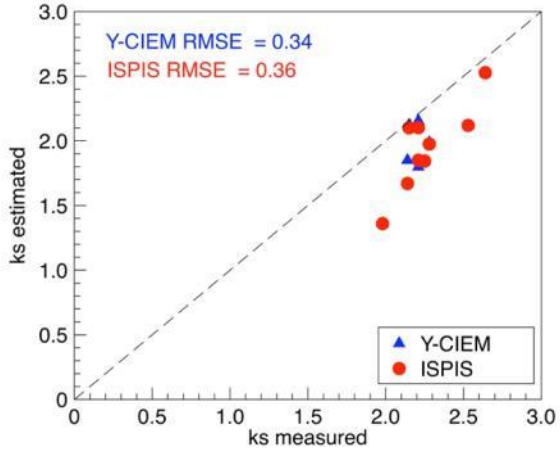
Y-CIEM RMSE = 0.34
ISPIS RMSE = 0.36
Y-CIEM
ISPIS
ks estimated
ks measured

(c)

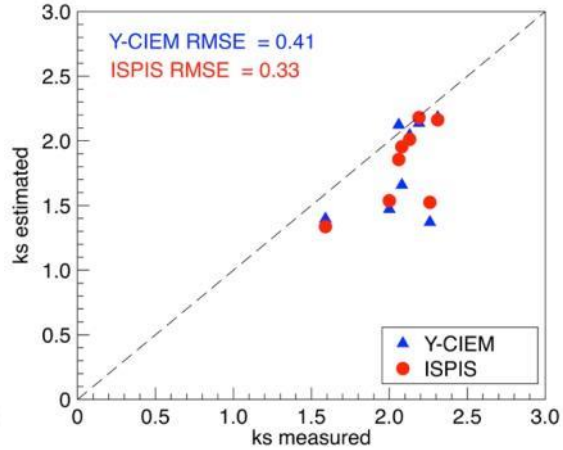
Y-CIEM RMSE = 0.41
ISPIS RMSE = 0.33
Y-CIEM
ISPIS
ks estimated
ks measured

(d)

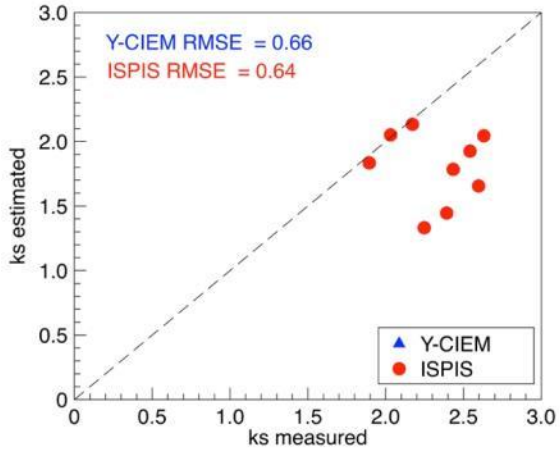
Y-CIEM RMSE = 0.66
ISPIS RMSE = 0.64
Y-CIEM
ISPIS
ks estimated
ks measured

(e)

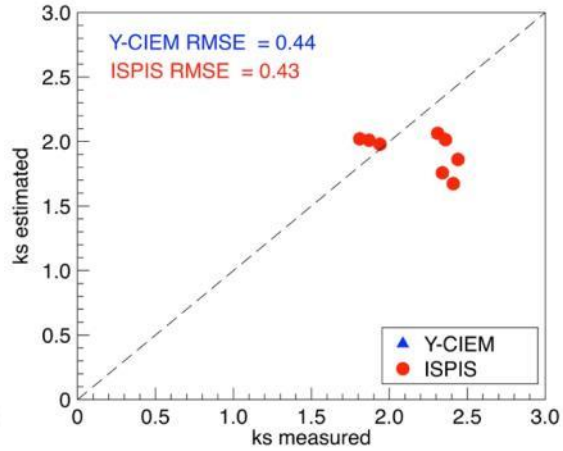
Y-CIEM RMSE = 0.44
ISPIS RMSE = 0.43
Y-CIEM
ISPIS
ks estimated
ks measured

(f)

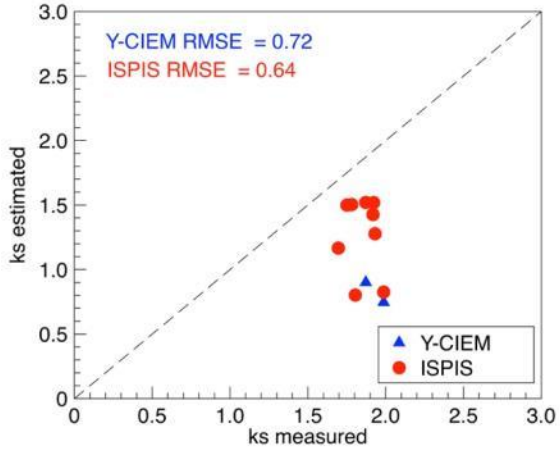
Y-CIEM RMSE = 0.72
ISPIS RMSE = 0.64
Y-CIEM
ISPIS
ks estimated
ks measured

(g)

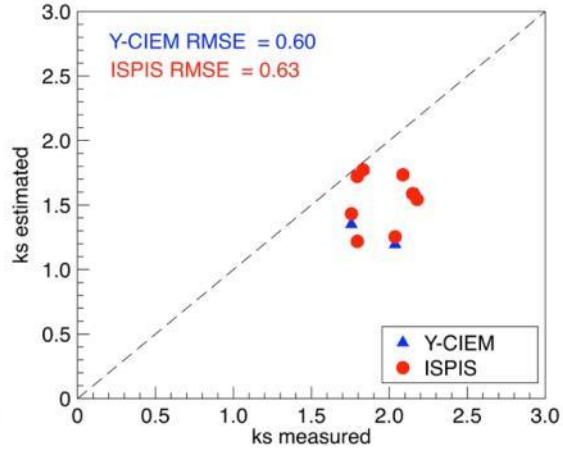
Y-CIEM RMSE = 0.60
ISPIS RMSE = 0.63
Y-CIEM
ISPIS
ks estimated
ks measured

(h)

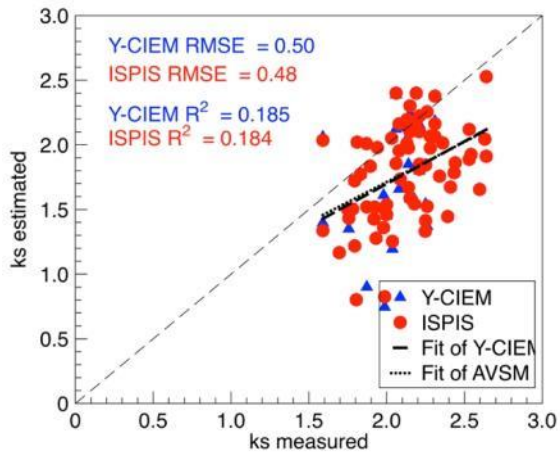

(i)

Figure 4-15. Measured and estimated surface roughness on different dates: (a) Corn field on May 4th (b) Soybean field on May 4th (c) Corn field on May 5th (d) Soybean field on May 5th (e) Corn field on May 18th (f) Soybean field on May 18th (g) Corn field on June 11th (h) Soybean field on June 11th (i) entire field on all days.

Before the beginning of May, the corn field had been ploughed showing mainly bare soils, and many smooth large size clods were left in the field, which makes the corn field very rough from the beginning of May to the middle of May. The soybean field also appear rough due to the fluctuation scattering caused by the corn residues. However, the seedbed preparation of both fields occurred at the end of May, resulted in a relatively smooth surface for both fields. That means the KS will be changing from a high value to a low value from May to June. Figure 4-14(c) and Figure 4-14(d) show this change, with average KS values of 1.22 and 1.32 in the corn fields and 1.43 and 1.41 in the soybean fields. This change has also been depicted in Figure 4-14(e), which shows the change of roughness from May to June, before and after the crop planting. The same as for the estimated soil moisture, the surface roughness is also obtained by averaging the pixels. It should also be noted that the peaks in the histograms of Figure 4-14(a) and Figure 4-14(b) on May 5th and May 18th are observed in both the corn and soybean fields. In the corn fields, there are around 30% and 15% pixels having values of 2.5 and 2.1 on May 5th and May 18th, respectively. It is primarily caused by the relatively large roughness during the ploughed stage as the ploughed field had large clods according to our measurements. Other studies have also reported that the majority of the averaged RMS heights are

approximately 2.6 cm, or as high as 4 cm (Alvarez-Mozos et al., 2006; Baghdadi et al., 2008), which are consistent with our measurements. For the soybean field, the peaks in the histograms have approximately 30% and 40% pixels with their roughness being approximately 2.5 and 2.1 respectively. The high peak is likely caused by the corn residues that were left in the soybean fields as shown in Figure 4-2(b), and the corn residues can cause fluctuated scatterings. The similar histograms observed on May 5th and May 18th in the soybean field can also demonstrate the consistent performance of the ISPIS. This is because the high peaks are observed on both dates except that the roughness on May 18th is less than that on May 5th due to the flattened residues caused by the human activities.

Figure 4-15 shows the KS derived by different methods on different dates. For both the ISPIS and Y-CIEM, the RMSE in the corn fields is lower than that in the soybean fields, which is primarily due to the crop stalks left in the corn fields, which caused the scattering to fluctuate. Specifically, on May 4th and May 5th in the corn fields, the surface roughness derived by the ISPIS and Y-CIEM did not change much on either date because they were both bare soils. We also know that the RADARSAT-2 data on the two dates had different orbits: one is ascending and the other is descending. However the orbit difference is not the primary reason causing the variation, as there were no prominent roughness patterns. In addition, both the ISPIS and the Y-CIEM have the issue of underestimation. This is because to avoid the speckle noise, a window size averaging process is adopted for the estimation of the soil roughness. This can influence the estimated results, because the roughness often shows little spatial dependency, which means that the surface roughness taken at one position often poorly represents its surrounding areas. Therefore, the averaging process for the estimation of surface roughness could lead to an underestimation.

We also observed that the estimated roughness of both Y-CIEM and ISPIS has no strong correlation with the ground truth, with their R^2 values of 0.184 and 0.185, respectively, which is perhaps caused by the small range of the roughness between 1.5 and 2.5, resulting in a biased correlation coefficients calculation. Both the ISPIS and Y-CIEM

have RMSEs less than 0.75 on different days in the corn and soybean fields. The overall RMSE of the ISPIS is around 0.48, which is very similar to that of the Y-CIEM with its value of 0.50. This similar RMSE is because the sample sites in the corn or soybean fields with bare soils that are dominated by surface scattering are also considered for the overall RMSE calculation. For the surface scattering dominant regions, the CIEM is employed by both the ISPIS and Y-CIEM for surface parameter inversion, because the H and α threshold to distinguish the surface and volume scattering employed in this chapter is both adopted by the Y-CIEM and ISPIS. Therefore, to invert the surface parameters of these surface scattering dominated pixels, their results will be almost the same as shown in Figure 4-15(c), Figure 4-15(e) and Figure 4-15(h). However, for fields covered with corn residues or short corn plants, the volume scattering is dominant. To invert surface parameters for these fields, the difference between the ISPIS and the Y-CIEM becomes larger compared with fields with bare soils as depicted in Figure 4-15(d) and Figure 4-15(g). From this perspective, we conclude that the ISPIS can describe more complex situations than the Y-CIEM, as the ISPIS can vary with the RVI, whereas the RVI of the Yamaguchi volume scattering model stays constant.

4.5.4 RVI and Vegetation Water Content (VWC) of Wheat

The ISPIS determines the optimum volume scattering model based on the RVI, which is related to the vegetation water content (VWC) of wheat (Kim et al., 2014), having a strong correlation with the coefficient 0.94 for the C band. The empirical relationship between the RVI and VWC developed by Kim et al. (2014) is adopted for wheat VWC inversion in this chapter, and the results are shown in Figure 4-16. The wheat planting time in our study area is different from that of Kim et al. (2014) since they are from different ecoregions, with a time difference of approximately 30 days through comparing the ground truth photos and phenology. To analyze the derived VWC qualitatively using the ISPIS, we treat the VWC derived by Kim et al. (2014) as the ground truth, and compare it with the VWC derived by the ISPIS, and the comparison is shown in Figure 4-16(e).

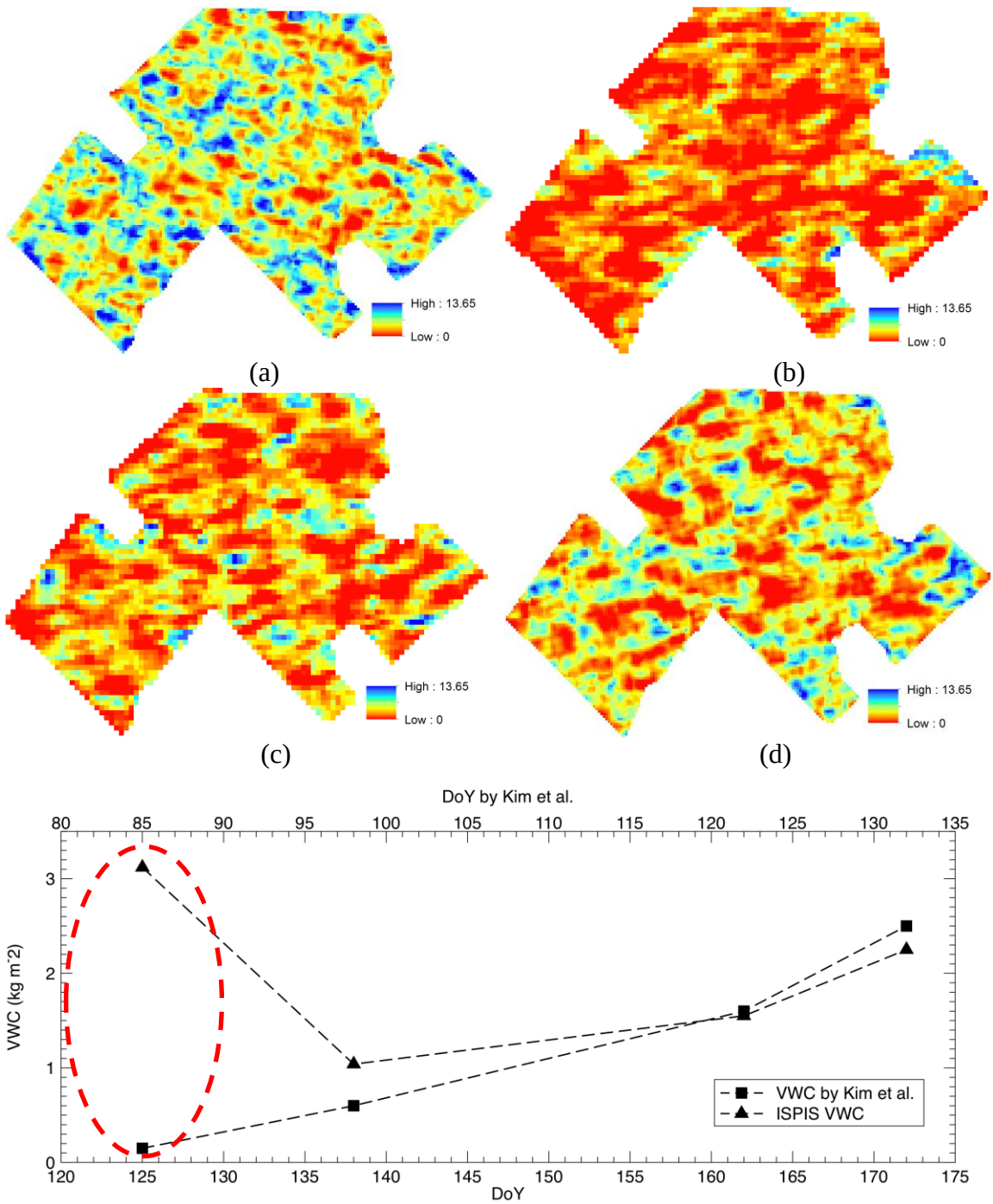

(e)

Figure 4-16. VWC of wheat on different days and its comparison with the ground truth measured by Kim et al.: (a) May 5th (b) May 18th (c) June 11th (d) June 21st (e) comparison between the ISPIS and the Kim et al. (2014) DoY: Day of Year. Note: the "DoY by Kim et al." means the day of year Kim et al.

(2014), which has the same phenology corresponding to the "DoY" in this chapter.

Figure 4-16(a) and Figure 4-16(e) depict the very high VWC on day 125 (May 5th), with a value greater than 3.0 kg m^{-2}, whereas the corresponding VWC by Kim et al. (2014) is approximately 0.1 kg m^{-2}. This significant difference is mainly caused by the interaction with the crop residue left in the wheat field on May 5th when the RADARSAT-2 can penetrate the sparse wheat canopy easily and the VWC is high. The ground truth photo shown in Figure 4-2(c) confirms this. In addition, as the wheat grew tall and dense, the VWC derived by the ISPIS is coherent with that by Kim et al. (2014) from June 11th due to the dominating volume scattering from the wheat canopy. From this view, we conclude that the crop residues also affect the RVI, especially when the RADARSAT-2 can penetrate the wheat canopy and reach the ground, resulting in the derived VWC being not very accurate. Therefore, the RVI is not only an index that describes the vegetation scattering but also an indicator that characterizes the randomness of scattering caused by crop residues.

4.5.5 Simple Analysis of the Two-way Attenuation by Crop Canopy

In this chapter, we treat the total backscattering as the sum of the surface scattering caused by the bare soil and the volume scattering caused by the crop canopy or the crop residues without considering the attenuation effect. This is primarily because the attenuation is relatively weak at the early growing stage. A simple analysis of the two-way attenuation caused by the vegetation and corn residues is performed in this section. The Michigan Microwave Canopy Scattering Model (MIMICS) developed by Ulaby in 1990 (Ulaby et al., 1990) is suitable for vegetation covered areas where the agents responsible for scattering have discrete configurations (Toure et al., 1994). They include wheat, corn residue, soybean and corn; and many studies have adapted this model to describe the scattering of crops such as wheat and soybean (Toure et al., 1994; De Roo et al., 2001). The MIMICS offers an efficient way and is employed for different crop attenuation analysis in this section. However, to apply the MIMICS for attenuation

analysis, some assumptions are required for each crop as the MIMICS was originally developed for the forest areas. In the MIMICS model, the trunk height is considered much larger than the wavelength in order to simplify the computation of the trunk's scattering matrix. However, in agricultural fields, particularly for corn, soybean and wheat where the stem heights are of the order of the wavelength for the C band earlier in the growing stage (Toure et al., 1994). Therefore, it is reasonable that we assume the wheat in tillering stage consisting of small-sized leaves without stems at the early growing stage from the end of April to the middle of May. The corn residue standing in the soybean field can be treated as a very dry primary branch with a vertical distribution without any leaves as they are slightly larger than the C-band radar wavelength. It should also be noted that on June 21st, the soybean had emerged but very small and the effects on the backscattering by their stems can be ignored. In terms of the corn, it can be assumed as consisting of a primary trunk with some broad leaves within its canopy. In addition, the soil conditions are also required in the MIMICS model. Although the soil conditions are variable in different fields, this chapter is focusing on the canopy attenuation analysis. Therefore, we treat all crop fields as having the same ground conditions. For attenuation analysis, crop parameters at different growing stages on May 5th 2014 (S01), May 18th 2014 (S02), June 4th 2014 (S03), and June 21st 2014 (S04) are listed in Table 4-7 with their corresponding two-way attenuation percentage shown in Figure 4-17. It should be noted that some parameters such as the height, leaf density and gravimetric moisture content are measured during field work while other parameters such as the dry density of leaf material or stem material are either referred to Toure et al. (1994) or using default values given by the MIMICS for a simple analysis. Finally, because the RADARSAT-2 data we adopted in this chapter has four modes with incidence angles of 24, 29, 35, and 39 degrees respectively, the analysis of the attenuation of these crops is performed on these four different incidence angles as the crop grows.

Table 4-7. Crop parameters of different agricultural fields in study area 2014 at different growing stages for C-band RADARSAT-2 data with its frequency of 5.405 GHZ. S01: 2014 May 5th; S02: 2014 May 18th; S03: 2014 June 04th; S04: 2014 June 21st.

Crops	Structure	Parameters	S01	S02	S03	S04
Ground	Soil Moisture (%)		20			
	RMS height (cm)		1			
	Correlation Length (cm)		10			
	Soil Texture	Clay (%)	25			
		Sand (%)	15			
Wheat	**Leaf**	Gravimetric Moisture Content (%)	80	80	75	-
		Dry density of leaf material (0-1)	0.1	0.1	0.1	-
		Thickness (cm)	0.02	0.02	0.02	-
		Length (cm)	6	11	16	-
		Width (cm)	0.4	0.9	1.5	-
		Density (N/m^3)	10000	7500	4500	-
	Canopy	Thickness (m)	0.10	0.15	0.25	
Corn Residue	**Stem**	Gravimetric moisture content (%)	10	-	-	-
		Dry density of stem material (0-1)	0.3	-	-	-
		Density (N/m^3)	15	-	-	-
		Diameters (cm)	2.5	-	-	-
		Length (m)	0.4	-	-	-
	Canopy	Thickness (m)	0.40			
Corn	**Stem**	Gravimetric moisture content (%)	-	-	70	70
		Dry density of stem material (0-1)	-	-	0.3	0.3
		Density (N/m^3)	-	-	350	140
		Diameters (cm)	-	-	0.5	0.8
		Length (m)	-	-	0.02	0.05
	Leaf	Gravimetric moisture content (%)	-	-	80	80
		Dry density of leaf material (0-1)	-	-	0.1	0.1
		Thickness (cm)	-	-	0.03	0.03
		Length (cm)	-	-	6	15
		Width (cm)	-	-	1.5	4
		Density (N/m^3)	-	-	170	120
	Canopy	Thickness (m)			0.08	0.25
Soybean	**Leaf**	Gravimetric moisture content (%)	-	-	-	80
		Dry density of leaf material (0-1)	-	-	-	0.1
		Thickness (cm)	-	-	-	0.05
		Length (cm)	-	-	-	3
		Width (cm)	-	-	-	2.5
		Density (N/m^3)	-	-	-	360
	Canopy	Thickness (m)	-	-	-	0.05

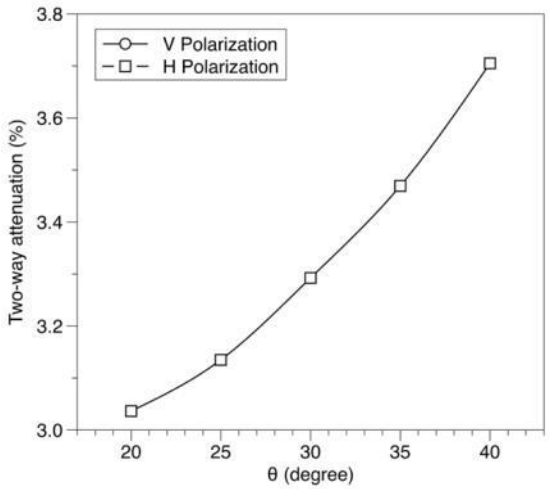
V Polarization
H Polarization
Two-way attenuation (%)
θ (degree)

(a)

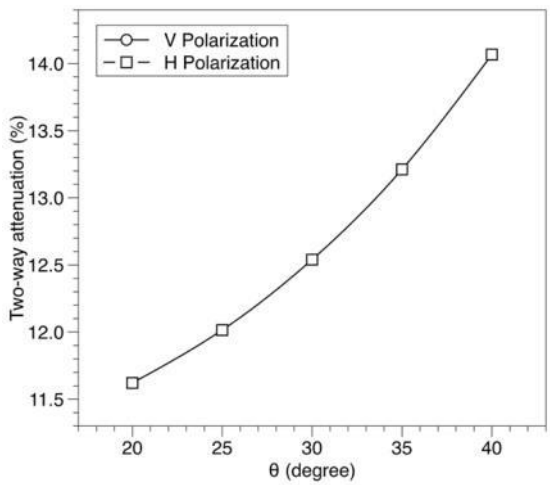
V Polarization
H Polarization
Two-way attenuation (%)
θ (degree)

(b)

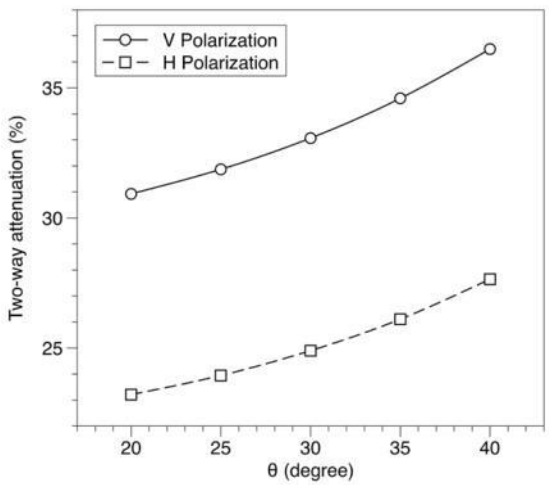
V Polarization
H Polarization
Two-way attenuation (%)
θ (degree)

(c)

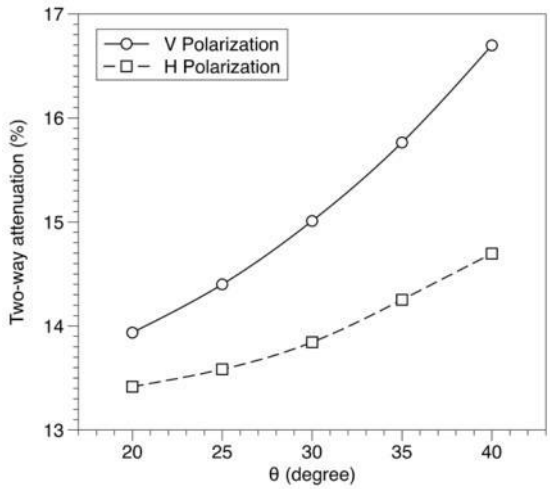
V Polarization
H Polarization
Two-way attenuation (%)
θ (degree)

(d)

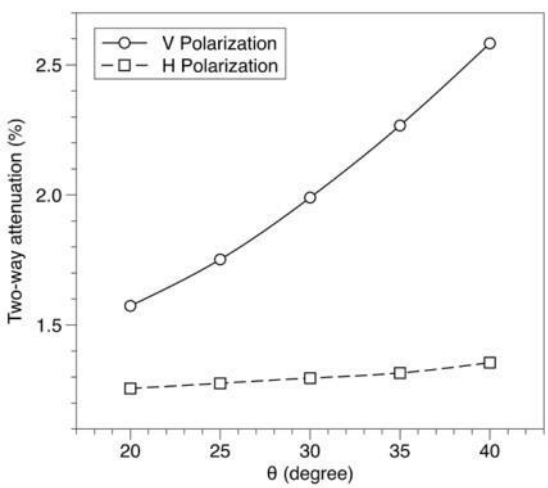
V Polarization
H Polarization
Two-way attenuation (%)
θ (degree)

(e)

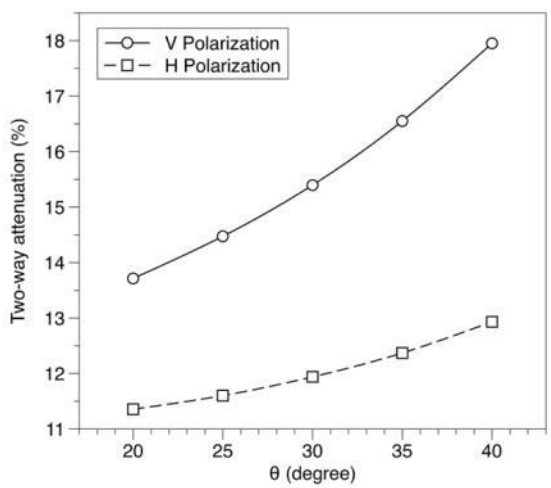
V Polarization
H Polarization
Two-way attenuation (%)
θ (degree)

(f)

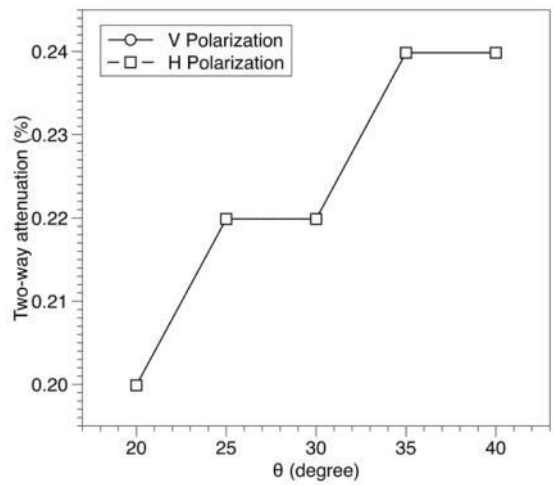

(g)

Figure 4-17. Two-way attenuation coefficients of different crops at different growing stages under different incident angles. (a) wheat field on May 5th 2014 (b) wheat field on May 18th 2014 (c) wheat field on June 04 2014 (d) soybean field on May 5th (e) corn field on June 4th 2014 (f) corn field on June 21st 2014. (g) soybean field on June 21st.

Generally, in corn, soybean and wheat fields, as the incidence angle increases, the two-way attenuation becomes more significant as shown in Figure 4-17. This is because the large incidence angle increases the path length through the vegetation which will cause an increase in the extinction coefficient, which is composed of both absorption and scattering losses. In addition, Figure 4-17 shows that the two-way attenuation of wheat is not significant until June 4th with its two-way attenuation being approximately greater than 30% for the V polarization and greater than 22% for the H polarization. On May 5th and May 18th, both the H and V polarizations have small two-way attenuation coefficients with values less than 4% and 15% respectively. For the corn residues left in the soybean field, they are very dry, with gravimetric water content being approximately 10%. This will cause a weak two-way attenuation with values less than 17% for V polarization and less than 15% for the H polarization when the incidence angle is less than 40 degrees. When the corn emerged on June 4th with a very few leaves and small stems, its two-way attenuation for the V polarization is less than 3% while for the H polarization it is less than 1.5%. As the corn continues to grow until June 21st, the two-way attenuation becomes larger than that of on June 4th but not significant with H

polarization less than 13% and V polarization less than 20%. In terms of the soybean, on June 21st only very small leaves were observed and their stems can be ignored. Hence, it seems apparent for both H and V polarization with their two-way attenuation much less than 1%. The proposed model in this chapter is focusing on the crops at the early growing stage; hence, it is reasonable to ignore the attenuation caused by the crop canopy during the early growing stages.

4.5.6 Discussion of Scattering over Bare Soils

The threshold of $H < 0.6\ and\ \alpha < 40°$ is adopted to distinguish the bare soils from other fields such as fields with crop residues and low vegetation cover. However, approximately 30% of pixels are dominated by the volume scattering even if it is bare soil, which is shown prominently on the two histograms for May 5th and May 15th 2014 in the corn field shown in Figure 4-18. High entropy values that are classified as volume scattering in the bare soil field are perhaps contributed by the randomly distributed crop residues or the dry soil penetration effect for high frequency radar that has been investigated by Baghdadi et al. (2013). The moisture profile (i.e., soil penetration) has small effect on the HH and VV backscattering signals, but it is important to use the same protocol to measure the ground truth soil moisture for accurate inversion (Le Morvan et al., 2008). In addition, the effects of the moisture profile on the HV backscattering signals still require further investigation. In addition, at the early growing stage when the crop is less dense, the volume scattering from the corn residues or vegetation and the surface scattering caused by the direct ground scattering are mixed together. Therefore, it is difficult to distinguish bare soils and the fields covered by vegetation completely. However, for the corn fields with bare soil on May 5th and May 15th most of the pixels (approximately 70%) are classified as surface scattering as shown in figure 18 when the threshold is applied. From this perspective, the threshold selected in this chapter is appropriate. Finally, the coefficients of the surface and the volume components of the bare soil on May 5th 2014 and May 15th 2014 are shown in Figure 4-19. It shows that even though approximately 30% of pixels are occupied by the volume scattering, their backscattering coefficients are much less than that of the surface scattering.

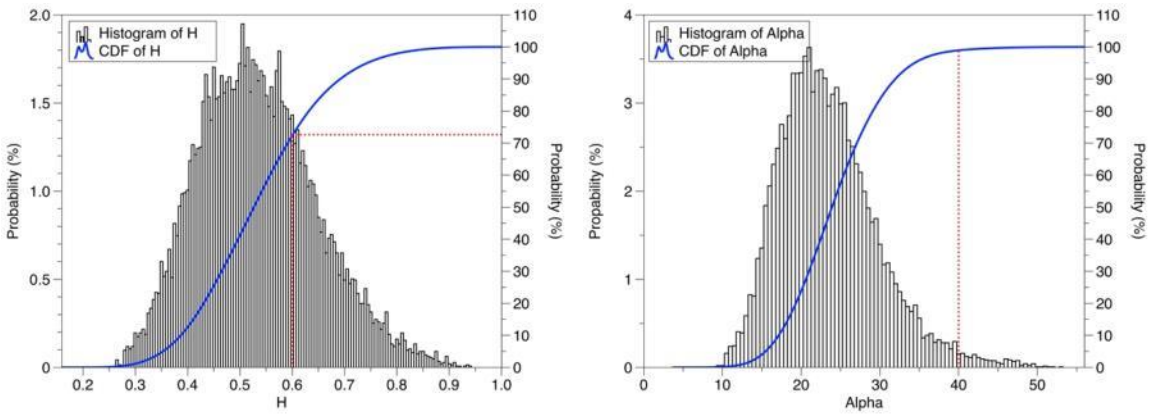

(a)

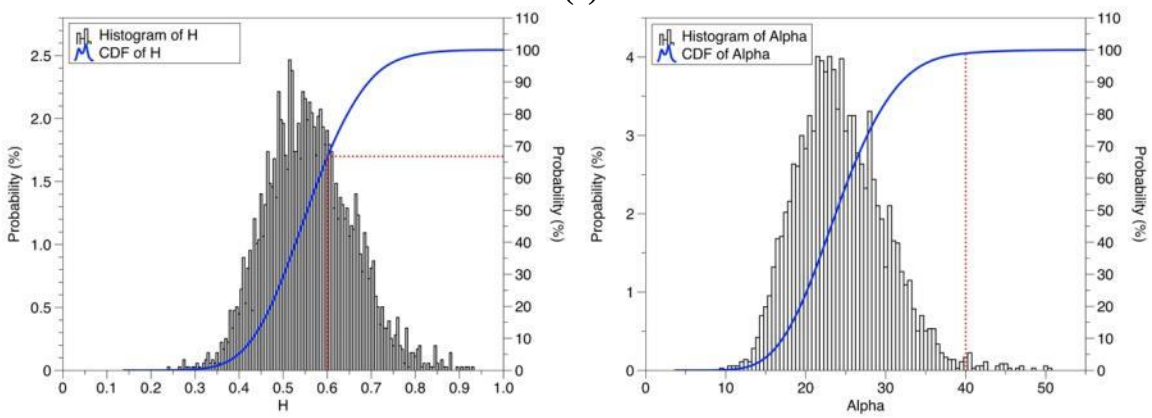

(b)

Figure 4-18. Histograms and cumulative distribution of functions (CDF) of H and α in C2 field on May 5th and May 15th.

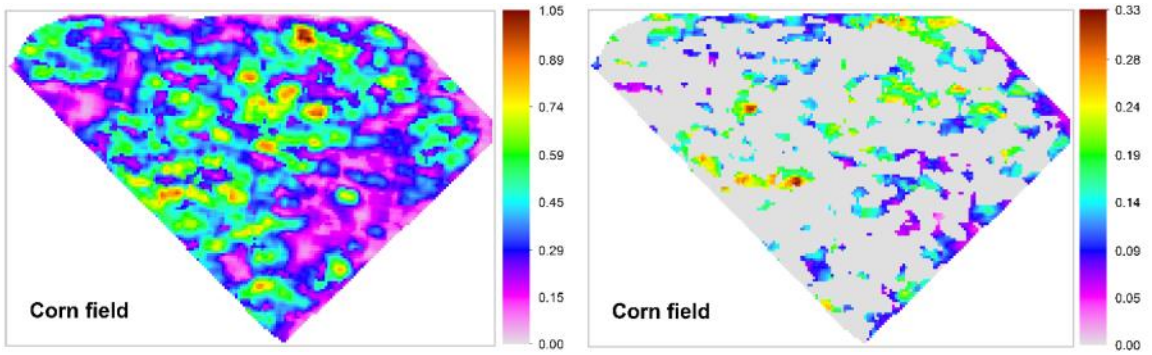

(a)

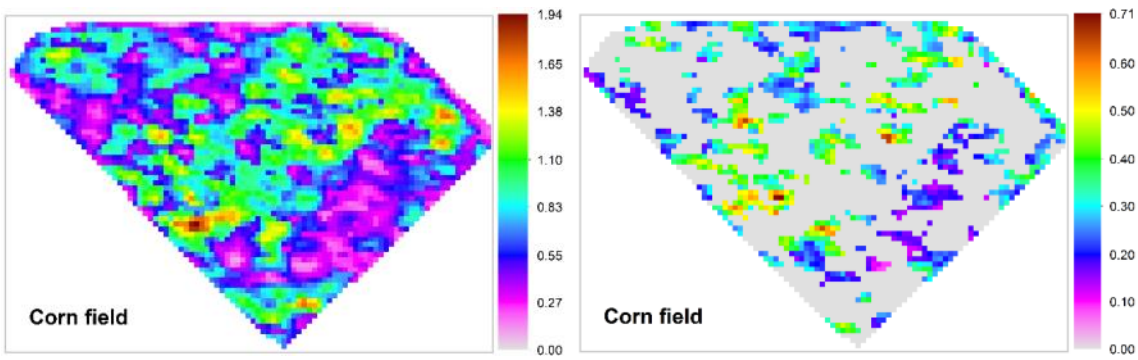

(b)

Figure 4-19. The coefficients of the surface and volume components for the bare soils on May 5th and May 15th (from left to right is the surface and volume coefficient respectively).

4.6 Conclusion

An integrated surface parameter inversion scheme is developed in this chapter, integrating the calibrated IEM and a simplified adaptive volume scattering model. The analysis of the H-α decomposition shows that the dominant scatterings are surface and volume scatterings in wheat, soybean and corn fields at their early growing stages. The dominant surface scattering caused by the bare soil and the dominant volume scattering by crop residues and fields under vegetation cover are distinguished by an H less than 0.6 and an α less than 40 degrees. For the inversion of the soil moisture, both the Y-CIEM and ISPIS have lower RMSE in the corn fields than in the soybean fields, which is due to the fluctuated scattering caused by the corn residues. However, the Y-CIEM has an overall RMSE of 8.35 [vol. %], which is higher than the 6.12 [vol. %] of the ISPIS, demonstrating the advantage of the SAVSM over the Yamaguchi volume scattering model. In terms of the surface roughness, the Y-CIEM and ISPIS have very small differences in their overall RMSEs of 0.50 and 0.48, respectively, over bare soils. However, in fields covered with corn residues or vegetation, the ISPIS has lower RMSE and performs better than that of the Y-CIEM. It should also be noted that both methods have certain underestimation, which is caused by the averaging process to avoid the intrinsic speckles of radar. The VWC of wheat derived by the ISPIS is analyzed qualitatively through comparing with the results obtained by Kim et al. (2014), demonstrating that the RVI is not only an index that describes the vegetation scattering

but also an indicator that characterizes the randomness of scattering caused by the crop residues at the beginning of the crop growing stage.

Finally, two aspects must be considered when the ISPIS is applied: one is that in addition to the dominant surface scattering, there are many volume scatterings (approximately 30% in our experiments) over bare soils, which are perhaps caused by the crop residues or the dry penetration effects, and this issue requires further investigation. Whereas the other one is the two-way attenuation caused by the vegetation canopy that has not been considered in this chapter, as at the early growing stage the two-way attenuation rates are relatively weak according to the simulated results of the MIMICS. Future research will continue to improve the ISPIS by taking into consideration the attenuation effect caused by the crop canopy to extend the model application to the whole growing season even with dense crop canopy. In addition, a multi-angular polarimetric decomposition proposed by Jagduhuber et al. (2013) uses L band to estimate the soil moisture successfully. This method attempts to improve the inversion rate of soil moisture estimation whereas the inversion rate is not a key issue in ISPIS due to the mathematical fitting. However, multi-angular data increases the number of observations, which can improve solving the unknown parameters in ISPIS.

References

An, W., Cui, Y., Yang, J., & Member, S. (2010). Three-Component Model-Based Decomposition for Polarimetric SAR Data, *IEEE Transactions on Geoscience and Remote Sensing*, *48*(6), 2732–2739.

An, W., Xie, C., Yuan, X., Cui, Y., & Yang, J. (2011). Four-Component Decomposition of Polarimetric SAR Images with Deorientation. *IEEE Geoscience and Remote Sensing Letters*, *8*(6), 1090–1094.

Alvarez-Mozos, J., Casali J., Gonzalez-Audicana, M., & Verhoest, N. E. C. (2006). Assessment of the Operational Applicability of RADARSAT-1 Data for Surface Soil Moisture Estimation. *IEEE Transactions on Geoscience and Remote Sensing*, *44*(4), 913-924.

Arii, M., van Zyl J. J., & Kim, Y. (2010). A General Characterization for Polarimetric Scattering from Vegetation Canopies. *IEEE Transactions on Geoscience and Remote Sensing*, *48*(9), 3349-3357.

Baghdadi, N., Cerdan, O., Zribi, M., Auzet, V., Darboux, F., El Hajj, M. & Bou Kheir, R. (2008). Operational Performance of Current Synthetic Aperture Radar Sensors in Mapping Soil Surface Characteristics in Agricultural Environments: Application to Hydrological and Erosion Modelling. *Hydrological Processes*, *22*(1), 9-20.

Baghdadi, N., Dubois-Fernandez, P., Dupuis, X., & Zribi, M. (2013). Sensitivity of Main Polarimetric Parameters of Multifrequency Polarimetric SAR Data to Soil Moisture and Surface Roughness over Bare Agricultural Soils. *IEEE Geoscience and Remote Sensing Letters*, *10*(4), 731-735.

Baghdadi, N., Gherboudj, I., Zribi M., Sahebi, M., King, C., & Bonn, F. (2004). Semi-Empirical Calibration of the IEM Backscattering Model Using Radar Images and Moisture and Roughness Field Measurements. *International Journal of Remote Sensing*, *25*(18), 3593-3623.

Baghdadi, N., Holah, N., & Zribi, M. (2006). Calibration of the Integral Equation Model for SAR Data in C-Band and HH and VV Polarizations," *International Journal of Remote Sensing*, *27*(4), 805-816.

Baghdadi, N., King, C., Chanzy, A., & Wigneron, J. P. (2002). An Empirical Calibration of the Integral Equation Model Based on SAR Data, Soil Moisture and Surface Roughness Measurement over Bare Soils. *International Journal of Remote Sensing*, *23*(20), 4325-4340.

Ballester-Berman, J. D., Vicente-Guijalba, F., & Lopez-Sanchez, J. M. (2013). Polarimetric SAR Model for Soil Moisture Estimation over Vineyards at C-Band. *Progress in Electromagnetics Research-Pier*, *142*, 639-665.

Chen, S. W., Wang, X. S., Li, Y. Z., & Sato, M. (2014). Adaptive Model-Based Polarimetric Decomposition Using PolInSAR Coherence. *IEEE Transactions on Geoscience and Remote Sensing*, *52*(3), 1705-1718.

Chen, S. W., Wang, X. S., Xiao S. P., & Sato, M. (2014). General Polarimetric Model-Based Decomposition for Coherency Matrix. *IEEE Transactions on Geoscience and Remote Sensing*, *52*(3), 1843-1855.

Cloude, S. R. (1992). *Uniqueness of Target Decomposition Theorems in Radar Polarimetry*. New York: Kluwer Academic.

Cloude, S. R. (2010). *Polarisation: Applications in Remote Sensing*. New York: Oxford University Press.

Cloude, S. R., & Pottier, E. (1997). An Entropy Based Classification Scheme for Land Applications of Polarimetric SAR. *IEEE Transactions on Geoscience and Remote Sensing*, *35*(1), 68-78.

De Roo, R. D., Du, Y., Ulaby, F. T., & Dobson, M. C. (2001). A Semi-Empirical Backscattering Model at L-Band and C-Band for a Soybean Canopy with Soil Moisture Inversion. *IEEE Transactions on Geoscience and Remote Sensing*, *39*(4), 864-872.

Dubois, P. C., van zyl, J. J., & Engman, T. (1995). Measuring Soil Moisture with Imaging Radars. *IEEE Transactions on Geoscience and Remote Sensing*, *33*(4), 915-926.

Freeman, A., & Durden, S. L. (1998). A Three-Component Scattering Model for Polarimetric SAR Data. *IEEE Transactions on Geoscience and Remote Sensing*, , *36*(3), 963-973.

Fung, A. K., Li, Z. Q., & Chen, K. S. (1992). Backscattering from a Randomly Rough Dielectric Surface. *IEEE Transactions on Geoscience and Remote Sensing*, *30*(2), 356-369.

Hajnsek, I., Jagdhuber, T., Schon, H., & Papathanassiou, K. P. (2009). Potential of Estimating Soil Moisture under Vegetation Cover by Means of PolSAR. *IEEE Transactions on Geoscience and Remote Sensing*, *47*(2), 442-454.

Hajnsek, I., Pottier, E., & Cloude, S. R. (2003). Inversion of Surface Parameters from Polarimetric SAR. *IEEE Transactions on Geoscience and Remote Sensing*, *41*(4), 727-744.

Hallikainen, M. T., Ulaby, F. Dobson, T., M. C., Elrayes, M. A., & Wu, L. K. (1985). Microwave Dielectric Behavior of Wet Soil-Part1: Empirical Models and Experimental Observations. *IEEE Transactions on Geoscience and Remote Sensing*, *GE-23*(20), 25-34.

Henderson, F. M. & Lewis, A. J. (1998). *Principles and applications of imaging radar*. New York: Wiley.

Huang, X., & Wang, J. (2014)., An Adaptive Volume Scattering Model for Fully Polarimetric RADARSAT-2 Data. *10th European Conference on Synthetic Aperture Radar*, Berlin, Germany, 568-571.

Jin, Y. Q., & Xu, F. (2013). *Polarimetric Scattering and SAR Information Retrieval*. John Wiley & Sons.

Jagdhuber, T., Hajnsek, I., Bronstert, A., & Papathanassiou, K. P. (2013). Soil Moisture Estimation under Low Vegetation Cover Using a Multi-Angular Polarimetric Decomposition. *IEEE Transactions on Geoscience and Remote Sensing*. *51*(4), 2201-2215.

Jagdhuber, T., Hajnsek, I., Bronstert, A., & Papathanassiou, K. P. (2014)., An Iterative, Generalized, Hybrid Decomposition on Fully Polarimetric SAR Data for Soil Moisture Retrieval under Vegetation, *10th European Conference on Synthetic Aperture Radar*, Berlin, Germany, 818-821.

Kim, Y., Jackson, T., Bindlish, R., Hong, S., Jung G., & K. Lee. (2014). Retrieval of Wheat Growth Parameters with Radar Vegetation Indices. *IEEE Geoscience and Remote Sensing Letters, 11*(4), 808-812.

Kim, Y., Jackson, T., Bindlish, Lee, H., & Hong, S. (2012). Radar Vegetation Index for Estimating The Vegetation Water Content of Rice and Soybean. *IEEE Geoscience and Remote Sensing Letters, 9*(4), 564-568.

Kim, Y., & van Zyl J. J. (2001). Comparison of Forest Estimation Techniques Using SAR Data. *IEEE International Geoscience and Remote Sensing on Geoscience and Remote Sensing Symposium*, Sydney, Australia, 1395-1397.

Kim, Y., & van Zyl, J. J. (2009). A Time-Series Approach to Estimate Soil Moisture Using Polarimetric Radar Data. *IEEE Transactions on Geoscience and Remote Sensing*, *47*(8), 2519-2527.

Le Morvan, A., Zribi, M., Baghdadi, N., & Chanzy, A. (2008). Soil Moisture Profile Effect on Radar Signal Measurement. *Sensors, 8*(1), 256-270.

Lopez-Sanchez, J. M. & Ballester-Berman, J. D. (2009). Potentials of Polarimetric SAR Interferometry for Agriculture Monitoring. *Radio Science*, *44*(2), 395-397.

Lopez-Sanchez, J. M., Hajnsek, I., & Ballester-Berman, J. D. (2012). First Demonstration of Agriculture Height Retrieval with PolInSAR Airborne Data. *IEEE Geoscience and Remote Sensing Letters, 9*(2), 242-246.

McNairn, H., Duguay, C., Brisco, B., & Pultz, T. J. (2002). The Effect of Soil and Crop Residue Characteristics on Polarimetric Radar Response. *Remote Sensing of Environment*, *80*, 308-320.

McNairn, H., Merzouki, A., Pacheco, A., & Fitzmaurice, J. (2012). Monitoring Soil Moisture to Support Risk Reduction for The Agriculture Sector Using RADARSAT-2. *IEEE Journal of Selected Topics in Applied Earth Observations and Remote Sensing, 5*(3), 824-834.

Oh, Y. (2004). Quantitative Retrieval of Soil Moisture Content and Surface Roughness from Multipolarized Radar Observations of Bare Soil Surfaces. *IEEE Transactions on Geoscience and Remote Sensing*, *42*(3), 596-601.

Oh, Y., Sarabandi, K., & Ulaby, F. T. (1992). An Empirical Model and an Inversion Technique for Radar Scattering from Bare Soil Surfaces. *IEEE Transactions on Geoscience and Remote Sensing*, *30*(2), 370-381.

Park, S. E., Moon, W. M., & Kim, D. (2009). Estimation of Surface Roughness Parameter in Intertidal Mudflat Using Airborne Polarimetric SAR Data. *IEEE Transactions on Geoscience and Remote Sensing*, *47*(4), 1022–1031.

Ponnurangam, G. G., Rao, Y.S., & Bhattacharya, A. (2014). Evaluation of Various Polarimetric Parameters for Soil Moisture Inversion Using Polarimetric SAR Data, *10th European Conference on Synthetic Aperture Radar*, Berlin, Germany, 735-738.

Rice, S.O. (1963). *Reflection of Electromagnetic Waves by Slightly Rough Sufaces*, *Interscience*, New York.

Sato, A., Yamaguchi, Y., Singh, G., & Park, S. E. (2012). Four-Component Scattering Power Decomposition with Extened Volume Scattering Model. *IEEE Geoscience and Remote Sensing Letters*, *9*(2), 166-170.

Shi, J., Wang, J., Hsu, A. Y., O'Neill, P. E., & Engman, E. T. (1997). Estimation of Bare Surface Soil Moisture and Surface Roughness Parameter Using L-Band SAR Image Data. *IEEE Transactions on Geoscience and Remote Sensing*, *35*(5), 1254-1266.

Stiven, G. A. & Khan, M. A. (1966). Saturation Percentage as a Measure of Soil Texture in The Lower Indus Basin. *Journal of Soil Science*, *17*(2), 255-273.

Toure, A., Thomson, K. P. B., Edwards, G., Brown, R. J., & Brisco, B. G. (1994). Adaptation of The MIMICS BackscatteringModel to The Agricultural Context-Wheat and Canola at L and C Bands. *IEEE Transactions on Geoscience and Remote Sensing*, *32*(1), 47-61.

Ulaby, F. T., Moore, R. K., & Fung, A. K. (1986). *Microwave remote sensing: Active and passive. Volume 3 - From theory to applications*. New York: Addison-Wesley Pub. Co., Advanced Book Program/World Science Division.

Ulaby, F. T., Sarabandi, K., McDonald, K., Whitt, M., & Dobson, M. C. (1990). Michigan Microwave Canopy Scattering Model. *International Journal of Remote Sensing*, *11*(7), 1223-1253.

van Zyl J. J., Arii, M., & Kim, Y. (2011). Model-Based Decomposition of Polarimetric SAR Covariance Matrices Constrained for Nonnegative Eigenvalues. *IEEE Transactions on Geoscience and Remote Sensing*, *49*(9), 3452-3459.

Verhoest, N. E., Lievens, H., Wagner, W., Álvarez-Mozos, J., Moran, M. S., & Mattia, F. (2008). On the Soil Roughness Parameterization Problem in Soil Moisture Retrieval of Bare Surfaces from Synthetic Aperture Radar. *Sensors*, *8*(7), 4213-4228.

Wegmüller, U., Mätzler, C., Hüppi, R., & Schanda, E. (1994). Active and Passive Microwave Signature Catalogue on Bare Soil (2–12 GHz). *IEEE Transactions on Geoscience and Remote Sensing*, *32*(3), 698-702.

Woodhouse, I. H. (2006). *Introduction to Microwave Remote Sensing*. Boca Raton: Taylor & Francis.

Yamaguchi, Y., Moriyama, T., Ishido, M., & Yamada, H. (2005). Four-Component Scattering Model for Polarimetric SAR Image Decomposition. *IEEE Transactions on Geoscience and Remote Sensing*, *43*(8), 1699-1706.

Yamaguchi, Y., Sato, A., Boerner, W. M., & Sato, R. (2011). Four-Component Scattering Power Decomposition with Rotation of Coherence Matrix. *IEEE Transactions on Geoscience and Remote Sensing*, *49*(6), 2251-2258.

Yajima, Y., Yamaguchi, Y., Sato, R., & Yamada, H. (2008). PolSAR Image Analysis of Wetlands Using a Modified Four-Component Scattering Power Decomposition. *IEEE Transactions on Geoscience and Remote Sensing*, *46*(6), 1667-1673.

Yamaguchi, Y., Yajima, Y., & Yamada, H. (2006). A Four-Component Decomposition of POLSAR Images Based on The Coherency Matrix. *IEEE Geoscience and Remote Sensing Letters*, *3*(3), 292-296.

Chapter 5 Application of Polarization Signature to Crop Monitoring and Classification*

5.1 Introduction

Synthetic Aperture Radar (SAR) with its all-weather day and night data acquisition capability provides a more reliable data source than optical sensors, which are limited by solar illumination, cloud cover, and haze (Woodhouse, 2006). In particular, Polarimetric SAR (PolSAR) with four polarization channels has more potential to reveal the target scattering mechanisms than the single polarization SAR does, which can help better capture the scattering of various targets with different shapes and structures so as to distinguish them (Lee & Pottier, 2009). More encouragingly, several countries are in preparation to launch radar constellations which will significantly reduce the revisit time and increase the multi-angle and InSAR capability. Some examples are the RADARSAT Constellation Mission (RCM) in Canada, TerraSAR (TerraSAR-X, Tandem-X and Tandem-L) in Germany, and the Sentinel constellation (Sentinel-1, Sentinel-2, and Sentinel-3, etc.) by the European Commission. The short revisit time means that repeat data coverage can be achieved within shorter intervals to avoid data gaps during key crop growth stages. It will also help the development of multi-temporal classification and analysis method.

To analyze the scattering mechanisms of the target, the widely used methods in PolSAR are based on two primary target decomposition theories: the coherent decomposition that is based on the single look scattering matrix and the incoherent decomposition that is based on the multi-look scattering matrix (Huang et al., 2015). The coherent decomposition is usually applied to analyze stationary targets such as buildings in urban

---

* A version of this chapter has been submitted and under review as "Huang, Xiaodong, Wang, Jinfei, and Shang, Jiali (2016). Application of Polarization Signature to Crop Monitoring and Classification Using Multi-Temporal C-Band Polarimetric RADARSAT-2 Imagery, *Remote Sensing of Enviroment.*"

areas, and the representative ones are the Krogager and the Cameron decompositions (Krogager et al., 1997; Cameron et al., 1996). The incoherent decomposition is mostly applied to targets that vary with time, and its representative ones are the eigen-based decomposition (Cloude & Pottier, 1997) and the model-based decomposition (Freeman & Durden, 1998). To analyze the scattering mechanisms of the targets, their decomposed polarimetric parameters are always adopted in the analysis in a mathematical way; whereas the polarization signature as a 3D plot can fully characterize responses of a target as the orientation angle and the ellipticity angle of the polarization ellipse of the target changes in a visual way (van Zyl et al., 1987), hence permits easier visual identifications of subtle changes in scattering characteristics. Over the year, many researchers have employed the polarization signature for the target scattering analysis or the coherent targets identification (Evans et al., 1998; Jafari et al., 2015; Strzelczyk & Porzycka-Strzelczyk, 2014), and we will carry on adopting the polarization signature to perform the scattering analysis in this chapter.

For land use classification, many researchers have developed various algorithms for analyzing the PolSAR data. The algorithms can be divided into three categories: 1) scattering based method, represented by the eigen-value decomposition method proposed by Cloude and Pottier (1997), which classifies targets as eight classes according to eight preset zones divided in its H-α plot. This method has been widely used in polarimetric image segmentations (Cao et al., 2007; Park & Moon, 2007). While this method is easy to use, the predefined number of classes does not always correspond to the number of classes in the PolSAR data, and misclassification can occur when the classes fall on the boundaries between the preset zones on the H- α plot. 2) statistic-based method: in which the widely used one is based on the maximum likelihood classification (MLC) with the Wishart distribution (Lee et al., 1999; Lee et al., 1994). It makes full use of the scattering matrix, so it is more suitable for the PolSAR classification; however, the physical scattering characteristics are always ignored in the Wishart classification. 3) Integrated method: to overcome the shortcoming of the Wishart classification, Lee et al. (2004) integrated the Freeman decomposition and Wishart classification to preserve the scattering mechanisms. However, misclassification occurs between the rough bare soil

and vegetation, especially for the short wavelength such as C- and X-band. In summary, all these classification methods are mostly applied to the single-date image, and targets that change over time such as crops will have reduced classification accuracy due to the similar scattering mechanisms caused by their similar geometric structure that the PolSAR primarily senses. Therefore, to improve the classification accuracy using multi-temporal images, the time dimension needs to be considered and a multi-temporal classification scheme needs to be developed. Jiao et al. (2014) made use of the multi-temporal polarimetric RADARSAT-2 data for crop mapping and obtained a higher classification accuracy than that of the single-date image when the object-oriented classification method is adopted. Based on the pixel-based classification method, Liu et al. (2013) also obtained high classification accuracy through making use of the multi-year RADARSAR-2 data. Hence, both the pixel- and object-based methods demonstrate the potential of the multi-temporal data on improving the classification accuracy. In this chapter, a new supervised binary-tree classification scheme based on the maximum difference of polarization signature (MTSBTCS-MDPS) is proposed for multi-temporal full polarimetric SAR data classification.

In addition to its application of the scattering analysis, the MTSBTCS-MDPS also takes the polarization signatures into consideration. Polarization signature has the potential to maximize the difference between two targets in certain orientation angle and ellipticity angle (van Zyl et al., 1987), which could help improve land use and land cover classification. The MTSBTCS-MDPS attempts to construct a binary tree, in which each pair of targets are distinguished based on a newly generated col-polarization or cross-polarization power image with an optimum polarization basis on an optimum data acquisition date. The optimum polarization basis is determined by the optimum orientation angle and ellipticity angle that could maximize the difference of col-polarization or cross-polarization power through comparing the polarization signatures of both targets date by date. The organization of this chapter is as follows: an introduction of the polarization signature as well as the correlation coefficient and the pedestal height (PH) is given in section 5.2; the multi-temporal binary-tree classification scheme with the maximum difference of polarization signature is given in section 5.3. The scattering

analysis and classification are performed in section 5.4. The conclusion is given in the last section.

5.2 Polarization Signature (PS)

5.2.1 Polarization Ellipse

When the propagation medium is free of mobile electric charges, the solution of the Maxwell's equation is a monochromatic plane wave, and the spatial evolution of the plane monochromatic wave shows a helical trajectory with its temporal trajectory being a polarization ellipse at a fixed position as shown in Figure 5-1.

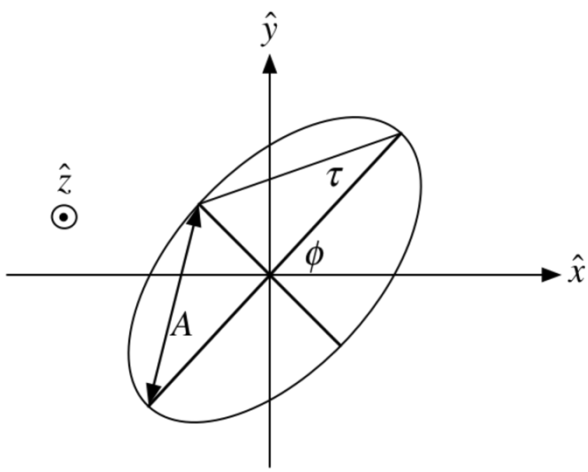

Figure 5-1. Polarization ellipse.

Figure 5-1 depicts that the geometry of the polarization ellipse is primarily described by two parameters: one is the orientation angle (ϕ) with its range from -90 degrees to 90 degrees, while the other is the ellipticity angle (τ) with its range from -45 degrees to 45 degrees. As both parameters change, the geometry of polarization ellipse changes correspondingly. Specifically, when τ is equal to 0 degrees, it becomes the linear polarization. When τ is equal to 45 or -45 degrees, it is the circular polarization. Others are the elliptical polarizations. The sign of τ determines the rotation direction of the polarization ellipse. By convention, the sense of rotation is determined while looking in the direction of propagation. When its sign is negative, it is a right hand rotation; while it

is positive, the polarization ellipse shows left hand rotation. For the current SAR antennas, only the Cartesian polarization basis is adopted, which means it transmits the H (horizontal) or V (vertical) polarization and receives the H or V correspondingly. Then, a 2 by 2 Sinclair matrix in Cartesian basis is formed to relate the transmit and receive electric field vectors (Lee & Pottier, 2009),

$$S_{(x,y)} = e^{j\phi_{hh}} \begin{bmatrix} |S_{hh}| & |S_{hv}|e^{j(\phi_{hv}-\phi_{hh})} \\ |S_{vh}|e^{j(\phi_{vh}-\phi_{hh})} & |S_{vv}|e^{j(\phi_{vv}-\phi_{hh})} \end{bmatrix} \tag{5-1}$$

where the $e^{j\phi_{hh}}$ is the absolute phase term and can be ignored. When the Stokes vector is applied, the Muller matrix that relates the transmit and receive Stokes vectors will be described as,

$$M = \begin{bmatrix} |S_{hh}|^2 & |S_{hv}|^2 & Re(S_{hv}^* S_{hh}) & -Im(S_{hv}^* S_{hh}) \\ |S_{vh}|^2 & |S_{vv}|^2 & Re(S_{vh}^* S_{vv}) & -Im(S_{vh}^* S_{vv}) \\ 2Re(S_{vh}^* S_{hh}) & 2Re(S_{vv}^* S_{hv}) & Re(S_{vv}^* S_{hh} + S_{hv}^* S_{hv}) & -Im(S_{vv}^* S_{hh} - S_{hv}^* S_{hv}) \\ 2Im(S_{vh}^* S_{hh}) & 2Im(S_{vv}^* S_{hv}) & Im(S_{vv}^* S_{hh} + S_{hv}^* S_{hv}) & Re(S_{vv}^* S_{hh} - S_{hv}^* S_{hv}) \end{bmatrix} \tag{5-2}$$

where M is the Stokes matrix while $Re(\cdot)$ means the real part and $Im(\cdot)$ means the imagery part.

5.2.2 Polarization Signature

As seen from the above section, either the Sinclair matrix or the Muller matrix only represents the polarization in the Cartesian polarization basis. To present the scattering matrix in other polarization basis, the theory of the polarization signature proposed by van Zyl et al. (1987) provides an efficient way to fully characterize the polarimetric responses of a target with its formula shown as,

$$\sigma^{\circ}(\tau_i, \phi_i, \tau_j, \phi_j) = \frac{4\pi}{k^2} \begin{pmatrix} 1 \\ cos\,2\tau_i\, cos\,2\phi_i \\ cos\,2\tau_i\, sin\,2\phi_i \\ sin\,2\,\phi_i \end{pmatrix} \cdot \left(\sum_{n=1}^{N} [M^{(n)}] \right) \begin{pmatrix} 1 \\ cos\,2\tau_j\, cos\,2\phi_j \\ cos\,2\tau_j\, sin\,2\phi_j \\ sin\,2\,\phi_j \end{pmatrix} \tag{5-3}$$

Where σ° is the polarimetric response, while τ_j and ϕ_j are the orientation angle and ellipticity angle of the receiving antenna. The τ_i and ϕ_i are the orientation angle and ellipticity angle of the transmitting antenna. The M is the Muller matrix. For each pair of transmitting and receiving orientation and ellipticity angles, there exists a corresponding polarization response. Hence, a 3D plot can be constructed when all pairs are combined together. Commonly, there are two different types of polarization signatures widely used currently: one is the co-polarization signature (col-PS) with the orientation and ellipticity angles of the receive and transmit polarizations being identical, the other one is the cross-polarization signature (cross-PS) with the orientation and ellipticity angles of the receive and transmit polarization being orthogonal. In this chapter, both polarization signatures are adopted. In practice, the coherency matrix is more widely used than the Muller matrix due to its underlying physical meanings. When the reciprocity theorem is fulfilled, the 3 by 3 coherency matrix in Cartesian polarization basis is shown as,

$$T_{3(x,y)} = \frac{1}{2}\begin{bmatrix} |\langle S_{hh}+S_{vv}\rangle|^2 & \langle S_{hh}+S_{vv}\rangle\langle S_{hh}-S_{vv}\rangle^* & 2\langle S_{hh}+S_{vv}\rangle\langle S_{hv}\rangle^* \\ \langle S_{hh}-S_{vv}\rangle\langle S_{hh}+S_{vv}\rangle^* & |\langle S_{hh}-S_{vv}\rangle|^2 & 2\langle S_{hh}-S_{vv}\rangle\langle S_{hv}\rangle^* \\ 2\langle S_{hv}\rangle\langle S_{hh}+S_{vv}\rangle^* & 2\langle S_{hv}\rangle\langle S_{hh}-S_{vv}\rangle^* & 4|\langle S_{hv}\rangle|^2 \end{bmatrix} \quad (5\text{-}4)$$

where the $|\langle S_{hh}+S_{vv}\rangle|^2$ represents the dominant surface scattering, the $|\langle S_{hh}-S_{vv}\rangle|^2$ represents the double-bounce scattering, and the $4|\langle S_{hv}\rangle|^2$ represents the volume scattering. The procedure of generating the polarization signature based on the coherency matrix is shown below (Lee & Pottier, 2009),

$$T_{3(u,u_\perp)} = U_{3T}(2\phi, 2\tau, 2\alpha)^{-1} T_{3(x,y)} U_{3T}(2\phi, 2\tau, 2\alpha) \quad (5\text{-}5)$$

where,

$$U_{3T}(2\phi, 2\tau, 2\alpha) = U_{3T}(2\phi)U_{3T}(2\tau)U_{3T}(2\alpha)$$

$$U_{3T}(2\phi) = \begin{bmatrix} 1 & 0 & 0 \\ 0 & cos2\phi & sin2\phi \\ 0 & -sin2\phi & cos2\phi \end{bmatrix}$$

$$U_{3T}(2\tau) = \begin{bmatrix} cos2\tau & 0 & jsin2\tau \\ 0 & 1 & 0 \\ jsin2\tau & 0 & cos2\tau \end{bmatrix}$$

$$U_{3T}(2\alpha) = \begin{bmatrix} cos2\alpha & jsin2\alpha & 0 \\ jsin2\alpha & cos2\alpha & 0 \\ 0 & 0 & 1 \end{bmatrix}$$

Where the $T_{3(u,u_{\perp})}$ is the coherency matrix in another polarization basis; $U_{3T}(2\phi, 2\tau, 2\alpha)$ is the rotation matrix to change the Cartesian polarization to other polarizations. It should be noted that $U_{3T}(2\alpha)$ is only related to the phase, and it's independent of the power of the polarization signature; hence, it is set to 0 degree. The powers of co-polarization and cross-polarization are,

$$Colpol = \left(Re(T_{11}) + Re(T_{22}) + 2 * Re(T_{12})\right)/2$$
$$Crosspol = Re(T_{33})/2 \tag{5-6}$$

where $T_{11} = |\langle S_{hh} + S_{vv}\rangle|^2/2$, $T_{12} = \langle S_{hh} + S_{vv}\rangle\langle S_{hh} - S_{vv}\rangle^*$, $T_{22} = |\langle S_{hh} - S_{vv}\rangle|^2/2$ and $T_{33} = 2|\langle S_{hv}\rangle|^2$. To analyze the target scattering, it is essential to understand some of the canonical scatterings such as the surface, double-bounce and helix scattering. Their coherency scattering matrices in the Cartesian polarization basis with their polarization signatures are shown in Table 5-1.

Table 5-1. Polarization signatures and coherency matrices of canonical scatterings.

Targets	**Coherency Matrix**	**Col-polarization signature**	**Cross-polarization signature**
Surface	$\begin{bmatrix} 1 & 0 & 0 \\ 0 & 0 & 0 \\ 0 & 0 & 0 \end{bmatrix}$	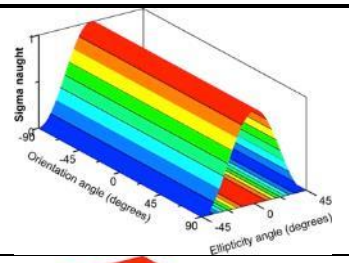	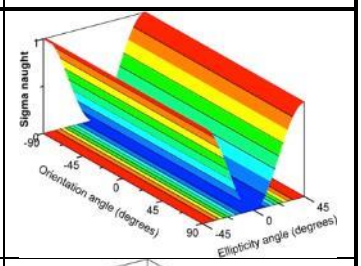
Double-bounce	$\begin{bmatrix} 0 & 0 & 0 \\ 0 & 1 & 0 \\ 0 & 0 & 0 \end{bmatrix}$	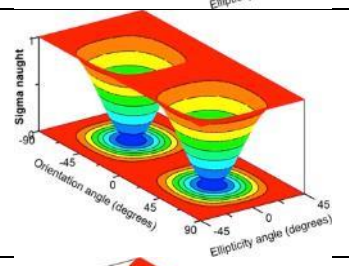	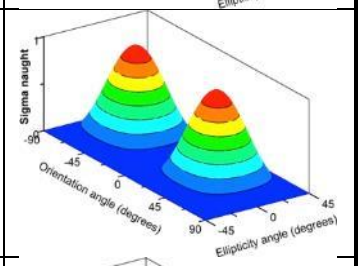
Helix	$\begin{bmatrix} 0 & 0 & 0 \\ 0 & 1/2 & 1/2\,j \\ 0 & -1/2\,j & 1/2 \end{bmatrix}$	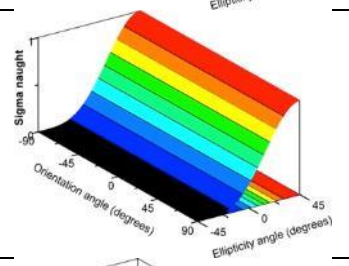	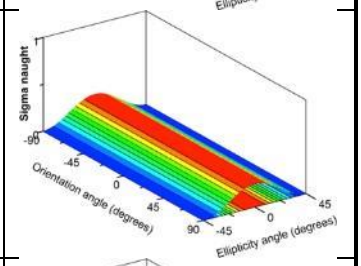
Dipole with 0 degrees	$\begin{bmatrix} 1/2 & 1/2 & 0 \\ 1/2 & 1/2 & 0 \\ 0 & 0 & 0 \end{bmatrix}$	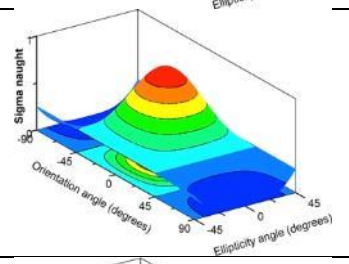	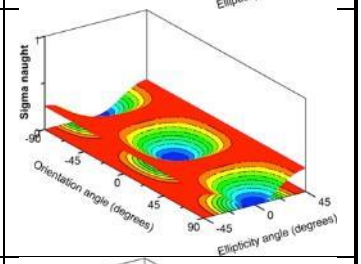
Dipole with 45 degrees	$\begin{bmatrix} 1/2 & 0 & 1/2 \\ 0 & 0 & 0 \\ 1/2 & 0 & 1/2 \end{bmatrix}$	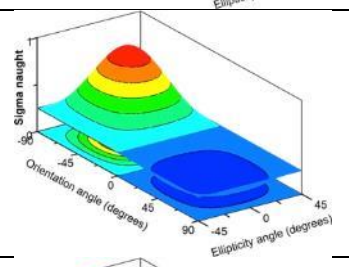	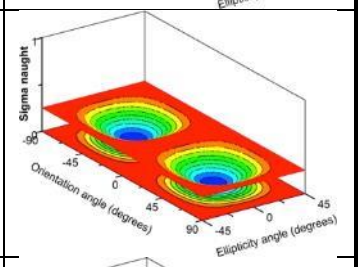
Dipole with 90 degrees	$\begin{bmatrix} 1/2 & -1/2 & 0 \\ -1/2 & 1/2 & 0 \\ 0 & 0 & 0 \end{bmatrix}$	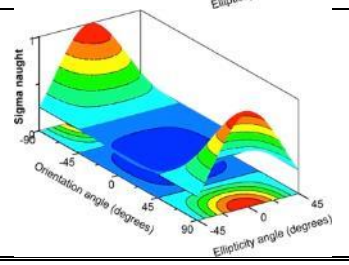	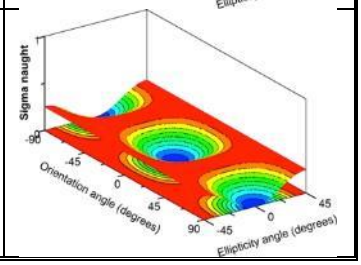

5.2.3 Correlation Coefficient and Pedestal Height of PS

The polarization signature is a full description of the scattering of the target in a 3D plot. To analyze the scattering mechanisms of the interested targets based on the polarization signatures, the Pearson correlation coefficient is employed, which is shown as,

$$r = \frac{n\sum p_1 p_2 - \sum_1^n p_1 \sum_1^n p_2}{\sqrt{[n\sum_1^n p_1^2 - (\sum_1^n p_1)^2][n\sum_1^n p_2^2 - (\sum_1^n p_2)^2]}} \tag{5-7}$$

where n is the number of the polarization states. The range of the Pearson correlation coefficient varies from -1 to 1, and the minus value means the negative correlation while the positive value means the positive correlation. Being the same as Jafari et al. (2015), it is normalized between 0 and 1 for simplicity, then the new correlation coefficient becomes,

$$P_c = 0.5 \times (r + 1) \tag{5-8}$$

Because both the col-polarization and cross-polarization signatures are adopted in this chapter, the modified correlation coefficient employed is shown as,

$$P = 0.5 \times (P_{col} + P_{crs}) \tag{5-9}$$

Where P is the correlation coefficient, and P_{col} and P_{crs} are the correlation coefficients of the col-polarization signature and the cross-polarization signature, respectively. To perform the scattering analysis, the correlation coefficient between the PS of the target and each PS of the canonical scatterings will be calculated, and the one having the highest value of P is considered to be the dominant scattering. Since the canonical scattering mentioned above are all completely polarized, to describe the un-polarized components, the pedestal height (PH) is employed and defined as,

$$PH = \frac{P_{min}}{P_{max}} \tag{5-10}$$

where PH is the pedestal height; the P_{min} is the minimum power of the PS while P_{max} is the maximum power of the PS. The value of PH is affected by different effects, while the first cause is when adjacent pixels really contain different types of scatterers, and others include multiple scattering and the presence of noise. The smaller the value of PH is, the more the backscatter cross section changes with a change in polarization with its value of zero meaning a null at some polarization; the higher value means the high un-polarization which contains many different kinds of scattering. For those canonical scattering in the previous section, all of their PH values are equal to zero, meaning the complete polarization and pure scattering.

5.3 Supervised Binary-Tree Classification Scheme (SBTCS)

5.3.1 Maximum Difference of Polarization Signature (MDPS)

The polarization signature provides a full description of the polarization response of the target in various polarization basis, which offers a potential way to discriminate the targets. Many researchers have applied its geometric shape to target discrimination or scattering analysis. However, the comparison of polarization signature shapes via the point-to-point comparison of each pair of ϕ and τ will be very time-consuming, especially when the increments of the ϕ and τ are very small. Moreover, as the number of input images (i.e., the multi-temporal images) increases, the issue becomes much more severe. In response, a simple way to distinguish two targets is developed by selecting an optimum polarization basis to maximize the difference of polarization signatures rather than comparing the shapes of the polarization signatures. The optimum ϕ and τ ($Opt(\phi, \tau, t)$) that can maximize the difference between two polarization powers are determined through comparing the power ratio of each pair of ϕ and τ. The $Opt(\phi, \tau, t)$ is determined by the maximum difference of the polarization signature (MDPS) proposed and is written as,

$$Opt(\phi,\tau) \leftarrow MDPS = max\left(\frac{max\left(PS_1(\phi_i,\tau_j), PS_2(\phi_i,\tau_j)\right)}{min\left(PS_1(\phi_i,\tau_j), PS_2(\phi_i,\tau_j)\right)}\right) \quad (5\text{-}11)$$

where the $MDPS$ is the maximum difference of the polarization signatures; $PS_1(\phi_i,\tau_j)$ and $PS_2(\phi_i,\tau_j)$ are the polarization signatures corresponding to each pair of ϕ and τ. $max(\cdot)$ and $min(\cdot)$ are the maximum and minimum value. The above equation is only suitable for the single-date image. When it is applied to the multi-temporal images, i.e., the time dimension needs to be considered in addition to the optimum ϕ and τ, and the optimum time (t) also needs to be determined, which is accomplished by the criterion that on this data acquisition date and with this pair of ϕ and τ, the ratio of power is maximum with its formula shown as,

$$Opt(\phi,\tau,t) \leftarrow MDPS = max\left(\frac{max\left(PS_1(\phi_i,\tau_j,t_k), PS_2(\phi_i,\tau_j,t_k)\right)}{min\left(PS_1(\phi_i,\tau_j,t_k), PS_2(\phi_i,\tau_j,t_k)\right)}\right) \quad (5\text{-}12)$$

Finally, as there are two different polarization signatures (the col-polarization signature and the cross-polarization signature), to make full use of them, either the col-polarization or the cross-polarization signature is adopted depending on which one has the maximum MDPS, and the optimum ϕ, τ and t is determined by,

$$\begin{cases} Opt(\phi,\tau,t) = Opt(\phi_{col},\tau_{col},t_{col}), & if\ (MDPS_{col} \geq MDPS_{crs}) \\ Opt(\phi,\tau,t) = Opt(\phi_{crs},\tau_{crs},t_{crs}), & if\ (MDPS_{col} < MDPS_{crs}) \end{cases} \quad (5\text{-}13)$$

Where $MDPS_{col}$ and $MDPS_{crs}$ are the maximum difference of polarization signatures of the col-polarization and cross-polarization signatures respectively; $(\phi_{col},\tau_{col},t_{col})$ and $(\phi_{crs},\tau_{crs},t_{crs})$ are the optimum orientation angles, ellipticity angles and time (date of acquisition) of col-polarization and cross-polarization respectively. Taking the surface and dihedral scatterings as an example, Table 5-1 shows that it is when the orientation and ellipticity angles are 0 degree and ± 45 degrees respectively, their values of PS have the maximum difference.

5.3.2 Supervised Binary-Tree Classification Scheme (SBTCS)

As each pair of targets can be maximally distinguished by an optimum polarization basis and date determined by the MDPS proposed in the previous section, a multi-temporal supervised binary-tree classification scheme based on the MDPS (MTSBTCS-MDPS) is developed. The core idea is that each pair of targets is distinguished in a new image generated by converting the data acquired on the optimum date with the optimum polarization basis determined by the MDPS. There are two primary steps included in the MTSBTCS-MDPS as listed below.

1. Look-Up Table Construction Based on MDPS

To perform the binary-tree classification, a Look-Up Table (LUT), containing the optimum ϕ, τ and t to distinguish each pair of targets, the polarization power, and polarization state (col-polarization or cross-polarization) on the MDPS, must be constructed. Firstly, a number of multi-temporal polarimetric SAR images are ingested in the algorithm. Then, the training samples of each target are selected and averaged with the mean coherency matrix to represent each target. The col- and cross- polarization signatures of each pair of targets on each date are generated using equation (5-5). Through comparing polarization signatures of each pair of targets, the optimum ϕ, τ and t to distinguish each pair of targets and the corresponding polarization power and state are determined via MDPS. Finally, a Look-Up Table (LUT) is constructed which includes the optimum ϕ, τ and t as well as the polarization power and state. This step is shown in the left side of Figure 5-2(b).

2. Binary-Tree Classification

Based on the LUT constructed from the previous step, a binary-tree classification scheme is proposed. Firstly, an initial classification map is created to include only the first class, and the value of each pixel is numbered to be 0. For each pair of targets (classes), the $\mathrm{Opt}(\phi, \tau, t)$ is selected from the constructed LUT, and the data acquired on the optimum

date will be converted to a new image with an optimum polarization basis by the optimum ϕ and τ. In this image, this pair of targets will be maximally distinguished. Then, for each pixel on this new image, either the col-polarization power or cross-polarization power will be employed based on the LUT. Then, the corresponding polarization power based on the optimum polarization basis is calculated for each pixel. Through comparing the polarization power of the unknown pixel with the power of each of the classes, this pixel is classified as this class if the distance between them is the minimum. The classification map is updated. Repeating the above procedures, other pairs of targets can be classified in the same way until the final pair is classified. This step is shown in the right side of Figure 5-2(b). The flowchart of the core algorithm of the binary-tree classification is shown in Figure 5-2(a).

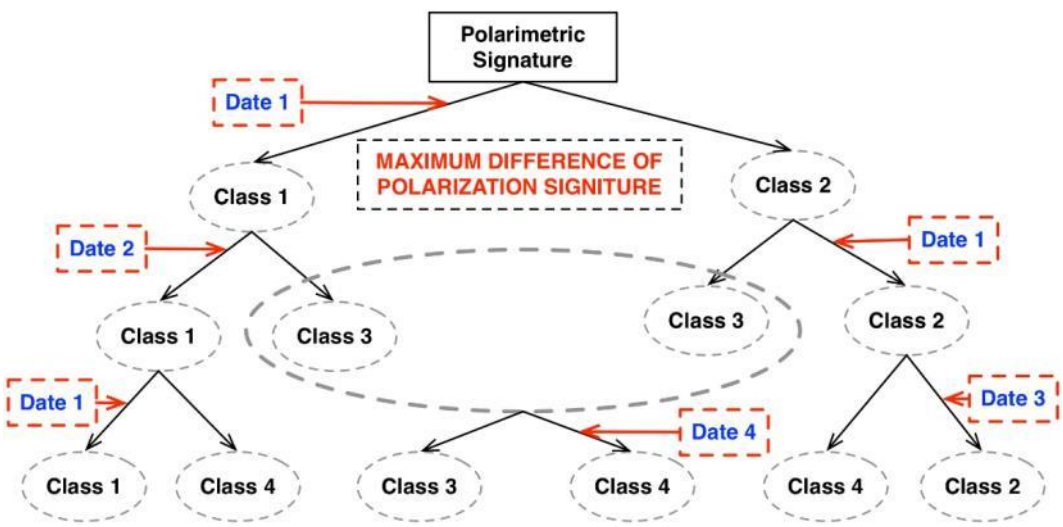

(a)

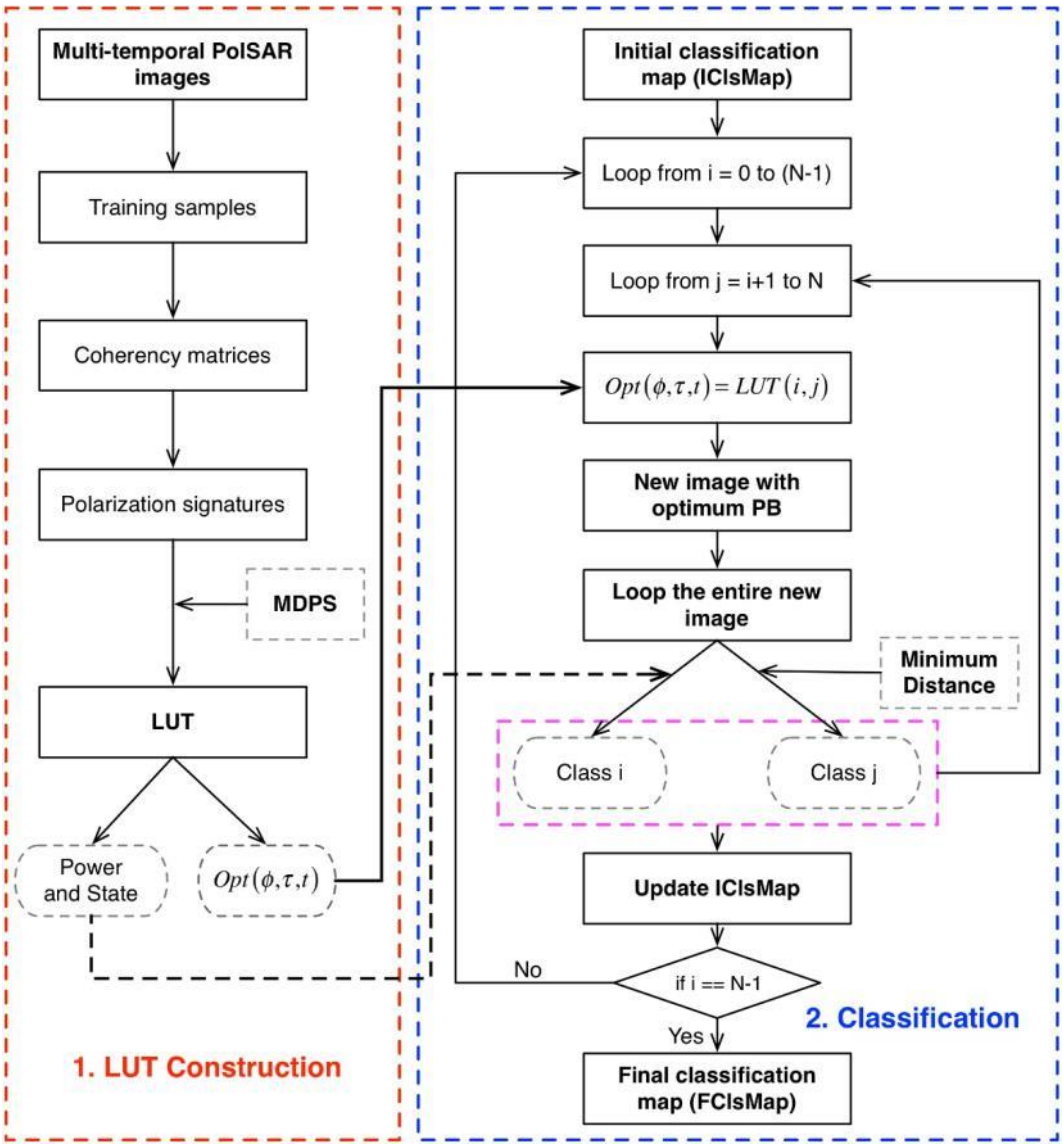

(b)

Figure 5-2. Flowchart of MTSBTCS-MDPS. (a) the core algorithm of the binary-tree classification scheme, taking 4 classes as an example, and the Date means the data acquired on that date. (b) flowchart of the MTSBTCS-MDPS. Note: PB is the polarization basis.

5.4 Scattering Analysis and Classification Validation

5.4.1 Dataset, Data Process and Ground Truth Photos

The study area is located in southwestern Ontario, Canada, and the pauli RGB from May 7th 2014 is shown in Figure 5-3. There are three main crops growing in this area: corn,

soybean and wheat. There are also some alfalfa and hay growing in this area and are referred to as grass. Figure 5-3 depicts that the urban areas are dominated by double-bounce scattering and shown in red; the forest area is dominated by volume scattering and shown in green color. As on May 7th, many fields were bare with no crops planted yet, they are shown in blue in Figure 5-3(d) with the surface scattering dominating the scene. In addition, the ground truth map as well as reference data collected in the fieldwork is also shown at the upper-right corner of Figure 5-3. The ground truth photos of corn, soybean and wheat are shown in Figure 5-4, Figure 5-5, and Figure 5-6. According to the ground truth, six classes are determined and will be classified. They are corn, soybean, wheat, grass (alfalfa, hay), forest and urban, and training samples are selected based on them as well. In terms of the available dataset, as the polarization signature can be affected by the incidence angle (Jafari et al., 2015), to avoid the effects of incidence angle variation, seven C-band fully polarimetric RADARSAT-2 data with the same mode (FQ21-40.2°) covering the entire growing stages are included in the classification (Table 5-2). Prior to performing the classification, a 9 by 9 window size Boxcar filter is applied first to reduce the image noise. Then, the MapReady software developed by the ASF facility is adopted to perform the geo-correction with an output cell resolution of 10 m by 10 m.

Table 5-2. Dataset.

Date	**Sensor mode**	**Orbit**	**Look Direction**
20120507	FQ21-40.2°	Ascending	Right
20120531	FQ21-40.2°	Ascending	Right
20120624	FQ21-40.2°	Ascending	Right
20120718	FQ21-40.2°	Ascending	Right
20120811	FQ21-40.2°	Ascending	Right
20120904	FQ21-40.2°	Ascending	Right
20120928	FQ21-40.2°	Ascending	Right

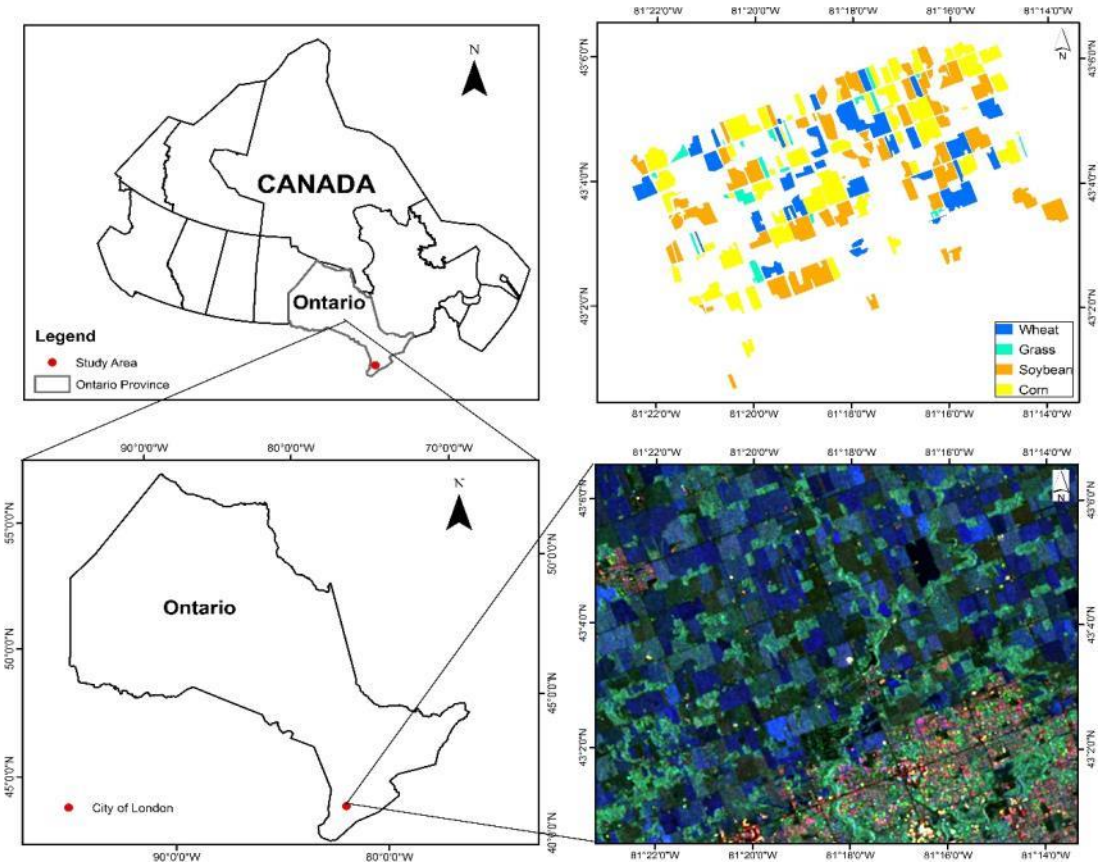

Figure 5-3. Study area and reference data.

(a) (b) (c) (d)

Figure 5-4. Ground truth photos of corn. (a) May 7th, (b) May 31st, (c) August 11th, (d) September 28th.

(a) (b) (c) (d)

Figure 5-5. Ground truth photos of soybean. (a) May 7th, (b) May 31st, (c) September 4th, (d) September 28th.

(a) (b) (c) (d)

Figure 5-6. Ground truth photos of wheat. (a) May 7th, (b) May 31st, (c) June 24th, (d) July 18th.

5.4.2 Polarization Signature Analysis

To analyze the scattering mechanisms of each target over time, the correlation coefficients between the target and the canonical targets are first calculated, which are shown in Figure 5-7. Their corresponding polarization signatures are shown in Figure 5-8, Figure 5-9, Figure 5-10, Figure 5-11, Figure 5-12 and Figure 5-13.

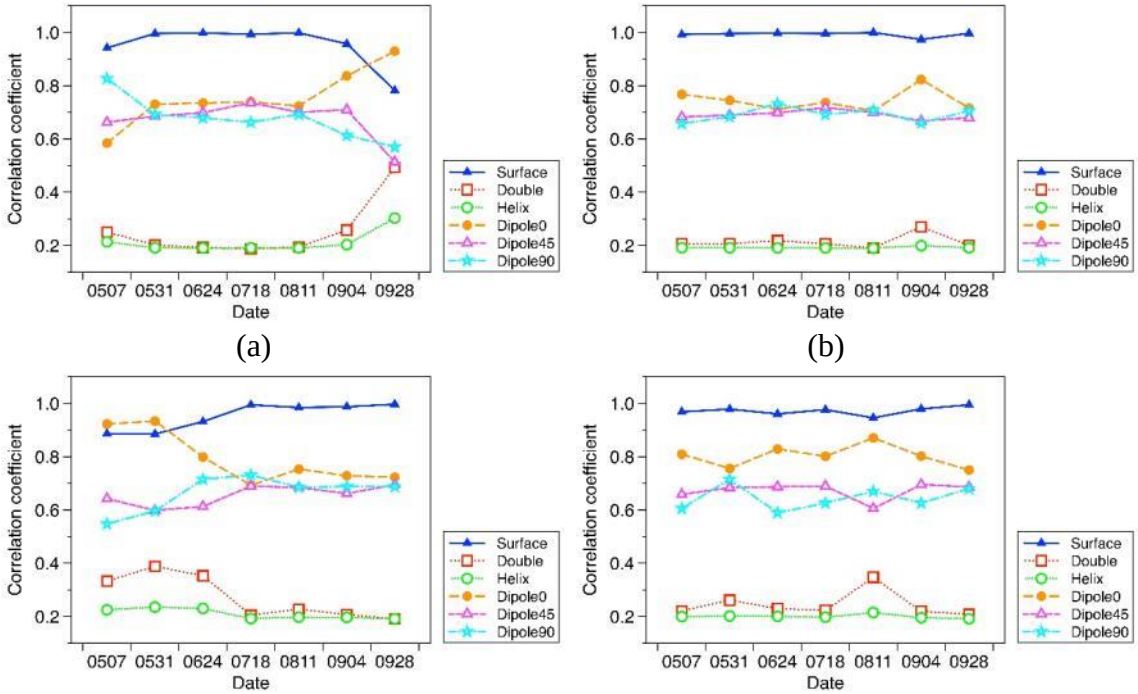

(c) (d)

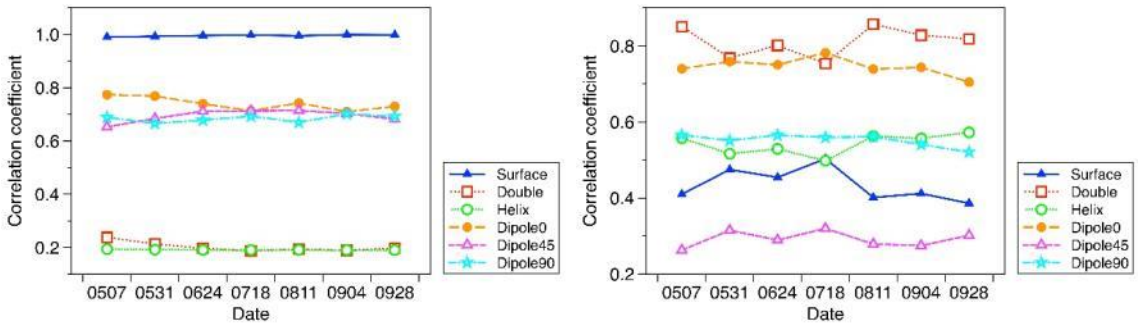

(e) (f)

Figure 5-7. Correlation coefficients of different classes on different days. (a) corn, (b) soybean, (c) wheat, (d) grass, (e) forest, (f) urban.

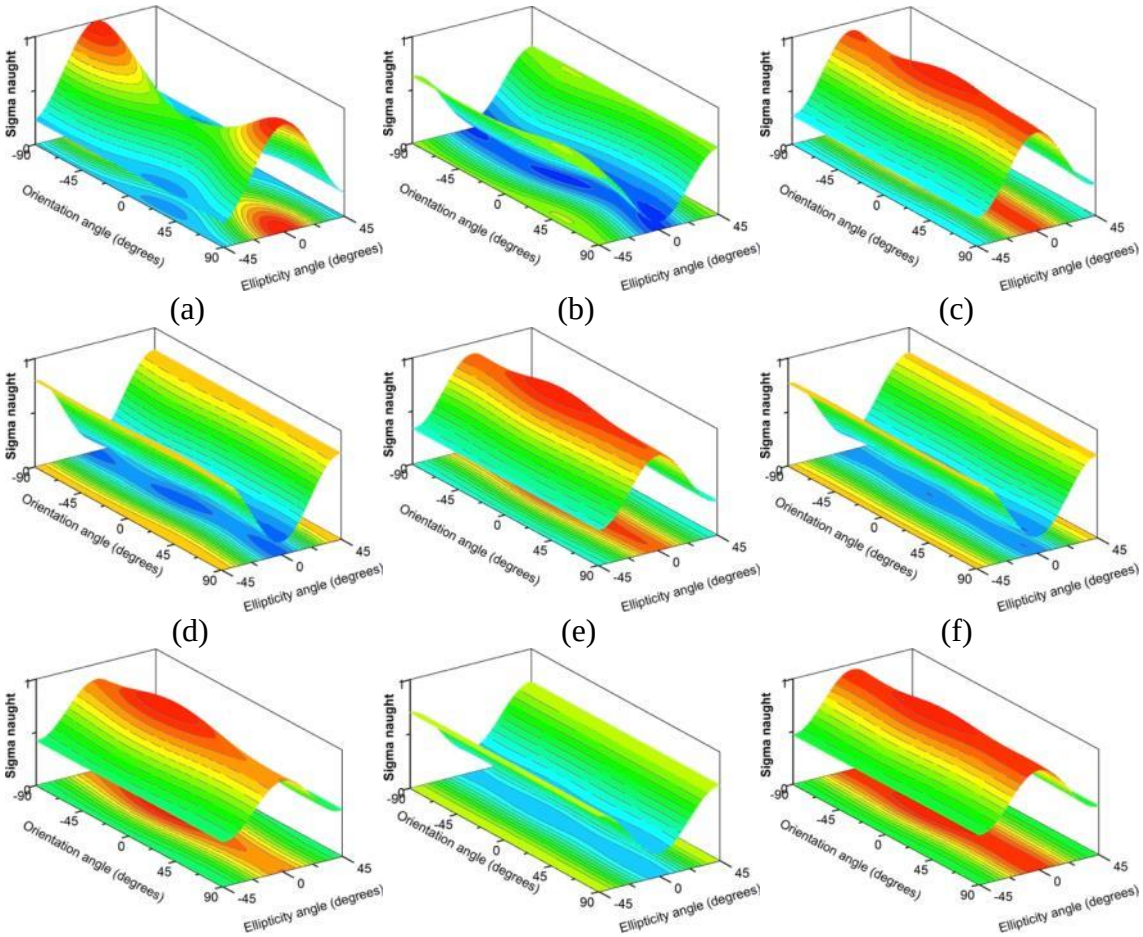

(a) (b) (c)

(d) (e) (f)

(g) (h) (i)

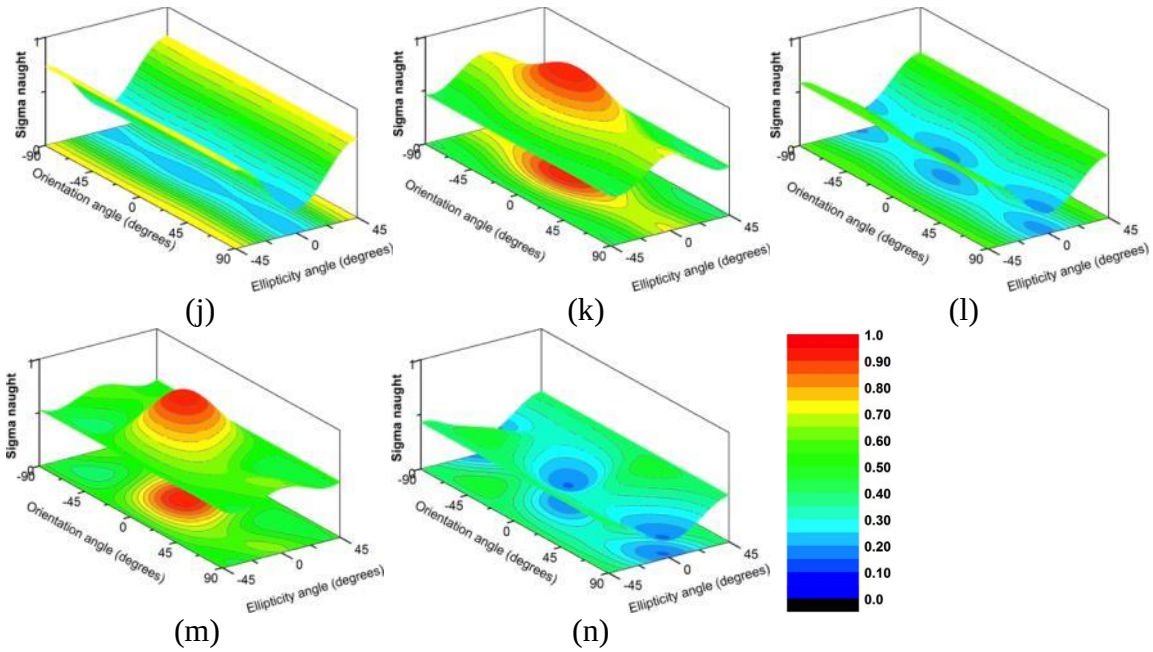

Figure 5-8. Polarization signatures of corn on different dates. (a) col-PS on May 7th, (b) cross- PS on May 7th, (c) col-PS on May 31st, (d) cross-PS on May 31st, (e) col-PS on June 24th, (f) cross-PS on June 24th, (g) col-PS on July 18th, (h) cross-PS on July 18th, (i) col-PS on August 11th, (j) cross-PS on August 11th, (k) col-PS on September 4th, (l) cross-PS on September 4th, (m) col-PS on September 28th, (n) cross-PS on September 28th.

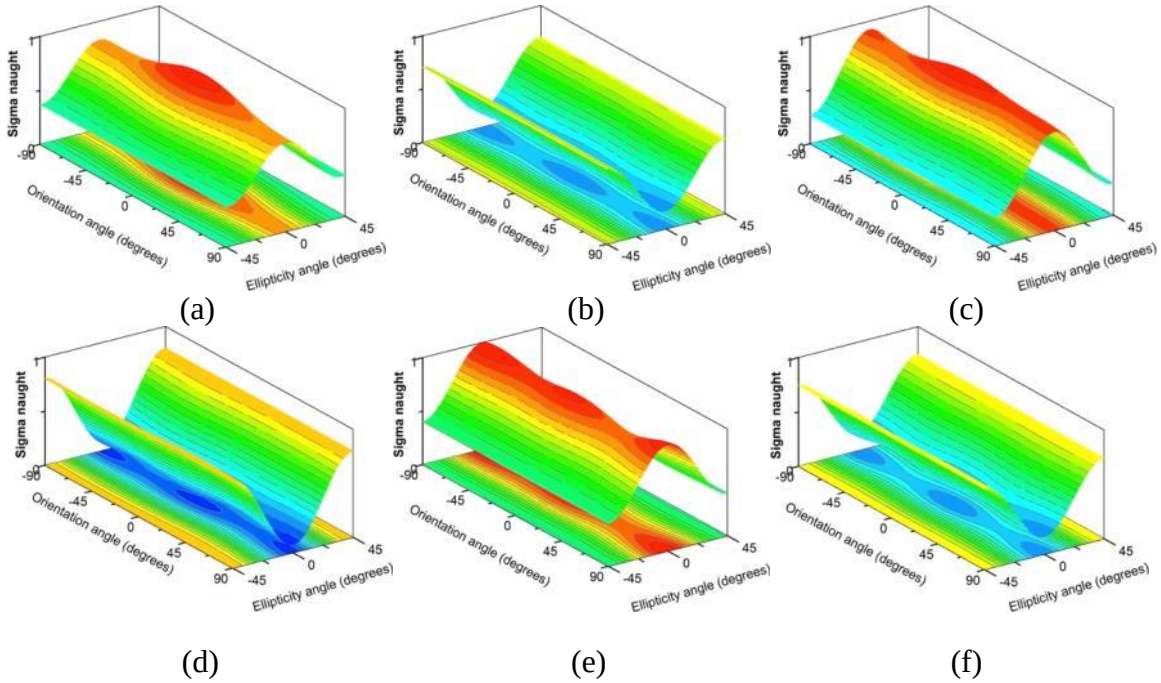

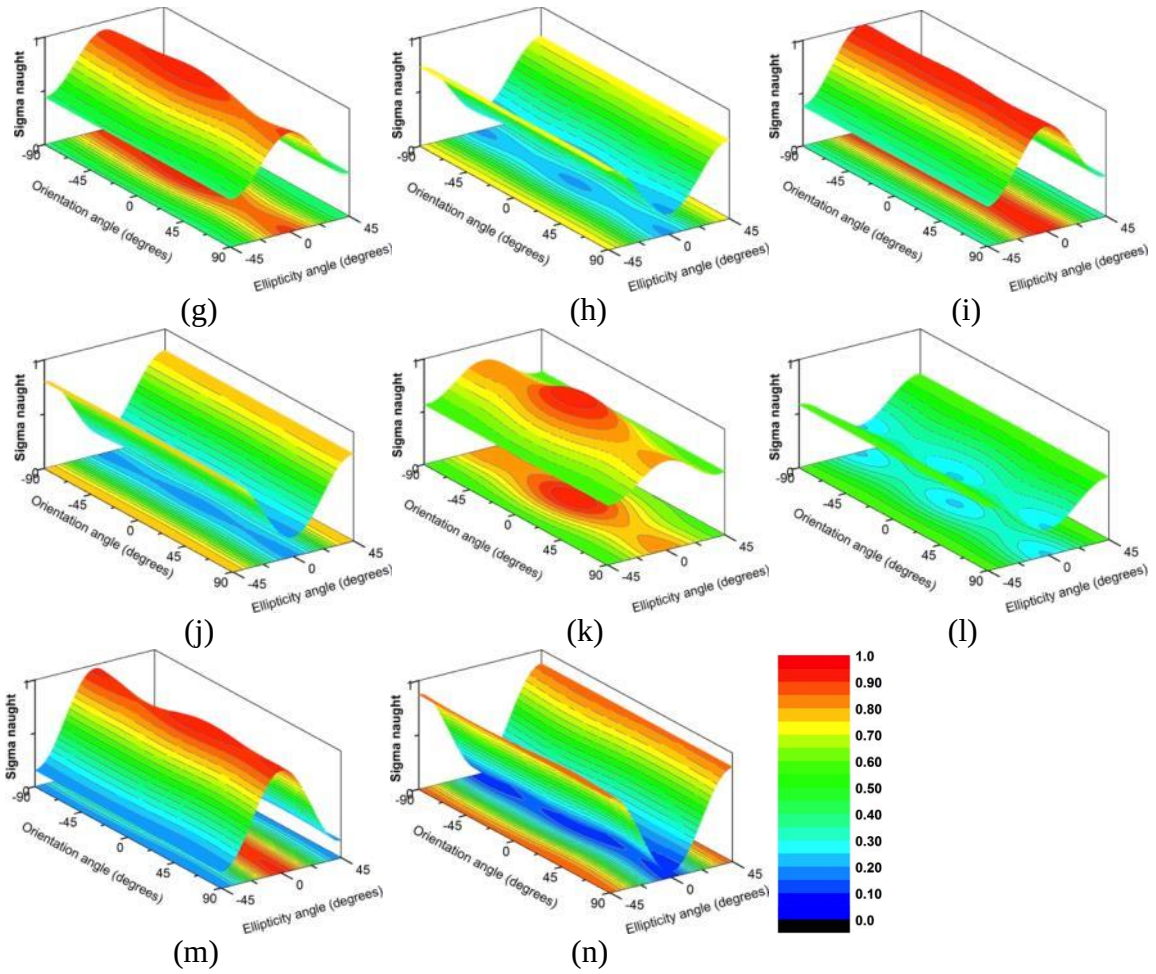

Figure 5-9. Polarization signatures of soybean on different dates. (a) col-PS on May 7th, (b) cross-PS on May 7th, (c) col-PS on May 31st, (d) cross-PS on May 31st, (e) col-PS on June 24th, (f) cross-PS on June 24th, (g) col-PS on July 18th, (h) cross-PS on July 18th, (i) col-PS on August 11th, (j) cross-PS on August 11th, (k) col-PS on September 4th, (l) cross-PS on September 4th, (m) col-PS on September 28th, (n) cross-PS on September 28th.

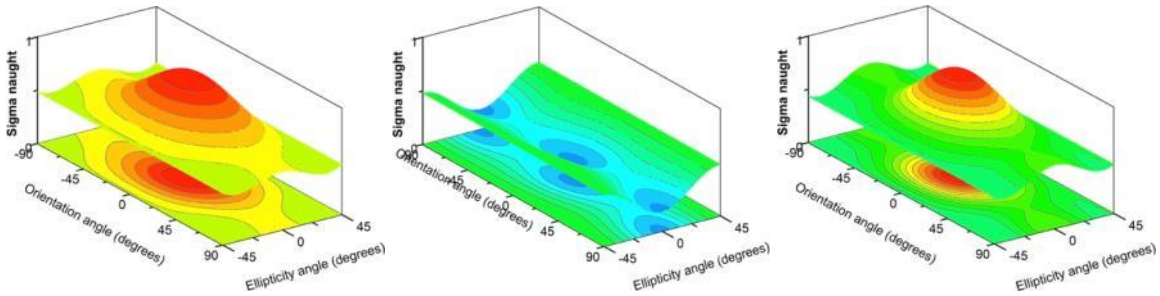

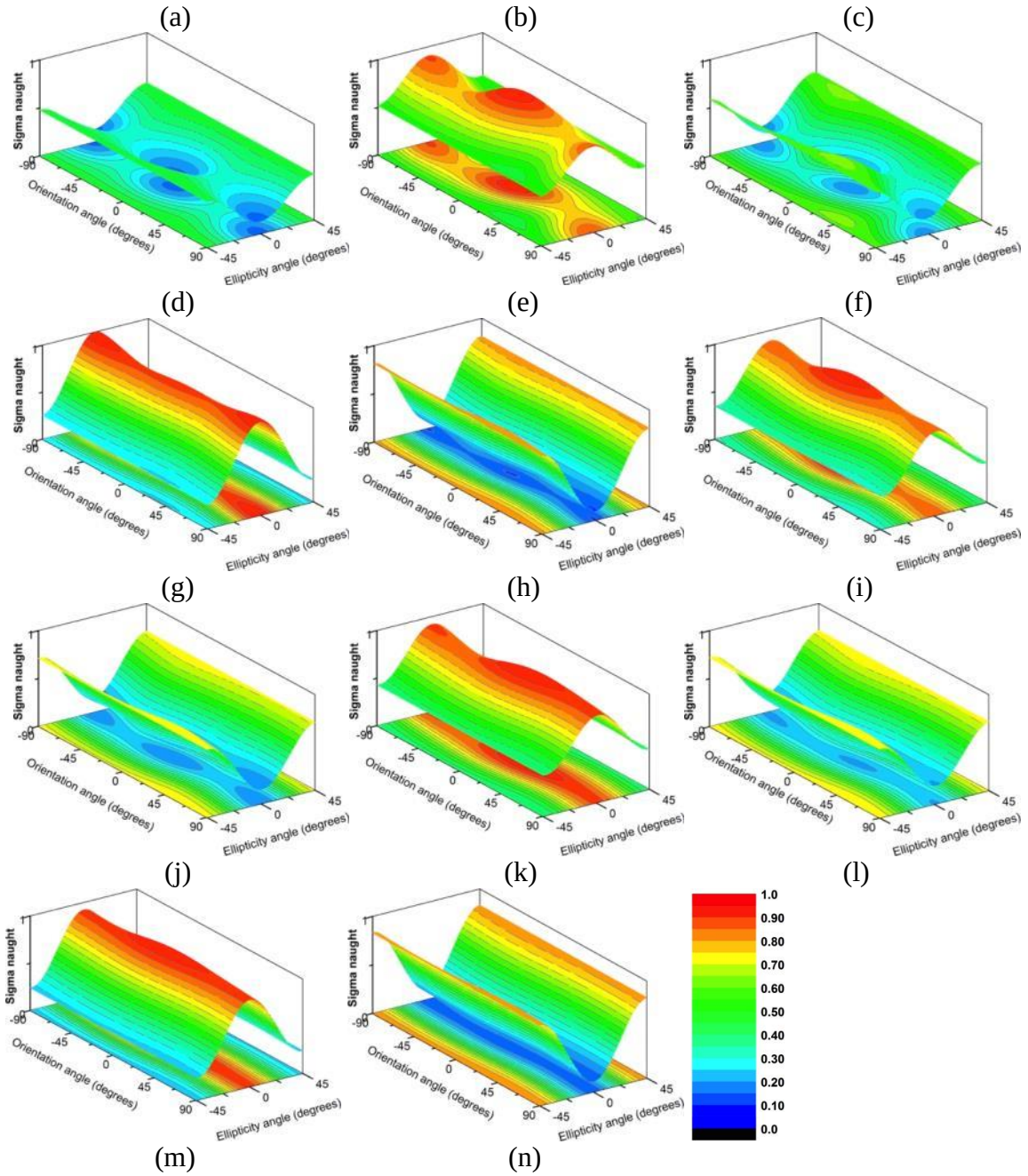

Figure 5-10. Polarization signatures of wheat on different dates. (a) col-PS on May 7th, (b) cross-PS on May 7th, (c) col-PS on May 31st, (d) cross-PS on May 31st, (e) col-PS on June 24th, (f) cross-PS on June 24th, (g) col-PS on July 18th, (h) cross-PS on July 18th, (i) col-PS on August 11th, (j) cross-PS on August 11th, (k) col-PS on September 4th, (l) cross-PS on September 4th, (m) col-PS on September 28th, (n) cross-PS on September 28th.

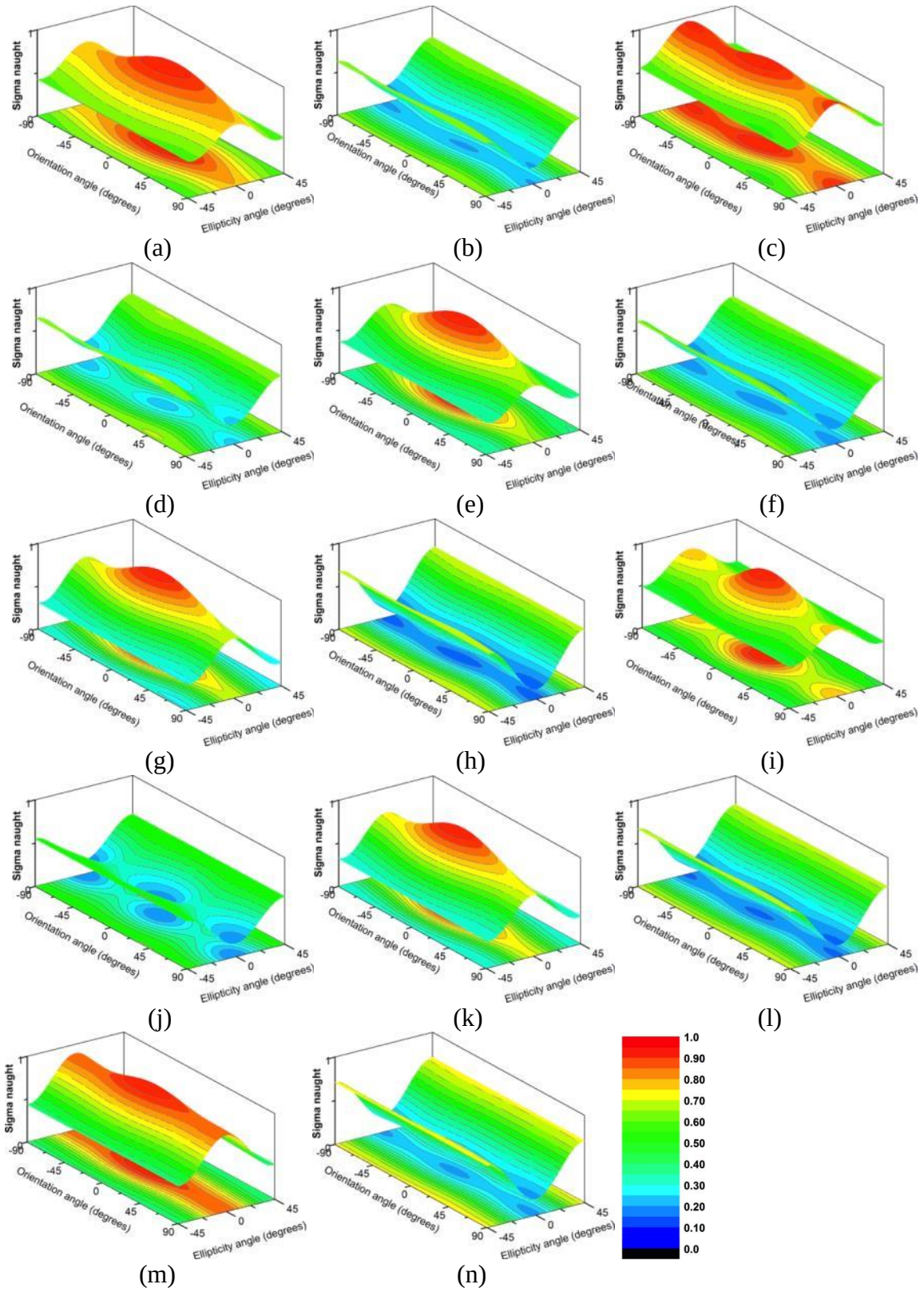
Sigma naught
Orientation angle (degrees)
Ellipticity angle (degrees)
(a)
(b)
(c)
(d)
(e)
(f)
(g)
(h)
(i)
(j)
(k)
(l)
(m)
(n)
1.0
0.90
0.80
0.70
0.60
0.50
0.40
0.30
0.20
0.10
0.0

Figure 5-11. Polarization signatures of grass on different dates. (a) col-PS on May 7th, (b) cross-PS on May 7th, (c) col-PS on May 31st, (d) cross-PS on May 31st, (e) col-PS on June 24th, (f) cross-PS on June 24th, (g) col-PS on July 18th, (h) cross-PS on July 18th, (i) col-PS on August 11th, (j) cross-PS on August 11th, (k) col-PS on September 4th, (l) cross-PS on September 4th, (m) col-PS on September 28th, (n) cross-PS on September 28th.

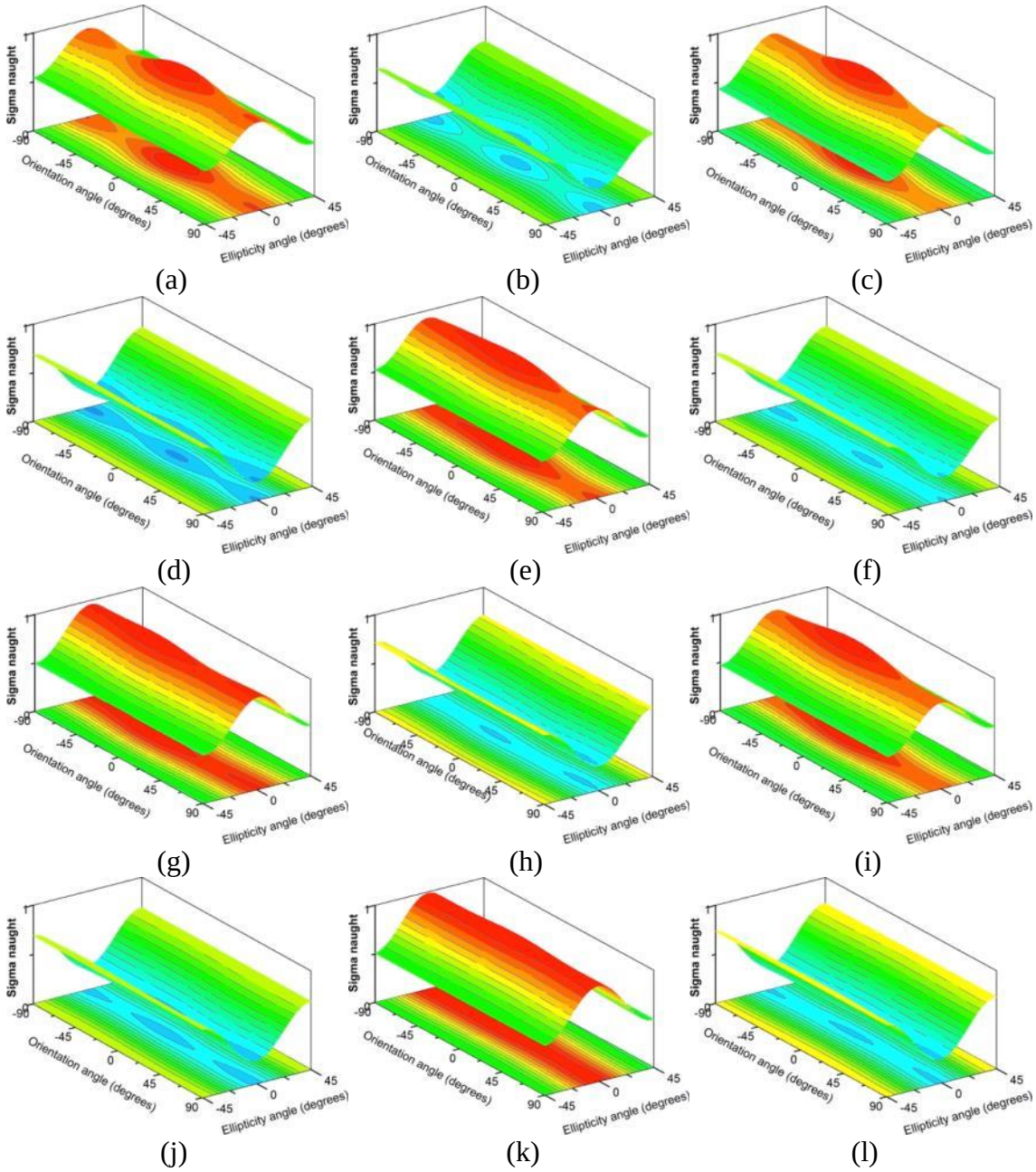

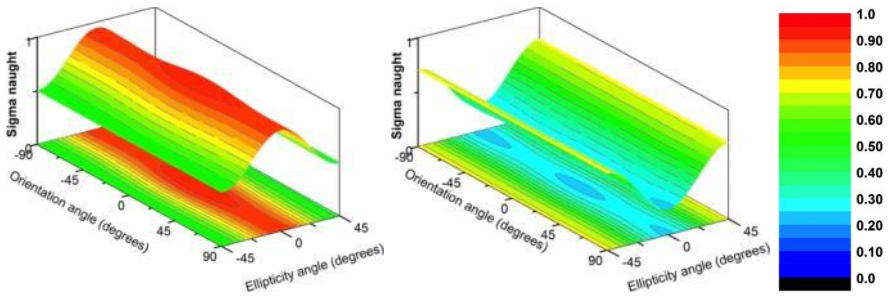

(m) (n)

Figure 5-12. Polarization signatures of forest on different dates. (a) col-PS on May 7th, (b) cross-PS on May 7th, (c) col-PS on May 31st, (d) cross-PS on May 31st, (e) col-PS on June 24th, (f) cross-PS on June 24th, (g) col-PS on July 18th, (h) cross-PS on July 18th, (i) col-PS on August 11th, (j) cross-PS on August 11th, (k) col-PS on September 4th, (l) cross-PS on September 4th, (m) col-PS on September 28th, (n) cross-PS on September 28th.

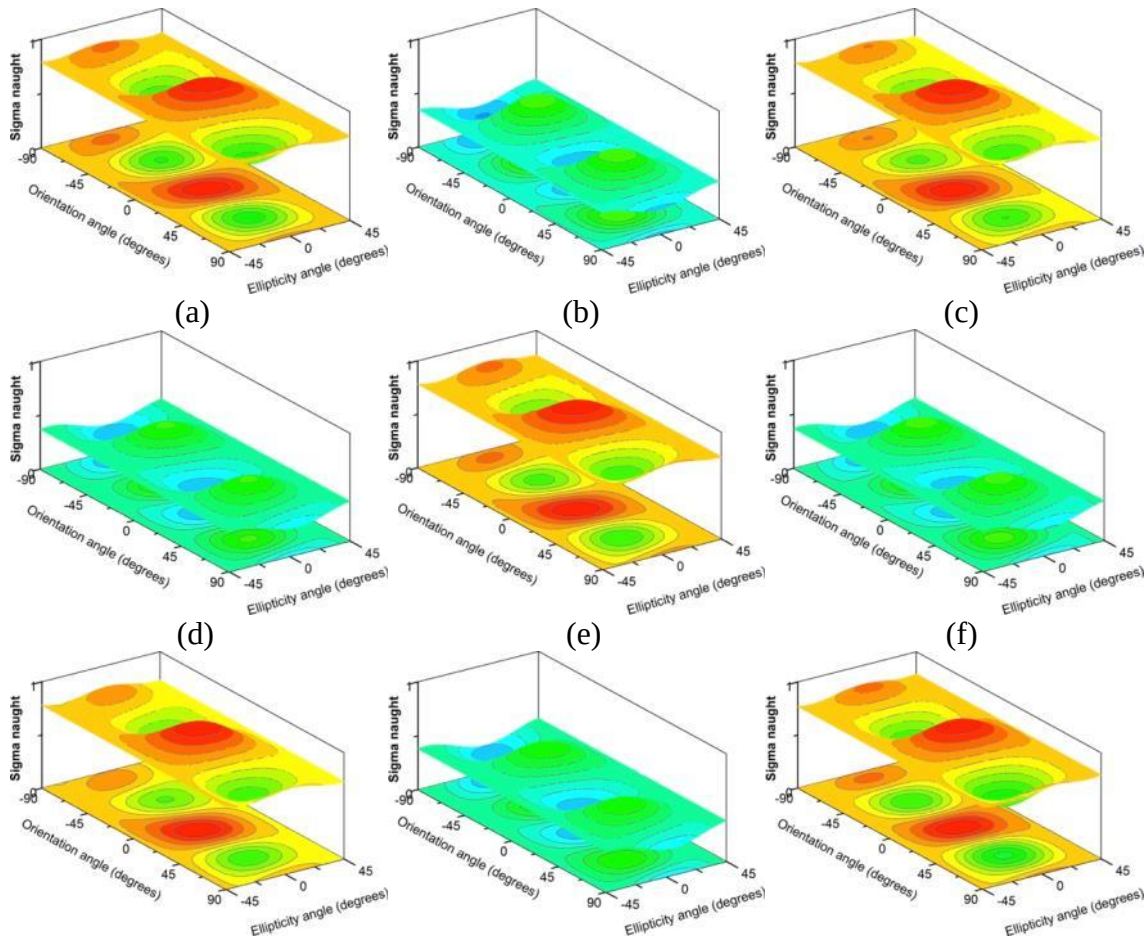

(a) (b) (c)

(d) (e) (f)

(g) (h) (i)

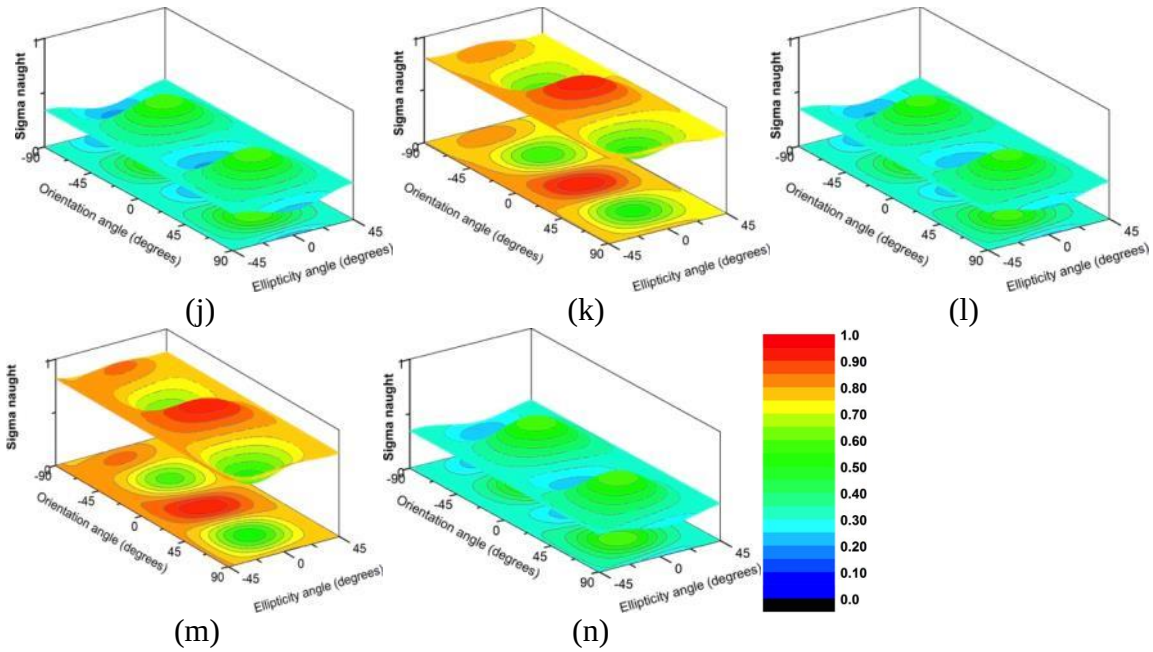

Figure 5-13. Polarization signatures of urban on different dates. (a) col-PS on May 7th, (b) cross-PS on May 7th, (c) col-PS on May 31st, (d) cross-PS on May 31st, (e) col-PS on June 24th, (f) cross-PS on June 24th, (g) col-PS on July 18th, (h) cross-PS on July 18th, (i) col-PS on August 11th, (j) cross-PS on August 11th, (k) col-PS on September 4th, (l) cross-PS on September 4th, (m) col-PS on September 28th, (n) cross-PS on September 28th.

Table 5-3. Pedestal height (PH).

	20120507	**20120531**	**20120624**	**20120718**	**20120811**	**20120904**	**20120928**
Corn	0.1672	0.2679	0.3268	0.4213	0.4630	0.4387	0.4250
Soybean	0.3717	0.2084	0.3997	0.4070	0.3758	**0.5664**	0.1540
Wheat	0.4256	0.4023	0.4845	**0.2395**	0.3360	0.4058	0.2389
Grass	0.3985	0.5452	0.3512	0.2674	0.4845	0.3092	0.4071
Forest	0.5428	0.4354	0.5007	0.4985	0.4743	0.4964	0.4962
Urban	0.5208	0.5498	0.5547	0.5623	0.4909	0.5190	0.5120

Figure 5-7(a) and Figure 5-8(a) reveal that on May 7th, the corn field was plowed with rough bare soils as shown in Figure 5-4(a), and the dominant scattering is surface scattering with the value of correlation coefficient of approximately 0.9. At this time, the helix and double-bounce scattering are rather week with both values less than 0.3. It is also observed that the dipole with 90 degrees also shows stronger than other dipole scattering, which is caused by Bragg scattering from the rough surface, in which the VV polarization is higher than the HH polarization according to the simulation of the physical

surface models (Rice, 1951; Valenzue, 1967). By May 31st, the corn field had been flattened for seed preparation; hence, the Bragg scattering is degraded to specular scattering caused by the very smooth surface, making its polarization signature being similar to the canonical surface scattering shown in Table 5-1. On both days, their PH values are very low with their values less than 0.3 as shown in Table 5-3, which means weak un-polarization. From May 31st to August 11th, the polarization signatures are rather similar to the canonical surface scattering as shown in Table 5-1, which suggests that the surface scattering is always dominant during this period of time, which are primarily caused by the broad corn leaves of the corn canopy due to the limited capacity of wave penetration as corn grows denser and denser. The coefficient correlation values of three kinds of dipoles are almost equal, demonstrating a random scattering with high PH with its value of approximately 0.45. When time goes to September, the water content of corn leaves decrease and the corn leaves start to become yellow and dry as shown in Figure 5-4(d). The C-band wave can penetrate the corn canopy more easily during this time; hence, the scattering caused the interaction among the corn stalks increases while the surface scattering decreases with its correlation coefficient reducing to approximately 0.8. The double-bounce scattering caused by the interaction between the crop stems and the ground also increases with its value being up to 0.5. The helix scattering caused by the interaction among the corn stems also increases. It also shows that during this time the scattering from the dipole with 0 degrees (HH polarization) is much higher than that of the VV polarization (dipole with 90 degrees), which is perhaps caused by the attenuation effects where the VV polarization attenuated much more than that of the HH polarization according to the scattering simulation by Michigan Microwave Canopy Scattering Model (MIMICS) (Huang et al., 2016). These polarization signatures are shown in Figure 5-8(k), Figure 5-8(l), Figure 5-8(m), and Figure 5-8(n).

In terms of the soybean, at the beginning of its growth, many small pieces of corn residues layered on the soybean field. Hence, the scattering caused by the corn residues as shown in Figure 5-5(a) results in the scattering from the dipole with 0 degrees higher than that of other dipole scattering as shown in Figure 5-9(a), but the surface scattering is still dominant as shown in Figure 5-7(b). Its PH is also high with a value of

approximately 0.4, caused mainly by the multiple scattering resulted from the corn residues. As the soybean grows taller and denser, its PH increases from 0.2 to up to 0.56 as shown in Table 5-3, but the surface scattering keeps almost unchanged as shown from Figure 5-9(c) to Figure 5-9(j) with their values of correlation coefficients all greater than 0.9. These surface scattering are primarily caused by the broad leaves of the soybean. During this period of time, it also should be noted that the correlation coefficients of all dipoles are almost the same and no dominant dipole scattering exists, which means a high randomness of the scattering. Similar to the corn field, as the leaves of the soybean become yellow as shown in Figure 5-5(c), the C-band wave penetrates the soybean canopy resulting in multiple scattering due to the interaction among the small soybean branches. Hence, many kinds of scattering are induced, which result in a very high PH value on September 4th. Figure 5-7(b) shows that on September 4th, the double-bounce scattering increases while the surface scattering decreases but still dominated, and the scattering from the dipole with 0 degrees also increases as shown in Figure 5-9(k) and Figure 5-9(l). Finally, as the soybean becomes much dryer and lost almost its leaves at this stage, only the stems and pods existed, the C-band wave can penetrate it completely, the surface scattering is only from the smooth bare soils.

For the wheat field, at its early growing stages, Figure 5-7(c) shows that the surface scattering and the dipole scattering are dominant, which can also be seen from their polarization signatures shown in Figure 5-10(a) to Figure 5-10(d). Both values of correlation coefficient are around 0.7 with their values of PH greater than 0.4. It demonstrates that the wheat leaves at their early growing stages cause prominently the dipole scattering with 0 degree. As the wheat grows taller and denser, the heads of wheat and the stems are coming out as shown in Figure 5-6(b), and the scattering from the dipoles with 90 degrees caused by the stems and heads increases with their polarization signatures shown in Figure 5-7(c). In addition, as the leaves of wheat become dry and yellow as shown in Figure 5-6(c), the scattering from the dipoles with 90 degrees caused by its stems increases with its correlation coefficient greater than that on May 31st when the leaves were green. This is also observed from its polarization signature as shown in Figure 5-10(e) and Figure 5-10(f). During this time, its PH value increases to

approximately 0.5, due to the multiple scattering caused by the interaction among the wheat stems. On July 8th, the wheat was harvested, and the stubbles left on the ground were very dry; hence, the surface scattering from the bare soil are dominant with the value of PH at approximately 0.2, while the double-bounce scattering caused by the wheat stem and the ground surface also decreases as shown in Figure 5-7(c). After that, the grass started to grow on the harvested wheat field, and their scattering will be analyzed in the next paragraph.

Due to the limited ground truth photos of the grass, its scattering is merely analyzed according to its polarization signatures. The grasses growing in this region are primarily alfalfa and hay, which have similar appearance to wheat at the early growing stages. Hence, we infer that the surface scattering is dominant as can be seen from Figure 5-7(d), and the polarization signatures also show similar geometric shape to surface scattering as shown from Figure 5-11(a) to Figure 5-11(h). In addition, the scattering from the dipole with 0 degree, which are perhaps caused by the grass leaves, has much higher values of correlation coefficients than that of other dipoles. At the final growing stages, the grass becomes mature and dry, the surface scattering from the ground increases, and the scattering from the dipole with 0 degree decreases. In terms of its PH, when it grew denser till June 24th, its PH increases. On July 18th, its PH decreases significantly with its value at approximately 0.25. From this we could perhaps infer that the grass had been harvested before this date.

The scattering of the forest is very interesting, with its polarization signatures over the entire growing seasons remain the same as the surface scattering as can be seen from Figure 5-12. This is because forest regions are in the trihedral scattering component, which corresponds to the flat and sphere targets while the forest leaves are very broad, which also demonstrates the limited capacity of short wavelength penetration. Table 5-3 depicts that its PH value is always high over the entire growing season due to its dominant volume scattering with its value almost higher than 0.5. There are some minor differences as can be seen from Figure 5-7(e). At the beginning of May, the leaves of the trees were not coming out yet; hence, the C-band wavelength can penetrate the forest

canopy more easily. The scattering from the dipole with 0 degrees caused by the tree branches is higher than other dipole scatterings. Meanwhile, the double-bounce scattering caused among the small branches is also higher at this stage than that at other stages. However, as the forest canopy grows denser and denser, the surface scattering is primarily caused by the top of the forest canopy. We also observe that during this time, its HH polarization is slightly greater than VV polarization, and this is because in heavily forested area, the return for the horizontal and vertical linear polarization is very similar, but the vertical is being slightly smaller as demonstrated by Durden et al. (1989). That is the reason why the HH polarization is slightly higher than that of the VV polarization during the time between May 31st and August 11th as shown in Figure 5-12(c) to Figure 5-12(j). In terms of the dipole scatterings, as the leaves of the forest become denser, values of the dipole with 0 degree, 45 degrees and 90 degrees are almost equal, which suggests the completely random scattering.

Finally, as urban is a stationary target, its polarization signatures are almost the same and very similar to that of the double-bounce scattering over time, which can be seen from Figure 5-13. In theory, its PH value should be lower than that of the vegetation; however, Table 5-3 shows that all the values of the PH are almost greater than 0.5 owing to the relatively high unpolarized return from this area, while this unpolarized component is directly caused by multiple scatters or heterogeneity (Zhang et al., 2015). Urban area consists of a mixture of low- and high-entropy processes, which are due to the different street/building classes that are aligned along the radar look direction or aligned somewhat off bore sight or 45 degrees aligned. As shown in Figure 5-7(f), the double-bounce scattering caused by the wall of the building and the ground is always dominant with its value of correlation coefficient at around 0.8 on each date. Meanwhile, the helix scattering is also very high compared with other targets such as the forest, corn, soybean, wheat, and grass, which is in agreement with Yamaguchi et al. (2005) on that the urban areas can easily cause the helix scattering. The scattering from the dipole with 0 degree is also very high. The surface scattering is much lower compared with that of the crop.

5.4.3 Classification

To perform the proposed classification scheme on multi-temporal polarametric SAR data, the Look-Up Table (LUT) contains the optimum ellipticity angle, orientation angle, and the optimum data acquisition date is constructed first, which is shown in Table 5-4. It depicts that each pair of classes can be maximally distinguished only by the linear polarization because the optimum ellipticity angles are almost 0 degree. In addition, when seven images are input to the algorithm, only three of them are selected for classification. They are May 7th, July 18th, and September 28th, which are the dates at the beginning, the middle, and the end of the growing season. It also should be noted that the polarization signatures employed are all cross-polarization signatures. Combining the LUT and the binary-tree classification scheme developed, the classification results are shown in Figure 5-14. For validation purpose, this classification method is also compared with the traditional Wishart classification in two aspects. The first one is to compare the MDPS with the Wishart distance (WD), and both MDPS and WD are applied to the binary-tree classification scheme on the single-date data; while the second one is comparing them when they are applied to multi-temporal images within the binary-tree classification scheme as well. It should be noted that as the WD does not depend on the polarization basis, there are no optimum orientation angle and ellipticity angles to be determined. It should also be noted that the calibrated sigma naught (i.e., backscattering coefficient) is almost less than 1, hence, the log operation in the Wishart classifier will lead to a negative value. To avoid this issue and not affect the classification results, the value of each pixel is multiplying by 10^5. Then, the optimum dates determined for the classification are shown in Table 5-5. Compared with the MDPS, it depicts that when seven images are applied to the binary-tree classification scheme, only five images are selected as the input images, while the MDPS only has three. Moreover, for each pair of classes, their WD are all at approximately 40 even though some are greater than 50. The classification results are shown in Figure 5-14.

Table 5-4. Look-Up Table of MTSBTCS-MDPS.

		Corn	**Soybean**	**Wheat**	**Grass**	**Forest**	**Urban**
Corn	*Date*		20120928	20120718	20120928	20120507	20120507
	Phi		33.0	2.0	-47.0	89.0	57.0
	Tau		3.0	0.0	-6.0	-1.0	1.0
	IsCol		0	0	0	0	0
	Power 1		0.0597	0.0232	0.0672	0.0057	0.0075
	Power 2		0.0084	0.0020	0.0168	0.0291	0.1071
Soybean	*Date*	20120928		20120718	20120507	20120507	20120507
	Phi	33.0		-88.0	-1.0	3.0	57.0
	Tau	3.0		0.0	0.0	0.0	1.0
	IsCol	0		0	0	0	0
	Power 1	0.0597		0.0201	0.0034	0.0034	0.0055
	Power 2	0.0084		0.0020	0.0106	0.0292	0.1071
Wheat	*Date*	20120718	20120718		20120718	20120718	20120718
	Phi	2.0	-88.0		3.0	-89.0	-30.0
	Tau	0.0	0.0		0.0	0.0	-1.0
	IsCol	0	0		0	0	0
	Power 1	0.0232	0.0201		0.0020	0.0020	0.0032
	Power 2	0.0020	0.0020		0.0088	0.0328	0.1000
Grass	*Date*	20120928	20120507	20120718		20120718	20120718
	Phi	-47.0	-1.0	3.0		90.0	57.0
	Tau	-6.0	0.0	0.0		-1.0	2.0
	IsCol	0	0	0		0	0
	Power 1	0.0672	0.0034	0.0020		0.0088	0.0122
	Power 2	0.0168	0.0106	0.0088		0.0329	0.1036
Forest	*Date*	20120507	20120507	20120718	20120718		20120928
	Phi	89.0	3.0	-89.0	90.0		52.0
	Tau	-1.0	0.0	0.0	-1.0		-1.0
	IsCol	0	0	0	0		0
	Power 1	0.0057	0.0034	0.0020	0.0088		0.0298
	Power 2	0.0291	0.0292	0.0328	0.0329		0.1110
Urban	*Date*	20120507	20120507	20120718	20120718	20120928	
	Phi	57.0	57.0	-30.0	57.0	52.0	
	Tau	1.0	1.0	-1.0	2.0	-1.0	
	IsCol	0	0	0	0	0	
	Power 1	0.0075	0.0055	0.0032	0.0122	0.0298	
	Power 2	0.1071	0.1071	0.1000	0.1036	0.1110	

Table 5-5. Look-Up Table of the MTSBTCS-WD.

		Corn	Soybean	Wheat	Grass	Forest	Urban
Corn	*Date*		20120928	20120718	20120928	20120507	20120531
	WD		39.0382	41.9817	37.3879	38.4119	43.7008
Soybean	*Date*	20120928		20120718	20120811	20120531	20120531
	WD	39.0382		41.2173	37.7661	40.4564	47.4302
Wheat	*Date*	20120718	20120718		20120811	20120718	20120718
	WD	41.9817	41.2173		36.4559	46.2753	55.5681
Grass	*Date*	20120928	20120811	20120811		20120718	20120531
	WD	37.3879	37.7661	36.4559		37.6831	40.6814
Forest	*Date*	20120507	20120531	20120718	20120718		20120531
	WD	38.4119	40.4564	46.2753	37.6831		38.7469
Urban	*Date*	20120531	20120531	20120718	20120531	20120531	
	WD	43.7008	47.4302	55.5681	40.6814	38.7469	

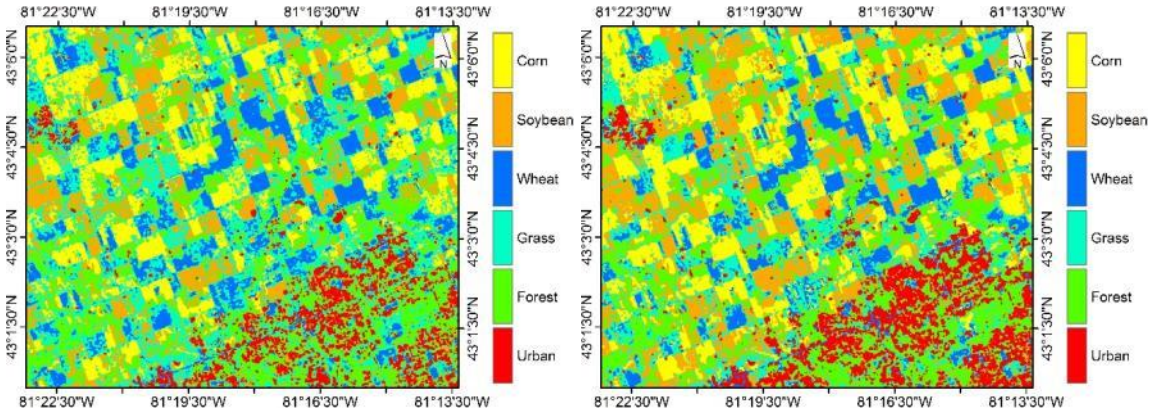

(a)

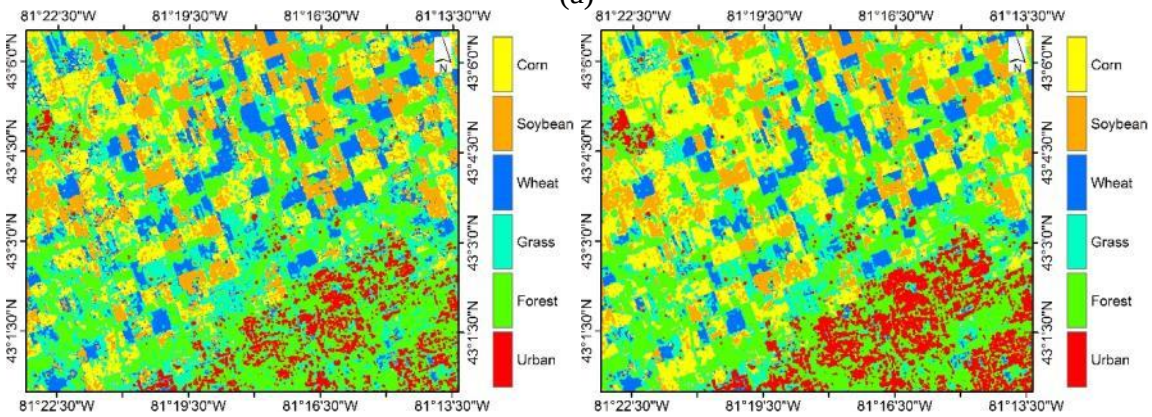

(b)

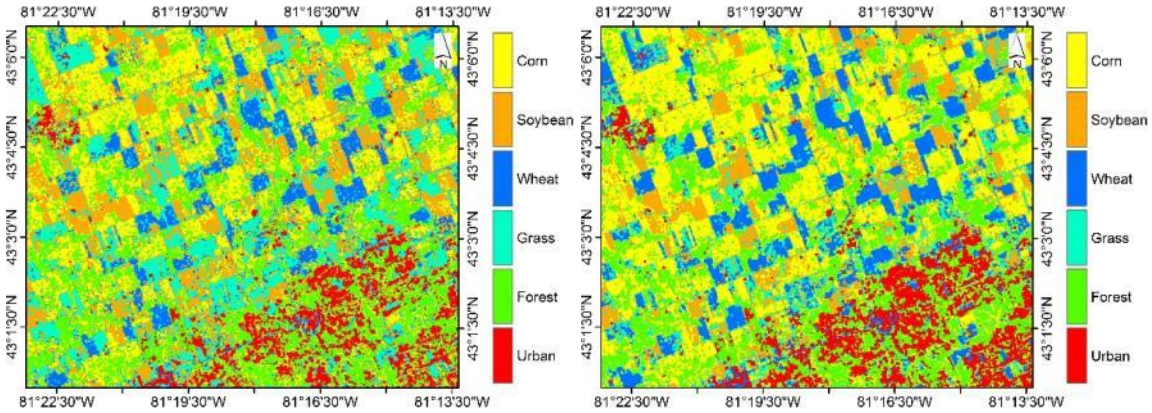
81°22'30"W
81°19'30"W
81°16'30"W
81°13'30"W
43°6'0"N
43°4'30"N
43°3'0"N
43°1'30"N
Corn
Soybean
Wheat
Grass
Forest
Urban

(c)

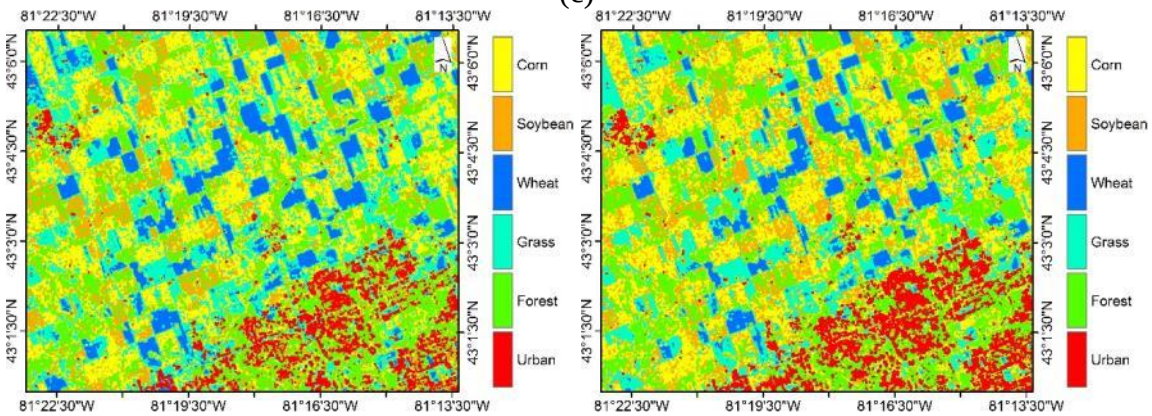
81°22'30"W
81°19'30"W
81°16'30"W
81°13'30"W
43°6'0"N
43°4'30"N
43°3'0"N
43°1'30"N
Corn
Soybean
Wheat
Grass
Forest
Urban

(d)

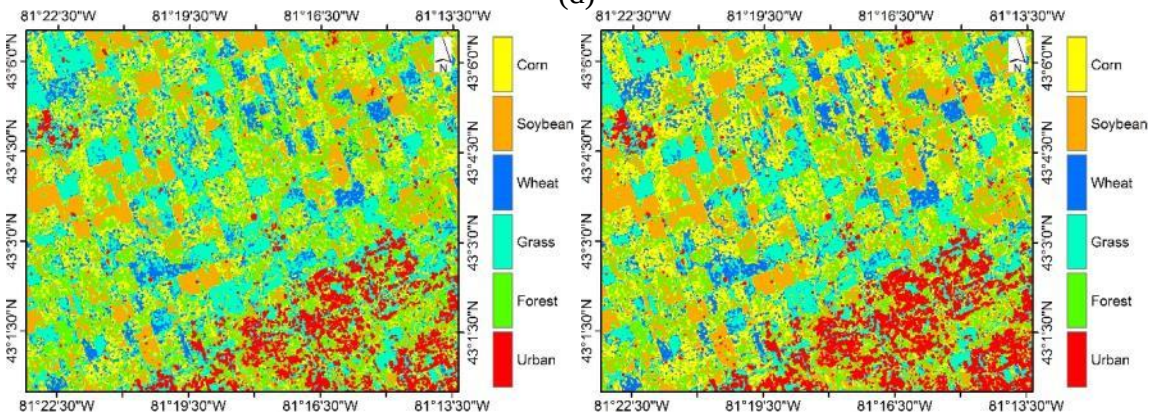
81°22'30"W
81°19'30"W
81°16'30"W
81°13'30"W
43°6'0"N
43°4'30"N
43°3'0"N
43°1'30"N
Corn
Soybean
Wheat
Grass
Forest
Urban

(e)

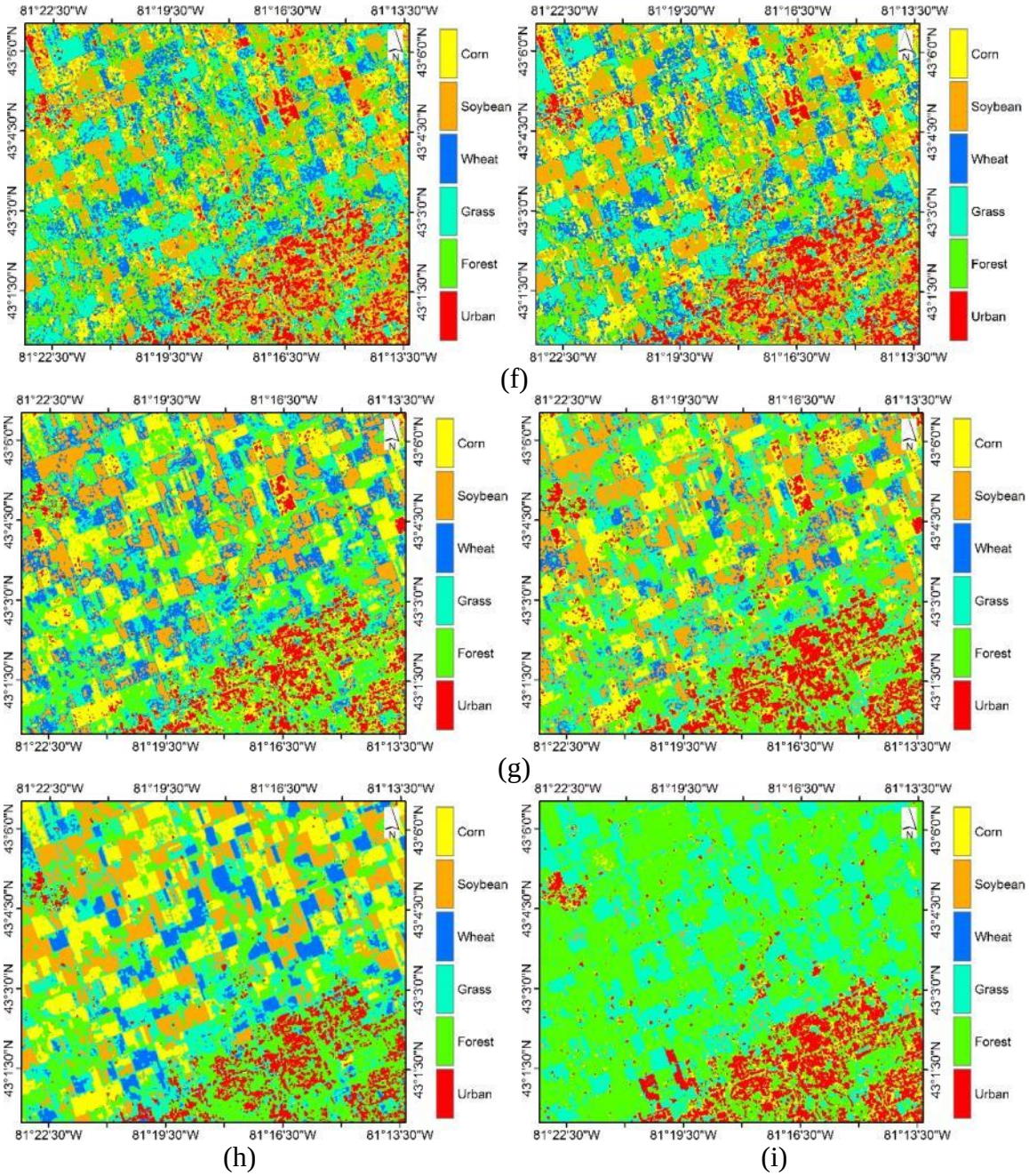

Figure 5-14. Classification maps. (a) May 7th. The left is MDPS and the right is WD. (b) May 31st. The left is MDPS and the right is WD. (c) June 24th. The left is MDPS and the right is WD. (d) July 18th. The left is MDPS and the right is WD. (e) August 11th. The left is MDPS and the right is WD. (f) September 4th. The left is MDPS and the right is WD. (g) September 28th. The left is MDPS and the right is WD. (h) the MTSBTCS-MDPS (i) the MTSBTCS-WD.

Table 5-6. Overall accuracy and kappa coefficient of MDPS and WD when they are applied to the single-date image.

	MDPS		**WD**	
	OA (%)	Kappa	OA (%)	Kappa
20120507	71.59	0.65	83.00	0.79
20120531	71.74	0.65	72.36	0.64
20120624	69.67	0.63	75.14	0.69
20120718	73.88	0.68	70.30	0.63
20120811	52.76	0.42	66.15	0.58
20120904	50.55	0.40	54.55	0.45
20120928	60.66	0.51	71.77	0.66
MTSBTCS	**87.50**	**0.85**	**30.80**	**0.20**

Table 5-7. Confusion matrix of MTSBTCS-MDPS. Note: OA is overall accuracy, UA is user accuracy, and PA is producer accuracy.

Categories	**Reference Data (Pixels)**							
	corn	soybean	wheat	grass	forest	urban	Total	UA (%)
corn	413	9	1	6	1	4	434	95.16
soybean	32	468	2	0	2	0	504	92.86
wheat	0	1	345	15	0	1	362	95.30
grass	35	34	26	155	24	4	278	55.76
forest	9	23	2	8	401	57	500	80.20
urban	0	0	0	0	4	317	321	98.75
Total	489	535	376	184	432	383	2399	
PA (%)	84.46	87.48	91.76	84.24	92.82	82.77		
OA (%)	87.50							
Kappa	0.85							

Compare the MDPS with the Wishart classification for the single-date image, Figure 5-14(a) to Figure 5-14(g) and Table 5-6 show that as the crops grow denser and denser, the issue of the misclassification becomes much more severe, which makes the overall accuracy lower and lower. This is because as the crop grows denser, the scattering from the crop, grass and forest become similar, which are all dominated by the volume scattering, and this can also be demonstrated by their polarization signatures in the previous section. In addition, from Table 5-6, we can observe that the Wishart classification has higher classification accuracy than that of the MDPS when it is applied to the single-date image. Sometimes, its overall accuracy is even as high as 83% (i.e., May 7th). It also should be noted that, the worst classification is observed on September

4th, as discussed in the previous section, the leaves of soybean and corn become yellow and dry on this date. In addition to the scattering from the crop canopy, some scatterings from the crop stems are also emerging due to its penetration, which makes the scattering much more complicated. In addition, when the MDPS and WD are applied to the binary-tree classification scheme, Figure 5-14(h) depicts that the classification boundaries between different classes look much smoother than other classification maps, while the classified agricultural fields also have less noise than other classification maps, whereas the MTSBTCS-WD shows much severe misclassification as shown in Figure 5-14(i) with its overall accuracy at only 30.8%, and its kappa coefficient is also very low. In contrast, the MTSBTCS-MDPS has much higher classification accuracy than that of the Wishart classification with an overall accuracy of 87.5% and the kappa coefficient of 0.85 respectively. To demonstrate it further, the confusion matrix of the MTSBTCS-MDPS is listed in Table 5-7. Table 5-7 depicts that there are some misclassifications between the grass and crops. The urban and forest also shows some misclassifications with the producer accuracy of urban around 83% as shown in Table 8, which is perhaps due to the alignment of building (Lee et al., 2004). For those buildings that not aligned with the flight direction, they are more easily to be misclassified. From this perspective, we could perhaps conclude that the WD has higher overall classification accuracy than that of the MDPS when they are applied to the single-date RADARSAR-2 data; whereas when they are applied to the multi-temporal images, the MTSBTCS-MDPS has much higher overall accuracy than that of the MTSBTCS-WD with their overall accuracy of 87.5% and 30.8%, respectively. It also should be noted that the WD method on single-date image achieves the overall accuracy of 83% on May 7th. Although it has the similar OA compared with the MTSBTCS-WD, in practice, on which day it could obtain the highest OA is still unpredictable. Hence, the multi-temporal data is still required.

Finally, to validate the efficiency of this algorithm, the time consumed by this algorithm is also compared with other algorithms, which is listed in Table 5-8.

Table 5-8. Execution time of algorithms (unit: s). All algorithms are implemented by the 64-bit python program using a desktop with four cores of CPU E3-1226 3.3 GHZ. The operating system is a 64bit windows 8.1. The RAM is 16g.

Algorithms	**Time (s)**
Single-date image with MDPS	1240
Single-date image with WD	880
Single-date image with PS	1350000
MTSBTCS-WD	4200
MTSBTCS-MDPS	1680

Note: polarization signatures are compared with the increment of 5 degrees for both orientation angle and ellipticity angle and the image size is 1338 by 1125.

Table 5-8 depicts that when the geometric shape of the polarization signature is used for the classification, the time it consumes is approximately 1000 times more than that of other algorithms. This is due to the fact that the point-to-point comparison between two different classes is much more time-consuming. Compared with the WD and MDPS, when they are applied to the single-date image, the WD consumes less time than that of the MDPS. This is because the process of the LUT consumes much more time in the MDPS classification scheme. However, when they are applied to multi-temporal images, the LUT is only constructed once before the classification, then the MTSBTCS-MDPS consumes much less time than that of the MTSBTCS-WD with its value around 3 times less than that of the MTSBTCS-WD. Overall, we could conclude that the MTSBTCS-MDPS is much more efficient in classifying multi-temporal images than MTSBTCS-WD, in addition to the high overall classification accuracy and kappa coefficient.

5.5 Conclusion

In this chapter, the polarization signature was employed to analyze the scattering of targets over time and applied to the multi-temporal polarimetric SAR classification. A multi-temporal supervised binary-tree classification scheme based on the polarization signature was also proposed. The criterion of the maximum difference of polarization signatures was developed to determine the optimum orientation angle, ellipticity angle, and data acquisition date. The results show that the VV polarization is greater than the

HH polarization due to the Bragg scattering when the targets are bare soils; while crops and grasses are dominated with surface scattering, and the HH polarization is greater than that of other dipole scattering at C band. The double-bounce and helix scattering are rather weak over the entire growing season, but they increase in corn field due to the interaction between the ground and corn stalks. As the crop and grass grow taller and denser, their pedestal height values increase, demonstrating the dominance of un-polarized components such as multiple scattering and volume scattering. For forest area, its polarization signature is very similar to surface scattering over the entire growing season, but its HH polarization is slightly greater than that of the VV polarization when it is in full canopy. In urban areas, the dominant scattering is the double-bounce scattering, and the helix scattering is much stronger than that of other classes. In terms of the classification, the Wishart classification shows much higher accuracy than that of the MDPS when applied to the single-date image, and the execution time is also less than that of the MDPS. However, when applied to multi-temporal images, the MTSBTCS-MDPS proposed in this chapter achieved much higher accuracy than that of the MTSBTCS-WD with its overall accuracy at 87.5% and kappa coefficient at 0.85, and the executive time is round 3 times less than that of the MTSBTCS-WD, demonstrating the high accuracy and efficiency of the newly proposed multi-temporal classification method.

References

Cao, F., Hong, W., Wu, Y. R., & Pottier, E. (2007). An Unsupervised Segmentation with an Adatpive Number of Clusters Using the SPAN/H/Alpha/A Space and the Complex Wishart Clustering for Fully Polarimetric SAR Data Analysis. *IEEE Transactions on Geoscience and Remote Sensing*, *45*(11), 3454-3467.

Cameron, W. L., Youssef, N. N., & Leung, L. K. (1996). Simulated Polarimetric Signatures of Primitive Geometrical Shapes. *IEEE Transactions on Geoscience and Remote Sensing*, *34*(3), 793-803.

Cloude, S. R., & Pottier, E. (1997). An Entropy Based Classification Scheme for Land Applications of Polarimetric SAR. *IEEE Transactions on Geoscience and Remote Sensing*, *35*(1), 68-78.

Durden, S. L., van Zyl, J. J., & Zebker, H. A. (1989). Modeling and Observation of the Radar Polarization Signature of Forested Areas. *IEEE Transactions on Geoscience and Remote Sensing*, *27*(3), 290-301.

Evans, D. L., Farr, T. G., van Zyl, J. J., & Zebker, H. A. (1988). SAR Polarimetry: Analysis Tools and Applications. *IEEE Transactions on Geoscience and Remote Sensing*, *26*(6), 774-789.

Freeman, A., & Durden, S. L. (1998). A Three-Component Scattering Model for Polarimetric SAR Data. *IEEE Transactions on Geoscience and Remote Sensing*, , *36*(3), 963-973.

Huang, X., Wang, J., and Shang J. (2015). A Simplified Adaptive Volume Scattering Model and Scattering Analysis of Crops over Agricultrual Fields Using the RADARSAT-2 Polarimetric SAR Imagery, *Journal of Applied Remote Sensing*, *9*(1), 096026-1-096026-18.

Huang, X., Wang, J., and Shang J. (2016). An Integrated Surface Parameter Inversion Scheme over Agricultural Fields at Early Growing Stages by Means of C-Band Polarimetric RADARSAT-2 Imagery, *IEEE Transactions on Geoscience and Remote Sensing*, *54*(5), 2510–2528.

Jafari, M., Maghsoudi, Y., & Zoej, M. J. V. (2015) A New Method for Land Cover Characterization and Classification of Polarimetric SAR Data Using Polarimetric

Signatures. *IEEE Journal of Selected Topics in Applied Earth Observations and Remote Sensing*, *8*(7), 3595-3607.

Jiao X., Kovacs, J., Shang, J., McNairn, H., Walters, D., Ma, B., & Geng, X. (2014). Object-Oriented Crop Mapping and Monitoring Using Multi-Temporal Polarimetric RADARSAT-2 Data. *ISPIS Journal of Photogrammetry and Remote Sensing*, *96*, 38-46.

Krogager, E., Boerner, W. M. & Madsen, S. N. (1997). Feature-Motivated Sinclair matrix (sphere/diplane/helix) Decomposition and Its Application to Target Sorting for Land Feature Classification. *Proc. SPIE Conference on Wideband Interferometric Sensing and Imaging Polarimetry*, *3120*(1), 144-154.

Lee, J. S., Grunes, M. R., Ainsworth T. L., Du, L. J., Schuler D. L., & Cloude S. R. (1999). Unsupervised Classification using Polarimetric Decomposition and The Complex Wishart Classifier. *IEEE Transactions on Geoscience and Remote Sensing*, *37*(5), 2249-2258.

Lee, J. S., Grunes, M. R., & Kwok, R. (1994). Classification of Multi-Look Polarimetric SAR Imagery Based on Complex Wishart Distribution. *International Journal of Remote Sesning*, *15*(1), 2299-2311.

Lee, J. S., Grunes, M. R., Pottier, E., & Ferro-Famil, L. (2004). Unsupervised Terrain Classification Preserving Polarimetric Scattering Characteristics. *IEEE Transactions on Geoscience and Remote Sensing*, *42*(4), 722-731.

Lee, J. S. & Pottier, E. (2009). *Polarimetric radar imaging : from basics to applications*. Boca Raton: CRC Press.

Liu, C., Shang, J. L., Vachon, P. W., & McNairn, H. (2013). Multiyear Crop Monitoring Using Polarimetric RADARSAT-2 Data. *IEEE Transactions on Geoscience and Remote Sensing*, *51*(4), 2227-2240.

Park, S. E., & Moon, W . M. (2007). Unsupervised Classifcation of Scattering Mechanisms in Polarimetric SAR Data Using Fuzzy Logic in Entropy and Alpha Plane. *IEEE Transactions on Geoscience and Remote Sensing*, *45*(8), 2652-2664.

Rice, S. O. (1963). *Reflection of Electromagnetic Waves by Slightly Rough Sufaces, Interscience*, New York.

Strzelczyk, J. and Porzycka-Strzelczyk, S. (2014). Identification of Coherent Scatterers in SAR Images Based on the Analysis of Polarimetric Signatures. *IEEE Geoscience and Remote Sensing Letters*, *11*(4) 783-787.

Valenzue, G. (1967). Depolarization of EM Waves by Slightly Rough Surfaces. *IEEE Transactions on Antennas and Propagation*, *15*(4), 552-557.

van Zyl, J. J., Zebker, H. A., & Elachi, C. (1987). Imaging Radar Polarization Signatures: Theory and Observation. *Radio Science*, *22*(4), 529-543.

Woodhouse, I. H. (2006). *Introduction to Microwave Remote Sensing*. Boca Raton: Taylor & Francis.

Yamaguchi, Y., Moriyama, T., Ishido, M., & Yamada, H. (2005). Four-Component Scattering Model for Polarimetric SAR Image Decomposition. *IEEE Transactions on Geoscience and Remote Sensing*, *43*(8), 1699-1706.

Zhang, L., Sun, L., Zou, B., & Moon, W. M. (2015). Fully Polarimetric SAR Image Classification via Sparse Representation and Polarimetric Features. *IEEE Journal of Selected Topics in Applied Earth Observations and Remote Sensing*, *8*(8), 3923-3932.

Chapter 6 Conclusion and Discussion

6.1 Summary

This thesis addresses two important applications of PolSAR: 1) surface parameter inversion under vegetation cover and 2) multi-temporal land cover mapping. Surface parameters are critical determining factors of crop growth and its final yield. Therefore, it is important to understand the state of the surface parameters of each crop through its entire growing cycle. With the recent advancement of the high-resolution SAR satellites and satellite constellations, the revisit time has largely reduced from several weeks to few days and even daily. For example, the Italian X-band COSMO SkyMed (COnstellation of small Satellites for Mediterranean basin Observation) mission consists of four medium satellites, which offers a frequent revisit. The Canadian C-band RADARSAT Constellation Mission (RCM), with a scheduled launching date in 2018, is made of three identical satellites and offers both frequent revisit and interferometry capability. This leads closer to the realization of continuous, near-real-time monitoring of crop growth and surface parameters. It also satisfies the need for multi-temporal data to develop advanced image classification methods that can take advantage of the rich temporal information.

Many semi-empirical or physical surface scattering models have been developed to retrieve the surface parameters (soil moisture and surface roughness) for bare soil. However, for a long period of time through the year, the field is covered with the crops or other vegetation, and the usefulness of these models designed under the ideal condition of bare soil is challenged. To solve the problem of retrieving surface parameters in real-world situation, with crop cover, the method should be able to separate the scattering of the underlying bare soil from the volume scattering caused by the vegetation canopy. In other words, the primary issue is to develop an advanced volume scattering model to better characterize the scattering of crops. In view of the PolSAR, the assumption to model the volume scattering is to treat the crops as consisting of a cloud of dipoles with their orientation angles with respect to the line of sight (LOS) satisfying certain feasible probability density functions. Then, the corresponding volume scattering models are

constructed using the second-order statistical integration. In general, the traditional probability density functions are uniform, first-order sine or first-order cosine functions. In this way, the derived volume scattering model is in a constant manner, and can only describe the crops that are completely random or having a certain orientation. However, the appearance (i.e. structure) of the crop is always changing as they grow and go through different development stages through the growth cycle over time. To overcome this issue, the first task is to develop a more feasible volume scattering model than the existing constant models. In Chapter 2, a simplified adaptive volume scattering model (SAVSM) to employ the nth power of sine and cosine functions is developed. Unlike the existing constant models that include only the uniform and first-order sine or cosine functions, the SAVSM model uses the nth power of sine and cosine functions where n can vary to include other situations.

With the SAVSM in place, the next step is to apply it to estimate the soil moisture under vegetation cover by removing the effect of the volume scattering from the crop canopy. The Freeman-Durden decomposition is a classic model-based polarimetric decomposition, which models the total backscattering as the composition of the surface, double-bounce and volume scattering. Due to its efficiency and intuitiveness, many new methods were built based on the Freeman-Durden concept, such as the Yamaguchi decomposition (Yamaguchi et al., 2005; 2006). In Chapter 3, the model-based decomposition framework is also adopted and applied to the winter wheat fields as a case study. Due to the limited penetration depth of the C-band RADARSAT-2 data, soil moisture estimation is only targeted at the early growing stages. Firstly, the eigen-based decomposition proposed by Cloude and Pottier (1997) is performed to investigate the scattering mechanisms over bare soil and soil with winter wheat cover. Then, an adaptive two-component model-based decomposition (ATCD) is developed to estimate the soil moisture over wheat fields, in which the surface scattering is the X-Bragg surface scattering model while the volume scattering is the SAVSM developed in Chapter 2. The X-Bragg model is developed based on the Bragg surface scattering model derived from the small perturbation model, and is only suitable for describing very smooth surfaces with very low roughness values. However, the surface would look much rougher in short-wavelength configuration than

that in long wavelength. Hence, for C-band RADARSAT-2 data, the surface scattering with higher roughness must be employed to estimate the soil moisture. Therefore, the X-Bragg model is proposed to describe rougher surfaces than that of the Bragg model. The X-Bragg model is constructed by integrating the Bragg model with the orientation angle induced by the azimuthal slope satisfying the zero mean normal distribution. However, before applying the ATCD for soil moisture estimation, the issue of the negative power must be solved, i.e., the decomposed power of the surface scattering is negative, which is inconsistent with reality. Therefore, the Non-Negative Eigen-value Decomposition (NNED) method is employed to determine the volume scattering component to avoid this issue. Finally, the relative dielectric constant is determined from the X-Bragg surface scattering model, and an empirical relationship between the relative dielectric constant and soil moisture is adopted to invert the soil moisture over winter wheat fields.

In reality, agricultural fields do not often exist in the form of bare soils; they are usually covered with crop residues that are left for moisture retention, preventing wind erosion, and maintaining soil carbon balance. To extend the application of the ATCD to agricultural fields under crop cover (early growing stage), an integrated surface parameter inversion scheme is developed in Chapter 4, in which bare soil and vegetation/residue covered fields are treated separately. Firstly, the eigen-based decomposition is employed to derive the H and α thresholds for distinguishing the bare soil fields from the fields with crop or residue cover. Then, the bare soil is characterized using a calibrated Integration Equation Model (CIEM) while the others are described by the ATCD. The difference between Chapter 4 and Chapter 3 lies in the use of the X-Bragg model to describe surface scattering. In Chapter 4, a calibrated IEM (CIEM) model is employed, which could describe higher rough surfaces than the X-Bragg model does. The reason why the CIEM is adopted rather than the IEM is because the measurement of the surface correlation length is always problematic, and three unknown values are reduced to two, which can simplify the equation solving. In ATCD, the surface scattering is replaced by the CIEM instead of the X-Bragg model while the volume scattering is still the SAVSM. Like in Chapter 3, the NNED is employed to determine the volume scattering component to avoid the negative power issue.

In addition, the soil moisture and roughness extraction algorithms are also dependent on the crop types and crop conditions, whereas crop conditions can be determined by the crop phenology for different crop, so the crop mapping can be very useful for surface parameter retrieval. Therefore, a multi-temporal supervised binary-tree classification scheme (MTSBTCS) with a criterion that maximizes the difference between the polarization signatures (MDPS) of two different targets is developed (MTSBTCS-MDPS) in Chapter 5 for crop growth monitoring. With MTSBTCS, each target can be characterized by a 3D plot—the polarization signature (PS) with its response changing with the orientation angle and ellipticity angle. For each pair of two different targets, an optimum pair of orientation angle and ellipticity angle can always be found to maximize the difference of these two targets. For targets changing with time, such as crops, an optimum time can also be found to maximally distinguish these two targets. Therefore, to perform the MTSBTCS-MDPS, a binary tree is first constructed, in which each pair of targets is maximally differenced by choosing the optimum orientation angle and ellipticity angle at an optimum data acquisition time by means of the MDPS. Then, the image acquired on the optimum date will be converted to a new image based on the optimum orientation angle and ellipticity angle, and these two targets will be classified based on the newly generated image. When other targets are added to the binary three, they are classified in the same way. This algorithm will stop until all targets are classified.

6.2 Conclusions and Contributions

The main objective of this thesis is to validate the application of the fully polarimetric SAR data towards the quantitative estimation of surface parameters (soil moisture and surface roughness) over agricultural fields under vegetation cover and qualitative land cover mapping. Four specific objectives are introduced in Section 1.5, and they have all been met. Overall, the research suggests that the RADARSAT-2 fully polarimetric SAR data has the potential to estimate the soil moisture and surface roughness at the crop early growing stages as well as for fields covered with crop residues. In addition, when the multi-temporal PolSAR data is applied, the classification accuracy is improved significantly, which leads to a high potential of the SAR data for high accuracy

classification especially when the re-visit time of satellites are reduced to a few days in future. The innovations this thesis has achieved and its contribution to the scientific literature are summarized as follows:

1) A simplified adaptive volume scattering model (SAVSM) was developed in this thesis, which considers the distribution of the dipoles as the nth power of sine and cosine probability density functions. It can better describe the scattering caused by vegetation canopy. Compared with the traditional methods as represented by Freeman-Durden and Yamaguchi volume scattering models, the SAVSM achieves the best performance over agricultural fields measured with the highest percentage of the power of remainder matrix (less than 0.001). The decomposed surface, double-bounce and volume scattering components of wheat, soybean and corn tested at various growth stages are consistent with the crop phonological development observed in the fields.

2) Due to the limited penetration depth of the short wavelength C-band RADARSAT-2, the soil moisture is estimated only at the early crop growing stages when the crop is short and sparse. An adaptive two-component model-based decomposition (ATCD) on soil moisture estimation is developed that considers the surface and volume scattering caused by the soil and crop canopy, separately. The surface scattering adopted is a X-Bragg scattering, whereas the volume scattering is described by SAVSM developed in Chapter 2. The fully polarimetric RADARSAT-2 data acquired in 2013 and 2015 over two study areas are used for model validation. The results revealed that the volumetric soil moisture derived from the ATCD is more consistent with the verifiable ground conditions than with other existing model-based decomposition methods. Moreover, the suitability of this model to other crops still needs further investigation.

3) An integrated surface parameter inversion scheme (ISPIS) based on the analysis of H-α parameters is proposed for surface parameter inversion at the early crop growing stages, in which the surface scattering is described using the calibrated Integral Equation Model (CIEM) while the volume scattering model is still the SAVSM. This is to compensate the bias of soil moisture estimation when the soil moisture content is greater than 30 [vol.%],

especially when the SAR incidence angle is low. This is because the X-Bragg surface scattering model was developed by the Small Perturbation Method (SPM) which is only suitable for longer wavelength where the surface appears smooth. For short-wavelength C-band RADASAT-2, surface scattering model like ISPIS is more suitable. Compared with other methods, the ISPIS derived volumetric soil moisture and surface roughness are more consistent with the verifiable field observations with the lowest overall RMSE 6.12 [vol.%] and 0.48, respectively.

4) A multi-temporal supervised binary-tree classification scheme with a criterion that maximizes the difference of polarization signatures (MTSBTCS-MDPS) of two different targets is developed for land use classification using multi-temporal polarimetric SAR. Compared with the MDPS with the traditional Wishart Distance (WD), the classification accuracy of WD is higher than that of the MDPS when a single-date image is used. When multi-temporal images are used, the newly developed MTSBTCS-MDPS achieved much higher accuracy with an overall accuracy of 87.5% and kappa coefficient of 0.85. The MTSBTCS-MDPS also has a much-reduced execution time, approximately 2.5 times less than that of the MTSBTCS-WD.

6.3 Future Research

This thesis has developed three models to quantitatively estimate the surface parameters under vegetation cover. A classification scheme is also developed for land cover mapping using multi-temporal SAR data. Although results from these newly developed methods have shown increases in both feasibility and efficiency, there is always room for improvement in the quest for better methods.

6.3.1 Volume Scattering Model Considering the Shape Parameter

The SAVSM developed in this thesis was based on the dipole assumption, which is most suitable for describing vegetation with long wavelength RADAR configuration as the size of the stem or branches of the vegetation is smaller compared with the wavelength. However, in real world situations, the leaves of different vegetation species can have

different geometric structures and be in various shapes. For example, the leaves of wheat are seen as needles while the leaves of soybean are seen as disks. When using high frequency SAR to model crop canopies, the non-spherical particles including spheroids and disk-like plate are usually used (Ishimarum, 1978). Lee et al. (2014) and Wang et al. (2014) modeled the volume scattering using a generalized scattering matrix that takes into consideration the shape factor of the vegetation based on the probability density functions mentioned in Section 1.2. In future work, the SAVSM will be further improved by including the shape parameter and validated with more experiments. The change of shape with a shape factor $|\delta|$ is shown in Figure 6-1. The scattering matrix of a particle is defined as

$$[S] = \begin{bmatrix} S_{hh} & 0 \\ 0 & S_{vv} \end{bmatrix} \tag{6-1}$$

For simplicity, S_{hh} and S_{vv} are assumed to be real. The shape factor is defined as

$$\delta = \left(\frac{S_{hh} - S_{vv}}{S_{hh} + S_{vv}}\right) \tag{6-2}$$

and its coherency matrix can be derived as proportional to equation (6-3).

$$[T_\delta] = \frac{1}{1 + |\delta|^2} \begin{bmatrix} 1 & \delta & 0 \\ \delta & |\delta|^2 & 0 \\ 0 & 0 & 0 \end{bmatrix} \tag{6-3}$$

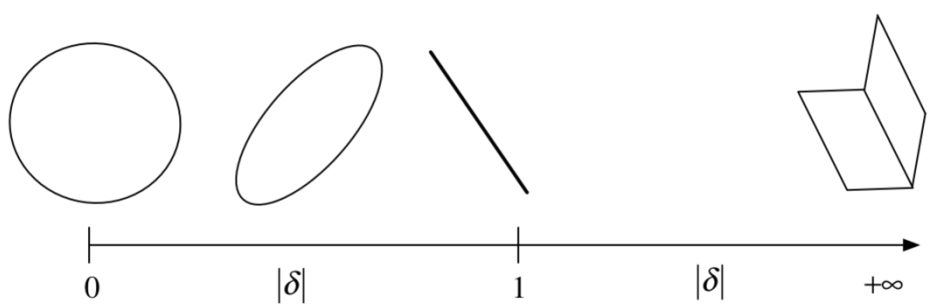

Figure 6-1. Schematic representation of the scatterer shape changing with $|\boldsymbol{\delta}|$.

6.3.2 Surface Parameter Inversion under Dense Vegetation Cover

To estimate the surface parameter under vegetation cover, Chapter 4 presents an integrated surface parameter inversion scheme (ISPIS) through integrating the CIEM and ATCD without considering the attenuation effects caused by the water content of the vegetation canopy, even though the attenuation effects are rather weak at the crop early growing stages. To further extend the application of the ISPIS to dense vegetation cover, the attenuation effects must be considered.

Currently, the semi-empirical water cloud model (WCM) is the most widely used model assuming that the vegetation consists of a collection of spherical water droplets that are held in place structurally by dry matter (Attema & Ulaby, 1978). The WCM is based on the fact that the dielectric constant of dry vegetation matter is much smaller than that of the water content of vegetation, and more than 99% air by volume is contained in vegetation canopy. Therefore, such a model was developed assuming that the canopy "cloud" called the water cloud contains identical water droplets randomly distributed with the canopy with its figure shown as in Figure 1-6. It has been widely used for the surface and biophysical parameters estimation until now due to its simplicity (Gherboudj et al., 2011; Lievens & Verhoest, 2011). However, the WCM can only be suitable to describe the vegetation canopy with dense canopy and is only a simple solution of the first-order radiative transfer model. Most importantly, WCM requires ground truth data to fit the unknown parameters, which limits its application to areas without the support of ground data. The Michigan Microwave Canopy Scattering (MIMICS) model developed by Ulaby et al. (1990) provides a rigorous solution, considering not only the multiple scattering but also all scatterings shown in Figure 1-5. It is also suitable for vegetation-covered areas where the agents responsible for scattering have discrete configurations, and many studies have adapted it to characterize the scattering of crops such as wheat and soybean (Toure et al., 1994; De Roo et al., 2001). However, too many parameters need to be determined before applying it to surface parameter retrieval. In remote sensing applications, it is desirable to treat the microscopically complicated mixture as

macroscopically homogeneous and characterize it by an effective permittivity, while many natural heterogeneous media have been widely studied from this point of view including vegetation canopy (Sihvola & Kong, 1988). Therefore, to overcome the issues of the WCM and MIMICS to develop a simple and reliable method, it is feasible to treat the vegetation canopy as a homogeneous medium characterized by an effective dielectric constant, which is shown in Figure 6-2. Then, the solution will be solved by the wave propagation theories.

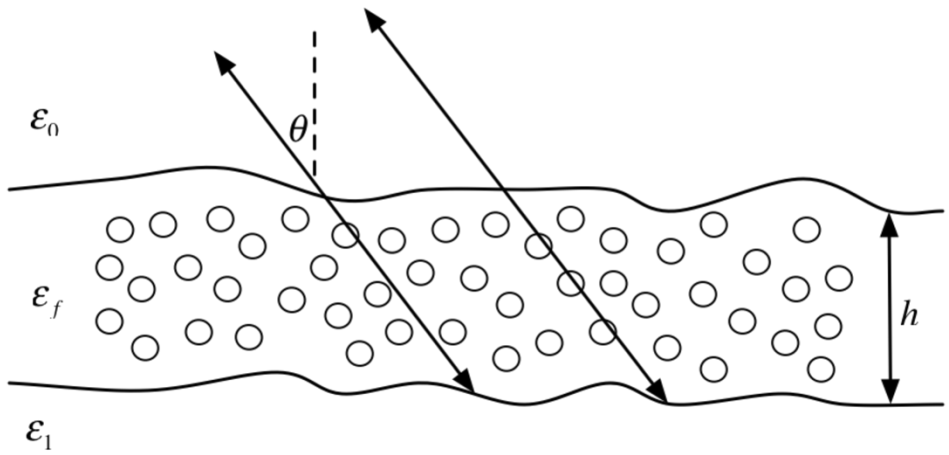

Figure 6-2. Scattering with a homogeneous medium.

6.3.3 Integration of Land Cover Map and Surface Parameter Inversion Scheme

The soil moisture and roughness extraction algorithms are also dependent on the crop types and crop conditions, whereas crop conditions can be determined by the crop phenology for different crop, so the crop mapping can be very useful for surface parameters estimation. Different crops show various structures and orientations, and to estimate surface parameters accurately, it is also essential to construct specific volume scattering model for each crop as shown in Figure 6-3 especially for physical scattering models such as coherent models for soybean by Huang, et al. (2016) and rice by Liu et al. (2015). Therefore, crop types should be identified before applying the surface parameter inversion scheme to estimate the underlying surface parameters. The land cover map and the surface parameters inversion algorithms should be integrated, but in this thesis,

although a multi-temporal classification scheme is proposed, it is not integrated to the surface parameter inversion developed in Chapter 3 and Chapter 4. This needs to be further investigated in future.

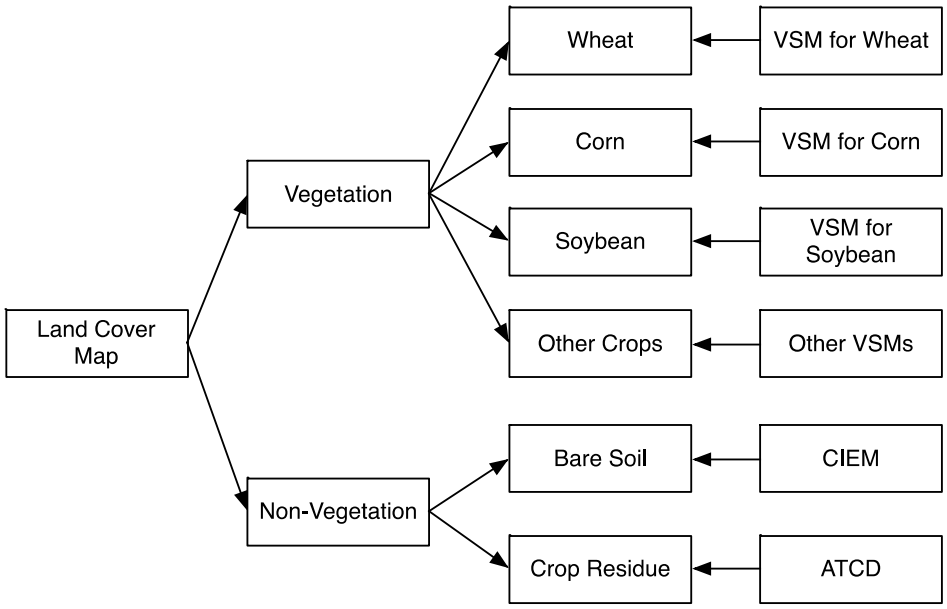

Figure 6-3. Integration of land cover map and surface inversion scheme.

6.3.4 Relations with the RCM

The methods developed in this thesis are merely based on the fully polarimetric RADARSAT-2 data, which is being different from the compact SAR transmitting circular polarizations and receiving two orthogonal mutually-coherent linear polarizations. The compact mode will be operated by the RCM that will be launched by Canadian Space Agency in 2018. Accordingly, to adapt the developed methods to the compact SAR mode, it still needs further investigation due to the reduced information of the compact SAR. In addition, the compact SAR has double swath-width of that of the fully PolSAR, and is suitable for the task of large-area coverage applications, but the developed methods are in field level and to apply them for the large areas such as country level requires further investigation as well. However, methods that will be applied to a larger scale need to be validated in the field level first.

References

Attema, E. P. W., & Ulaby, F. T. (1978). Vegetation Modeled as a Water Cloud. *Radio Science*, *13*(2), 357-364.

Cloude, S. R., & Pottier, E. (1997). An Entropy Based Classification Scheme for Land Applications of Polarimetric SAR. *IEEE Transactions on Geoscience and Remote Sensing*, *35*(1), 68-78.

De Roo, R. D., Du, Y., Ulaby, F. T., & Dobson, M. C. (2001). A Semi-Empirical Backscattering Model at L-Band and C-Band for a Soybean Canopy with Soil Moisture Inversion. *IEEE Transactions on Geoscience and Remote Sensing*, *39*(4), 864-872.

Freeman, A., & Durden, S. L. (1998). A Three-Component Scattering Model for Polarimetric SAR Data. *IEEE Transactions on Geoscience and Remote Sensing*, , *36*(3), 963-973.

Gherboudj, I., Magagi, R., Berg, A. a., & Toth, B. (2011). Soil Moisture Retrieval over Agricultural Fields from Multi-Polarized and Multi-Angular RADARSAT-2 SAR Data. *Remote Sensing of Environment*, *115*(1), 33-43.

Huang, H., Kim, S. B., Tsang L., Xu, X., Liao, T. H., Jachson, T. J., & Yueh S. H. (2016). Coherent Model of L-Band Radar Scattering by Soybean Plants: Model Development, Evalutaton, and Retrieval. *IEEE Journal of Selected Topics in Applied Earth Observation and Remote Sensing*, *9*(1), 272-284.

Ishimaru, A. (1978). *Wave Propagation and Scattering in Random Media*, New York : Academic Press.

Lee, J. S., Ainsworth T. L., Thomas L., & Wang Y. (2014). Generalized Polarimetric Model-Based Decompositions Using Incoherent Scattering Models. *IEEE Transactions on Geoscience and Remote Sensing*, *52*(5), 2474-2491.

Lievens, H., & Verhoest, N. E. C. (2011). On the Retrieval of Soil Moisture in Wheat Fields from L-Band SAR Based on Water Cloud Modeling, the IEM, and Effective Roughness Parameters. *IEEE Geoscience and Remote Sensing Letters*, *8*(4), 740-744.

Liu, L., Li, K., Shao, Y., Pinel, N., Yang, Z., Gong, H., & Wang, L. (2015). Exension of the Monte Carlo Coherent Microwave Scattering Model to Full Stage of Rice. *IEEE Geoscience and Remote Sensing Letters*, *12*(5), 740-744.

Sihvola, A. H., & Kong, J. O. (1988). Effective Permittivity of Dielectric Mixtures. *IEEE Transactions on Geoscience and Remote Sensing*, *26*(4), 420-429. Toure, A., Thomson, K. P. B., Edwards, G., Brown, R. J., & Brisco, B. G. (1994). Adaptation of The MIMICS BackscatteringModel to The Agricultural Context-Wheat and Canola at L and C Bands. *IEEE Transactions on Geoscience and Remote Sensing*, *32*(1), 47-61.

Ulaby, F. T., Sarabandi, K., McDonald, K., Whitt, M., & Dobson, M. C. (1990). Michigan Microwave Canopy Scattering Model. *International Journal of Remote Sensing*, *11*(7), 1223-1253.

Wang, Y., Liu, H., & Bo, J. (2014). Coherency Matrix Decomposition Based on Constrained Sparse Representation. *IEEE Transactions on Geoscience and Remote Sensing*, *52*(9), 5906-5922.

Yamaguchi, Y., Moriyama, T., Ishido, M., & Yamada, H. (2005). Four-Component Scattering Model for Polarimetric SAR Image Decomposition. *IEEE Transactions on Geoscience and Remote Sensing*, *43*(8), 1699-1706.

Appendix A: Polarization and Polarization Ellipse

The time-space behavior of electromagnetic waves is ruled by the Maxwell equation set defined as

$$\nabla \times \vec{E}(\vec{r},t) = -\frac{\partial \vec{B}(\vec{r},t)}{\partial t}$$

$$\nabla \times \vec{H}(\vec{r},t) = \overrightarrow{J_T}(\vec{r},t) + \frac{\partial \vec{D}(\vec{r},t)}{\partial t} \tag{A-1}$$

$$\nabla \cdot \vec{D}(\vec{r},t) = \rho(\vec{r},t)$$

$$\nabla \cdot \vec{B}(\vec{r},t) = 0$$

where $\vec{E}(\vec{r},t)$, $\vec{H}(\vec{r},t)$, $\vec{D}(\vec{r},t)$ and $\vec{B}(\vec{r},t)$ are the wave electric field, magnetic field, electric induction and magnetic induction, respectively. The total current density $\overrightarrow{J_T}(\vec{r},t) = \overrightarrow{J_a}(\vec{r},t) + \overrightarrow{J_c}(\vec{r},t)$ with $\overrightarrow{J_a}(\vec{r},t)$ corresponding to a source term and $\overrightarrow{J_c}(\vec{r},t)$ depending on the conductivity of the propagation medium. When the propagation medium is free of mobile electric charges, the solution of the Maxwell equation can be significantly simplified by considering the complex expression $\vec{E}(\vec{r})$ of the monochromatic time-space electric field $\vec{E}(\vec{r},t)$, defined as

$$\vec{E}(\vec{r},t) = Re\left(\vec{E}(\vec{r})e^{j\omega t}\right) \tag{A-2}$$

The propagation equation may be written as,

$$\Delta\vec{E}(\vec{r}) + \omega^2\mu\underline{\varepsilon}\left(1 - j\frac{\sigma}{\omega\underline{\varepsilon}}\right)\vec{E}(\vec{r}) = \Delta\vec{E}(\vec{r}) + k^2\vec{E}(\vec{r}) = 0 \tag{A-3}$$

where the complex dielectric constant $\underline{\varepsilon}$ is given by

$$\underline{\varepsilon} = \varepsilon - j\frac{\sigma}{\omega} \tag{A-4}$$

and the wavenumber k is given by

$$k = \omega\sqrt{\mu\underline{\varepsilon}} \tag{A-5}$$

Without any loss of generality, the electric field may be represented in an orthogonal basis $(\hat{x}, \hat{y}, \hat{z})$ defined so that the direction of propagation $\hat{k} = \hat{z}$. When the is assumed to be loss free, then, the expression of the electric field becomes

$$\vec{E}(z,t) = \begin{bmatrix} E_{0x}cos(\omega t - kz + \delta_x) \\ E_{0y}cos\big(\omega t - kz + \delta_y\big) \\ 0 \end{bmatrix} \tag{A-6}$$

At a fixed position $z = z_0$, as time evolves, the wave propagates through equi-phase planes and describes a characteristic elliptical locus, which is called polarization as shown in Figure A-1. The nature of the temporal wave trajectory may be determined from the following parametric relation between the components of $\vec{E}(z_0, t)$.

$$\begin{aligned} \left[\frac{E_x(z_0,t)}{E_{0x}}\right]^2 - 2\frac{E_x(z_0,t)E_y(z_0,t)}{E_{0x}E_{0y}}cos\big(\delta_y - \delta_x\big) + \left[\frac{E_y(z_0,t)}{E_{0y}}\right]^2 \\ = sin\big(\delta_y - \delta_x\big) \end{aligned} \tag{A-7}$$

This expression is the equation of an ellipse, which we call polarization ellipse that describes the wave polarization.

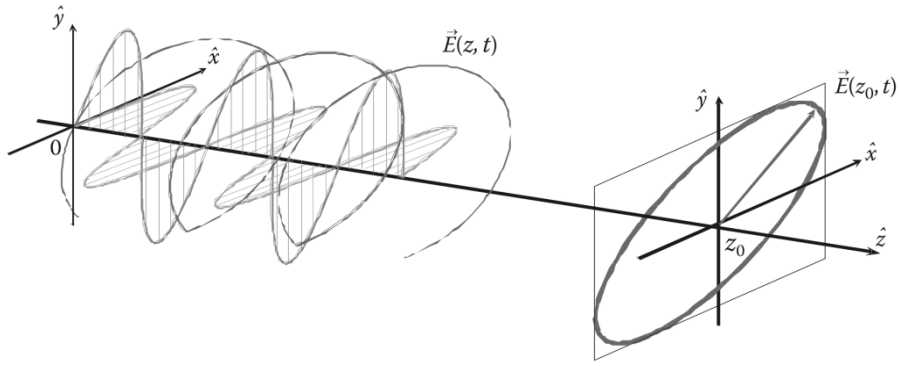

Figure A-1. Temporal trajectory of a monochromatic plane wave at a fixed abscissa $\boldsymbol{z = z_0}$. Adapted from Lee & Pottier (2009).

The polarization ellipse shape may be characterized using three parameters as shown in Figure A-2. A is called the ellipse amplitude and is determined from the ellipse axis as

$$A = \sqrt{E_{0x}^2 + E_{0y}^2} \tag{A-8}$$

$\phi \in \left[-\frac{\pi}{2}, \frac{\pi}{2}\right]$ is the ellipse orientation and is defined as the angle between the ellipse major axis and $\hat{x}$:

$$tan2\phi = 2\frac{E_{0x}E_{0y}}{E_{0x}^2 - E_{0y}^2} cos\left(\delta_y - \delta_x\right) \tag{A-9}$$

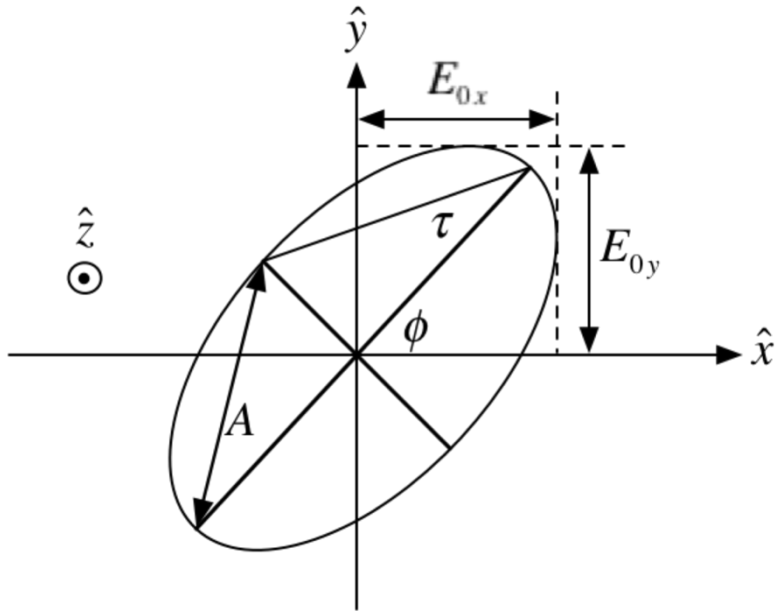

Figure A-2. Polarization ellipse.

Reference

Lee, J. S., & Pottier, E. (2009). *Polarimetric radar imaging : from basics to applications*. Boca Raton: CRC Press.

Appendix B: Polarimetric Scattering Cross Section and Scattering Amplitude Matrix

Compared with the optical sensors, SAR is an active remote sensing technique, which receives the scattering cross section through transmitting a long wavelength electromagnetic wave interacting with the target. To simply understand the scattering cross section, we consider an electromagnetic wave impinging upon an object shown in Figure B-1 and the derivation of the scattering cross section is a simplified version introduced by Tsang et al. (2000).

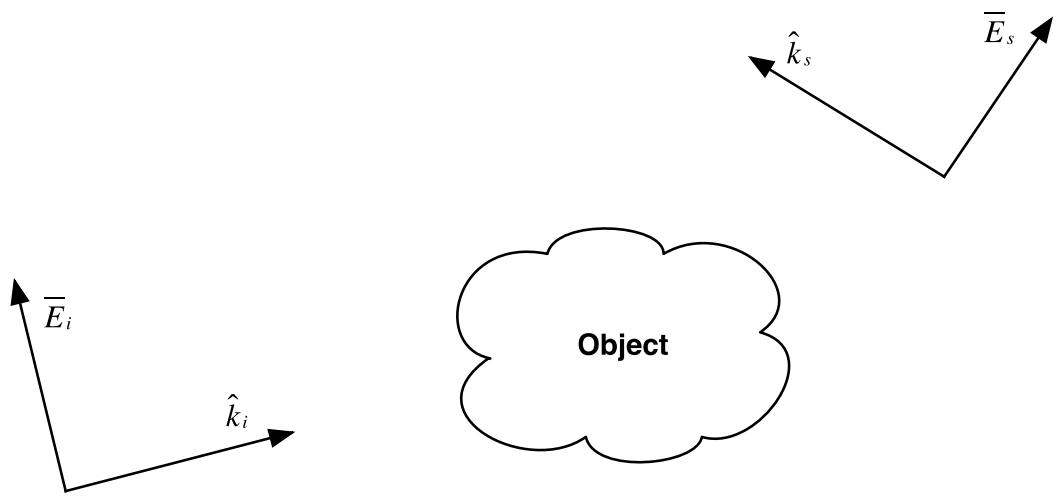

Figure B-1. Scattering of a plane electromagnetic wave by an object.

The incident wave is in direction $\hat{k}_i$ and has electric field in direction $\hat{e}_i$ that is perpendicular to $\hat{k}_i$, and the electric field of the incident wave is

$$\bar{E}_i = \hat{e}_i E_0 e^{ik\hat{k}_i \cdot \bar{r}} \tag{B-1}$$

where $\bar{r}$ is the position vector, $k = 2\pi/\lambda$ is the wavenumber with λ the wavelength, and E_0 is the amplitude of the electric field. In the far field, the scattered field is that of a spherical wave with dependence e^{ikr}/r, where r is the distance from the particle. Let $\bar{E}_s$ be the far field scattered field in direction of $\hat{k}_s$, and $\bar{E}_s$ is written as

$$\bar{E}_s = \hat{e}_s f(\hat{k}_s, \hat{k}_i) E_0 \frac{e^{ik\hat{k}_s \cdot \bar{r}}}{r} \tag{B-2}$$

where $\hat{e}_s$ is perpendicular to $\hat{k}_s$. The $f(\hat{k}_s, \hat{k}_i)$ is the scattering amplitude from direction $\hat{k}_i$ into direction $\hat{k}_s$. The Poynting vector denoting power flow per unit area is

$$\bar{S}_i = \frac{1}{2} Re(\bar{E}_i \times \bar{H}_i^*) = \frac{|E_0|^2}{2\eta} \hat{k}_i \tag{B-3}$$

Similarly, for the scattered wave, its Poynting vector is

$$\bar{S}_s = \frac{1}{2} Re(\bar{E}_s \times \bar{H}_s^*) = \frac{\left|f(\hat{k}_s, \hat{k}_i)\right|^2}{r^2} \frac{|E_0|^2}{2\eta} \hat{k}_s \tag{B-4}$$

where $\eta = \sqrt{\mu/\varepsilon}$ is the wave impedance. Considering a differential solid angle $d\Omega_s$ in the scattered direction $\hat{k}_s$, in the spherical coordinate system at a distance r, the surface area subtended by the differential solid angle $d\Omega_s$ is

$$dA = r^2 d\Omega_s = r^2 sin\theta_s d\theta_s d\phi_s \tag{B-5}$$

Then, the differential scattered power dP_s through dA is

$$dP_s = |\bar{S}_s| dA = \left|f(\hat{k}_s, \hat{k}_i)\right|^2 \frac{|E_0|^2}{2\eta} d\Omega_s \tag{B-6}$$

It is convenient to define a differential scattering cross section $\sigma_d(\hat{k}_s, \hat{k}_i)$ by

$$\frac{dP_s}{|\bar{S}_i|} = \sigma_d(\hat{k}_s, \hat{k}_i) d\Omega_s \tag{B-7}$$

Integrating the above equation, the scattered power is

$$P_s = |\bar{S}_i| \int \sigma_d(\hat{k}_s, \hat{k}_i) d\Omega_s = \sigma_s |\bar{S}_i| \tag{B-8}$$

where σ_s is the scattering cross section which is written as,

$$\sigma_s = \int \sigma_d(\hat{k}_s, \hat{k}_i) d\Omega_s = \int \left| f(\hat{k}_s, \hat{k}_i) \right|^2 d\Omega_s \tag{B-9}$$

Assuming that $\left| f(\hat{k}_s, \hat{k}_i) \right|^2$ is independent of the coordinate, σ_s is written as,

$$\sigma_s = 4\pi \left| f(\hat{k}_s, \hat{k}_i) \right|^2 \tag{B-10}$$

In the polarization's perspective, for the incident wave, the electric field $\bar{E}_i$ is perpendicular to the direction of propagation $\hat{k}_i$. There are two linearly independent vectors that are perpendicular to $\hat{k}_i$. We name them $\hat{a}_i$ and $\hat{b}_i$ respectively, and the incident electric field is written as,

$$\bar{E}_i = \left(\hat{a}_i E_{a_i} + \hat{b}_i E_{b_i} \right) e^{ik\hat{k}_i \cdot \bar{r}} \tag{B-11}$$

Similarly, the scattered wave is written as

$$\bar{E}_s = \left(\hat{a}_s E_{a_s} + \hat{b}_s E_{b_s} \right) \frac{e^{ik\hat{k}_s \cdot \bar{r}}}{r} \tag{B-12}$$

The scattered field components E_{a_s} and E_{b_s} are linearly related to E_{a_i} and E_{b_i}. The relationship can be presented by a 2 by 2 scattering amplitude matrix,

$$\begin{bmatrix} E_{a_s} \\ E_{b_s} \end{bmatrix} = \begin{bmatrix} f_{aa}(\hat{k}_s, \hat{k}_i) & f_{ab}(\hat{k}_s, \hat{k}_i) \\ f_{ba}(\hat{k}_s, \hat{k}_i) & f_{bb}(\hat{k}_s, \hat{k}_i) \end{bmatrix} \begin{bmatrix} E_{a_i} \\ E_{b_i} \end{bmatrix} \tag{B-13}$$

where the Sinclair matrix is described as

$$S_2 = \begin{bmatrix} f_{aa}(\hat{k}_s, \hat{k}_i) & f_{ab}(\hat{k}_s, \hat{k}_i) \\ f_{ba}(\hat{k}_s, \hat{k}_i) & f_{bb}(\hat{k}_s, \hat{k}_i) \end{bmatrix} \tag{B-14}$$

Let $f_{aa}(\hat{k}_s, \hat{k}_i) = S_{11}$, $f_{ab}(\hat{k}_s, \hat{k}_i) = S_{12}$, $f_{ba}(\hat{k}_s, \hat{k}_i) = S_{21}$, and $f_{bb}(\hat{k}_s, \hat{k}_i) = S_{22}$, the Sinclair matrix is written as

$$S_2 = \begin{bmatrix} S_{11} & S_{12} \\ S_{21} & S_{22} \end{bmatrix} \tag{B-15}$$

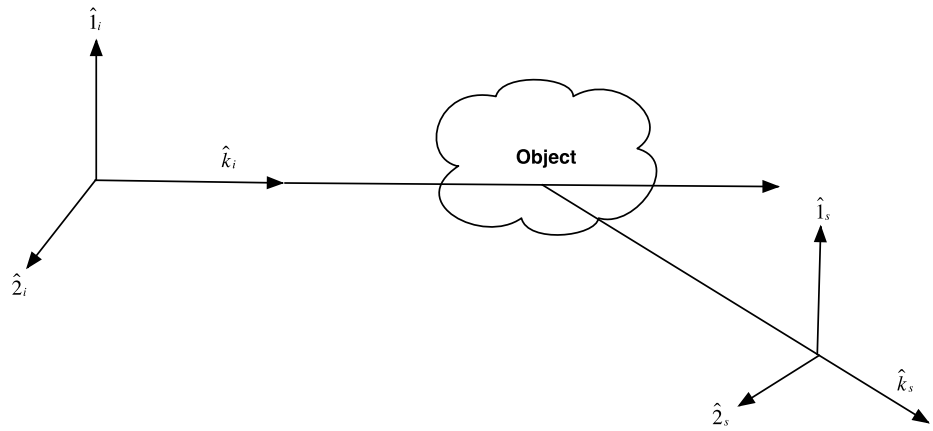

(a)

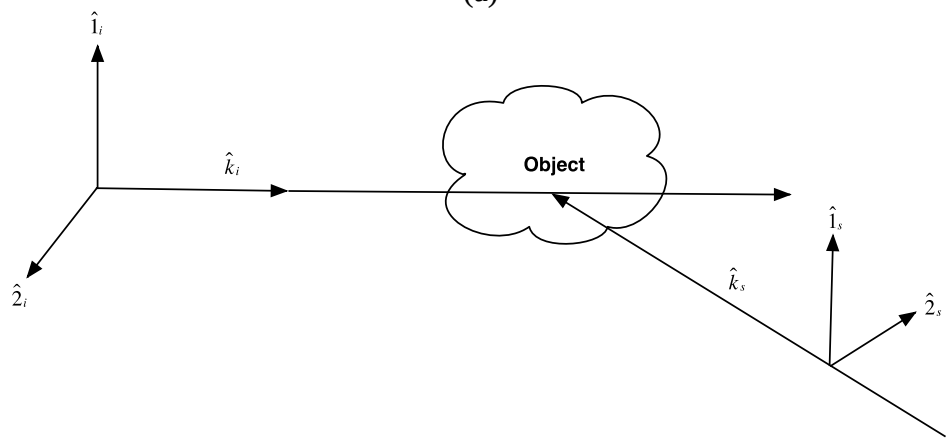

(b)

Figure B-2. Geometry for defining the orthonormal unit system based on scattering plane. (a) forward scatter alignment (FSA). (b) back scatter alignment (BSA).

Figure B-2 shows the geometry of the scattering coordinate frameworks, in which the forward scattering is shown in Figure B-2(a) while the backscattering one is shown in Figure B-2(b). The relationship between the Sinclair matrices in these two coordinates are written as,

$$S_{BSA} = \begin{bmatrix} -1 & 0 \\ 0 & 1 \end{bmatrix} S_{FSA} \tag{B-16}$$

where S_{BSA} and S_{FSA} are the Sinclair matrices of the backscattering and forward scattering respectively. We use the BSA convention in our thesis, which is because the BSA convention is for a monostatic configuration when the transmitting and receiving antennas are collocated (Lee & Pottier, 2009), whereas, the polarimetric SAR data we employ in this thesis are from a space borne satellite with its transmitting and receiving antennas collocated.

Reference

Lee, J. S., & Pottier, E. (2009). *Polarimetric radar imaging : from basics to applications*. Boca Raton: CRC Press.

Tsang, L., Kong, J. A., & Ding, K.-H. (2000). *Scattering of electromagnetic waves. Theories and applications*. New York: Wiley.

Appendix C: Polarimetric Scattering Matrices

As shown in Appendix B, the incident and scattered electric fields are connected by a 2×2 scattering matrix (Equation B-14). In the monostatic backscattering case, where the transmitting and receiving antennas are placed at the same location, the incident and scattered electric fields are expressed in the same orthogonal basis. Without loss of generality, let us define a local Cartesian basis for convenience, the 2×2 complex backscattering matrix can be expressed as

$$S = \begin{bmatrix} S_{HH} & S_{HV} \\ S_{VH} & S_{VV} \end{bmatrix} \tag{C-1}$$

The elements S_{HH} and S_{VV} produce the power return in the copolarized channels and the elements S_{HV} and S_{VH} produce the power return in the cross-polarized channels. If the role of the transmitting and the receiving antennas are interchanged, the reciprocity theorem requires that the backscattering matrix be symmetric, with $S_{HV} = S_{VH}$. In practice, not all radar targets are stationary, but generally are situated in a dynamically changing environment and are subject to spatial and temporal variations. Such scatters are called partial scatters or distributed targets. However, even if the environment is dynamically changing, one has to make assumptions concerning stationarity, homogeneity, and ergodicity. This can be analyzed more precisely by introducing the concept of space and time varying stochastic processes, where the target or the environment can be described by the second order moments of the fluctuations which will be extracted from the polarimetric coherency or covariance matrices. When the reciprocity is fulfilled, the coherency matrix and covariance are defined as,

$$\begin{aligned} T &= \langle k \cdot k^H \rangle \\ &= \frac{1}{2}\begin{bmatrix} |\langle S_{HH} + S_{VV}\rangle|^2 & \langle S_{HH} + S_{VV}\rangle\langle S_{HH} - S_{VV}\rangle^* & 2\langle S_{HH} + S_{VV}\rangle\langle S_{HV}\rangle^* \\ \langle S_{HH} - S_{VV}\rangle\langle S_{HH} + S_{VV}\rangle^* & |\langle S_{HH} - S_{VV}\rangle|^2 & 2\langle S_{HH} - S_{VV}\rangle\langle S_{HV}\rangle^* \\ 2\langle S_{HV}\rangle\langle S_{HH} + S_{VV}\rangle^* & 2\langle S_{HV}\rangle\langle S_{HH} - S_{VV}\rangle^* & 4|\langle S_{HV}\rangle|^2 \end{bmatrix} \end{aligned} \tag{C-2}$$

$$C = \langle \Omega \cdot \Omega^H \rangle = \begin{bmatrix} |\langle S_{HH} \rangle|^2 & \sqrt{2}\langle S_{HH} S_{HV}^* \rangle & \langle S_{HH} S_{VV}^* \rangle \\ \sqrt{2}\langle S_{HV} S_{HH}^* \rangle & 2|\langle S_{HV} \rangle|^2 & \sqrt{2}\langle S_{HV} S_{VV}^* \rangle \\ \langle S_{VV} S_{HH}^* \rangle & \sqrt{2}\langle S_{VV} S_{HV}^* \rangle & |\langle S_{VV} \rangle|^2 \end{bmatrix} \tag{C-3}$$

where H represents the conjugate transpose and k and Ω are defined as

$$k = \frac{1}{\sqrt{2}}[S_{HH} + S_{VV} \quad S_{HH} - S_{VV} \quad 2S_{HV}]^T$$
$$\Omega = \begin{bmatrix} S_{HH} & \sqrt{2}S_{HV} & 2S_{VV} \end{bmatrix}^T \tag{C-4}$$

The total power is defined as

$$Span = |k|^2 = |\Omega|^2 = |\langle S_{HH} \rangle|^2 + 2|\langle S_{HV} \rangle|^2 + |\langle S_{HV} \rangle|^2 \tag{C-5}$$

Meanwhile, there is a conversion between the covariance and coherency matrices, and it is defined as

$$C = \frac{1}{2}\begin{bmatrix} 1 & 1 & 0 \\ 0 & 0 & \sqrt{2} \\ 1 & -1 & 0 \end{bmatrix} \cdot T \cdot \begin{bmatrix} 1 & 0 & 1 \\ 1 & 0 & -1 \\ 0 & \sqrt{2} & 0 \end{bmatrix} \cdot \tag{C-6}$$

Appendix D: Eigen-Value Decomposition

The eigenvector-based decomposition proposed by Cloude and Pottier (1997) has been suggested as the alternative to the Huynen decomposition because the eigenvalue is automatically basis invariant. A set of three uncorrelated targets can be obtained through diagnosing the averaged coherency matrix. Then, its coherency matrix is written in the following two forms,

$$T_3 = U_3 \sum {U_3}^{-1}$$

$$T_3 = \sum_{i=1}^{3} \lambda_i \, u_i u_i^{*T} = T_{01} + T_{02} + T_{03} \tag{D-1}$$

A coherency matrix can be written as the summation of three independent targets each of which representing a deterministic scattering mechanism associated with a single equivalent scattering matrix. If only one eigenvalue is nonzero then the coherency matrix corresponding to the pure target and can be related to a single scattering matrix. If the other eigenvalues are equal, then three orthogonal scattering mechanisms with equal amplitudes; it means the target is random and no correlated polarized structure at all. The entropy and polarimetric angle (alpha) derived from the eigen-based decomposition led to a well-known classification Scheme in terms of entropy and alpha (Cloude & Pottier, 1997). The entropy and alpha, and their plot are shown as,

$$H = \sum_{i=1}^{3} -P_i log_3 P_i \, , P_i = \lambda_i \Big/ \sum_{j=1}^{3} \lambda_j , \bar{\alpha} = \sum_{i=1}^{3} P_i acos(e_i) \tag{D-2}$$

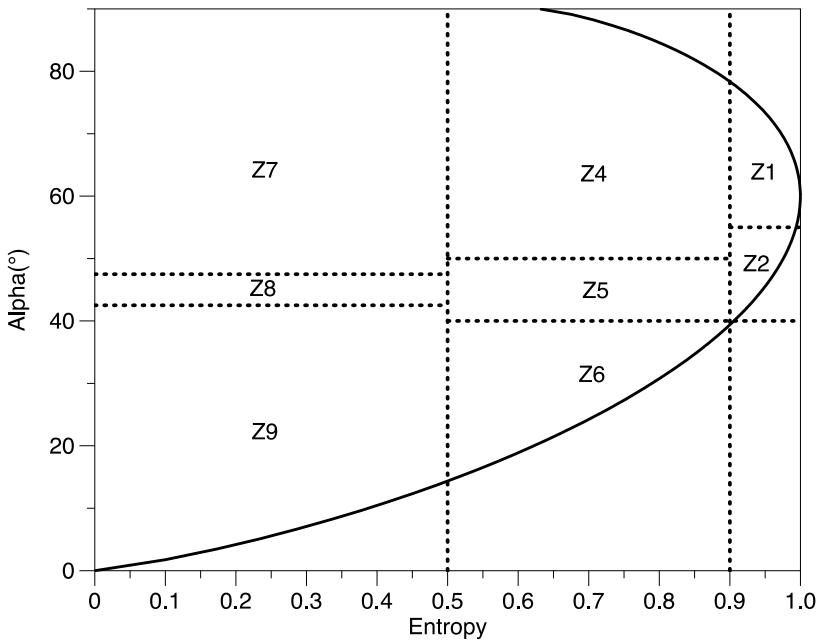

Figure D-1. H-$\boldsymbol{\alpha}$ zones.

They classify targets into eight different classes according the zones shown. Z1 is the high entropy multiple scattering. Z2 is the high entropy vegetation scattering. Z3 is the high entropy surface scatter. Z4 is the medium entropy multiple scattering. Z5 is the medium entropy vegetation scattering. Z6 is the medium entropy surface scatter. Z7 is the low entropy multiple scattering events. Z8 is the low entropy dipole scattering. Z9 is the low entropy surface scatter (Cloude & Pottier, 1997).

Reference

Cloude, S. R., & Pottier, E. (1997). An Entropy Based Classification Scheme for Land Applications of Polarimetric SAR. *IEEE Transactions on Geoscience and Remote Sensing*, *35*(1), 68-78.

Appendix E: Surface Parameters over Bare Soil

The surface parameters over bare soil are consisting of soil moisture, standard deviation of surface height and the surface correlation length. The TDR (Time-Domain Reflectometry) Probe shown in Figure E-1 is used to measure the volumetric soil moisture, while surface roughness is measured by a one-meter long needle profiler shown in Figure E-2.

Figure E-1. Time-Domain Reflectometry.

The TDR probe responds to the soil relative dielectric constant (ε_r), which is strongly dependent on the water content, many authors have shown that there is a simple relationship between the square root of ε_r, and the volumetric water content (mv), as follows:

$$\sqrt{\varepsilon_r} = a0 + a1 \times mv \qquad \text{(E-1)}$$

Where $a0$ and $a1$ are soil specific parameters being unique for each soil type. They are used to convert the sensor output (ε_r) into soil moisture readings. Table E-1 depicts the examples of these two parameters according to Roth et al. (1992) with mineral and organic soils.

Table E-1. Specific parameters for each soil type.

	$a0$	$a1$
Mineral soils	1.6	8.4
Organic soils	1.3	7.7

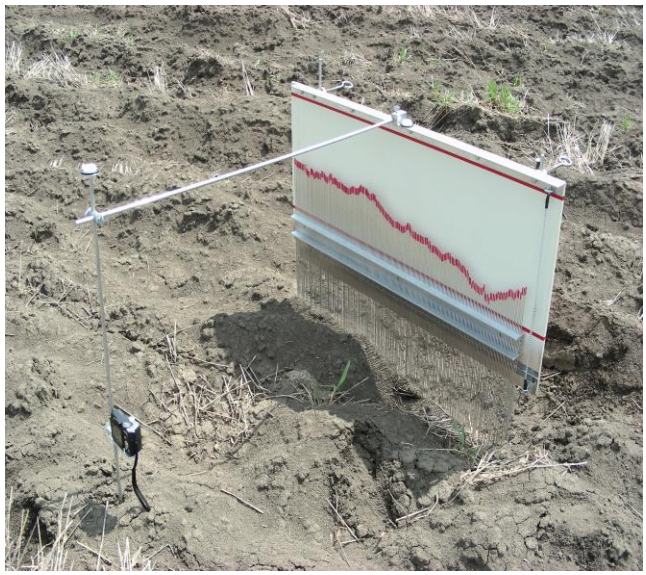

Figure E-2. Needle profiler.

The standard deviation of surface height and the surface correlation length describe the statistical variation of the random component of surface height relative to a reference surface. Consider a surface in the $x - y$ plane. For a statistically representative segment of the surface, of dimensions L_x and L_y, centered at the origin, the mean height of the surface is

$$\bar{z} = \frac{1}{L_x L_y} \int_{-L_x/2}^{L_x/2} \int_{-L_y/2}^{L_y/2} z(x, y)\, dxdy \tag{E-2}$$

and the second moment is

$$\overline{z^2} = \frac{1}{L_x L_y} \int_{-L_x/2}^{L_x/2} \int_{-L_y/2}^{L_y/2} z^2(x, y)\, dxdy \tag{E-2}$$

The standard deviation of the surface height (RMS) is then given by

$$\sigma = \sqrt{\overline{z^2} - \bar{z}^2} \tag{E-3}$$

For one-dimensional surface profile shown in Figure E-4, σ is computed, in practice, by digitizing the profile into discrete values $z_i(x_i)$, at an appropriate spacing Δx. Then, the standard deviation σ for the discrete one-dimensional case is given by

$$\sigma = \left[\frac{1}{N-1}\left(\sum_{i=1}^{N} (z_i)^2 - N(\bar{z})^2\right)\right]^{1/2} \tag{E-4}$$

where

$$\bar{z} = \frac{1}{N}\sum_{i=1}^{N} z_i \tag{E-5}$$

The normalized autocorrelation function for a one-dimension surface profile $z(x)$ is defined as

$$\rho(\acute{x}) = \frac{\int_{-L_x/2}^{L_x/2} z(x) z(x + \acute{x})\, dx}{\int_{-L_x/2}^{L_x/2} z^2(x)\, dx} \tag{E-6}$$

and is a measure of the similarity between the height z at a point x and at a point $\acute{x}$ distant from x. For the discrete case, the normalized autocorrelation function for a spatial displacement $\acute{x} = (j-1)\Delta x$. Then, the surface correlation length l usually is defined as the displacement $\acute{x}$ for which $\rho(\acute{x})$ is equal to $1/e$:

$$\rho(l) = 1/e \tag{E-7}$$

The correlation length of a surface provides a reference for estimating the statistical independence of two points on the surface; if the two points are separated by a horizontal distance greater than l, then their heights may be considered to be statistically independent of one another. In the extreme case of a perfectly smooth surface, every point on the surface is correlated with every other point with a correlation coefficient of unity. Hence, $l = \infty$ in this case.

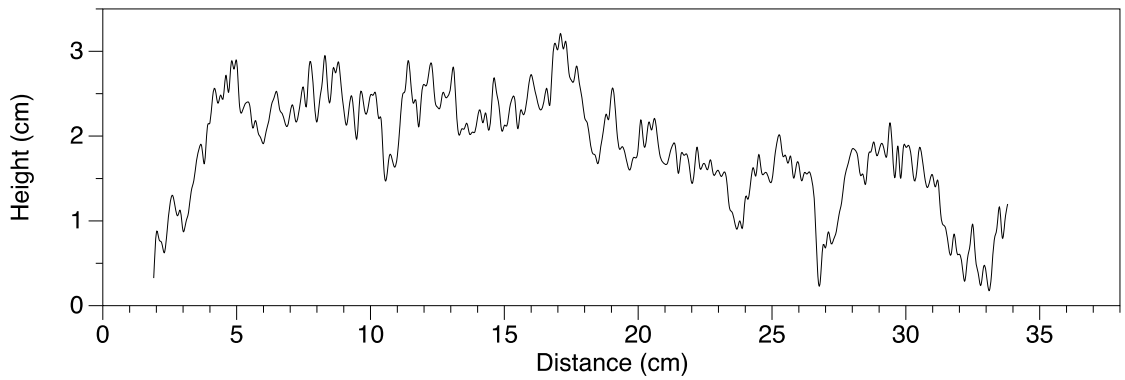

Figure E-3. Surface height profile.

Reference

Roth, C. H., Malicki, M. A., & Plagge, R. (1992). Empirical Evaluation of the Relationship between Soil Dielectric Constant and Volumetric Water Content as the Basis for Calibrating Soil Moisture Measurements by TDR. *Journal of Soil Science*, *43*(1), 1-13.

Ulaby, F. T., Moore, R. K., & Fung, A. K. (1986). *Microwave remote sensing: Active and passive. Volume 3 - From theory to applications*. New York: Addison-Wesley Pub. Co., Advanced Book Program/World Science Division.

Appendix F: Surface Roughness Measurement

To measure the surface roughness, three steps are required: geometric correction, digitalization, and calculation. The PCI Geomatics software is adopted.

GEOMETRIC CORRECTION

As surface roughness needle profiler photo images contain geometric distortion, we perform geometric correction to the images. The geometric correction is carried out in a two-step process:

(1) Transformation of Pixel Coordinates: The geometric relationship between the input pixel location (line number and pixel number) and the associated map coordinate of this same point (x and y) must be identified. For example, polynomial functions will be fitted to describe the relationship. Then, each pixel in the target (georeferenced) image can be transformed according to the polynomial (1st order or higher order) to determine a sampling location in the input (uncorrected) image.

(2) Resampling: Resampling is used to determine the pixel brightness values for the georeferenced (output) image based on the spatial interpolation from the uncorrected (input) image (using nearest neighbour, bilinear or cubic convolution method).

Here I use an example: We will register the uncorrected image: P1030848.pix, to the corrected image: ref838.pix.

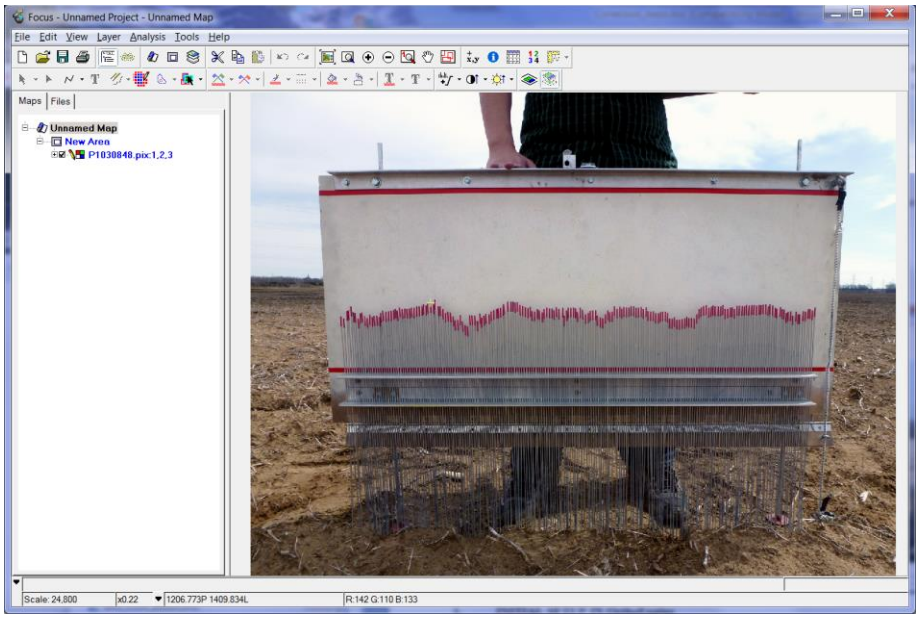

Figure F-1. Uncorrected image: P1030848.pix.

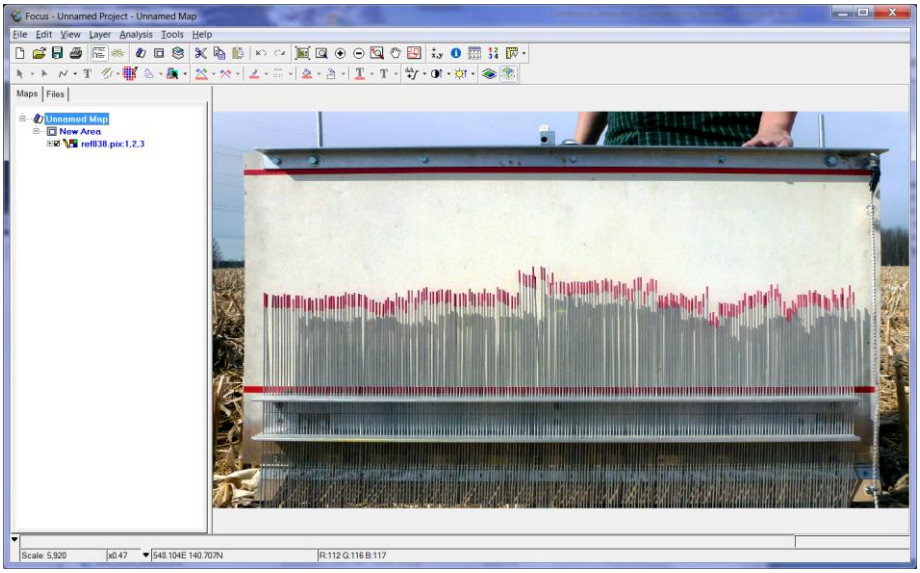

Figure F-2. The reference image: ref838.pix.

1. INITIAL SETUP IN OrthoEngine

1.1. Start OrthoEngine. The first step is setup, which involves choosing what kind of geometric correction or registration you will be doing with **OrthoEngine**. You will need to setup your new project, by choosing File>New. This will bring up the Project

Information panel. Make sure to name your project, for example 848 and save the *.prj file in a suitable location. Choose Polynomial Math Modeling Method and click OK.

1.2. Now you will need to set the Projection for the Output image and the GCPs. Click on Earth Model. Select "WGS 1984" (D000) and accept. (You can click on the "Set GCP Projection Based on Output Projection" button to ensure that your projections are the same.) Set the output pixel and line spacing to 0.5 meter each. Here 1 meter represents 1 mm. Click "OK".

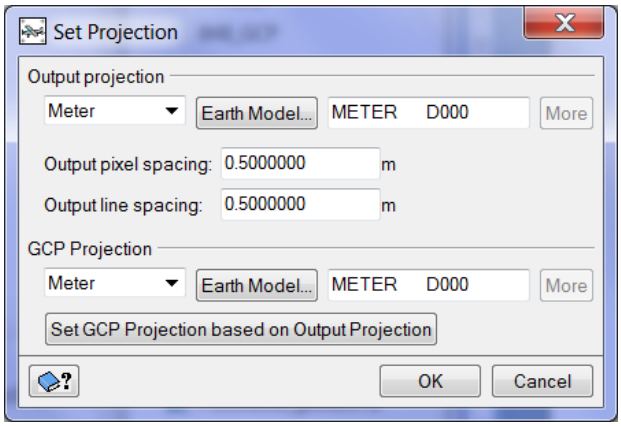

Figure F-3. Setting up projection.

1.3. Now we can open the image we would like to geometrically correct. In the Processing Step drop down box, select GCP Collection and click on the "Open new or existing file" button. '**Select Uncorrected Image**' and click on the "New Image" button. Select P1030848.pix to load it into the list box. Now open the image using the 'Quick Open and Close' Button. You should now be able to browse the image in the Viewer window. Try clicking on a point in the image. You should see a red cross where you clicked.

2. COLLECTING GROUND CONTROL POINTS

2.1. To begin collecting GCPs, select "GCP Collection" in the Processing step drop-down box, and select the "Collect GCPs manually" button. For "Ground control source", select "geocoded image" from the pull down menu. Then specify the reference image "ref838.pix". Click "Open". Select the RGB channels. Click on "Load and close".

Using your image Viewer and the reference image, find a common point that is easily discernible on both. Zoom in close enough so that you are within one pixel accuracy.

2.2. Once you are confident that you have located the right point on the imagery, click on the location in the Viewer, and select the “Use Point” button at the top of the Viewer to transfer uncorrected coordinates (pixel and line numbers) to the GCP Collection panel. You will locate the matching point in the uncorrected and geocoded image by using the viewers for both. Zoom into a common point on the reference image and select “Use Point”. Make sure your coordinates appear in the GCP collection panel. Select "accept". You will see this point added to the list of accepted GCPs and the GCP ID will automatically increase to the next ID number. Repeat these steps until you have collected enough GCPs. You should select at least 6 GCPs: Four at the four corners (such as the ends of the red lines) and two in the middle. GCPs should spread over the image. Use 1st order polynomial in most cases. You can select more points and use 2nd order or 3rd order polynomial if there is obvious distortion in the image. For a more accurate result, the RMS errors should be less than 1 pixel, or 0.5 m.

2.3. Once you have collected enough GCPs, save your project by using the **File** menu in the main OrthoEngine panel. By saving your project, you will also be saving your GCPs as well. You will also need to export your GCPs to a text file. You will need to close the “GCP Collection” window before you can export. In the main OrthoEngine panel, select **Options**>Export>GCPs… Make sure to export as a text file. Name the export file “848.txt” (don’t forget to add the .txt extension) and Apply the default formatting.

2.4. Within OrthoEngine, the actual geometric correction (registration) is done using the ‘**Geometric Correction’** panel. You can access this by selecting “Geometric Correction” in the drop-down box. Select the “Schedule geometric correction” button. In the following window, add your uncorrected image P1030848 to the “Images to Process” list box. Make sure you include all channels (six 8-bit channels). Name the new “corrected” file as oP1030848.pix. You can set your Resampling Method to “Nearest” if you use first order polynomial. Please set the output extent to: Upper left: -54 X, 486 Y; Lower right: 1150 X, -200 Y. See Figure below.

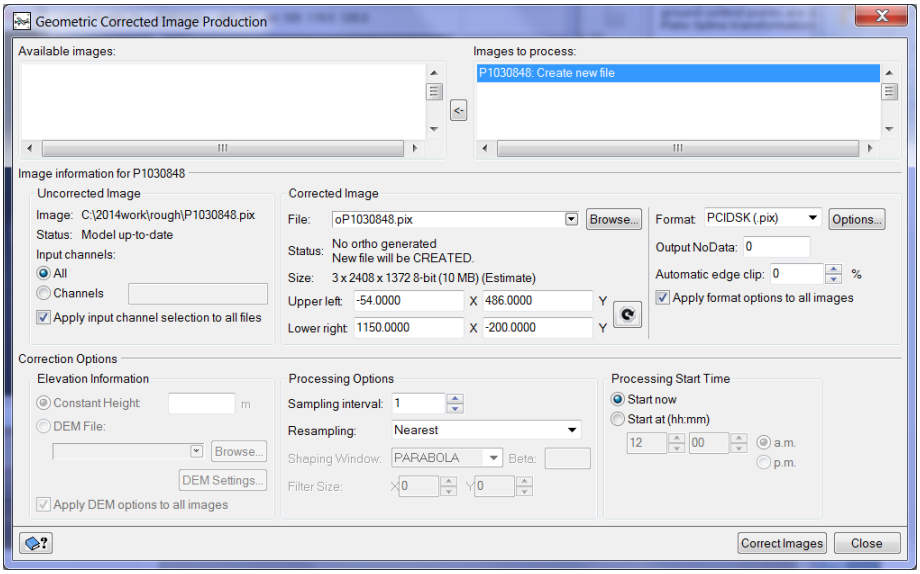

Figure F-4. Setting the output image extent: upper left and lower right coordinates.

Now you can correct the image. Then open oP1030848.pix in Focus.

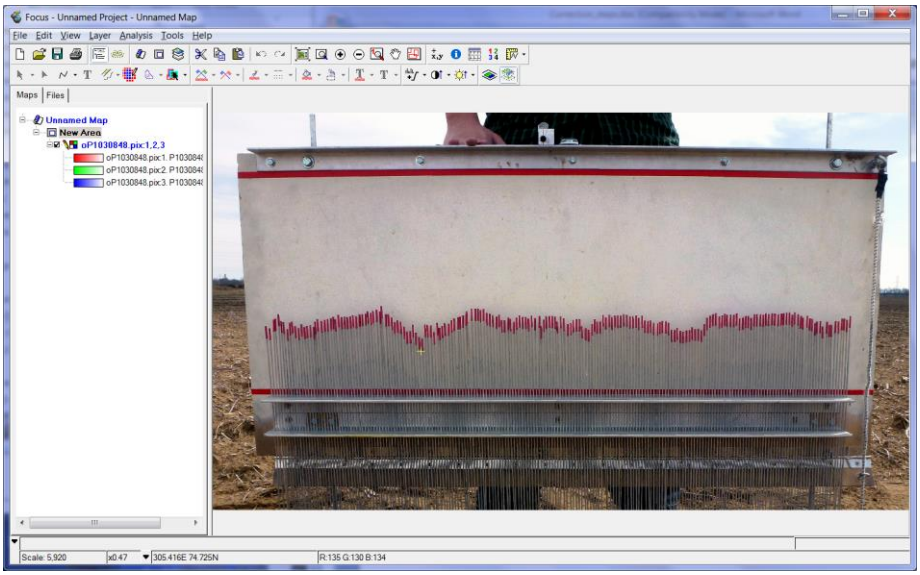

Figure F-5. Corrected image: oP1030848.pix.

IMAGE DIGITIALIZATION

1. Open the corrected image oP1030848 using **Focus** in PCI,

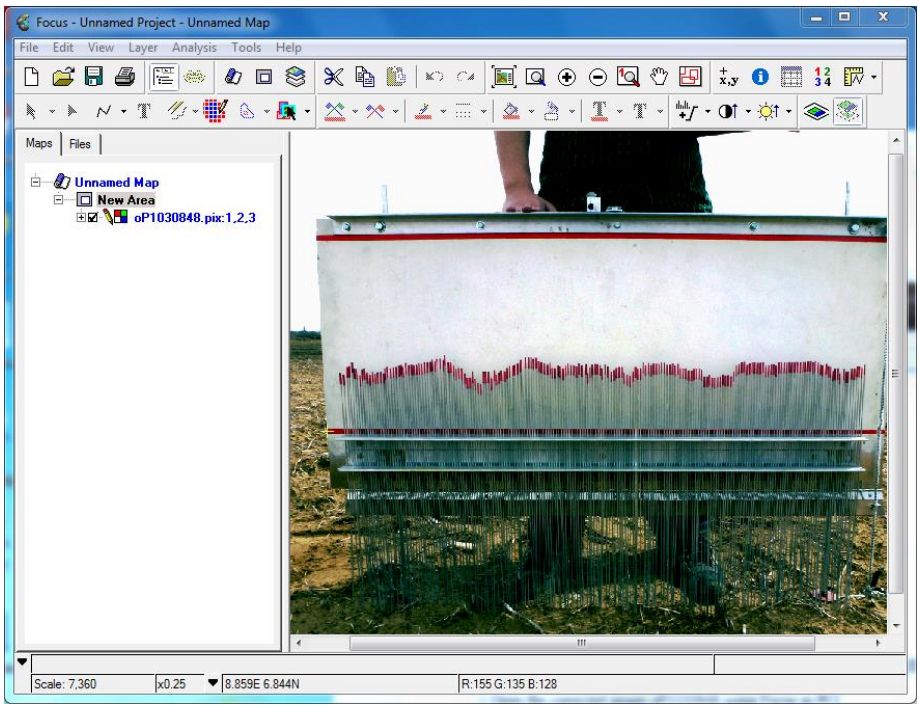

2. Right click "**New Area**", and click "**New Vector layer**"

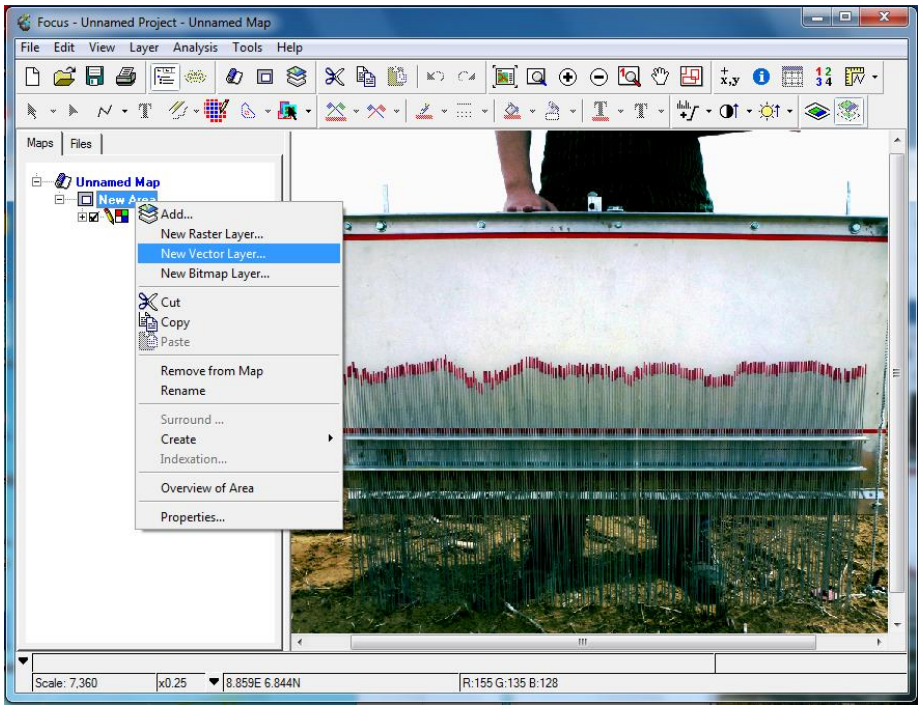

3. A dialog is opened and select "**Point**" and "**Use Layer Georeferencing** " then click "**Ok**"

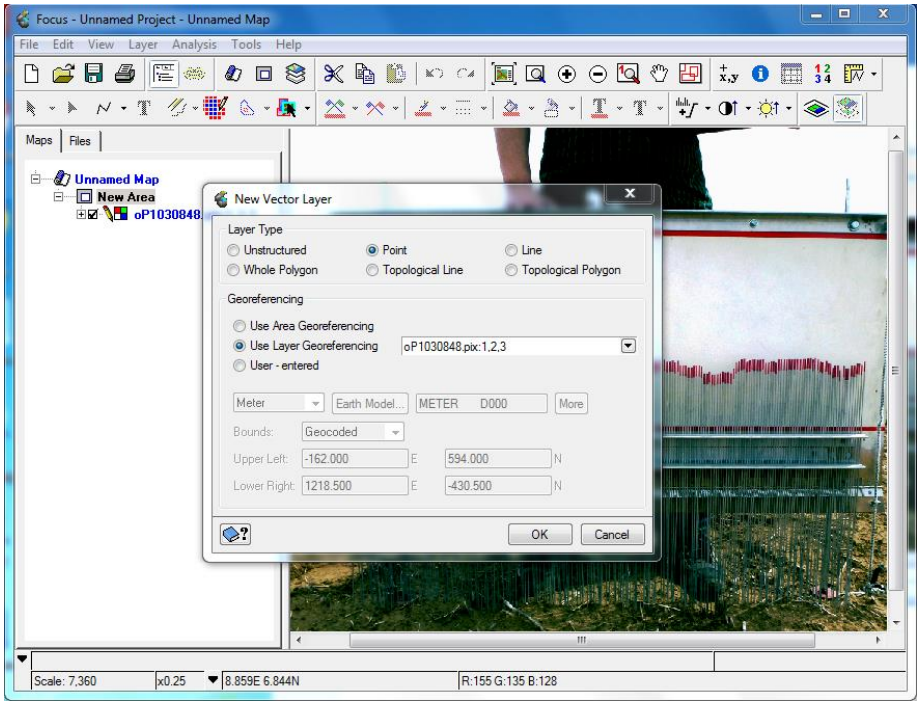

4. Select "**Point**" in the "**Tool Bar**"

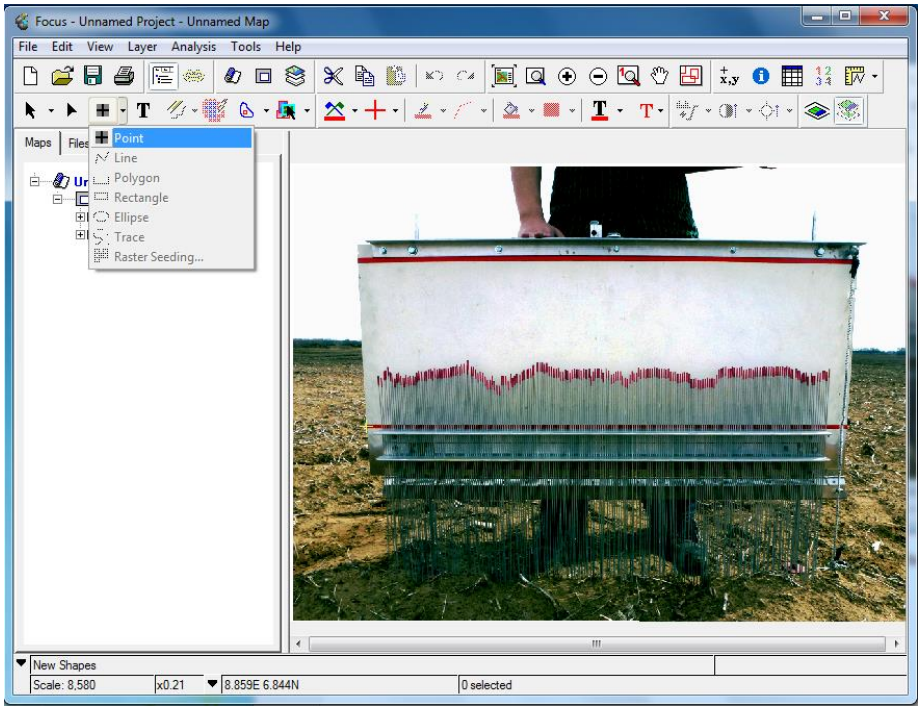

5. Digitalize the point in order from left to right (**MUST BE IN ORDER!!**), and **ONLY DIGITALIZE THE POINTS ON TOP OF PIN**.

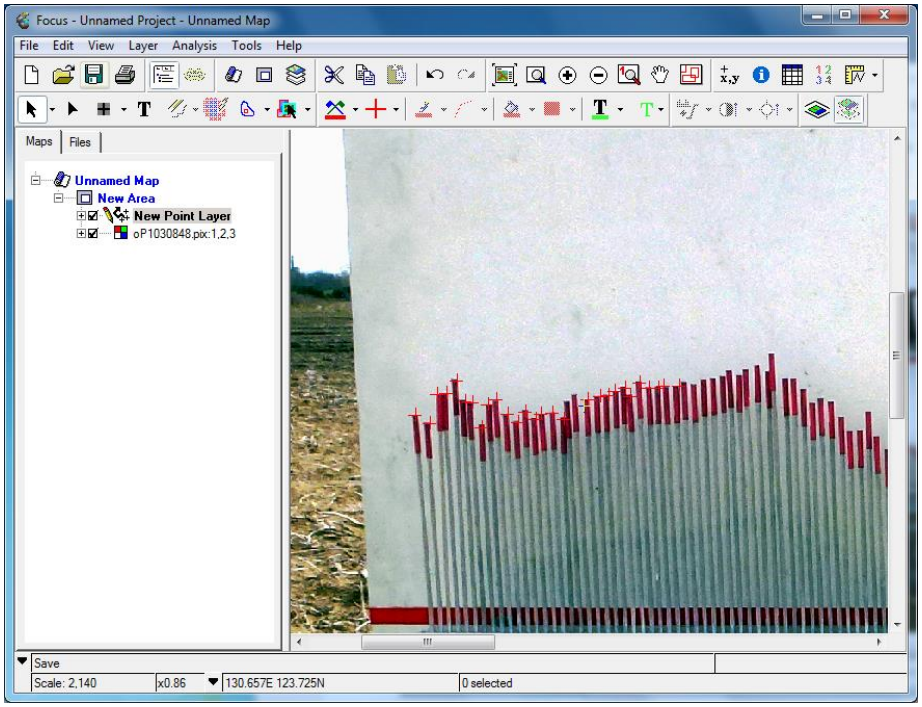

6. After you finish all points, right click "**New Point Layer**", and click "**Save as…**"

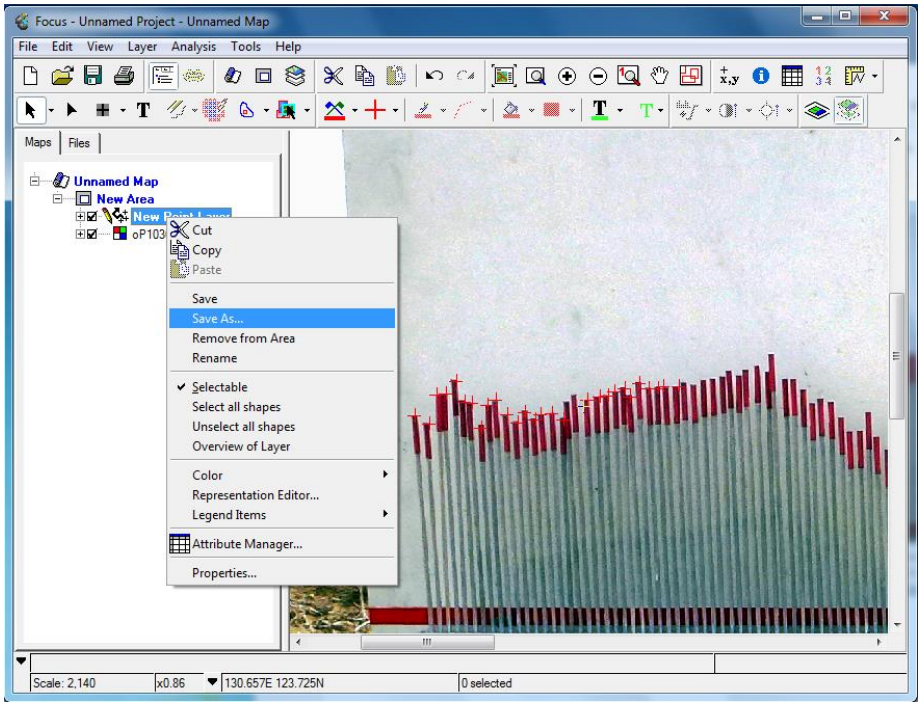

7. Do not check any check-box in the opened dialog, and **File Format** must be "**Generic ASCII Vector (.txt)**", and output file is named via "**Site Name + Photo #**".

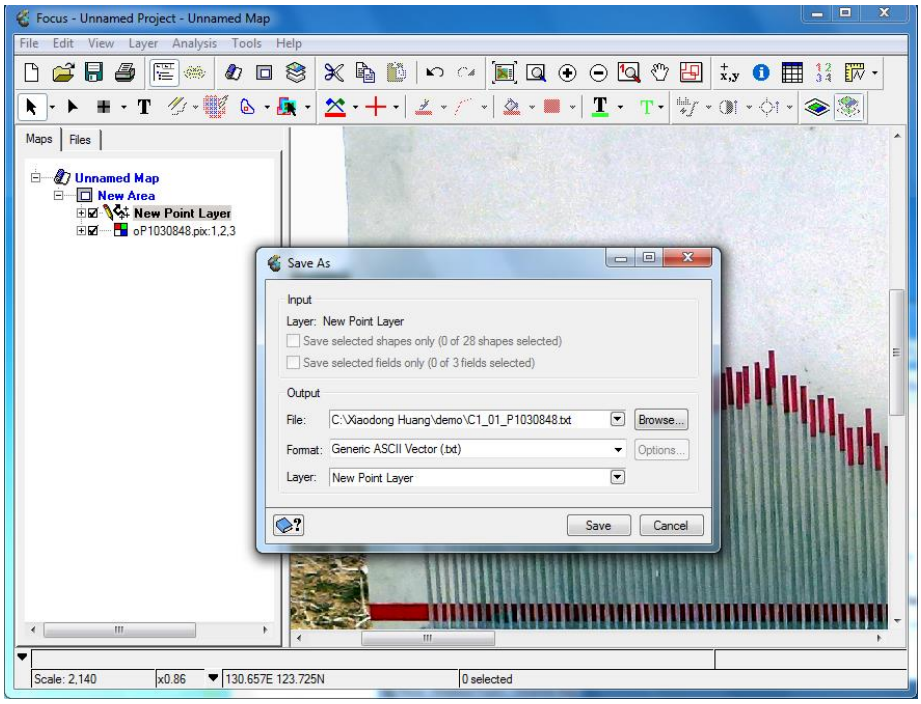

8. Please check the output "**C1_01_P1030848.txt**"file is looking like Figure F-6.

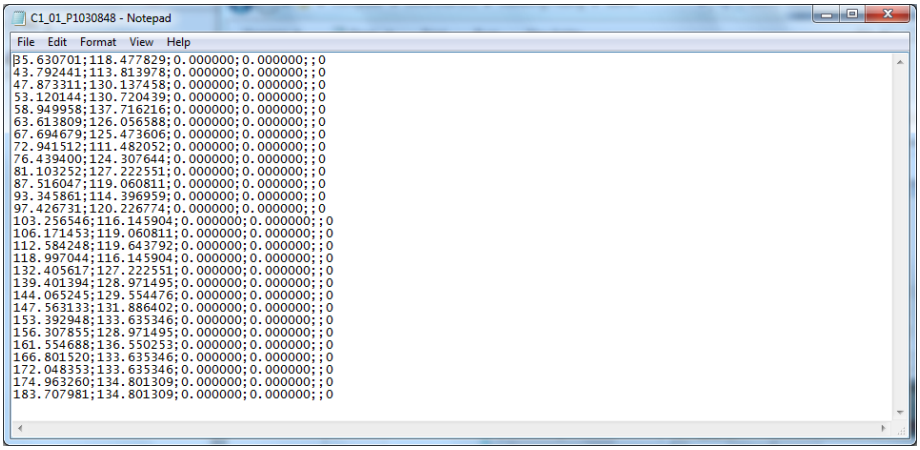

Figure F-6. C1_01_P1030848.txt

<u>SOIL ROUGHNESS CALCUALTION</u>

The roughness is calcuated by the programm we made through reading the text file generated in Step 2.

1. Open the "**surface_roughenss.exe**".

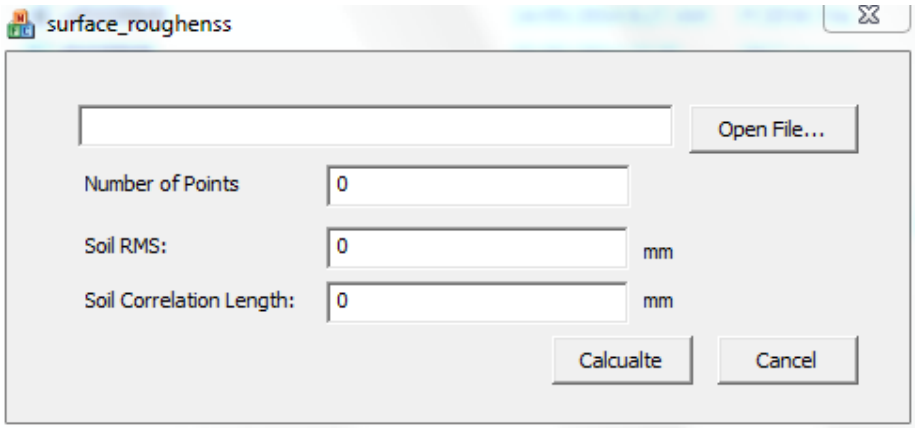

2. Click "Open File", select the "**C1_01_P1030848.txt**", and click "**Calculate**"

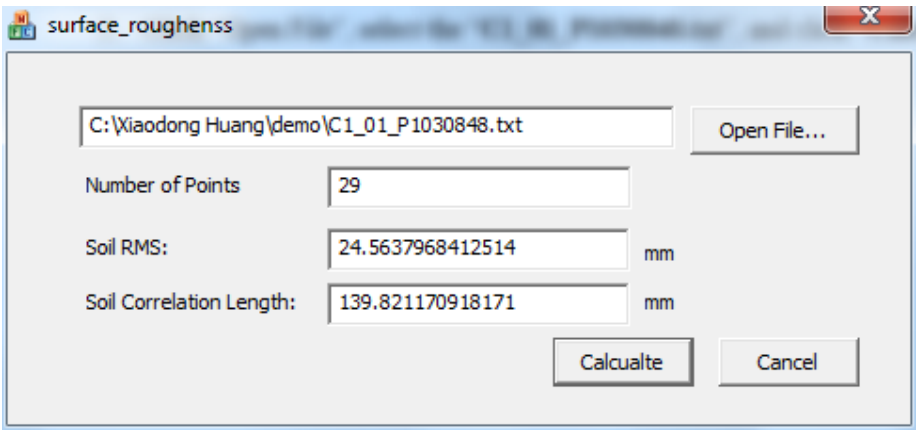

Appendix G: Copyright Releases from Publications

Chapter 2:

From: Gwen Weerts
Date: April 14, 2016 at 11:04:59 PM GMT+8
To: "Xiaodong Huang"
Cc: Eric Lochridge

Subject: RE: JARS 15179R Decision Letter

Dear Xiaodong,

Yes, SPIE copyright permits authors to reuse published material in a PhD thesis. Please cite the original publication in your references:

X. Huang, J. Wang, and J. Shang, "A simplified adaptive volume scattering model and scattering analysis of crops over agricultural fields using the RADARSAT-2 polarimetric SAR imagery,"
J. Appl. Remote Sens. **9**(1), 096026(2015), http://dx.doi.org/10.1117/1.JRS.9.096026.

Regards,

Gwen Weerts
Managing Editor, Journals
SPIE

SPIE is the international society for optics and photonics.
http://SPIE.org

Chapter 3 and Chapter 4:

The IEEE does not require individuals working on a thesis to obtain a formal reuse license, however, you must follow the requirements listed below:

Full-Text Article

If you are using the entire IEEE copyright owned article, the following IEEE copyright/ credit notice should be placed prominently in the references: © [year of original publication] IEEE. Reprinted, with permission, from [author names, paper title, IEEE publication title, and month/year of publication]

Only the accepted version of an IEEE copyrighted paper can be used when posting the paper or your thesis on-line.

In placing the thesis on the author's university website, please display the following message in a prominent place on the website: In reference to IEEE copyrighted material which is used with permission in this thesis, the IEEE does not endorse any of [university/educational entity's name goes here]'s products or services. Internal or personal use of this material is permitted. If interested in reprinting/republishing IEEE copyrighted material for advertising or promotional purposes or for creating new collective works for resale or redistribution, please go to http://www.ieee.org/publications_standards/publications/rights/rights_link.html to learn how to obtain a License from RightsLink.

If applicable, University Microfilms and/or ProQuest Library, or the Archives of Canada may supply single copies of the dissertation.

http://www.ieee.org/publications_standards/publications/rights/permissions_faq.pdf

Curriculum Vitae

Name:	Xiaodong Huang
Post-secondary Education and Degrees:	China University of Geosciences Wuhan, Hubei, China 2006-2010 B.E. China University of Geosciences Wuhan, Hubei, China 2010-2013 M.E. The University of Western Ontario London, Ontario, Canada 2013-2016 Ph.D.
Honours and Awards:	Professor Elaine Bjorklund Scholarship 2015
Related Work Experience	Teaching Assistant The University of Western Ontario 2013-2015 Research Assistant The University of Western Ontario 2013-2016

Publications:

Peer reviewed journal papers:

Huang, X., Wang, J, & Shang, J. (2016). Application of Polarization Signature to Crop Monitoring Classification Using Multi-Temporal C-Band Polarimetric RADARSAT-2 Imagery. *Remote Sensing of Environment*. Major Revision.

Huang, X., Wang, J, & Shang, J. (2016). An Adaptive Two-Component Model-Based Decomposition on Soil Moisture Estimation for C-Band RADARSAT-2 Imagery Over Wheat Fields at Early Growing Stages. *Geoscience and Remote Sensing Letters, IEEE*. 13(3), 414-418.

Huang, X., Wang, J, & Shang, J. (2015). An Integrated Surface Parameter Inversion Scheme Over Agricultural Fields at Early Growing Stages by Means of C-Band

Polarimetric RADARSAT-2 Imagery. *Geoscience and Remote Sensing, IEEE Transactions on*. 54(5), 2510-2528.

Huang, X., Wang, J, & Shang, J. (2015). Simplified Adaptive Volume Scattering Model and Scattering Analysis of Crops over Agricultural Fields Using The RADARSAT-2 Polarimetric SAR Imagery. Journa*l of Applied Remote Sensing*, 9(1):096026-1-096026-18.

Huang, X., Liu, X., Chen, Q., & Chen, Q. (2013). An Integrated Multi-Characteristics Buildings Segmentation Model of PolSAR Images. *Geomatics and Information Science of Wuhan University*, 38(4), 450-454. In Chinese.

Liu, X., **Huang, X.**, Chen, Q., & Jiang, P. (2013). Inconsistency Elimination in Freeman Decomposition for Polarimetric SAR Data Based on Normalization Method. *Geomatics and Information Science of Wuhan University*, 38(3), 257-261. In Chinese.

Liu, X., **Huang, X.**, Chen, Q., & Chen, Q. (2012). Three-Component Model-Based Decomposition Integrating De-Orientation and Generalized Volume Scattering Model. *Journal of Electronics and Information Technology*, 34(10), 2451-2457. In Chinese.

Conference papers:

Huang, X., Wang, J, & Shang, J. (2016, June). A Multi-Temporal Supervised Binary-Tree Classification Scheme for Polarimetric SAR with Maximum Difference of Polarimetric Signature. *In EUSAR 2016; 11th European Conference on Synthetic Aperture Radar*. Poster.

Huang, X., Wang, J, & Shang, J. (2015, October). A Supervised Binary-Tree Classification Scheme Based on Maximum Difference of Polarimetric Signarue.*10th ASAR WORKSHOP*. Montreal, Canada. Oral presentation.

Huang, X., Wang, J, & Shang, J. (2015, July). Surface Parameter Inversion Scheme Over Agricultural Fields with Crop Residues and under Low Vegetation Cover from RADARSAT-2 Imagery. *In Geoscience and Remote Sensing Symposium (IGARSS), 2015 IEEE International*.

Huang, X., Wang, J, & Shang, J. (2015, May). Evaluation of The Calibrated Integral Equation Model over Agricultural Fields for Surface Parameter Retrieval Using Polarimetric SAR. *In 36th International Symposium on Remote Sensing of Environment (ISRSE)*. Berlin, Germany.

Huang, X., & Wang, J. (2014, June). An Adaptive Volume Scattering Model for Fully Polarimetric Radarsat-2 Data. *In EUSAR 2014; 10th European Conference on Synthetic Aperture Radar; Proceedings of* (pp. 1-4). VDE.

Huang, X., Liu, X., & Chen, Q. (2013, July). A Four-Component Decomposition Integrating Selective De-orientation and Generalized Volume Scattering. *In Geoscience and Remote Sensing Symposium (IGARSS), 2013 IEEE International* (pp. 2447-2450).